



Title: Combined application of structural geology, the mechanics of discrete media and the analysis of in situ stresses and displacements for the modelling of mechanical behaviour of fractured rock masses

Hang Thi Thu Tran

► **To cite this version:**

Hang Thi Thu Tran. Title: Combined application of structural geology, the mechanics of discrete media and the analysis of in situ stresses and displacements for the modelling of mechanical behaviour of fractured rock masses. Modeling and Simulation. Université Montpellier 2, 2013. English. NNT : . tel-01799420

HAL Id: tel-01799420

<https://hal.science/tel-01799420>

Submitted on 24 May 2018

HAL is a multi-disciplinary open access archive for the deposit and dissemination of scientific research documents, whether they are published or not. The documents may come from teaching and research institutions in France or abroad, or from public or private research centers.

L'archive ouverte pluridisciplinaire **HAL**, est destinée au dépôt et à la diffusion de documents scientifiques de niveau recherche, publiés ou non, émanant des établissements d'enseignement et de recherche français ou étrangers, des laboratoires publics ou privés.

UNIVERSITY OF MONTPELLIER II
--SCIENCES AND TECHNICS OF LANGUEDOC--

THESIS

For the degree of

DOCTOR OF THE UNIVERSITY OF MONTPELLIER II

Discipline: Mechanics, Mechanical Engineering, Civil Engineering

Doctorate School: I2S – Information, Structures, Systems

By

Thi Thu Hang TRAN

22 April 2013

Title:

Combined application of structural geology, the mechanics
of discrete media and the analysis of *in situ* stresses and displacements
for the modelling of mechanical behaviour of fractured rock masses

BOARD OF EXAMINERS

André CHRYSOCHOOS	Professor, University of Montpellier II	President
Véronique MERRIEN-SOUKATCHOFF	Professor, “ <i>Ecole des Mines de Nancy</i> ”	Reporter
Didier HANTZ	Lecturer – HDR, University of Joseph Fourier	Reporter
Muriel GASC-BARBIER	Director of research, CETE-SO, LRPC of TOULOUSE	Examiner
Frédéric DUBOIS	Engineer of research, CNRS – LMGC, University of Montpellier II	Co-supervisor, Examiner
Marc VINCHES	Lecturer – HDR, “ <i>Ecole des Mines d’Alès</i> ”	Supervisor, Examiner

Realisation at the “*Ecole des Mines d’Alès*”, France

UNIVERSITY OF MONTPELLIER II
--SCIENCES AND TECHNICS OF LANGUEDOC--

THESIS

For the degree of

DOCTOR OF THE UNIVERSITY OF MONTPELLIER II

Discipline: Mechanics, Mechanical Engineering, Civil Engineering

Doctorate School: I2S – Information, Structures, Systems

By

Thi Thu Hang TRAN

22 April 2013

Title:

Combined application of structural geology, the mechanics
of discrete media and the analysis of *in situ* stresses and displacements
for the modelling of mechanical behaviour of fractured rock masses

BOARD OF EXAMINERS

André CHRYSOCHOOS	Professor, University of Montpellier II	President
Véronique MERRIEN-SOUKATCHOFF	Professor, “ <i>Ecole des Mines de Nancy</i> ”	Reporter
Didier HANTZ	Lecturer – HDR, University of Joseph Fourier	Reporter
Muriel GASC-BARBIER	Director of research, CETE-SO, LRPC of TOULOUSE	Examiner
Frédéric DUBOIS	Engineer of research, CNRS – LMGC, University of Montpellier II	Co-supervisor, Examiner
Marc VINCHES	Lecturer – HDR, “ <i>Ecole des Mines d’Alès</i> ”	Supervisor, Examiner

Realisation at the “*Ecole des Mines d’Alès*”, France

ABSTRACT

Aimed at studying the mechanical behaviour of rock mass and considering the presence of the discontinuity network in the intact rock, this research concentrates on how the rock can be represented in suitable geometrical models, on the basis of site measurements, and then appropriately analysed using computer tools developed for the study of granular media.

The first chapter deals with a bibliographical study on fractured rock and tunnel engineering. Different computational methods of rock mechanics are introduced. Simultaneously, three principal approaches for tunnel structural design are recalled. These studies lead to the proposition of a methodology from the *in situ* investigation to in-door modelling and mechanical analysis, presented in the second chapters. The rock mass is first geometrically represented through the distribution of discontinuities in the rock mass and the use of the RESOBLOK code based on the Discrete Fracture Network method. Mechanical models of rock mass are then presented from the data of historical studies on the rock mass and from laboratory and *in situ* measurements. The 3D computational models are analysed using the LMGC90 based on the Non Smooth Contact Dynamics method. The first two applications of the methodology are introduced: the generation of the numerical rock for the simulation of the triaxial compression test, and the simulation of multi-phase excavation of rock tunnel. The proposed methodology has been applied on the white marble of Saint B  at (Haute Garonne, France) and the initial results are given in the third chapter. The mechanical responses of the numerical rock mass are analysed and the bulk behaviour of the rock is evaluated.

Keywords: Rock mechanics, tunnel, fractured rock, *in situ* investigation, measurement, scan-line sampling, geo-statistics, clustering, geometrical modelling, mechanical modelling, simulation, mechanical analysis, mechanical behaviours, stability analysis, Discrete Fracture Network (DFN) method, RESOBLOK, Non-Smooth Contact Dynamics (NSCD) method, LMGC90, Saint B  at.

Realisation at the “*Ecole des Mines d’Al  s*”, 6 avenue de Clavi  res, 30319 Al  s Cedex, France.

RESUME

Titre : Application combinée de la géologie structurale, de la mécanique des milieux discrets et de l'analyse de contraintes et déplacements in situ à la modélisation du comportement mécanique de massifs rocheux fracturés

Résumé :

Pour étudier le comportement mécanique des massifs rocheux, en prenant en compte le réseau des discontinuités au sein de la roche intacte, cette recherche a pour objectif la représentation du massif par des modèles géométriques basés sur des relevés de terrain et l'analyse de ces modèles par l'utilisation d'outils informatiques adaptés pour les milieux granulaires.

Le premier chapitre fait l'état de l'art des roches fracturées, des méthodes numériques de la mécanique des roches et des approches du calcul de structure d'un tunnel. Ces études conduisent à la proposition d'une méthodologie depuis les recherches in situ jusqu'à la modélisation et l'analyse mécanique, présentée dans le deuxième chapitre. Le massif rocheux est d'abord représenté géométriquement par la distribution de ses discontinuités, et l'utilisation du logiciel RESOBLOK basé sur la méthode du Réseau de Fractures Discrètes. Les modèles mécaniques de massifs rocheux sont ensuite présentés à partir des données sur les études de l'histoire du massif, et des mesures faites sur site et en laboratoire. Les modèles numériques en 3D sont analysés par l'utilisation du logiciel LMGC90 basé sur la méthode de la Dynamique des Contacts Non Réguliers. Les premières applications de la méthodologie sont exposées : la création d'une roche numérique pour simuler un essai de compression triaxiale, et la simulation d'une excavation multi phases d'un tunnel au rocher. La méthodologie proposée a été appliquée sur le marbre blanc de Saint Bât (Haute Garonne, France) et les résultats préliminaires sont donnés dans le chapitre trois. Les réponses mécaniques du massif numérique sont analysées et son comportement est caractérisé.

Mots clés: Mécanique des roches, tunnel, roche fracturée, recherche in situ, ligne-scannée, géostatistique, regroupement, modélisation géométrique, modélisation mécanique, simulation, analyse mécanique, comportement mécanique, analyse de stabilité, méthode du Réseau de Fractures Discrètes (DFN), RESOBLOK, méthode de la Dynamique des Contacts Non-Réguliers (NSCD), LMGC90, Saint Bât.

Travaux réalisés à l'**Ecole des Mines d'Alès**, 6 avenue de Clavières, 30319 Alès Cedex, France.

ACKNOWLEDGEMENTS

This doctoral thesis was carried out at the *Ecole des Mines d'Alès* (France) from April 2010 to April 2013, in close collaboration with the LMGC laboratory, University of Montpellier 2 and CNRS (France), with the financial support from the overseas training programme of the Vietnamese government (the “322 grant”). I am grateful to all the facilities that my country has given to me.

I would like to express my gratitude to the following individuals and organisations for their support and assistance:

Marc VINCHES, my supervisor (*Ecole des Mines d'Alès*) and Frédéric DUBOIS, my co-supervisor (University of Montpellier 2) for their guidance with a special kindness, patience and respect that I will never forget.

André CHRYSOCHOOS (University of Montpellier 2), Véronique MERRIEN-SOUKATCHOFF (*Ecole des Mines de Nancy*), and Muriel GASC-BARBIER (LRPC of Toulouse) for participating in the thesis committee and for giving me precious advice.

Véronique MERRIEN-SOUKATCHOFF (*Ecole des Mines de Nancy*) and Thoma KORINI (Faculty of Geology and Mining, Tirana, Albania) for providing help on the use and on the generation of the geometrical modelling on RESOBLOK.

CALAMI team (CNRS at the LMGC laboratory, University of Montpellier 2) for the contribution to the connection between RESOBLOK and LMGC90 and for their help in using LMGC90.

Muriel GASC-BARBIER, Jérôme GUITTARD, and Didier VIRELY (LRPC of Toulouse) for giving me all the related technical documents of the project of the future tunnel of Saint B  at (France).

St  phanie MAHE (*Ecole des Mines d'Al  s*) for the participation in the survey team realised in the underground exploitation site of the OMG factory and for the discussions on geology and on the project of the future tunnel of Saint B  at.

Ecole des Mines d'Al  s for the warm welcome, convenient working conditions and supports during my stay in France.

CNRS (LMGC laboratory, University of Montpellier 2) and ARMINES for financing my attendance at the 9th Euroconference on Rock Physics and Geomechanics in Trondheim (Norway) in 2011.

All my friends for bringing help and joy during three years of nostalgia.

Last but not the least, I would like to deeply thank my family for encouraging and supporting me spiritually throughout my life.

TABLE OF CONTENTS

INTRODUCTION	1
1. Starting point	1
2. Problem definition	2
3. Scope and objectives of research	2
4. Research methodology	3
5. Thesis Organization	3
CHAPTER 1:	5
STATE-OF-THE-ART OF THE FRACTURED ROCK ENGINEERING	
1.1. Nature of fractured rock mass	5
1.1.1. Structure of rock and its nature	5
1.1.2. Presence and influences of discontinuities on the rock mass	10
1.1.2.1. Discretization of intact rock medium	10
1.1.2.2. Modification of mechanical characteristics	11
1.1.2.3. Instability mechanisms	13
1.1.3. Scale effect in rock mechanics	15
1.1.4. Failure behaviours of the fractured rock mass	17
1.1.4.1. Failure of the rock material	18
1.1.4.2. Failure of the rock mass	19
1.1.5. Conclusion	27
1.2. Numerical methods for rock mechanics	28
1.2.1. Introduction	28
1.2.2. Analysis methods	30
1.2.2.1. Mechanical framework of the classical mechanics	30
1.2.2.2. Continuous methods	34
1.2.2.3. Discrete methods	42

1.2.2.4. Hybrid methods	52
1.2.3. Generation methods	52
1.2.4. Non Smooth Contact Dynamics method	56
1.2.4.1. General introduction	56
1.2.4.2. Dry friction contact analysis by NSCDs	59
1.2.5. Conclusion	61
1.3. Structural design approaches in tunnel engineering	62
1.3.1. Tunnel support structures	64
1.3.1.1. Lining structures	64
1.3.1.2. Rock strengthening	67
1.3.1.3. Steel support structures	69
1.3.2. Structural design approach in tunnel engineering	69
1.3.2.1. Empirical approach	69
1.3.2.2. Analytical approach	73
1.3.2.3. Observational approach	76
1.3.3. Conclusion	77
1.4. Forward a new methodology for the modelling of rock tunnels	79
1.4.1. Introduction	79
1.4.2. Application of the numerical methods on the block generation and the tunnel modelling	81
1.4.2.1. Block generation solutions	81
1.4.2.2. Tunnel modelling	81
1.4.3. Recommendation of the 3D modelling and analysis	85
1.4.4. Conclusion	85
CHAPTER 2:	87
COMPREHENSIVE METHODOLOGY FOR THE MODELLING OF ROCK MASSES: FROM GEOLOGICAL SURVEYS TO DEM-BASED MODELLING AND ANALYSIS	
2.1. In situ discontinuity measurements	90

2.1.1. Scan-line method	93
2.1.2. Window sampling	94
2.1.3. Conclusion	94
2.2. Geological and data processing	95
2.2.1 Geological and graphical presentation of discontinuities	96
2.2.2 Discontinuity clustering into main families	99
2.2.2.1 The spectral method of R. Jimenez-Rodriguez and N. Sita	100
2.2.2.2 The Fuzzy K-means method of R.E Hammah and J.H. Curran	102
2.2.2.3 Method of S. Priest	104
2.2.3. Data processing in each family	105
2.2.3.1. Centre of the family	106
2.2.3.2. Average semi-variograms of the discontinuity distribution on the scan-line	107
2.2.3.3. Statistical processing	108
2.2.4. Conclusion	110
2.3. Geometrical modelling in 3D on RESOBLOK	112
2.3.1. Block generation theory of D. Heliot	112
2.3.1.1. “Block database”	113
2.3.1.2. Algorithm for the block splitting	114
2.3.1.3. Algorithm for the discontinuity generation	115
2.3.2. BGL written on RESOBLOK	116
2.3.3. Geometrical modelling in 3D of a fractured rock object	117
2.3.2.1. Model generation	117
2.3.2.2. Various simulations of a model generation	120
2.3.2.3. Selection of a representative simulation by the stability-analysis-based statistics	120
2.3.3. Geometrical modelling in 3D of a cylindrical specimen for the triaxial compression tests	124
2.3.4. Geometrical modelling in 3D of the excavation process of a tunnel	125

2.3.4.1. Approach 1	125
2.3.4.2. Approach 2	126
2.3.4.3. Approach 3	127
2.3.5. Conclusion	128
2.4. Mechanical modelling of the rock mass	129
2.4.1. Models of the mechanical behaviours of the rock	130
2.4.1.1. Classification based on the deformation capability of rock	130
2.4.1.2. Classification based on the restitution capability of rock	130
2.4.1.3. Classification based on the characteristics of the stress-strain relation curve	131
2.4.2. Contact laws between the discontinuities and the rock blocks	132
2.4.3. Measurements of the <i>in situ</i> stresses of the rock mass	133
2.4.3.1. Indicative methods	133
2.4.3.2. Field-based methods	134
2.4.3.3. Core based methods	135
2.4.4. Conclusion	136
2.5. Discrete simulation and analysis in 3D on LMGC90	137
2.5.1. LMGC90 – a robust DEM-based solution for discrete media	137
2.5.2. The connection between RESOBLOK and LMGC90	142
2.5.3. Simulation setting	143
2.5.3.1. Boundary conditions of the model	143
2.5.3.2. Loading conditions of the model	144
2.5.3.3. Numerical simulation and calculation parameters	145
2.5.4. Limitation of the RESOBLOK – LMGC90 coupling	146
2.5.5. Simulation of a conformed triaxial compression test in rock engineering	149
2.5.5.1. Fundamental notion	149
2.5.5.2. Simulation setting	150
2.5.6. Simulation of a multi-phase-excavation in rock masses	152

2.5.6.1. Simulation of the excavation progress	152
2.5.6.2. Simulation setting	156
2.5.6.3. Commentaries on the proposed solutions of the excavation simulation	161
2.5.7. Conclusion	162
CHAPTER 3:	164
APPLICATIONS OF THE METHODOLOGY ON THE MARBLE OF SAINT BEAT (HAUTE GARONNE, FRANCE)	
3.1. Marble of Saint B��at and the construction project of the Saint B��at tunnel	164
3.1.1. Saint B��at town and the marble of Saint B��at	164
3.1.2. The construction project of the Saint B��at tunnel	166
3.1.2.1. General introduction	166
3.1.2.2. Study on the technical documents of the project	168
3.2. In situ discontinuity measurements	172
3.3. Discontinuity data processing	176
3.3.1. Clustering discontinuities into main families	176
3.3.1.1. Identification of discontinuity families	177
3.3.1.2. Determination of the centre of each discontinuity family	178
3.3.1.3. Geo-statistical processing	180
3.3.2. Statistical processing	184
3.3.2.1 Distance distribution	184
3.3.2.2. Orientation distribution	186
3.3.3. Commentaries on the obtained results	188
3.3.3.1. Identification of the main families	188
3.3.3.2. Determination of the centre of the main families	189
3.3.3.3. Spatial distribution of the discontinuity densities of each family	189
3.3.3.4. Statistical distribution of the discontinuities in their family	191
3.3.4. Conclusion	191

3.4.	Geometrical modelling of the marble of Saint Béat	192
3.4.1.	Scenarios of the geometrical modelling	193
3.4.2.	Generation of a cylindrical model	194
3.4.3.	Generation of a tunnel excavation model	195
3.4.3.1	Approach 1	195
3.4.3.2	Approach 2	196
3.4.3.3	Approach 3	196
3.4.4.	Selection of the representative simulations by the preliminary stability analysis on RESOBLOK	198
3.4.4.1.	Approach 3	198
3.4.4.2.	Approach 2	199
3.4.5.	Initial determination of the sufficient quantity of simulations for each scenario of the model generation	200
3.4.6.	Conclusion	201
3.5.	Mechanical modelling of the marble of Saint Béat	202
3.6.	Study of the mechanical behaviours of the marble of Saint Béat under a numerical triaxial compression test	205
3.6.1.	Modelling and simulation	206
3.6.1.1.	Reconstruction of the geometrical model in LMGC90	206
3.6.2.2.	Simulation setting	207
3.6.3.	Results and interpretation	211
3.6.3.1.	Deformations of specimen during the time of simulation	211
3.6.3.2.	Relation between pressures and deformations	214
3.6.3.3.	Variation of contacts inside the model	215
3.6.3.4.	Failure procedure of the model	222
3.6.3.5.	Evolution of sliding planes occurring in the specimen during the simulation	228
3.6.4.	Conclusions	230
3.7.	Study of the simulation of a tunnel excavation in the rock mass of Saint Béat	231

3.7.1. Introduction	231
3.7.2. Numerical models	233
3.7.2.1. Numerical model of the rock mass	233
3.7.2.2. Boundary and loading conditions	234
3.7.2.3. Numerical models and the excavation algorithms of the excavation process	236
3.7.3. Results and interpretation of the Combination 2 under the 1 st loading case	243
3.7.3.1. Movements of rock blocks during the tunnelling schedule	244
3.7.3.2. Contact forces between the rock blocks	246
3.7.3.3. Contact pressures between the rock blocks	251
3.7.4. Results and interpretation of the Combination 2 under the 2 nd loading case	254
3.7.5. Results and interpretation of the Combination 2 under the 3 rd loading case	256
3.7.5.1. Movements of rock blocks during the tunnelling schedule	256
3.7.5.2. Contact forces between the rock blocks	258
3.7.3.3. Contact pressures between the rock blocks	261
3.7.6. Comparison of the mechanical behaviours of the model under two loading cases	261
3.7.7. Conclusions	265
CONCLUSION AND RECOMMENDATION	267
APPENDIX A: FURTHER RESULTS OF THE MODEL GENERATION ON RESOBLOK	A_1
APPENDIX B: FURTHER RESULTS OF THE TRIAXIAL COMPRESSION SIMULATION	B_1
APPENDIX C: FURTHER RESULTS OF THE EXCAVATION SIMULATION	C_1
REFERENCE	R_1

INTRODUCTION

1. Starting point

For the construction of a tunnel in rock, the most conventional method for the excavation work is to use explosives. With the development of the tunnelling technics, the method has achieved many advances such as the accuracy of the blasting, the diminution of the working hazards, or the improvement of the environmental aspects. This method is very popular thanks to its economic efficiency, the increased mechanical availability of the drilling machines and the fast progress of the construction. However, its biggest default is the perturbation of the host rock mass caused by the explosions. The blasting does not only affect the excavation volume but also its surroundings. The presence of the discontinuity network (also called rock structure) in the initial rock mass influences its geo-mechanical behaviour, and generally defines it as an assembly of distinct blocks. The destruction of the initial rock blocks during the blasting operation creates the opening in the medium and disturbs the stability state of the neighbouring blocks. Some discontinuities are created or modified, and the blocks slide on their contact faces and even detach from the boundary of the excavation. The fall of some individual blocks can spread the instability in the vast region around them, whereas the occurrence of the consequent failure is either prompt or delayed after a period of “self-standing” time. The design of the excavation blasting procedures envelops the determination of the amount and the arrangement of the explosives, their ignition sequence, the stabilization of the tunnel structure and the surrounding rock mass, often taking into account the application of the dynamic loads and the accumulation effect of the sequential blasting cycles. Moreover, the long-term destabilization process of the hosting rock mass and the aging of the tunnel structures must be controlled. The final goal is to guarantee a long service life of the tunnel, in a secure condition that is specified by the planned use of the tunnel.

From this practical engineering problem, several matters of research are found:

- The stability analysis of the rock mass in the vicinity of the excavation under the effects of the tunnelling excavation planning and method;
- The tunnel structure design for the temporal and/or permanent stabilization of the boundary of the excavation and the hosting rock mass;

- The influence of the pre-existing discontinuities on the potential instability of the excavation and its surroundings;
- The prediction of the working state of the tunnel structure and of its surrounding rock mass, during the tunnelling procedure and the service life of the tunnel.

The ambition of the application of several computer tools used in rock mechanics for a deep understanding of such matters leads us to the numerical simulation and analysis of the rock mass with a special consideration of its discontinuity network.

2. Problem definition

Fractures, with complex spatial distribution and from multiple origins, strongly affect the characteristics and behaviour of the rock mass to which they belong. For a long period of time, rock mass was considered as a continuous medium, an assumption that lead to many damageable consequences. The distinct block approaches in rock mechanics have proven their great capability for robust computation, even confronted with difficult mathematical problem and proposed far reaching possibilities in the analysis of results. The simulation of a discontinuity network and its vicinity permits the numerical reconstruction of the objects, in their loaded states, and relative positions, for detailed and appropriate analysis. The precision and the relevance of the technical information for such a problem govern the realisation of the work on site, and the reliability of the results. The *in situ* investigations and measurements on the rock mass supply the input data for the description of the geometrical configuration and the mechanical characteristics of the rock mass. Taking into account both types of data, the obtained records allow the generation of the representative numerical models of the rock mass, for the simulation and result analysis purposes. As a matter of fact, the combination of the geo-mechanical measurements, the modelling of the geometry, the mechanical behaviour of the rock and discontinuities, as well as the numerical simulation of the block systems and its results analysis offer a comprehensive tool box to tackle rock engineering problems.

3. Scope and objectives of research

The presence of the discontinuity network in the rock masses is evident and its influence on the hosting rock mass mechanical behaviour is strong and complex. The consideration of the discontinuities in rock is thus necessary, although it remains a challenge. Converting a fractured rock into an equivalent ideal homogenous medium or finding an equivalent model using some standard regular-shaped elements, leads to an easier analysis but the relevance of the results can always be questioned. Discrete element methods, considering collections of

many solids, can be considered as an alternative to tackle the problem of the discontinuous nature of the rock mass. The complete simulation of a rock mass must include the natural configuration of the discontinuity network and the geo-mechanical characteristics of the intact rock. This fact leads to the demand of geometrical and mechanical modelling for the generation of the qualified numerical models of the rock mass.

4. Research methodology

The thesis introduces an original approach for the modelling of the rock masses taking into account the presence of the discontinuity network. At first, *in situ* scan-line measurements are carried out at exposed rock faces to obtain the required information: position, orientation, dimension, filling conditions of discontinuities. Second, those rock discontinuities are clustered in main families by geo-mathematical tools and their representative laws of distribution can be analysed using geo-statistics. Third, one creates a 3D geometrical model made of blocks using the RESOBLOK code in order to produce an input file to the LMGC90 code. Simultaneously, the mechanical models of the intact rock and of the contact behaviour in the discontinuities are declared. The combination of the two models of one rock mass creates the equivalent numerical rock model on LMGC90 for the simulation and analysis under the light of the Non Smooth Contact Dynamics method. Thanks to that, realistic behaviours of rock media, including the main discontinuity families and the actual geometries of the discontinuity networks, can be examined. The responses of the modelled objects are assessed for a deeper understanding of their mechanical behaviours.

The bibliographical study forms the background knowledge of the thesis and guides us to the definition of this methodology. The real applications on the marble of Saint B  at tunnel project (Haute-Garonne, France) illustrate the detailed development of the methodology and validate its use in an engineering environment.

5. Thesis Organization

This thesis is organized in three chapters, a conclusion and recommendation section, and four appendices. The contents of each part are briefly described below.

In the first chapter, through the bibliographical study on the state of the art of the nature of rocks, the variety in the computational methods in rock mechanics and the principal approaches for tunnel structural design, the background knowledge of the thesis is presented.

The second chapter is a proposition of a methodology for rock engineering as the combination of the *in situ* measurements, the geometrical and mechanical modelling, the numerical simulation, and the mechanical analysis of the discrete model results.

The third chapter introduces the application of the developed methodology on the rock mass of the Saint Béat marble rock mass, using two examples. The first example is the modelling of a large-scale triaxial compression test and the second example is the modelling of a multi-phase-excavation.

Finally, a conclusion and recommendations are presented, as a summary and a critical assessment of the proposed methodology, with some proposals for its future improvements.

The appendices exhibit the experimental geo-mechanical parameters of the marble of Saint Béat, and complementary detailed results on the real applications.

CHAPTER 1: STATE-OF-THE-ART OF THE FRACTURED ROCK ENGINEERING

1.1. Nature of fractured rock mass

1.1.1. Structure of rock and its nature

Rock is one of the main materials which formed this planet. Many different geological definitions can be found in various related documents. For instance:

- “Rock is a solid substance that occurs naturally because of the effects of three basic geological processes: magma solidification; sedimentation of weathered rock debris; and metamorphism” [1];
- “Rock is an assemblage of compact crystalline grains, ... they can be defined as an assemblage of minerals that have different relations due to their geological histories” [2]
- “Rock is an assemblage of minerals” [3].



Figure 1.1.1: Fractured marble on the Cap du Mount at Saint B  at (Haute Garonne, France)

In brief, rock is defined as a naturally occurring and coherent assembly of minerals (with or without fossils) after long natural tectonic processes. Rock can be found almost everywhere around us with various appearances. At a macroscopic scale, some rock can be considered as solid and homogenous. However, the discontinuous network in rock can always be found, at natural scale by naked eyes or at a micro scale by microscope. T. Rammamurthy [4] confirmed that “rock mass is non-homogenous, anisotropic and discontinuous medium; often it is a pre-stressed mass”.

Rocks can be distinguished based on their basic appearance characteristics, structures and configurations of crystalized components or bedding positions. Classified by the forming origin, rocks are divided into three major groups: igneous, sedimentary and metamorphic one [2]:

- Igneous rocks: formed from the solidification of molten material (magma). Depending on where this phenomenon took place and the cooling rate of the magma, several types of igneous rock were created with different characteristics. However, they are usually strongly fractured, anisotropic with a low porosity. Some of the strongest rocks belong to this group [4].
- Sedimentary rocks: formed from the accumulation of fragmental rock materials and organic materials or by chemical precipitation. There are various sedimentary rocks with rich characteristics. A sedimentary rock mass is either isotropic or anisotropic depending on the mineralogical variations of the grains in layers, the bond between grains and the layer boundaries [4].
- Metamorphic rocks: formed by alteration of existing rocks through the action of heat and pressure. In comparison with the two above groups, the complexity of this group is highest due to the large diversity of the characteristics of its components. They are mostly anisotropic [4].

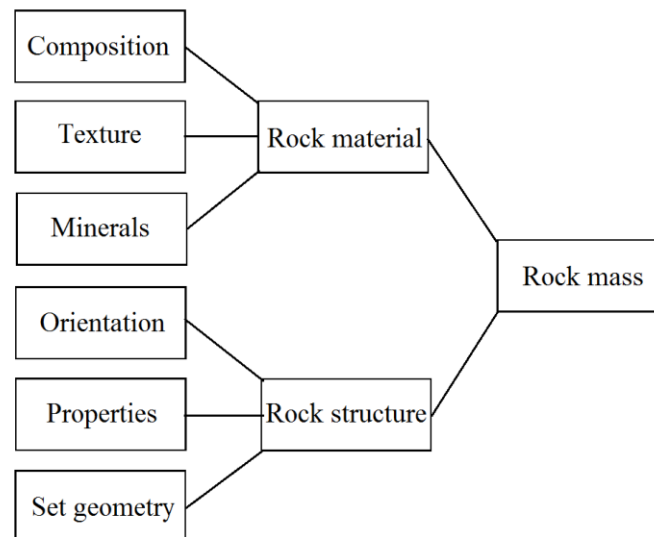


Figure 1.1.2: Illustration of the rock mass (sourced and modified from [7])

From a structural viewpoint, a rock mass is described by the rock material and the rock structure. Rock material, which can be called the non-fractured rock matrix, intact rock,

forms the medium in which there are systems of discontinuities, called the rock structure [5]. The term “discontinuity” designates all physical interruptions of the continuity in the rock material [5], or in a more detailed way “any significant mechanical break or fracture of negligible tensile strength in a rock” [6]. The term “rock mass” is defined as the assemblage of the rock material and the 3D structure of discontinuities through an illustration of C. Edlbro, [7], cited in the figure 1.1.2.

The rock material can be described through four criteria proposed by the USACE [8]:

- Degree of weathering: in five grades (unweathered, slightly weathered, moderately weathered, highly weathered and decomposed);
- Hardness: in five grades (very soft, soft, moderately hard, hard and very hard);
- Texture: in four grades for sedimentary rock (coarse, medium, fine, very fine) and in four grades for igneous and metamorphic rocks (coarse, medium, fine, aphanite);
- Lithology, macro description of mineral components: use standard adjectives such as shaly, sandy, silty and calcareous.

The rock structure, which describes the distribution of discontinuity on the rock medium, can be classified into many grades based on three criteria [8]:

- Thickness of bedding: four grades (massive, thick, medium and thin);
- Degree of fracturing: five grades (unfractured, slightly, moderately, highly and intensely fractured);
- Dip of bedding or discontinuity: three grades (flat, dipping and steeply);
- Shape of rock blocks: three grades (blocky, elongated, tabular).

There are many specific terms that can be referred to the rock structure, proposed by the AFTES [5]:

- Bedding planes: surface separations of the sedimentary rock strata;
- Joints: discontinuities between two rock compartments without any apparent relative movement between them;
- Faults: results of the relative movements between two rock compartments where they lie, caused by the stress field during the relevant tectonic episode;

- Schistosity planes: separation of rock into thin layers due to the action of the tectonic stresses;
- Fracture zone: assemblages of discontinuities of variable persistence and orientation, organised in a more or less planar pattern;
- Lithological contact surfaces: virtual discontinuities formed between host rock and veins.

Discontinuities can be classified as natural and artificial (due to the causing origin); as stratigraphic joints, diaclasses, extensive fractures and faults (due to the natural status); as major and minor (due to their size in relation with the studied object). In fact, “discontinuity” is a collective term that includes many detailed definitions; each one has some synonymous names. For instance, published in [9]:

- Bedding plane or fold;
- Foliation or rock cleavage: slaty cleavage for rock cleavage in slates; schistosity for schists and gneissosity for gneisses;
- Fracture or joint: fault, shear, gash, fissure or vein;

A. A. Afrouz [10] has divided discontinuities into nine types due to the nature of rock material to which they belong:

- On all kinds of rock material: tectonic joint, fault, sheeting joint and lithological boundary;
- On sedimentary rock: bedding plane or bedding plane joint, slaty cleavage and random fissure;
- On igneous rock: cooling joint;
- On metamorphic rock: slaty cleavage.

There is another classification of discontinuities on the rock mass based on their shear displacements:

- Discontinuities that have shear displacements: Faults are the type of discontinuities that have strongest shear displacements. They are often found within a fault zone. Shears are in the same group but have much smaller displacements than faults.

- Discontinuities that have almost no shear displacements: Joints belong to this group. They were often created due to the combination of tectonic stresses. The small local discontinuities due to tension are called tension cracks.

Usually, discontinuities are grouped in families (which can be called sets or clusters, too) that have the same or similar geo-structural characteristics. Besides, some discontinuities exist individually and do not belong to any family. They can be faults, shear planes, dykes, veins and tension cracks, for instance. Each type of discontinuities has its appearance zone, the distribution tendency and its own geological and mechanical characteristics that are given by the origin creation mechanism of the initial rock, the undergoing tectonic and geological operations together with loading conditions of the medium during the rock life. In turn, quick identification of rock can be realised based on the nature of the discontinuities of the rock mass.

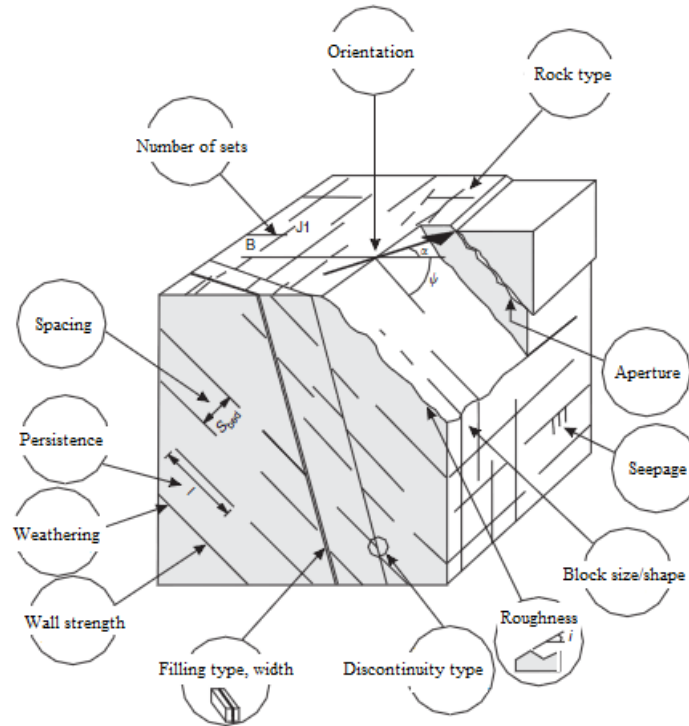


Figure 1.1.3: Characteristics of discontinuities in rock masses (sourced from [11])

A discontinuity is described by the following characteristics: orientation, density (distance or spacing), organisation in main families (or main sets), opening and continuity status, persistence (or extension), material filling and its nature, morphology, wall weathering, presence of water, strength and other mechanical properties. The figure 1.1.3 cited from D.C. Wyllie and C.W. Mah [11] is a good illustration of the characteristic description of the discontinuities in rock masses.

1.1.2. Presence and influence of discontinuities on the rock mass

Almost all natural rocks are more or less fractured. It is said that the totally intact rocks only exist in theories. Presented in the rock mass, the discontinuities strongly affect the characteristics and behaviour of the rock mass to which they belong. The strength of a rock mass is considered as the combined strength of the rock material and the rock structure. In general, discontinuities that belong to main families play an important role on the behaviour of the rock mass while individual discontinuities may only affect the local regions around them but do not influence the whole rock mass. R.E.Hammah *et al.* [14] considered that in some circumstances “discontinuities exert greater influence on behaviour than do intact rock properties”. The influence of the rock structure to the rock mass is presented in brief through three aspects: the discretization of the intact rock medium, the modification of mechanical characteristics and the instability mechanism of the rock mass.

1.1.2.1. Discretization of intact rock medium

The most direct and obvious effect of discontinuities to their rock mass is the separation of intact rock into discrete rock blocks [6] so that the rock mass can be represented as the assemblage of rock blocks [12]. The origin and development of the discontinuity network in rock are produced by the complex combination of various features from the geological nature of the intact rock, the geological and tectonic conditions of the region where the rock is found, the external force conditions applied to the mass. The presence of this network on the rock medium is different from one rock to another, diverse from evident to quasi-negligible. However, with a sufficient small scale of study, the discontinuities are always found in rock.

The presence of the rock structure on the rock mass is not as simple as the appearance of smooth cuttings on the intact rock. The morphology of discontinuities is complex with uneven wall and aperture, with or without filling. Each characteristic of the discontinuities has its own impact to the behaviour of the rock mass. For instance, when discontinuities are extremely closely arranged, rock blocks are so small that it makes the rock behave like a granular soil. The aperture and the filling promote or inhibit the shear displacement of the discontinuities and the sliding of rock mass along their discontinuities. The influence of the roughness of the discontinuities on their shear strength is clearly presented in the following figure, cited from E. Hoek [13]. The shear strength – normal stress curves of the two types of discontinuities are shown:

- For smooth discontinuities *i.e.* when roughness is neglected in analysis;
- For rough discontinuities *i.e.* when roughness is taken into account.

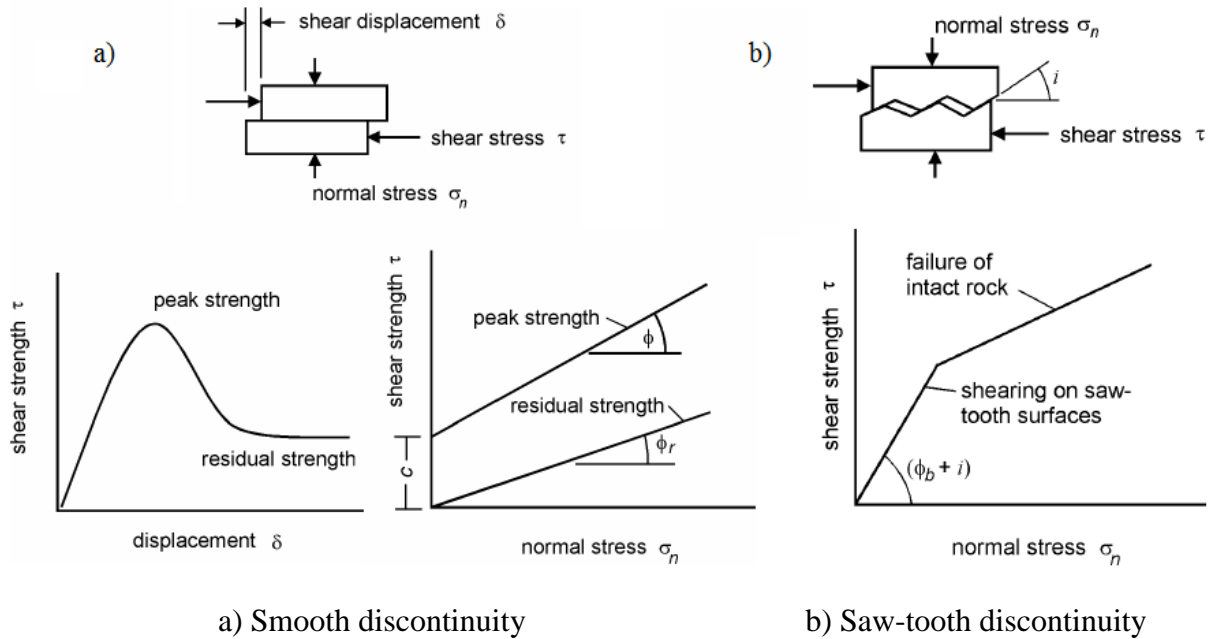


Figure 1.1.4: Shear strength of the discontinuities (sourced from [13])

Considering that the rock structure discretizes the intact rock mass into various rock blocks, the block interactions can be described by several types of contact that will be presented in the scope of the discrete numerical method in the section 1.3 of this chapter. The continuous homogenous medium of the intact rock is replaced by a discontinuous medium with a different behaviour from the original.

1.1.2.2. Modification of mechanical characteristics

An ordinary rock mass is made up of an interlocking assemblage of discrete blocks. These blocks may have been weathered to varying degrees and the contact surfaces between the blocks may vary from clean and fresh to clay covered and slickenside [13]. Hence, almost all mechanical characteristics of the rock mass are always lower than those of the present intact rock. The compressive strength of the rock mass is far different to the one of intact rock [4]. This phenomenon is caused by the interruption in the continuous stress field in the rock mass: Considering that each block is a sub-region that is limited by the contact walls with the adjacent blocks, the whole rock mass is composed of an indefinite number of sub-regions. Mathematically, the whole continuous region of the intact rock is equal to the sum of the infinite disturbed discrete sub-regions but the correlation between mechanical behaviour of the former and the latter cannot be simply expressed through an equation. The

smooth transmission of forces is perturbed and the stresses distribution in the rock mass is no more continuous or regular. The discontinuities are found to affect the strength, deformation modulus and the stress - strain responses in a non - linear and anisotropic manner that make difficult to predict the real behaviour of the rock mass [14]. The presence of discontinuities in the rock mass is said to alter the elastic behaviour of the intact rock and to induce the nonlinear behaviour of the rock mass [15].

The strength of the fractured rock mass was the subject that interested many researchers in rock engineering and can be found in many basic books and manuals of rock theories. Due to the negligible tensile strength of the discontinuities, the shear strength of the rock mass is strongly affected by the presence of the rock structure [6]. Meanwhile, the shear strength of discontinuities is normally assumed as a function of the friction angle which is proven by using the Mohr-Coulomb failure criterion with the null cohesion [16]. With a same loading condition, the stress-displacement curve of the rock mass is more inclined than the one of the rock structure but less than the one of the intact rock. A simplified comparison of the three curves is illustrated in the Figure 1.1.5.

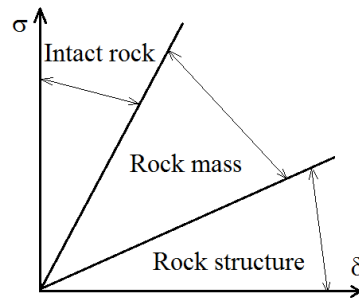


Figure 1.1.5: Located zones of the stress-displacement curves in a rock mass
(sourced from [16])

If the rock mass is assumed to be elastic, the overall Young's modulus is given by [16]:

$$E_{mass} = \frac{\sigma}{\varepsilon} = \frac{1}{\frac{1}{E_i} + \frac{\lambda}{E_d}}$$

With:

E_{mass} : Young's modulus of the rock mass

E_i : Young's modulus of the intact rock

E_d : Young's modulus of the discontinuity

λ : Frequency of the discontinuity

However, this expression is a very simplified case when there is only one family of discontinuity that is regularly distributed in the rock mass. The variation of the Young's modulus of the rock mass versus the frequency of the discontinuity can be expressed by the curved in the figure 1.1.6 of which the estimated value of Young's modulus E_{field} from the *in situ* measurements is about approximated 10% of the value of Young's modulus of intact rock [16]

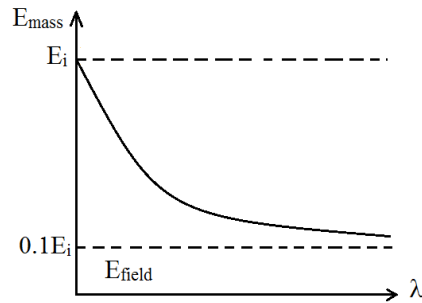


Figure 1.1.6: Young's modulus - frequency of the discontinuity curve of a rock mass
(sourced from [16])

When there are more than one family of discontinuities in the rock mass, each one creates a weak plane where the failure of the rock mass may take place but the angular position of the strength minima would not coincide with the other plane. As a result the rock is weakened in several different directions simultaneously [16].

Through many theories, laboratory and *in situ* tests, simulations on experimental physical and numerical models of the fractured rock mass, the researchers have proven the importance of this effect. The rock structure in the rock mass causes the decrease of the strain modulus [17], unevenly distribution of fluid flow and mass transportation [18], and lower value of the geotechnical behaviour indexes in comparison with those of the intact rock.

1.1.2.3. Instability mechanisms

Under the external and internal conditions of the rock mass, the adjacent blocks slide on their contact faces and become unstable by some typical failure types such as free falling under gravity, plane failure, wedge or rotational failure. N. Hataf and M. Baharloo [15] wrote that the physical behaviour of rock mass is the opening of discontinuities and sliding along them that leads to the deformation by the sliding of blocks. The stability of rock blocks depends on their positions. H.A. Keykha *et al.* [19] suggested that the most common

types of failure of blocks around an excavation were those involving wedges falling from the roof or sliding out of the sidewalls of the openings.

The falling of individual blocks may lead to the instability of the vast region around them. Those absences create the voids in the medium, break the initial structure of the rock mass that can bring out the total failure of the whole rock mass. P.M. Warburton [20], [71] proposed the “Block theory” which is one of the most common for the study of the instability of discrete rock blocks. R.E. Goodman and G. Shi [21], without referencing to the research of P.M. Warburton, proposed their own block theory that shared most of the same principles with the former. Based on this theory, H.A. Keykha *et al.* [19] proposed five types of blocks around an excavation section:

- Type I being moveable;
- Type II having key potential to move;
- Type III has no movement because of its position in basement;
- Type IV has no movement because of blocking with neighbouring blocks;
- Type V, a jointed block without any free space in rock mass.

The key blocks (I and II) described as potentially instable blocks in rock mass and should be given great consideration. The stability of these blocks was examined by a kinematic method.

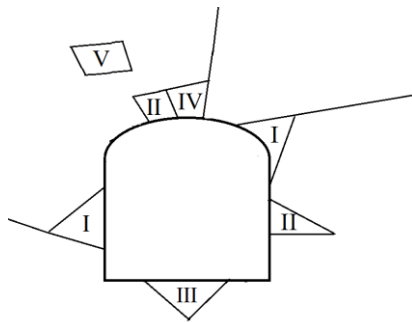


Figure 1.1.7: Types of blocks around an excavation section (sourced from [19])

L. Scholtes and F.V. Donze [22] wrote that the instability of the rock masses was often related to the presence of pre-existing discontinuities and the destabilization process often relates to the complex interaction between the discontinuities and the rock mass through the progressive breakage of rock bridges. Due to the strong effect of the rock structure to the rock material, the rock structure must be taken into account in all related researches.

Neglecting their presence or trying to replace a fractured rock medium by a theoretical intact rock is confirmed to be an unwise intention.

1.1.3. Scale effect in rock mechanics

The scale effect decides the methodology of the analysis. This effect is due to the presence of the rock structure in the rock mass and controls the whole analysis procedure for all rock objects. The term “scale” here is not only restricted to the meaning of the macroscopic or microscopic scale but refers also to the size of the domain of interest in the scope of the analysis.

The illustration of E. Hoek and E.T. Brown [23] in Figure 1.1.5 serves as a good demonstration of this concept. When the specimen stays completely in a non-fractured region of the rock mass, the discontinuities do not have any obvious tendency so that it can be approximated as intact rock. Otherwise, the fracture nature cannot be omitted. Ö. Aydan *et al.* [24] proposed that when the domain of interest is much smaller than rock blocks (*i.e.* the first cases), the characteristics of the intact rock can be used as the representation of the rock mass. When the domain is much larger than the blocks (*i.e.* the two last case), the rock mass properties need to take into account the rock structure. Otherwise (*i.e.* the two remaining cases), the discontinuities govern the behaviour of the medium.

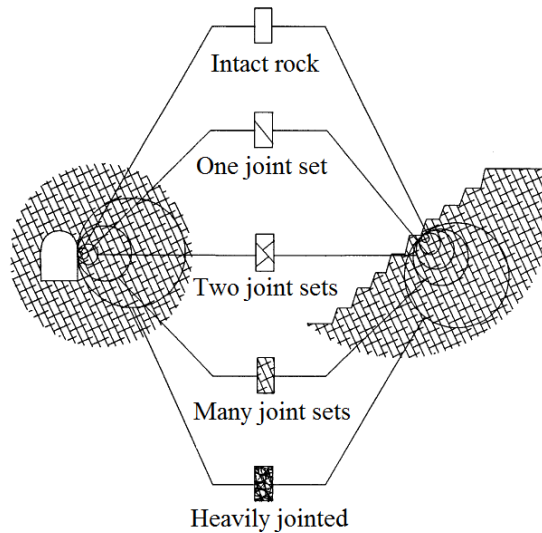


Figure 1.1.8: Relation of Discontinuity Spacing and Size of the Problem (source from [23])

The figure 1.1.9, cited from [7], shows three tunnels of different sizes located in the same rock mass, which is considered as another presentation of the Figure 1.1.8. If the discontinuity spacing is significantly greater than the dimensions of the studied object, the effect of the discontinuities to the object can be approximately neglected. In the contrary,

when the discontinuities have a spacing similar to or less than the studied objects, they will play the dominant role on the behaviour of the object. Hence, the rock medium around the smallest tunnel can be modelled as continuous, in the contrary the middle tunnel is recommended to be modelled in a fractured mass (where discrete numerical methods of analysis are evidently suggested). In the case of the biggest tunnel, the arrangement of the discontinuities can be considered as regular so that a continuous analysis for the regular discrete medium can be executed (FEM, introduced in the section 1.4, is a smart choice).

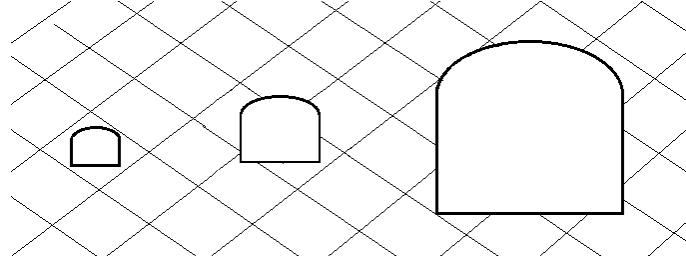


Figure 1.1.9: Different construction sizes in the same rock mass (redrawn from [7])

Moreover, when the specimen size increases, the strength is significantly reduced. E. Hoek and E.T.Brown [25] suggested that this reduction is due to the greater opportunity for failure through and around grains, the “building blocks” of the intact rock. The strength reaches a constant value when the size of individual rock pieces is sufficiently small with regard to the overall size of the structure being considered.

The scale effect is also represented through the influence of the orientation of the discontinuities to the strength of the model [4]. Assumed that there is only one discontinuity that makes an angle of β to the sense of the major principal stress, when $\beta = 0$ or 90° , the discontinuity has no effect on the strength. Otherwise, the strength of the model is strongly affected by the orientation of the discontinuity. The lowest strength occurs when $\beta = 45^\circ - \varphi/2$ where φ is the internal friction angle of the rock mass.

Ö. Aydan *et al.* [24] proposed that choosing the right model that is representative of the rock mass affected by the structure (*i.e.* tunnels, rock slopes, mines, *etc.*) is an important task in rock engineering. For the modelling and analysis of civil structures in a rock mass, the size of the model should be determined in consideration with the calculation method. If the domain methods (*i.e.* when the interior of rock mass is divided into basic elements or blocks) are applied, the model is big since the outer boundaries of the model must be sufficiently far from the structure to minimize the boundary effect to the structure. If the boundary methods (*i.e.* when only the boundaries are discretized into basic elements) are

used, the model is smaller than the former because the far field requirement is specified as stresses applying on the entire rock mass [13]. Further details of those calculation tools are found in the introduction of numerical methods in rock mechanics at the section 1.3.

1.1.4. Failure behaviour of the fractured rock mass

The failure of rock starts very early, even during the formation process of the rock, and then develops through an extremely complex process of micro-crack initiation and propagation. Some types of damage can take place at local zones, creating the local failure which sometimes does not lead to the total failure of the rock mass. Other types of damage occur very suddenly at a high rate that brings out the immediate failure to the whole rock mass.

All natural rock masses are undergoing various complex loading conditions. Aside the artificial loads caused by the human being work around the rock mass, the natural stresses that have the most influence on rock are:

- Litho-static stresses: The weight of overlying rock strata;
- Tectonic stresses: The large-scale motions of lithospheric plates driven by convection in the mantle;
- Hydrostatic stresses: The pressure exerted by fluids (mainly water) in the pore or fracture space of the rock masses.

Each rock is specified by its own characteristics under the application of the loading combinations at particular conditions. The same rock mass is damaged with different failure mechanisms due to the different combinations of acting stresses. Determination of strength of an *in situ* rock mass by laboratory tests is generally not practical. Hence this strength must be estimated from geological observations and from test results on individual rock pieces or rock surfaces which have been removed from the rock mass [14]. Due to this reason, the “strength criteria” of rock are widely applied. They are normally expressed as algebraic equations correlating the principal stresses (σ_1 , σ_2 and σ_3) or the normal and shear stresses at the failure moment (σ and τ). The mentioned values can be obtained from the *in situ* and/or experimental data measurements on the real rock mass, by the application of the empirical methods and/or from the numerical analysis on equivalent rock models. The criteria are used for checking if the rock can support the combination of the three principal stresses predicted at a given location [26].

For the study of the failure mechanism of a rock mass, one usually pays attention to the failure of the intact rock and the failure of the rock mass with the presence of the rock structure.

1.1.4.1. Failure of the rock material

Three deformation mechanisms can occur when a rock material is undergone the external loading conditions: the brittle, the semi-brittle and the ductile one. At the same acting load, the response of rock is influenced by the loading rate and the loading time [26].

- Brittle failure: is the sudden loss of rock strength after the reach of the maximal strength while the ductile failure happens when the yield limit is reached with or without the reduction of strength [7]. Characterised by the broken form of the rock, this damage occurs at low temperature, low confining pressures with high deviator stresses when the stable crack propagation takes important role in the inelastic rock deformation. The propagation which is facilitated by the pore fluids leads to the coalescence and an eventual formation of failure planes. Two typical phenomena of this failure are the “dilatancy hardening” in dense rock and “dilatancy softening” in porous rock [26]. Faults are the consequence of brittle failure in rock.
- Ductile failure: occurs at high temperature, high confining pressures, specified by the low strain rate. Characterised by the bending or flowing form of rock, this damage takes place at the intracrystalline level and no obvious influences of confining pressure with the presence of dilatancy are found on the rock. Folds are the consequence of ductile failure in rock.



a) Faults caused by the brittle failure



b) Folds caused by the ductile failure

Figure 1.1.10: Fractures of rock

- Semi-brittle failure: can be called the transition from the brittle to the ductile failure. It happens at high temperature when the confining pressure is increasing. The rock strains are distributed on the whole rock mass and the rock turns into the inelastic

deformation with the creep in the crystalline. E. Hoek and E.T. Brown [28] suggested in their failure theory that the transition is varied from one rock to another. T. Ramamurthy [4] recommended to estimate this transition of the intact rock to foresee the type of behaviour of the rock mass before the realisation of the detailed analysis.

Hard intact rocks tend to have the brittle failure and weak and/or weathered intact rocks tend to have the ductile failure. The brittle-ductile boundary of an intact rock is defined as the ratio of the effective principal stresses $\frac{\sigma_1}{\sigma_3}$ acting on the specimen of rock under the triaxial compression test.

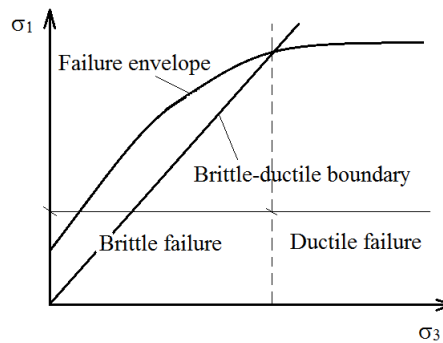


Figure 1.1.11: Brittle – ductile transition of the intact rock (sourced from [4])

1.1.4.2. Failure of the rock mass

The failure type of the rock mass is influenced by the arrangement of the rock structure on the rock material. The instabilities occurring in rock slopes are generally related to the presence of pre-existing discontinuities [27]. The factor that influences the performance of the rock mass is the orientation of discontinuities relative to the direction of the applied stresses. T. Ramamurthy [4] found that when the fracture families are orthogonal of which one is continuously dipping, five main failure types that depend on β can happen on the rock mass:

- Splitting of the rock material: when $\beta < 10^\circ$ or $\beta > 80^\circ$;
- Shearing of the rock material: when $\beta < 20^\circ$ or $70^\circ \leq \beta \leq 80^\circ$;
- Sliding along the mentioned fracture family: when $30^\circ \leq \beta = 45^\circ - \frac{\varphi}{2} \leq 60^\circ$ where φ is the internal friction angle of the discontinuity;
- Rotation of rock blocks: when $10^\circ \leq \beta \leq 20^\circ$;

- Buckling of thin layers: is a special case of the rotation type when

$$\frac{\beta}{t} = 0.5\pi \cdot (M_{rj} \cdot t)^{0.5}$$

With:

β : Angle of the mentioned fracture family with the vertical axis (°)

t: Thickness of the layer of rock (m)

M_{rj} : Modulus ratio of the rock material

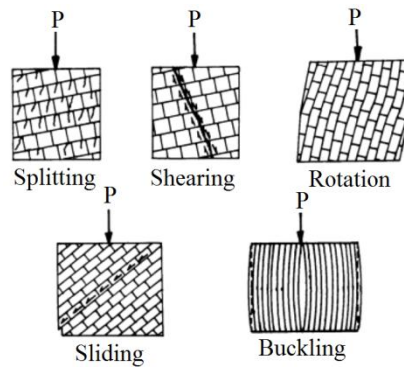


Figure 1.1.12: Different modes of failure observed on jointed specimens (sourced from [4])

The failure criteria for the rock mass based on the correlation between the two principal stresses of the rock (σ_1 , σ_3) are obtained from the experiments (at laboratory / *in situ*) and/or from the analysis of the rock mass classification systems. However, Hoek and Brown [28] recommended that a rock mass criterion should only be used where there are a sufficient number of closely spaced discontinuities that isotropic behaviour involving failure on discontinuities can be assumed. The rock mass criteria were found to be the extensions of the strength criteria for the present intact rock with the modification process based on model tests, small sample testing and limited experience. They tend to over predict the strength for poor quality rock masses at the low stresses common to failure surfaces in slopes [29]. L. Scholtes and F.V. Donze [22] underlined that the non-persistent discontinuities are involved in the failure process, and the breakage of rock bridges between discontinuities mainly causes the destabilization to the rock mass. Hence, they proposed to use the progressive failure mechanisms of rock bridges, leading to global failure, along with the modelling of the stability analysis that should encompass the nucleation or activation of cracks within the rock, the possible coalescence of which would then lead to the creation of critical failure surfaces.

In rock engineering, several failure criteria of the rock mass have been proposed and applied in practice. Some common criteria in rock mechanics for the rock mass are Mohr – Coulomb criterion for rock mass, the Hoek – Brown criterion for rock mass, the Yudhbir criterion, the Sheorey *et al.* criterion and the T. Ramamurthy one. Some criterion related to some rock classification systems: RMR and GSI for the first criteria, Q and RMR for the second and the third. Those failure criteria are briefly presented here.

a) Mohr – Coulomb criterion for rock mass

The Mohr-Coulomb failure criterion expresses the relationship between the shear stress and the normal stress at failure along a hypothetical failure plane. The Mohr-Coulomb criterion is suitable at high confining pressures when rock generally fails through the development of shear planes [16].

The Mohr-Coulomb shear strength τ , for a given normal stress σ_n

$$\tau_{\text{peak}} = c + \tan\varphi \cdot \sigma_n$$

The relation between the major and minor principal stress is given by:

$$\sigma_1 = \frac{2c \cdot \cos\varphi}{1 - \sin\varphi} + \frac{1 + \sin\varphi}{1 - \sin\varphi} \sigma_3$$

With:

φ : Internal friction angle (rad/°), equivalent to the angle of inclination of a surface sufficient to cause sliding of a block of similar material

c : Cohesion, represents the shear strength of the rock when no normal stress is applied

τ_{peak} : Maximal shear strength (N/m²)

σ_1 : Major principal stress (N/m²)

σ_3 : Minor principal stress (N/m²)

This is the most applied criterion in rock and soil engineering, it is especially significant and valid for discontinuities and discontinuous rock masses. However, some limitations are found [16]:

- The existence of the major shear fracture at maximal strength at a specific angle does not always agree with experimental observations;

- A shear failure was predicted to occur on a plane in uniaxial tension that made an angle $\theta = 45^\circ - \frac{\varphi}{2}$ with σ_3 but in fact $\theta = \pm 90^\circ$;
- The experimental maximal strength envelopes are generally non-linear. They can be considered linear only over limited ranges of confining pressures.

b) Hoek – Brown criterion for rock mass

The Hoek – Brown criterion for rock mass has several versions and update from 1980 to 2002. It is the most widely applied in rock slope and tunnel engineering. C. Edlbro [7] suggested that this criterion is the only one for the estimation of the strength of various kind of rock mass if the necessary parameters can be measured or estimated and if their influence on the strength of the rock mass reflects the real behaviour.

- The original (1980) version:

$$\left(\frac{\sigma_1 - \sigma_3}{\sigma_c}\right)^2 = \frac{m\sigma_3}{\sigma_c} + s$$

- The 1988 update:

For undisturbed rock mass: $m = m_i e^{\frac{RMR_{basic}-100}{28}}$

$$s = e^{\frac{RMR_{basic}-100}{9}}$$

For disturbed rock mass: $m = m_i e^{\frac{RMR_{basic}-100}{14}}$

$$s = e^{\frac{RMR_{basic}-100}{6}}$$

- The 1992 modified version:

$$\sigma_1' = \sigma_3' + \sigma_c \left(m_b \frac{\sigma_3'}{\sigma_c} \right)$$

- The 1995 generalised version:

$$\sigma_1' = \sigma_3' + \sigma_c \left(m_b \frac{\sigma_3'}{\sigma_c} + s \right)^a$$

$$m_b = m_i e^{\frac{RSI-100}{28}}$$

When $RSI > 25$: $s = e^{\frac{RSI-100}{9}}$

$$a = 0.5$$

When $RSI < 25$: $s = 0$

$$a = 0.65 - \frac{GSI}{200}$$

- The 2002 version:

$$\sigma_1' = \sigma_3' + \sigma_c \left(m_b \frac{\sigma_3'}{\sigma_c} + s \right)^a$$

$$m_b = m_i e^{\frac{RSI-100}{28-14D}}$$

$$s = e^{\frac{RSI-100}{9-3D}}$$

$$a = \frac{1}{2} + \frac{1}{6} \left(e^{\frac{-GSI}{15}} - e^{\frac{-20}{3}} \right)$$

With:

σ_1 : Major principal stress (N/m²)

σ_1' : Major effective principal stress (N/m²)

σ_3 : Minor principal stress (N/m²)

σ_3' : Minor effective principal stress (N/m²)

s: Constant depended on the properties of the rock mass

m_i : Material constant for intact rocks

a, m_b : Material constant for broken rocks

RMR: Rock Mass Rating basic value

GSI: Geological Strength Index value

D: factor depended on the degree of disturbance of the rock mass

E. Hoek *et al.* [30] shown that their criterion satisfied the Mohr – Coulomb criterion through an average linear relationship when the internal friction angle and the cohesive strength of the latter are replaced by the effective values.

The effective value of the internal friction angle:

$$\phi' = \sin^{-1} \left[\frac{6am_b(s + m_b \sigma'_{3n})^{a-1}}{2(1+a)(2+a) + 6am_b(s + m_b \sigma'_{3n})^{a-1}} \right]$$

The effective value of the cohesive strength:

$$c' = \frac{\sigma_{ci}[(1 + 2a)s + (1 - a)m_b \sigma'_{3n}](s + m_b \sigma'_{3n})^{a-1}}{(1 + a)(2 + a)\sqrt{1 + (6am_b(s + m_b \sigma'_{3n})^{a-1}/[(1 + a)(2 + a)])}}$$

And:

$$\sigma_{3n} = \frac{\sigma'_{3max}}{\sigma_{ci}}$$

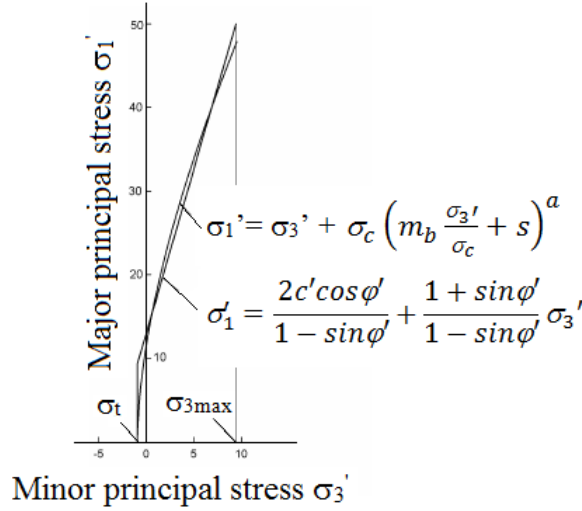


Figure 1.1.13: Relationships between major and minor principal stresses for Hoek-Brown and equivalent Mohr-Coulomb criteria (sourced from [30])

The relation between the major and minor effective principal stress of the Mohr - Coulomb criterion is given by:

$$\sigma'_1 = \frac{2c' \cdot \cos \phi'}{1 - \sin \phi'} + \frac{1 + \sin \phi'}{1 - \sin \phi'} \sigma'_3$$

With:

σ_1 : Major principal stress (N/m²)

σ'_1 : Major effective principal stress (N/m²)

σ_3 : Minor principal stress (N/m²)

σ'_3 : Minor effective principal stress (N/m²)

σ'_{3max} : Upper limit of confining stress (N/m²)

σ_{cm} : Uniaxial compressive strength of the rock mass (N/m²)

σ_{ci} : Uniaxial compressive strength of the intact rock (N/m²)

s: Constant depended on the properties of the rock mass

m_i : Material constant for intact rocks

a, m_b : Material constant for broken rocks

RMR: Rock Mass Rating basic value

GSI: Geological Strength Index value

D: factor depended on the degree of disturbance of the rock mass

c) Yudhbir criterion

$$\frac{\sigma_1'}{\sigma_c} = A + B \left(\frac{\sigma_3'}{\sigma_c} \right)^\alpha$$

The value of A and B can be found in the checking table or calculated from the value of Q and RMR index:

$$A = 0.0176.Q^\alpha$$

$$A = \exp \left[7.65 \left(\frac{RMR-100}{100} \right) \right]$$

Q: Q system of the rock mass classification systems

RMR: Rock Mass Rating value

σ_1 : Major principal stress (N/m²)

σ_3 : Minor principal stress (N/m²)

σ_c : Uniaxial compressive strength of the equivalent intact rock (N/m²)

A: Parameter depended on the rock mass quality, 1 for intact rock and 0 for totally disintegrated rock masses

B: Rock material constant depended on the rock type

α : Constant and independent to rock type and rock quality, 0.65 or 0.6

Compared with the Hoek-Brown criterion, Yudhbir *et al.* [31] proposed that their criterion gives predictions for brittle and ductile rocks, while the Hoek-Brown criterion gives excellent predictions in brittle behaviour of the rock mass.

d) Sheorey *et al.* criterion

This criterion has two versions:

- The 1989 version [70]:

$$\sigma_1 = \sigma_{cm} \left(1 + \frac{\sigma_3}{\sigma_{tm}}\right)^{b_m}$$

- The 1997 version [184]:

$$\sigma_{cm} = \sigma_c \exp\left(\frac{RMR-100}{20}\right)$$

$$\sigma_{tm} = \sigma_t \exp\left(\frac{RMR-100}{27}\right)$$

$$b_m = b^{\frac{RMR_{76}}{100}} < 0.95$$

With:

RMR: Rock Mass Rating value

If $RMR_{76} \geq 18$: use the 1976 version of Rock Mass Rating. If not:

$$RMR = 9 \cdot \ln Q' + 44$$

$$Q = \frac{RQD}{J_n} \cdot \frac{J_r}{J_a}$$

σ_{cm} : Uniaxial compressive strength of the rock mass (N/m²)

σ_c : Uniaxial compressive strength of the equivalent intact rock (N/m²)

σ_{tm} : Uniaxial tensile strength of the rock mass (N/m²)

σ_t : Uniaxial tensile strength of the equivalent intact rock (N/m²)

Q: Q system of the rock mass classification systems

b: Constant

e) T. Ramamurthy criterion

There are two versions of the T. Ramamurthy criterion for the rock mass [4]:

- The 1994 version:

$$\sigma_1 = \sigma_3 + B_j \sigma_3 \left(\frac{\sigma_{cj}}{\sigma_3}\right)^{a_j}$$

$$\sigma_{cj} = \sigma_c \cdot \exp(-0.008 J_f)$$

$$B_j = \frac{B_i}{0.13} \exp\left(-2.037 \sqrt{\frac{\sigma_{cj}}{\sigma_c}}\right)$$

$$a_j = a_i \sqrt{\frac{\sigma_{cj}}{\sigma_c}}$$

$$J_f = \frac{J_n}{n \cdot r}$$

- The 2001 version:

$$\sigma_1' = \sigma_3' + B_j \sigma_3' \left(\frac{\sigma_{cj}}{\sigma_3'}\right)^{a_j}$$

With:

σ_1 : Major principal stress (N/m²)

σ_1' : Major effective principal stress (N/m²)

σ_3 : Minor principal stress (N/m²)

σ_3' : Minor effective principal stress (N/m²)

σ_c : Uniaxial compressive strength of the equivalent intact rock (N/m²)

σ_{cj} : Uniaxial compressive strength of the joints of the rock mass (N/m²)

J_n : Joint frequency in the direction of the major principal stress

n : Inclination parameter

r : Coefficient of friction

B_j : Joint inclination

1.1.5. Conclusion

The presence of the rock structure, including various types of discontinuities, strongly influences the behaviour of the rock mass to which it belongs. The description of the rock mass as the assemblage of rock blocks that are separated by the discontinuities network is recommended. This leads to the demand of the “discontinuity/discrete” solutions in rock mechanics. Even the conventional solutions, called “continuous”, need to be modified in dealing with this problem. In the next part, some principal numerical methods in rock mechanics are briefly introduced.

1.2. Numerical methods for rock mechanics

1.2.1. Introduction

Any rock, strongly or weakly fractured, can be defined as a continuous, discontinuous or hybrid medium when the scale of interest is macroscopic, microscopic or in between. The “continuous” or “discrete” nature of an object or a methodology is not absolute but relative and problem-specific, depending especially on the problem scale [32]. If the object is small enough to rest totally inside the intersection zone of the rock structure, it can be treated as a continuous medium. If the research region is bigger, with the presence of more and more families of discontinuities, the study must be executed by the discrete mechanics or by the application of the partial discretization of the continuous medium.

Figure 1.2.1 shows two opposite natural states of the marble of Saint B  at in Haute Garonne (France): a) very fractured on the rock cliff on which the rock structure can be easily observed; b) nearly intact on a cylindrical specimen of the direct shearing test in laboratory.



a) At natural scale at rock cliff:
fractured rock mass



b) At specimen scale ($D = 85\text{mm}$) for a direct
shearing test: quasi-intact rock mass

Figure 1.2.1: Two states of the white marble of Saint B  at (Haute Garonne)

A normal object can be considered either as an assemblage of indefinite continuous particles (under the “continuous” viewpoint) or a multiple discrete particles (under the “discrete” viewpoint). A simple demonstration can be found in the example of a taut string published by J.R. Taylor [33]. The string underwent a small motion along the vertical axis y from the initial position on the horizontal axis x . When the string was considered as a indefinite number of continuous particles, its position is specified by the function $u(x,t)$ which is continuous function for the expression of the string’s displacement from its initial position at requested time. When the string was replaced by a set of n point masses linked

by massless strings, its position is given by the n discrete positions $u_i(t)$ with $i = [1, n]$. The variable $u_i(t)$ is the vertical displacement of the i^{th} mass from the horizontal axis at time t .

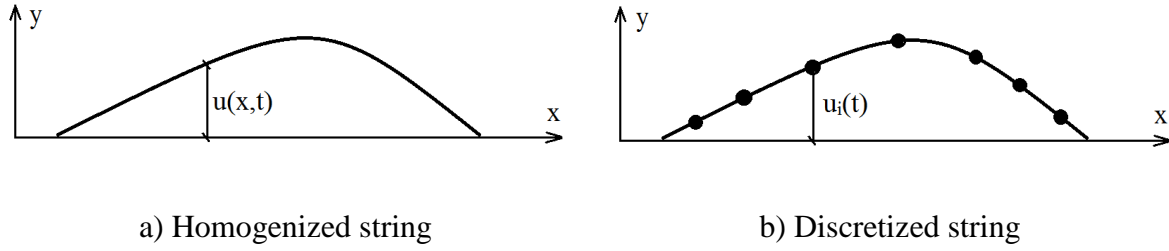


Figure 1.2.2: Displacement of a taut string in two cases of consideration (sourced from [33])

In two cases, the variable x in the function $u(x,t)$ and the index i of the displacement $u_i(t)$ of the i^{th} mass share the same role of the displacement expression. But they do not bring out the same signification when the index i only referred to a single particle of the string, the continuous variable x specified the infinitival particles of the string. Mathematically, $u(x,t)$ is a continuous two-variable-function and $u_i(t)$ is a discrete one-variable function. With the basic definitions of the velocity as the 1st-order-derivative of the position: $v(t) = \frac{du(t)}{dt}$; the acceleration is the 2nd-order one: $a(t) = \frac{dv(t)}{dt} = \frac{d^2}{dt^2}u(t)$; the momentum is the function of the mass and the velocity: $p(t) = m.v(t)$, the Newton's second law for the homogenized case is a partial differential equation for $u(x,t)$ which is the continuous derivative for x and t , respectively. For the discretized case, the law is expressed by a set of n ordinary/total differential equations which are derivative for t . Hence, the classical motion of the same body can be analysed continuously or discretely by the use of two types of differential equations. The solving task of differential equations is a basic mathematical problem that can be realised theoretically by hand. However, when the rock mass is multi-material, multi-phase, especially when the rock structure exists evidently, the differential equations (even in total or partial form) become complicated, high time consuming or even impossible to solve by hand. The available numerical tools to facilitate this task are thus necessary and practical.

In practice, to reach a quick or approximated engineering analysis, the presence of the discontinuities in the rock mass can be neglected and the characteristics of the intact rock mass can be used. This means that the rock media are considered as a CHILE material (Continuous, Homogenous, Isotropic and Linearly Elastic) [34]. The total rock mass can be thus assigned as the composition of several geological layers, the underground structures and some isolated geological objects. From that model, the behaviour of the underground

structures and their surrounding environment is found by manual approaches or with the help of many efficient computer tools which are based in general on the continuous media mechanics, of which the Finite Element Methods (FEMs) is the most popular. However, this approximation brings out an inaccurate image of the rock environment due to the lacking of its rock structures. Indeed, the presence of discontinuities strongly affects the characteristic and behaviour of the rock mass. Any rock mass is always DIANE (Discontinuous, Anisotropic, Inhomogeneous and Not-Elastic) [37]. Different solutions to overcome this problem that have been of interest for many researchers can be divided into two large paths: maintaining the application of the continuous media and finding another appropriate theoretical framework. The first thought is searching an equivalent homogenous rock environment to replace the real one (intact rock mass and its discontinuities). The variable about which equivalence is researched can be debated. However, the definition of a suitable model is a big challenge. The second option leads us to a discrete element environment where displacements and rotational degrees-of-freedom of element and contact conditions between elements is paid attention to, with the foundation of the Discrete Element Method (DEM) in which CHILE features are replaced by DIANE ones. In general, a supplement theory is needed to bring out a comprehensive approach for the concretization of the DEM in engineering analysis. The Non Smooth Contact Dynamics (NSCD) method ([38], [39]) is an alternative choice that deals with frictional unilateral contact between rigid or deformable bodies. It can be used for the numerical simulation of dynamic fracture of many materials and structures. It concerns the entire fracture process from crack initiation, growth, propagation, rupture to post fracture behaviour when solid fragments interact [40].

With the arbitrary forms of the blocks in the rock mass created by the arrangement of the rock structure, the use of some standard-shaped elements or grids to describe the constituted blocks in the medium is not appropriated or even impossible. Hence, besides the analysis methods of the mechanical behaviour of the rock mass, the numerical methods for the reconstruction of the rock mass with the presence of the complex rock structure take an important role in rock mechanics. The real rock mass is replaced by its mathematical and/or geometrical models for the representation and/or mechanical analysis. Many technics and relevant solutions have been proposed and applied recently.

1.2.2. Analysis methods

1.2.2.1. Mechanical framework of the classical mechanics

Before going in the details of the principal analysis methods in rock mechanics, the fundamental equations of the classical mechanics are recalled from [41]. Studying the mechanical behaviour of a body, one knows that the body is displaced and deformed, under the application of the external forces and the correlation with the neighbouring objects. The transformation of the body is characterized by:

- the translational displacement of the inertial centre;
- the rotational displacement characterized by the transformation of the orientation matrix;
- the deformation characterized by a deformation tensor.

For a rigid body, the position of each point on the body and the angle between two points is fixed on the material medium Ω .

The classical strong form of the equilibrium equation of the classical mechanics is given by:

$$\text{div}(\bar{\sigma}(x, t)) + \rho(x, t)f_v(t) = \rho(x, t)\dot{v}(x, t) \text{ with } \forall x \in \Omega(t)$$

With:

ρ : Volume mass of the body

f_v : Volume forces applied on the body

\dot{v} : Acceleration of the body

$\bar{\sigma}$: Stress tensor

t : Surface forces applied on the Γ_f with $t = \bar{\sigma} \cdot n$

n : Normal vector of the Γ_f

v : Velocity imposed on Γ_v

Γ : Closed boundary of the body

Ω : Material field of the body

Considering the space δV of virtual velocities defined by:

$$\delta V = \{\hat{v}(x) = \hat{v}_c + \hat{\omega} \times (x - x_c) + \hat{v}_D(x) \text{ with } \forall x \in \Omega(t) \text{ homogenous for the fixed dll}\}$$

With:

x_c : Position of the inertial centre

\hat{v}_c : Virtual velocity of the translational displacement

$\hat{\omega}$: Virtual velocity of the rotational displacement

\hat{v}_D : Virtual velocity of the deformation of the body

Using the virtual velocity of the translational displacement $\hat{v}(x) \in \delta V$, the weak form of the equilibrium equation is given by:

$$\int_{\Omega(t)} \rho(x) (\dot{v}(x, t) - f_v(t)) \cdot \hat{v}(x) d\Omega = \int_{\Omega(t)} \text{div}(\bar{\sigma}(x, t)) \cdot \hat{v}(x) d\Omega \quad \text{with } \hat{v}(x) \in \delta \mathcal{V}^0$$

Replacing the virtual velocity of the body:

$$\hat{v}(x) = \hat{v}_c + \hat{\omega} \times (x - x_c) = \hat{v}_D(x) \quad \text{with } \forall x \in \Omega(t)$$

And the acceleration of the body:

$$\dot{v} = \dot{v}_c + \dot{\omega} \times (x - x_c) + \omega \times (\omega \times (x - x_c)) + 2\omega \times v_D + \dot{v}_D$$

into the previous equation, we obtain three fundamental equations of the classical mechanics:

- The Newton equation:

$$\begin{aligned} \int_{\Omega(t)} \rho(x) \dot{v}(x, t) \cdot \hat{v}_c d\Omega &= m \dot{v}_c \cdot \hat{v}_c(t) \\ + \dot{\omega} \times \int_{\Omega(t)} \rho(x) (x - x_c) d\Omega \cdot \hat{v}_c(t) &+ \omega \times \left(\omega \times \int_{\Omega(t)} \rho(x) (x - x_c) d\Omega \right) \cdot \hat{v}_c(t) \\ + 2\omega \times \int_{\Omega(t)} \rho(x) v_D d\Omega \cdot \hat{v}_c(t) &+ \int_{\Omega(t)} \rho(x) \dot{v}_D d\Omega \cdot \hat{v}_c(t) \end{aligned}$$

When the body is rigid, we have:

$$\begin{aligned} \int_{\Omega(t)} \rho(x) v_D d\Omega &= 0 \\ \int_{\Omega(t)} \rho(x) (x - x_c) d\Omega &= 0 \end{aligned}$$

Hence, the Newton equation of the rigid bodies is expressed by:

$$m \dot{v}_c + \int_{\Omega(t)} \rho(x) \dot{v}_D d\Omega = \int_{\Omega(t)} \rho(x) f_v(t) d\Omega + \int_{\Gamma(t)} t(x, t) d\Gamma$$

- The Euler equation:

$$\begin{aligned} & \int_{\Omega(t)} \rho(x)(x - x_c) \times \dot{v}(x, t) \cdot \hat{\omega} d\Omega \\ & \int_{\Omega(t)} \rho(x)(x - x_c) d\Omega \times \dot{v}_c \cdot \hat{\omega} + J \dot{\omega} \cdot \hat{\omega} + \omega \times J \omega \cdot \hat{\omega} \\ & + 2 \int_{\Omega(t)} \rho(x)(x - x_c) \times \omega \times v_D(x) \cdot \hat{\omega} d\Omega + \int_{\Omega(t)} \rho(x)(x - x_c) \times \dot{v}_D \cdot \hat{\omega} d\Omega \end{aligned}$$

When the body is rigid, we have:

$$\int_{\Omega(t)} \rho(x)(x - x_c) \times \omega \times v_D(x, t) d\Omega = -\omega \times \int_{\Omega(t)} \rho(x)(x - x_c) \times v_D(x, t) d\Omega = 0$$

Hence, the Euler equation of the rigid bodies is expressed by:

$$\begin{aligned} & J \dot{\omega} + \omega \times J \omega + \int_{\Omega(t)} \rho(x)(x - x_c) \times \dot{v}_D(x, t) d\Omega = \\ & \int_{\Omega(t)} \rho(x)(x - x_c) \times f_v(t) d\Omega + \int_{\Gamma(t)} (x - x_c) \times t(x, t) d\Gamma \end{aligned}$$

- The Lagrange equation:

$$\begin{aligned} & \int_{\Omega(t)} \rho(x) \dot{v}(x, t) \cdot \hat{v}_D(x) d\Omega = \dot{v}_c \cdot \int_{\Omega(t)} \rho(x) \hat{v}_D(x) d\Omega \\ & + \dot{\omega} \cdot \int_{\Omega(t)} \rho(x)(x - x_c) \times \hat{v}_D(x) d\Omega + \omega \times \left(\omega \cdot \int_{\Omega(t)} \rho(x)(x - x_c) \times \hat{v}_D(x) d\Omega \right) \\ & + 2\omega \times \int_{\Omega(t)} \rho(x) v_D(x, t) \cdot \hat{v}_D(x) d\Omega + \int_{\Omega(t)} \rho(x) \dot{v}_D(x, t) \cdot \hat{v}_D(x) d\Omega \end{aligned}$$

Solving those three equations, the mechanical behaviour of the object of research is obtained. Based on the modelling viewpoint, the solutions for solving the differential equations of those fundamental equations, different numerical methods in rock mechanics can be found [32], [34], [35]:

- The continuous methods: The rock mass is discretized by the grids, cells or standard elements into a finite number of elements on the whole region or only one element for the boundaries. The Partial Differential Equations (PDEs) of the rock mass are then transformed to algebraic equations at grids, elements or boundaries. The unknown variables of the field are solved through the equation of motion at those

locations with the restriction of the continuous (without “jump”) movements between adjacent elements in all the domain;

- The discrete methods: The rock structure cut the rock mass into discrete blocks that contact with their adjacent blocks at vertices, edges and/or faces. The correlation between displacement, force and equilibrium of the rock mass is analysed with the acceptance of the relative movements between two adjacent blocks;
- The hybrid methods are the coupling of the two previous methods.

Besides, these methods can also be classified into two categories [36]:

- Domain methods: when the whole medium within the outer boundaries of the rock mass is geometrically discretized by the virtual grids/meshes into cells or elements or by the intersection of the discontinuities of the mass into discrete blocks.
- Boundary methods: when only the boundaries of the medium are geometrically discretized while the internal media are considered as continuous.

In this section, the introduction of the principal methods for the analysis is presented with the influence of two technical reviews [32] and [34] which are, in our knowledge, fairly broad in their aims and precisely dedicated to our domain of research.

1.2.2.2. Continuous methods

As the most popular branch of the family of numerical methods for almost all kinds of material, Continuous methods are classified into three sub-groups as follows:

- Finite Difference Method (FDM) and related methods;
- Finite Element Method (FEM) and related methods;
- Boundary Element Method (BEM) and related methods.

The divergence between them mainly comes from:

- The solving solutions of the Partial Differential Equations (PDEs) of the equations of motion;
- The discretization of the body at complex configuration regions;
- The modelling solutions for the discontinuities presence on the rock material.

The geometry discretization, as introduced in the previous section, is the important starting operation for the continuous numerical methods. The real configuration of the rock mass is

aimed at replacing by an artificial arrangement of which the continuous representation in terms of scalar or vector functions is used. This idea leads to the plain sampling of the field functions at a finite number of points usually called nodes within the domain [42]. The assemblage of nodes on the grids/meshes spreads out on the whole rock mass. Hence, the indefinite particles of the real mass are represented by the grids/meshes that are formed by finite number of nodes or elements in the modelling mass. This fact may answer why several methods of this group have names that begin with the word “Finite”. The terminology “meshing” can understand as the geometry discretization of the studied mass.

a) FDM and related methods

FDM is the numerical method for solving the PDEs using finite difference equations to approximate derivatives [43]. In another words, FDM applies the discretization of the governing PDEs by replacing partial derivatives with Finite Differences (FD) at the grid, transferring the original PDEs into the algebraic equations with the variables at grid nodes [32]. The solution of FDM is summarised as: i) Firstly, define the grid of nodes, which is usually a very regular one, and attach a local field quantity to each node; ii) Then, at each node, the differential operators are rewritten in a discrete expression by means of the mentioned FD formulas [42].

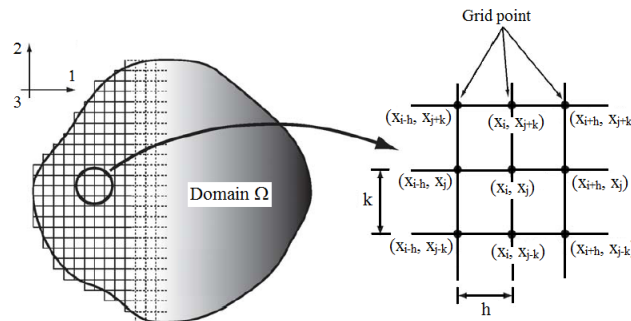


Figure 1.2.3: FD grid in 2D (sourced from [44])

The basic calculation procedure is given in some main steps [45], [46]:

- Discretize the research mass by a uniform grid of which the grid nodes are close enough to minimize the errors;
- At each node, approximate the derivatives by algebraic equation referring the adjacent nodes;
- Solve the algebraic equations for the dependent variable;
- Analyse the obtained results and errors.

FDM is the oldest in the family of continuous methods and is the basis of the explicit approach of DEM [32]. Some advantages of the analysis by this method can be listed [44]:

- Simple mathematical operations since the initial DEs are reduced to linear equations;
- Discontinuities can be modelled by the use of the grid nodes on each side of a discontinuity;
- Dynamic problem can be solved by the explicit time integration with small time interval steps;
- Non-linear behaviour are analysed through an explicit stepwise process with sufficiently small load intervals until the final state is reached so that no iteration of mapping is needed;

However, some limits are also noted:

- Only suitable for the regular geometry objects since the regular grid is used to mesh the object [32], [45].
- Super high number of time steps are often required for solving the dynamic problems [44];
- The mechanism of the fracture development can only be modelled “via a process of material failure or damage propagation at the grid points or cell centre, without creating fracture surfaces in the models” [3].

Finite Volume Method (FVM) is another continuous numerical method that can be considered to be in the same group with FDM. FVM discretizes the field equations by subdividing the problem domain into cells and building the integral field equations on these cells. C.Mattuissi [42] suggested that with the use of only integral approach, the requirements of the discretization are hardly to be fulfilled. Moreover, the discretization of time in FVM stands as a separated procedure that leads the analysis to a space-time co-boundary operator. In comparison with FDM, FVM is less popular. However, the irregular grids of the Finite Volume technics are more adapted for complex boundary conditions, different material properties than the regular ones of FDM. Originally, it was dedicated to the computational fluid mechanics but then modified to also capable with the solid mechanics. FLAC is the most famous group of the computer codes that bases on FVM/FDM [34].

These two methods are classed as the domain methods since the discretization by grids is executed on the entire medium. Conceded the role this group of methods in the mechanical analysis, FDM and FVM are found to be not suitable for the application in rock and tunnel engineering due to some reasons:

- Modelling of the rock structure is almost handicapped due to the use of the regular grids of FDM or the cell-based grids of FVM since the real appearance of the rock structure is much more complex with random configurations;
- Approximation of the fracture development are far to be obtained with reasonable accuracy.

Even further, C. Mattuissi [42] commented that FDM and FVM can only use for the non-structure field which can be translated as the denial of their application in rock mechanics. This group of methods is thus not recommended for our research target.

b) FEM and related methods

FEM is the numerical technic for finding the approximate solutions to PDEs by eliminating the spatial derivatives. The PDEs are replaced by a system of algebraic equations or a system of ordinary differential equations [47]. FEM divides the research domain into discrete small sub-domains (elements) which are in standard shapes. Each sub-domain is structured by the fixed number of discrete nodes that are situated on the vertices and/or on the edges [32]. A node has 6 Degrees Of Freedoms (DOFs) (3 are translational and 3 are rotational displacements). Loads apply always at the nodes of the mass. The field quantities that have been selected as unknowns are given a discrete representation in terms of a finite number of variables associated with geometric objects, which belong to the mesh [42].

FEM was built on two fundamental assumptions of displacement [44]:

- Displacements at any point in an element are interpolated from the displacements of the nodes of that element by the use of the appropriate interpolation function;
- When a small virtual displacement is applied on the body, the body is in equilibrium state only when the total internal force associated with the virtual displacement field are equal to the total virtual force work.

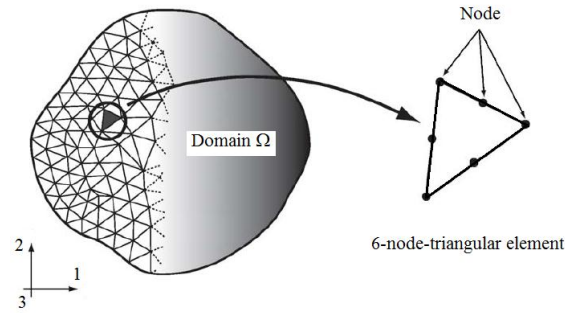


Figure 1.2.4: FE discretization in 2D (sourced from [44])

The basic calculation procedure with FEM is given in some main steps [48]:

- Discretise the research mass into standard elements and assign the displacement conditions of the nodes in the mass with loading conditions;
- Construct the system of linear or nonlinear algebraic equations as the correlations between the displacements and the forces of the elements and the nodes;
- Analyse the obtained results and errors.

The analysis interpolation in FEM is done by the used of two local character function:

- Shape functions to reconstruct the unknown field from its discrete representation;
- Weight functions to transform the PDEs of shape functions into algebraic equations.

C. Mattuissi [42] proposed that shape functions are used to reconstruct the fields in order to approximate the constitutive equations, whereas weight functions define the spread cells which constitute a continuous counterpart of the secondary mesh to which the corresponding topological equations are applied. With the discretization by standard elements in the entire domain by meshing, FEM is no doubt a domain method.

The discontinuities are explicitly represented by specific “joint elements”, the intersection of discontinuities can be modelled but requires increased computational expense (time consumption, available memory, the robustness of calculation tool, for instance) [36].

FEM is the most widely applied numerical method for most of materials and is the basis of the implicit approach of DEM [32]. There are plenty of FEM-based computer codes that have been taken an undeniable strong role in in many engineering fields, among them are ANSYS, SAP, ABACUS. For structural analysis, no other method can replace the place of FEM with the plentiful concretization in majority of available analysis softwares. One can find the principal advantages of FEM:

- Formed by multi-shape standard element, the meshing grids are not regular that leads to the higher complexity of the geometry and configuration of the studied fields than those of the FDM;
- Dynamic analysis are executed in less time steps in comparison with the FDM that helps to reduce the time consume [44];
- No need to a priori assume the failure mechanism of the body, thus different cases of analysis are possible to examine [14];

R.E. Hammah *et al.* [14] proposed two unique advantages of FEM (with the application of the Shear Strength Reduction (SSR) method) over the discrete numerical methods:

- Capable to generate different integrated components in the same model (rock mass and support structures, for instance);
- Handle the case when the discontinuities terminate in the intact rock before the intersection with other discontinuities.

In the scope of our knowledge, those two mentioned points are rather strong but not unique of FEM due to the capability of some actual discrete-based-software such as LMGC90 and RESOBLOK. Like any numerical methods, FEM has its own limits caused by its inherent disadvantages:

- Impossible to model the development of fractures;
- Cannot model the large strains or the detachment of rock blocks due to the assumption of the continuous condition of displacement at the nodes of grids [14];
- Require iteration for the analysis of non-behaviour body due to the application of the implicit solutions.
- Not robust in analysing the bodies in complex conditions (complex configuration, multi-phases, multi-material, fractured condition, grand opening discontinuities, for instance) and when the rotational motion of elements is need to be taken into account.
- In fact, those mentioned conditions can always be approximated but the generation of mesh becomes complicated due to the limit types of standard elements, the stiffness mass tends to be ill-conditioned and the continuous mass is strictly kept

from breaking into pieces [34]. As the result, the analysis is time consuming, less accurate and difficult to solve the PDEs.

Aimed at maintaining the widely application of FEM, some special versions such as the “enriched FEM”, “generalised FEM” have been proposed [34]. Furthermore, the SSR method is a modification of FEM for the analysis of blocky rock masses [14].

In the initial intention of our research, an equivalent continuous rock material was searched to aim at using FEM as the analysis and simulation tools for fractured rock masses. However, the task was found to be much more complicated than a material replacement and the results were forecasted to be not well representative for the real fractured rock mass. The biggest default of FEM is the impossibility of detachment modelling of rock blocks which is an inherent local and/or total failure phenomenon in tunnelling. Otherwise, when the rock mass is highly fractured, a FEM-based-analysis will lead to the complicated PDEs or low accuracy. Due to those reasons, this group of methods is not our suggestion.

c) BEM and related methods

In BEM, only the boundaries of the medium are discretized, which makes it different to the above methods in which this operation is executed on the entire medium. BEM solves the linear PDEs as boundary integral equations. For simple words, BEM keeps the domain to be infinite continuous inside but discretises its boundary. Hence, this is a boundary method.

The PDEs which concerned to the whole medium are then transformed to integral equations which consider only the boundary values. The solution is then approximated at the boundaries while equilibrium and compatibility are exactly satisfied inside the medium [44].

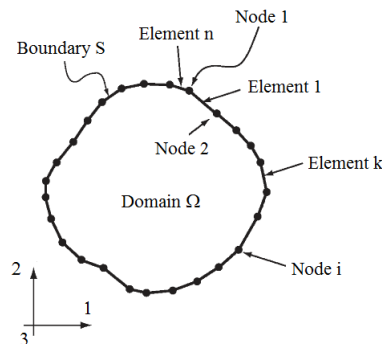


Figure 1.2.5: Boundary discretization in 2D (sourced from [44])

The basic calculation procedure with BEM is given in some main steps [49]:

- Build the mathematical model as a boundary value functions for PDEs and represent them by the formulas of boundary potentials to obtain the boundary integral equations;
- Solve the boundary integral equations by the trial functions as the boundary elements
- Generate the discrete functions with the solution of the linear system;
- Analyse the obtained results and errors.

There are two approaches for solving the unknown variables in the studied field ([36], [44]):

- Direct BEM: The unknown variables are solved directly for the specific boundary conditions;
- Indirect BEM: In the first step of the solution, the assumed unknown variables that satisfy prescribe boundary conditions are found. Then, the unknown variables are expressed in terms of those assumed values.

Some strong points of BEM are listed as [36]:

- Simplicity meshing and modelling since the rock mass is treated as an infinite extended continuum;
- Less number of elements in comparison with other methods, the solving rate tends to be faster without strong requirement of calculation tools;
- Capable to analyse the complicated couples of the bulk behaviour as the thermo-mechanics and hydro-mechanics;
- Being the most robust technics for the modelling of the fracture propagation and for the infinitely large domains [32]

Discretized only the boundaries but not the whole medium, the BEM is limited for some cases of analysis:

- Objects of which the ratios between surface and volume are small [44], [50];
- When stresses and displacements are only applied on the boundaries of the medium [44];
- For static continuum and elastic behaviour analysis.

This method has the difficulties in analyses of non-linear materials and inhomogeneous media due to the limitation of the sub-domains division [34]. Some special versions of BEMs as Dual BEM, Galerkin BEM or Dual Reciprocity Method (DRM) have been proposed to broaden the limitations of BEM.

1.2.2.3. Discrete methods

The discrete methods (or discontinuous methods) analyse the research domain as the assemblage of the rigid or deformable blocks that are created by the intersection of the discontinuities families or by isolated fractures. P.A. Cundall and R.D. Hart [51] proposed that the name “Discrete element” was attributed to a numerical tool if and if only:

- It permitted the finite displacements and rotations of discrete bodies as well as the complete detachment;
- It auto-recognized the new-born contacts during the evolution of calculation.

This definition reflects the main distinguishes of this group to the rest and also their unique advantages. The basic difference between the discrete and continuous methods is that the contact patterns between particles of the medium are continuously changing with the deformation process for the former, but are fixed for the latter [34].

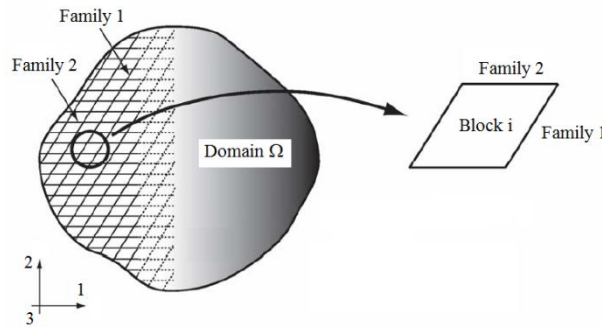


Figure 1.2.6: Discrete element discretization in 2D (sourced and modified from [44])

The detection of contact between blocks is the vital operation for a discrete method. First, the neighbour search is realised to list all possible in-contact blocks. Then, in each pair of blocks that were found in the previous step, the points and the planes of contact are determined. The distance between two nearest points of two adjacent blocks is considered as the shortest distance between them. The contact plane (or “common-plane” as called by Cundal) is “a plane that, in some sense, bisects the space between the two contacting polyhedral” [51]. Depended on the location of the points and the plane of contact, four main types of contact are given [52]:

- Face-to-face: when two nearest points are located on two faces of two blocks, respectively. The plane of contact is one of two faces;
- Vertex-to-face: when one nearest point is located on a vertex of the first block and the other nearest point is located on a face of the second block. The plane of contact is the mentioned face;
- Vertex-to-edge: when one nearest point is located on a vertex of the first block and the other nearest point is located on an edge of the second block. The plane of contact is passed through the edge and perpendicular with the nearest line between the vertex and the edge;
- Vertex-to-vertex contact: when the two nearest points are located on two vertices of two blocks, respectively. The plane of contact is perpendicular with the line connects two vertices and either passed one vertex or the mid-point of the mentioned line;
- Edge-to-edge: when the two nearest points are located on two edges of two blocks, respectively. The plane of contact is either passed through one edge or aligned the normal vector of the plane that connected two edges;

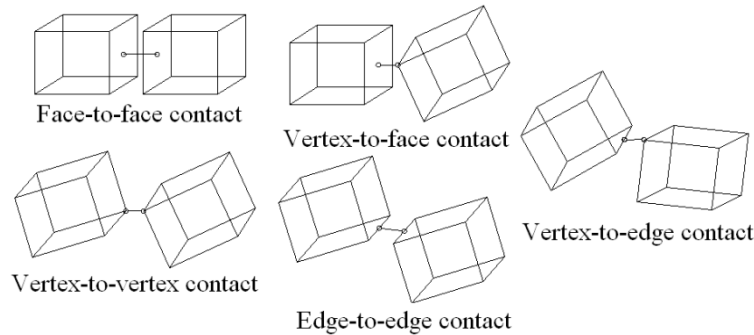


Figure 1.2.7: Main types of contacts between two adjacent blocks

There are two assumptions that can be used to describe a contact between two adjacent blocks. Depending on the correlation of the position and the normal contact forces between two blocks, the contacts can be described by two types of contact. The choice of applied assumption should be realised on the basis of physics rather than the available numerical solution [51]:

- Soft contacts: A non-linear normal stiffness exists between two contact blocks and the radius of the contact area is smaller than the radius of the blocks. The contact force is assumed to start from zero at the time of the first touch of two blocks. Since

the contact force is related to the contact displacements, a block must penetrate the other to produce a finite value of contact force. This type of contact is more suitable for deformable rock mass or for rigid blocks which are covered by soft material.

- Hard contacts: No penetration between contact blocks is allowed. The collision between them is considered as the instantaneous exchanges of momentum with or without the energy conservation.

Once the contacts are detected, the correlations between the movement, force and equilibrium of blocks are analysed. The interaction law between two adjacent blocks can be studied by two solutions [53]:

- When the interaction is a rough representation of what happens at the boundary scale: The motion is considered as rigid in large time scale that leads to the plastic behaviour of the rock mass. The equation of motions is given as a function of an implicit law between the external force R , the displacement U and the configuration g of the rock mass written by $f(R, U, g) = \text{true}$.
- When the interaction is a fine representation of what happens at the boundary and at the bulk scale: The motion is presented by the wave propagation in fine time scale that leads to the elastic and plastic behaviour of the rock mass. The equation of motions is given as a function of an explicit law between the external force R , the displacement U and the configuration g of the rock mass written by $R = f(U, g)$

The former leads to the non-smooth solution while the latter leads to the smooth one that will be further introduced in the next parts. With the acceptance of the relative movement between two adjacent blocks, discrete method is capable to model the large displacements, the block rotation and the detachment of rock blocks. This group of method is robust for analysing the large amount of particles, for various kinds of contact following various contact laws with the auto-recognition of new-born contacts during the calculation ([32], [44], [52]). Moreover, discrete methods are capable to model the propagation or the development of the fractures which is a weak point of the continuous methods. Three representations of the discrete methods are briefly introduced in the following parts:

- Group of Discrete Element Methods (DEMs);
- Discontinuous Deformation Analysis (DDA);
- Discrete Fracture Network (DFN) method.

The discontinuous mechanics and its numerical methods are widely applied in the rock engineering because its robust capacity in modelling the rock structure as its natural appearance. They are relatively young in comparison with the continuous ones but impressively rapidly develop in computational mechanics ([34], [54]).

a) Group of DEMs

This group of methods is considered to be the most widely applied for the granular material and for fractured domains. The rock mass is divided into small particles with random configuration and discrete features of mass, velocity, contact [55]. A common simulation by a DEM is formed by four principal components [51], [56]:

- Object representation: the rock mass is discretised into blocks by the intersection of the discontinuities in the mass. Each block is individual with its neighbours;
- Contact detections: the types, points and planes of contact are determined;
- Physics and mechanics behaviour: the correlation between force and displacement is expressed through the equation of motion. Iteration is realised in time steps with the different integration methods (implicit or explicit) with the different time evolution discretization solutions (even-driven or time-stepping);
- Visualisation and data treatments.

The force which is resulted by the interaction of adjacent blocks is acted at the boundaries and is composed of the normal and the tangential component. Hence, the relative movements between blocks generate the contact force at the boundaries. The motion equations of the blocks of the domain are solved by the continuous detections and the treatment between blocks. The forces at the interfaces are calculated by using a penalty method of which forces are related to the relative movements and the stiffness of the discontinuities [44]. The interpenetration among adjacent blocks exists or not depending on the type of contact (soft or hard), analysis solution (smooth or non-smooth) or the correlation of the contact forces with other elements of the motion equation (implicit or explicit solution).

Based on the different solutions of the contact discretization, the DEMs for rock engineering are distinguished into two groups of methods: smooth dynamics and non-smooth dynamics:

i) Smooth Dynamics methods (or regular approaches):

The function between the contact force and the displacement of rock blocks in the model is solved. The interpenetration is accepted and used to calculate the contact forces. As discussed in the aforementioned part, the Smooth Dynamics methods can be considered as the explicit solution of the discrete methods since it use the explicit discretization of time and is based on the theory of FDM [34], [57], [58], [53]. The state of the domain at the next time step is calculated from the one at the current time.

The equation of motion for the smooth contact in space system is given by ([53], [58], [59]):

$$\begin{cases} M(q) \frac{dv}{dt} + F(t, q, v) = 0 \\ v = \dot{q} \end{cases}$$

With:

$$F(t, q, v) = F_{inertia}(q, v) + F_{int}(t, q, v) - F_{ext}(t)$$

And the continuous boundary conditions:

$$t_0 \in \mathbb{R}, q(t_0) = q_0 \in \mathbb{R}^n, v(t_0) = v_0 \in \mathbb{R}^n$$

$$(t_0, T) \in \mathbb{R} \times \mathbb{R}, \Gamma(q(t_0), v(t_0), q(T), v(T)) = 0$$

M: inertial matrix

dt: Lebesgue measure

n: number of measure

q: Vector of generalized DOF (m)

v : Generalized velocity (m/s), $v = \dot{q}$

t_0 : Initial time (s)

T: Final time (s)

F: Contact force (N)

$F_{inertia}$: Inertial force (N)

F_{int} : Internal force (for deformable bodies) or nonlinear inertia terms (for centrifugal and gyroscopic) (N)

F_{ext} : External force (N)

The explicit discretization of time is used in the integration in each small time step: It calculates the state of the domain at the next time step from the one at the current time. Initial and boundary conditions must be added to fully describe the evolution of the system. Considering a rigid component, a more suitable dynamical equation may be used introducing two components of the velocities of the centre of mass. The previous equation of motion is replaced by the Newton-Euler system of equation. However, when there is a collision between two blocks, the equation of motion and the interaction law are not sufficient to describe properly all the physics of the problem. Hence, it must take into account [53]:

- Local phenomena as inelastic behaviour of materials at the interface depending on both the contact geometry and the material behaviour;
- Global phenomena as the wave propagation in the body bulk, body geometry dependency and boundary conditions;
- More complex effects: long distance effects due to simultaneous impact.

This demand leads to the Non-Smooth Dynamics method. The most popular representative is the Distinct Element method of Cundall [51] that is considered to be based on the theory of FDM ([32], [34]). This method was applied as the fundamental for the ITASCA software group of which UDEC, 3DEC and PFC codes are common.

ii) Non-Smooth Dynamics methods (or non-regular approaches):

The function between the contact force, the displacement and the configuration of rock blocks in the model is solved. The forces are bilateral and determined from the solution of local nonlinear equations by taking consideration of the restitution of: Newton type related to the velocity, Poisson type related to impulsion, Stronge type related to energy [53]. Avoiding the interpenetration of the contacts, a damping which is proportional to the stiffness and the size of the particles is added. The Coulomb friction law is used to express the constitution law for the tangential forces between contacting blocks. The non-smooth viewpoint is built from three nonlinear aspects:

- spatial non-linearity with non-interpenetration contact;
- time nonlinearity with shocks between particles;
- nonlinear contact law.

The collision and other non-smooth phenomena, which cannot be solved the Smooth Dynamics methods, are capable by this group of methods with the addition of the right continuous and the left continuous functions of the vector of generalized DOF in the equation of motion. The Lagrangian equation of motion for the non-smooth contact is thus given by:

$$\begin{cases} M(q)dv + F(t, q, v^+)dt = dr \\ v^+ = \dot{q}^+ \end{cases}$$

Of which:

$$v = \dot{q}$$

$$q(t) = q(t_0) + \int_{t_0}^t v^+(t)dt$$

$$F(t, q, v^+) = F_{inertia}(q, v^+) + F_{int}(t, q, v^+) - F_{ext}$$

With:

M: inertial matrix

dr: Reaction measure

dt: Lebesgue measure

v : Velocity (m/s)

v^+ : Right continuous of velocity

q : Vector of generalized DOF (m)

q^+ : Right continuous of displacement

t_0 : Initial time (t)

F: Contact force (N)

$F_{inertia}$: Inertial force (N)

F_{int} : Internal force (N)

F_{ext} : External force (N)

The implicit discretization of time is used for the integration in each large time step: It calculates the state of the domain at the next time step by involving the states in the current

and the next time step ([34], [57], [58], [59], [53]). It gives closed form integrations for the stiffness matrices [32]. Implicitly DEMs rely on the following hypotheses:

- the deformation concerns only the contact point neighbourhood → components of the system may be considered as rigid;
- the contact area is small behind the size of the component → locus of interaction may be supposed as punctual;
- interactions are binary (no effect of connected interaction by particle on their behaviour) → interaction law depends only on related component;

The principal representation of this group is Non-Smooth Contact Dynamics (NSCD) method that was developed by J.J. Moreau, M. Jean *et al.* ([38], [39], [60]). By utilising the basic mesh solution of FEM, the Non-Smooth methods are considered as hybrid DEM/FEM.

This group of methods is considered to be the most appropriate tools for the research of the rock fractures and for granular materials. The late naissance of this group did not obstruct it to be the most progressive numerical tools not only for rock engineering. In the scope of our research, the implicit DEM that is concretized through NSCDs method in LMGC90 is used for the simulation and analysis of the fractured rock mass where an excavation procedure of an opening is found.

b) Discontinuous Deformation Analysis (DDA) method

DDA is a discrete method that was proposed the first time by Shi in 1988. DDA can be considered as the combination of FEM's solution for stress – displacement problem with the DEM's detection of contact between discrete blocks along discontinuities [61]. DDA is a displacement method when considering the displacement as the unknown variables in solving the equations of equilibrium that are derived from minimizing the total potential energy of the analysed system. DDA shares the same implicit theory with the Non-Smooth Dynamics methods so that sometimes it is classed as a special case of that group.

In DDA, each block is described by 12 DOFs that are defined by the translational and the rotational displacement of the block, the normal and tangential strains in the blocks. The contact forces between contacting blocks are composed of the frictional, normal and tangential components.

S. Beyabini *et al.* [52] introduced a DDA typical algorithm as follow: First, the contact detection is executed to find out the types, points, planes of contact with an assumed tolerance level. Second, the set of simultaneous equilibrium equations are written as $K.D = F$ following the FEM convention [44] with:

- K is the generalised stiffness matrix K of which K_{ii} depend on the material properties of the i^{th} block and K_{ij} depend on the contact between the i^{th} and the j^{th} block ($i \neq j$);
- D is the deformation matrix;
- F is the matrix of contact force.

The equations are solved for the displacement variables with the constraints of the system of inequalities associated with block kinematics and Coulomb's friction for sliding along block interfaces. The "open-close" iteration is realised with the criterion of non-interpenetration (*i.e.* no tension and no penetration between contacting blocks): If the relative displacement between two blocks is smaller than their initial distance, no contact check is performed. If the interpenetration is found at a contact, a reaction force (represented by a stiff spring) is added to lock the movement in corresponding direction and keep the blocks separated. Then, the system is recalculated and new contacts are searched. The matrix K and F are updated with the position of new vertices and new stresses of contact. Iteration is ended when there is no interpenetration between blocks. At the end of each iteration, the reaction force is calculated. If the normal component of the contact force is tensile, the spring is removed. The velocity of blocks at the previous iteration is used as the initial value of the next iteration.

The implicit discretization of time is applied for the analyses by DDA with the hypothesis of very small change of block's position between two time steps. Hence, in one time step, the change of the contact type is neglected [52]. The large displacement or deformation of the rock mass, if any, is the accumulation of small displacements or deformations after the big amount of time steps [44]. For the static analysis, the initial velocities of blocks are set to be null.

Besides the common advantages coming from the group of discrete methods, DDA owns their specific strong points [61]:

- Energy dissipation due to the frictional resistance at contact without the requirement of artificial damping as in DEM;

- Robust for problems with small characteristics as time stepping scheme provides necessary numerical damping to control resonance interactions within and between blocks;
- Step-wise linear implicit time stepping for quasi-static solutions.

However, the most serious limitation considered by [61] is the reduction of numerical damping which occurs when the characteristic length of a problem increases.

Since DDA applies the implicit discretization of time and there is a developed version with the implementation of the FE mesh, DDA is sometimes classed an implicit DEM. However, based on the differences between DDA and DEM, that consideration is found to be unreasonable. Some typical distinguishes are listed:

- DEM is a force method (force is the unknown variable), while DDA is a displacement method (displacement is the unknown variable). In another word, the contact force is the function of displacements in DEM but the displacement is the function of contact forces in DDA;
- During the contact, interpenetration between blocks is permitted in DEM but restricted in DDA;
- In DEM, contact forces are composed by the normal and tangential components but in DDA, they are described by the normal, tangential and frictional components. The energy in DDA is dissipated naturally by the frictional force while virtual damping must be used in DEM;
- To solve the displacement - force correlation of the medium, the equation of motion is solved by the implicit or explicit discretization of time in DEM. Whereas, the system of simultaneous equilibrium equations is derived by potential energy in DDA.
- For the static problem, the damping is applied in DEM analysis while the null value is set for initial velocities of block in DDA.

Some important “milestones” in the development of DDA:

- From the original version in 2D (named 2D - DDA) upgraded to the 3D version (named 3D- DDA);
- Several theories of contact detection.

c) DFN method

If only considering the DFN method in the family of the analysis methods, it is the special DEM for the fluid flow analysis in fractured and karstic rock mass [34], for the identification of individual fractures and karsts [62]. It is defined as “analysis and modelling which explicitly incorporates the geometry and properties of discrete features as a central component controlling flow and transport” [62] that has been applied for the analysis in hydrogeology and for the stability assessment of rock blocks around the underground structures [12], [63]. The rock structure is modelled by the pipe model and the channel lattice model, which provide simpler representations of the fracture system geometry. The latter is more suitable for the complex flow behaviour inside the fractures, the “channel flow” phenomenon for instance [34]. DFN method has been applied for the numerical model construction of the rock mass in some generation theories. Some popular representations of the DFN-based codes are FRACMAN, FRACAFLOW and RESOBLOK.

1.2.2.4. Hybrid methods

The couple of some above methods for the analysis of a research domain enables the exploitation of the advantages of the components and diminish their weak points. The hybrid models are built from the integration of the hybrid methods such as BEM/FEM, DEM/FEM, DEM/FDM or DEM/BEM. The DEM/BEM couple is able to deal with the effects of the far-field most efficiently for 2D problems. The DEM/FEM couple utilises the standard FEM meshes over blocks and the contacts are treated in discrete solution using the penalty method. In fact, the couple of DEM/FDM can be considered as the explicit DEM and the couple of DEM/FEM links to the implicit DEM. Likewise, many FEM codes can be transformed into a DDA code without losing any inherent advantages [34].

1.2.3. Generation methods

As presented in the introduction of this part, the geometrical generation of the rock medium is an important part in the research of rock mechanics. The study is aimed at creating the numerical presentation of the rock mass with the reconstruction of the rock structure with its natural complexity of configuration. The achieved models are used as the representations of the real rock mass and replaced them in the structural studies, the analysis of the mechanical behaviour and stability of the rock mass.

A discontinuity can be analysed on two levels [64], [65]:

- At a morphological level, it is represented by a volume of which one dimension is very small compared to two others;
- At an architectural level, it is represented by an area with the negligible thickness so that its intersection with a rock surface is a line.

Many generation solutions are based on the DFN method but other methods can also be used. For instance, FEM has been applied in the approach proposed by Y. Zhang *et al.* [66]. Among many approaches for block generation that have been published, G. Fu *et al.* [65] classified them into two groups based on the viewpoint of the block generation:

- Block integration methods: the rock mass is generated by the combination of small rock blocks with various configurations;
- Block partition methods: the initial rock mass is divided into small rock blocks by the discontinuities of the rock structure.

Besides, M. Elmouttie *et al.* [67] distinguished the different algorithms of the block generation:

- Topology-based algorithm: using the block geometrical identification techniques that are applied for the block integration methods;
- Polyhedral detection algorithm: using the block splitting techniques that are used for the block partition methods.

Some methods can only model the discontinuities to be planar, smooth and without thickness ([64], [65], [68]) while others can generate non-planar structures with arbitrary morphology ([67]). The form of rock blocks in the model is either convex, concave or concave as the combination of some sub-convex-blocks.

A model is normally constituted of five types of component: vertices, edges, faces, polyhedral and planes that contain faces [68]. As an example of the polyhedral detection group, the method of D. Heliot [64] generates the model by splitting the initial block into new smaller blocks by the interaction of the isolated discontinuities and/or the main families of discontinuities and the boundary of the model. The model is built through the realisation of an appropriate database in which each component is generated with a strict description in chronological order and content. The details of this theory will be presented in the section 2.3.1 when it is applied for the geometrical modelling task in our proposed methodology for rock engineering research.

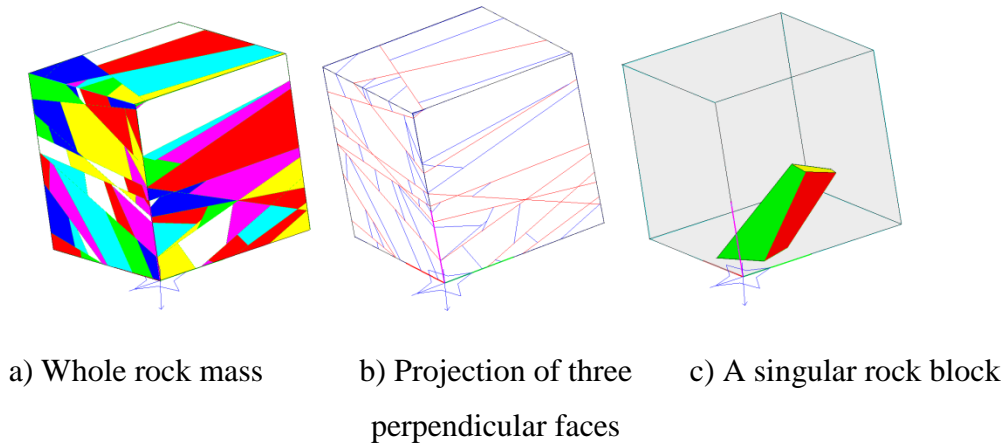


Figure 1.2.8: Model of a rock mass created by the method of D. Heliot [64] using RESOBLOK code

The polyhedral modelling method of M. Elmouttie *et al.* [67] is a topology-based method in which the 3D polyhedra are created by the intersection of the 3D polygons and triangulated surfaces with the maintenance of the oriented components. The construction of a model is a procedure from the truncation of polygons and surfaces, through the face tracing algorithm to the polyhedra tracing algorithm. The description of edges and faces of the blocks in the models during the procedure is recommended to be executed with a severe control to ensure no coincidence between existing objects and new-born ones with a suitable tolerance checking.

Furthermore, the application of the geo-statistics and the probabilistic functions for the generation of the rock model has been widely applied. Some examples are found as the UDEC or 3DEC solutions, the theory of D. Heliot [64] and the method proposed by A. Rafiee and M. Vinches [69]. In [69], the rock mass is simulated by using the joint pattern statistically based on the spacing, the orientation and the persistence of each discontinuity set. The discontinuities were considered as infinite planar surfaces which are differently orientated inside its tolerance range. The joint spacing and the orientation data were assumed to follow an exponential and a normal law, respectively. The density semi-variogram and the statistic features of the discontinuities were taken into account. The generation data were then employed in the AutoCAD code to create the rock structure by considering the number of discontinuities per segment and the statistical parameters of spacing distribution for each family.

Attention should be paid to the object order (*i.e.* vertices, edges, faces and blocks) in the generated model to ensure the unification of the sign convention in the model. Moreover,

when the generated models are mechanically analysed (by the same methods or by another specific analysis methods), the contact detection between two neighbouring objects is influenced by those order. Based on the block theory of R.E. Goodman and G.H. Shi [70], G. Fu *et al* [65] proposed two theorems of the structuring order for the model:

- Directed theorem: Edges, faces and blocks of the model are directional objects. An edge owns two opposite directions from one vertex to another. A face is directed if its boundary is closed and composed of directed edges; the normal vector of the boundary contour follows the right-handed rule [185]. If the normal vectors of all the boundary contours are pointing toward the inside of the block, the block is positive; otherwise it is negative.
- Closed theorem: In a block, each edge is attached to two boundary contours. Any edge of a block must have its matching edge in another block with opposite direction but same position.

In the theory of P.M. Warburton [68], the order of the edges around each face follows the right-handed rule advancing in the direction of the normal vector to the plane of the face. The edges are given a negative sign if their vertices are in the wrong order. The faces around polyhedra are given the same sign to indicate where unit normal are directed out of the polyhedra. It is noted that the sign conventions of different methods are not usually identical.

The post-processing of the model generation is usually the stability analysis or the research of the mechanical behaviour of the model under assumed loading conditions. Some generation methods contribute only for the model construction of the rock mass while many of them integrate the stability analysis. The Key Block Theory of P.M. Warburton [20] and the equivalent theory of R.E. Goodman and G.H. Shi [70] are common fundamental. The analysis is realised for single block ([6], [20]) or for the assemblage of rock blocks in the model ([6], [64], ([71])). Another trend is the combination of the geometrical modelling by a generation method and the mechanical analysis by a robust analysis method such as FEM [66], DEM [72]. In the chapter two, this idea is illustrated by a methodology as the integration of the generation theory of D. Heliot and the NSDC method which is following presented.

1.2.4. Non Smooth Contact Dynamics method

1.2.4.1. General introduction

The Non Smooth Contact Dynamics (NSCD) method, proposed and developed by J.J. Moreau and M. Jean, is a DEM-based theory that has been proven to be particularly successful for the analysis of rigid and deformable objects packed together ([38], [60]). This is the most prevalent non-smooth approach in granular media simulations. It is based on the use of the “coefficient of restitution” in order to represent changes in the relative velocity of a rigid particle before and after collision [73].

There are two principal characteristics of a contact between two objects:

- The contact is unilateral and punctual: There is no penetration of one body to another (the gap between them is not smaller than zero: $g \geq 0$). The contact happens at two nearest points on the boundary of two bodies.
- Two objects do not attract each other: The reaction force appears only when two objects contact.

Two discretization operations are realised in NSCDs [38], [60]:

- Time discretization: Due to the fact that the contact moment is usually unknown or difficult to determine, the discrete variables are not defined at the milestone time steps but over the intervals of time. Hence, the discrete contact relations are described by the intervals of time.
- Configuration discretization: The discrete configuration of the rock mass is caused by the material inhomogeneous, the complex boundary and the presence of the discontinuities in the research mass. The discretized configuration space $D_k(X)$ is the combinatorial model of the classical configuration space of k individual blocks in the X -dimensional-space. The evolution of the mass is then expressed by a continuous time function and the left and right limits of a point of time are used for other expression of the mass.

M. Jean [60] also proposed some other solutions for the discretization:

- Maintain all the unknown variables;
- Eliminate the local variables and maintain only the general ones;
- Eliminate the general variables and maintain only the local ones;

Well-presented these features, the Signorini condition is adopted in the NSCDs. Studying the contact between two neighbouring objects O and O' , O is called the candidate and O' is called the antagonist. Two objects are assumed to contact at the point P and P' on the boundary of O and O' , respectively. P and P' are the nearest points between O and O' and the distance PP' is the gap between two bodies. The normal component R_N of the contact vector is the unit vectors $\overrightarrow{P'P}$ of the O' to O at P' and $\overrightarrow{PP'}$ of the O to O' at P and is denoted as R_N . The tangential component R_T of the contact vector is perpendicular to N .

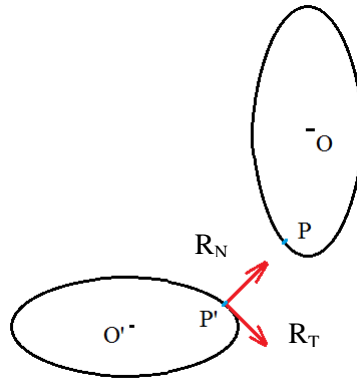


Figure 1.2.9: Local frame (sourced from [60])

The Signorini condition is expressed in formulas as:

$$\begin{cases} g \geq 0 \\ R_N \geq 0 \\ g \cdot R_N = 0 \end{cases}$$

With:

g : Gap between two objects

R_N : Normal component of the contact force

The “non-smooth” phenomenon is demonstrated by the discontinuity on the relative velocity of two contacting points when the contact happens. The velocity just before the contact U^- and the one just after the contact U^+ are not the same. In an interval of time t when the contact is smooth enough, $R_N(t) > 0 \rightarrow U_N^+(t) = 0$. The Signorini condition is replaced by the velocity Signorini condition [38], [60]. When two objects are deformable, the contact can be well presented by the Signorini condition. When they are rigid, the shock law is needed to include.

The dynamical equation when the contact is smooth is given by:

$$M\ddot{q} = F(q, \dot{q}, t) + r$$

or by the literal expression:

$$\text{Force of inertia} = (\text{Internal force} + \text{External force}) + \text{Contact force}$$

When shocks are included, the equation is rewritten as the form of differentials:

$$Md\dot{q} = F(q, \dot{q}, t)dt + r dv$$

With

M: inertial matrix

dt: Lebesgue measure

$d\dot{q}$: Acceleration measure

dv: Non-negative real measure to which $d\dot{q}$ becomes a density function and r is the one of local density of impulses at contact moment.

The implicit algorithm of time integration, which is more efficient for the analysis of the strong changeable variables of the large particle body, the contact phenomena, *etc.* is also applied for this method ([38], [53], [60]). The basic resolution scheme of a time step in NSCD is given in the Figure 1.2.10 by [53]:

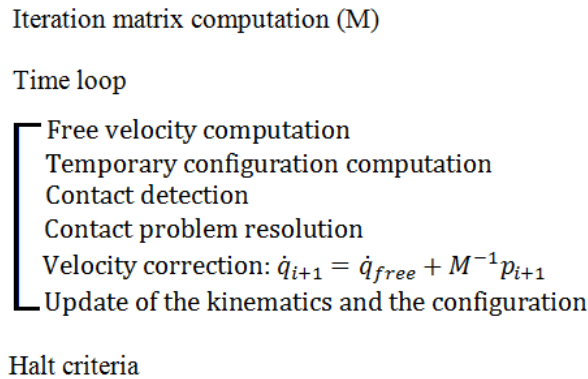


Figure 1.2.10: Basic implicit resolution scheme of a time step in NSCD (sourced from [53])

Notation: M: inertial matrix

p_{i+1} : Total impulsions over the time step

\dot{q} : Velocity

The Non Linear Gauss-Seidel (NLGS) algorithm of which some implementations can be chosen is applied for solving the equations [53]:

- Store Delassus Loop strategy (SDL) ;
- Exchange Local Global Strategy (ELG);
- Store Delassus Loop strategy (SDL): parallel treatment;
- Quasi NLGS.

1.2.4.2. Dry friction contact analysis by NSCDs

The friction contact law formed between two objects is express as $C(U, q_N, \mathcal{R})$. $U = (U_T, U_N)$ is the differential velocity vector, q_N is the coordinate of P in the local frame in the gap between two objects and $\mathcal{R} = (\mathcal{R}_T, \mathcal{R}_N)$ is the contact force of O' on O in the local frame.

Following the Coulomb's law of contact, the sliding at the contact points only appears when the tangential component of the contact forces between two objects are larger than the sliding threshold. This condition is given by:

$$\mathcal{R}_T \in [-\mu \mathcal{R}_N, \mu \mathcal{R}_N]$$

When $U_T > 0$: $\mathcal{R}_T = -\mu \mathcal{R}_N$

When $U_T < 0$: $\mathcal{R}_T = \mu \mathcal{R}_N$

With

$\mathcal{R} = (\mathcal{R}_T, \mathcal{R}_N)$: Contact force between one object to another

$U = (U_T, U_N)$: Sliding velocity vector between one object to another

μ : Friction coefficient, $\mu = \tan(\varphi)$

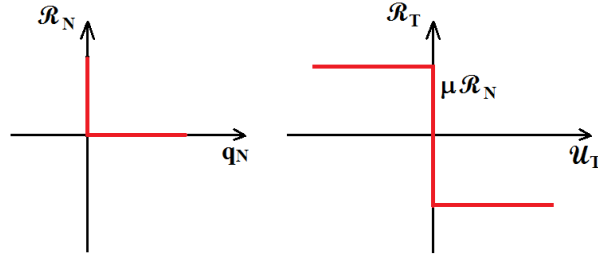
φ : Friction angle

There is a parameter $\rho > 0$ so that $\mathcal{R}_T = \text{proj}_C (\mathcal{R}_T - \rho U_T)$. J.J. Moreau [39] proposed an equivalent form of this expression by using Ψ_C^* , the conjugation of the indicate function of C:

$$\mathcal{R}_T \in \partial \Psi_C^*(-U_T)$$

In the 3D projection, C is a circle of which the centre is at the point 0 and the radius is $\mu \mathcal{R}_N$:

$$C = \{ \mathcal{R}_T : || \mathcal{R}_T || \leq \mu \mathcal{R}_N \}$$



a) Signorini condition b) Contact law of Coulomb

Figure 1.2.11: The relation curve of the contact in NSCD method (sourced from [60])

This relation curve was denominated as “GR-Coulomb (μR_N)” by M. Jean [60]. On the view point of convex analysis [38], this law of contact is presented as:

U_T and R_T are conjugated by the function Ψ_C^* and Ψ_C

Of which $C = \{R: ||R|| \leq g\}$ and $g = \mu R_N$

The inelastic shock contact between two rigid objects is expressed by:

$$(-U_T^+, R_T) \in \text{GR-Coulomb}(\mu R_N)$$

If the contact is discretised by the configuration of the medium, the field of the relative velocity $U(x)$ can be represented by a vector U of which the component U_k is the component of $U(x)$ on the generator $N_k(x)$:

$$U(x) = \sum_k U_k N_k(x)$$

The gap $q_N(x)$ between two objects can also be represented in the same way:

$$q_N(x) = \sum_k q_{N_k} N_k(x)$$

And the local contact force, too:

$$R(x) = \sum_k R F_k(x)$$

The general function of the dry friction contact $C(U(x), q_N(x), R(x))$ with $x \in \delta_C \Omega$ is rewritten as $C(U, q, R)$.

In the kinematical relation, the components of the general function are given by:

$$U^\alpha = H^{*\alpha}(q) \dot{q}$$

$$R^\alpha = H^\alpha(q) R^\alpha$$

$$U_N^\alpha = \dot{q}_N^\alpha$$

With

$H^\alpha(q)$: the linear application of R^n in R^2

$H^{*\alpha}(q)$: the transpose form of $H^\alpha(q)$

Hence, the general function is given by:

U_T^α and R_T^α are conjugated by the function $\Psi_C^{*\alpha}$ and Ψ_C^α

of which $C^\alpha = \{R: ||R|| \leq g\}$ and $g = \mu R_N^\alpha$

or by the equivalent form as:

the variables $-\dot{q}$ and R are conjugated by the function $GH_T^{*\alpha}$ and $(GH_T^{*\alpha})^*$

of which $G = \Psi_C^*$ and $G^* = \Psi_C$

The discrete contacts are solved by the application of the method of successive equilibrium [60]. These above expressions are graphically represented as:

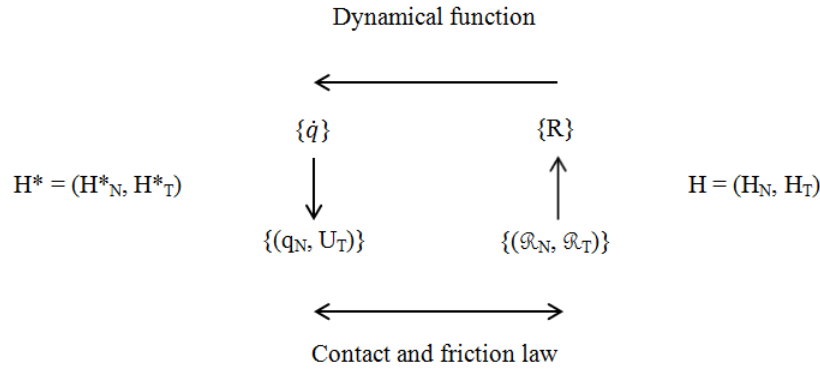


Figure 1.2.12: Successive equilibrium solution for the dry contact analysis in NSCD method (sourced from [60])

1.2.5. Conclusion

This part is dedicated to a brief introduction of the numerical methods for rock engineering. Two groups of methods for the rock analysis and the rock model generation have been presented. The first group is classified into the continuous, discrete and hybrid solutions. Each owns their inherent advantages and defaults with the suitable application fields. The second group is categorised by the viewpoint or the basis algorithm of the generating of a rock mass. The combination between two groups proposes a comprehensive solution in rock mechanics when the second group provides the computational models for the analysis

by the first group. Besides, there is always the integration between the geometrical generation of the rock mass and the discrete analysis in a discrete numerical solution. The NSCD method, presented in the previous part, is further presented since it is a prominent solution for the discrete analysis in rock and granular media. This method plays a fundamental part in the mechanical simulation and analysis performed in our research and has been applied in the methodology that will be proposed in the next chapter.

1.3. Structural design approaches in tunnel engineering

The design of a tunnel structure, or more commonly an underground excavation, is a complex procedure composed of many tasks. However, the principal aim of the design is always the harmonious cooperation of the support structures and the medium surrounding the tunnel. H.H. Einstein *et al.* [74] suggested that “the result of any ‘tunnel design method’ should be an optimum combination of support features and construction procedures for the particular ground conditions, opening dimensions and use”. E. Hoek, E.T. Brown [75] shared the same viewpoint when considering the design of underground excavations as the design of underground support systems. However, this design is recommended to be “not a deterministic process and the results should be assessed in the context of the quality of the site investigation and the estimated range of geo-mechanical properties” [76].

The following chart presents a typical complete process of the tunnelling design from the suggestion of the ITA “Working group on General approaches to the Design of tunnels” [77]. The next one proposes an analysis procedure with multiple feedback modes for tunnel design [78].

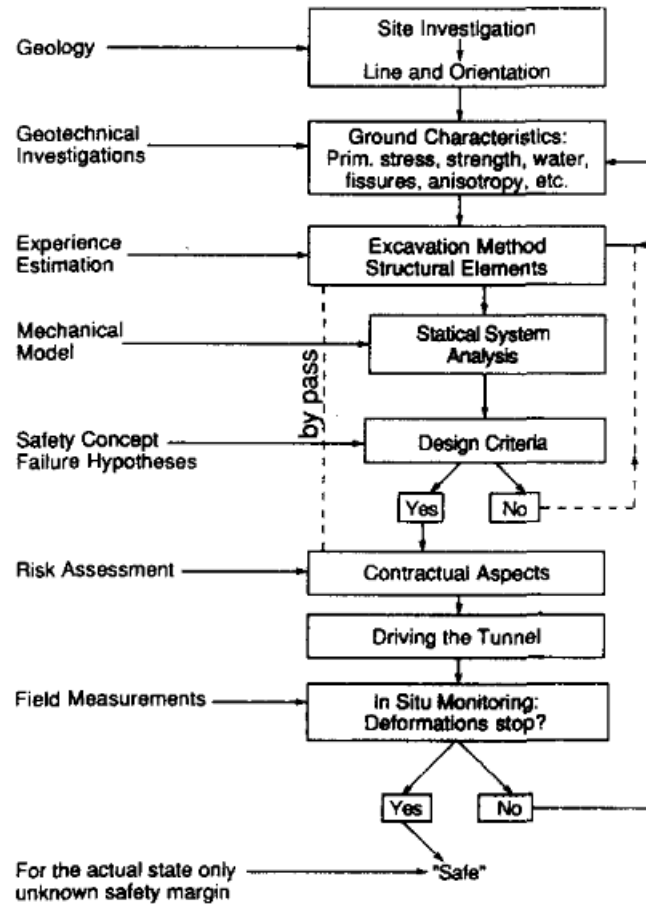


Figure 1.3.1: Design process for tunnelling (sourced from [77])

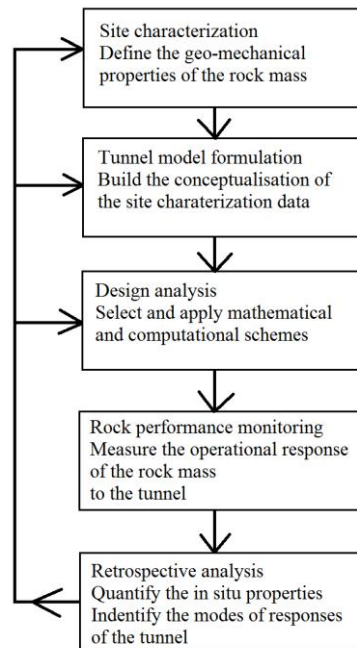


Figure 1.3.2: Flowchart with multiple feedback modes for tunnel design
(sourced from [78])

1.3.1. Tunnel support structures

Before going in the details of the structural design, it is worth to recall here the system of tunnelling support structures. Considering the structural task that a support structure is needed to fulfil once it is implemented into the surrounding medium of a tunnel, several types of support structures are listed [76]:

- Primary support system: The structures are installed to obtain a stable opening that aim at facilitating and stabilizing the excavation phase of the tunnel. Their presence may or may not form part of the permanent support system.
- Temporal supports: The structures are applied temporally on the rock face for short-term tasks, on the tunnel structure or to the excavation space of the tunnel to obtain desired purposes during the construction phases of the tunnel (for example: local reinforcement, construction scaffolding and supports, stabilized structure, *etc.*). Once the intention is fulfilled, the structures are liberated from the implementation location or leaved permanently in the working medium of the future tunnel. However, their presences, even if is permanent, are not counted into the permanent support of the tunnel.
- Permanent supports: The structures are installed for bearing the long-term loads predicted for the lining system. It may be a design requirement that part or all of the primary system is incorporated into the permanent lining.

1.3.1.1. Lining structures

The British Tunnelling Society [76] defined that “lining is the necessary permanent ground support system to the periphery of a tunnel or shaft excavation, and/or the material installed in the same position with an inner surface suitable for the specific end-use of the underground excavation”. The most complete lining structure of a tunnel is composed of several layers of steel-lining, shotcrete-lining, concrete-lining, geotechnical fabrics, grouting, air gap, *etc.* Each sub-structure can be a single or multi-layer structure or can be neglected in appropriated circumstances and/or particular construction types. The direct result of the design of underground support systems is the configurations of the lining structure as well as the relevant construction scheme. Normally, a lining structure is a permanent type but can be generated in the tunnelling phase for using as a temporal support and then be kept as a part of the complete lining structure. In the stable rock mass, the

lining system acts as the limited supports whereas in unstable ground, it works as the continuous supports. The principal lining structures/layers are shortly presented:

a) Shotcrete-lining:

This is a concrete-based mixture that is used to spray on the faces of the tunnel excavation for different proposes depending on the spraying moment, the thickness of the structure, the composition of the material. Due to the thickness $d(\text{mm})$ on the tunnel face, the Shotcrete-lining plays different roles in the structural system of the tunnel [79]:

- $d < 50\text{mm}$: it does not provide much structural support but can take role as a part of the waterproof structure or to improve the stability of waterway or the hydraulic efficiency of the medium around the tunnel or to provide the aesthetic visual for the tunnel (especially for the New Austrian Tunnelling Method (NATM) tunnel);
- $100 < d < 150 \text{ mm}$: it acts as rock reinforcement with the possibility of using the special agent or materials addition in the mixture (such as steel, cellulose or grass fibres, chemical additives) or the wire fabric matting of the spraying to obtain intentioned strengthening for the surrounding medium;
- $d > 250\text{mm}$: it is considered as an unreinforced concrete-lining structure. The reinforced structure can be added before the shotcrete spraying to create a reinforced one.

The regular cross section of a typical NATM tunnel consists of an initial shotcrete lining and a final, cast-in-place concrete or shotcrete lining. A waterproofing system is sandwiched between the initial and final linings [80]. Its detail is found in the Figure 1.3.3.

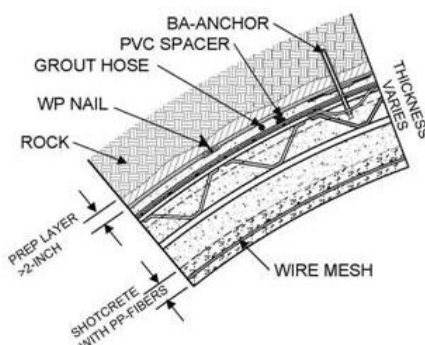


Figure 1.3.3: Typical shotcrete final lining detail (sourced from [80])

b) Concrete-lining structure (or *in situ* lining):

Used to be built with brick and masonry, it is now cast concrete that exists in two types: unreinforced and reinforced. The main purpose of this structure is the stabilization of the rock faces on the vicinity of the excavation. Otherwise, the pre-casted concrete-lining in shape of partial lining blocks that is then installed on the periphery of the excavation together with other lining layers.

c) Steel-lining structure:

It is applied for bearing the internal pressure during the excavation phase, the external hydraulic pressure during grouting or dewatering operations and the loading conditions during the transportation and erection [79]. It can exist in some forms: rib (or arch): rather used as the support during the excavation phase and the “reinforcement” for the shotcrete layer or unreinforced concrete-linings; plate (curved or plane): take role as the main permanent lining. Besides, the occasionally steel liner plates formed from pressing steel sheet are installed as a temporary support while an *in situ* concrete permanent lining is constructed [76].

d) Grouting:

This is a mortar-based mixture that is used to ensure the full contact between the *in situ* lining, the initial ground support and ground. In other hand, grouting can be used for the leakage prevention of the rock mass in the vicinity of the excavation. In this case, the grouting is considered as a type of the impermeable lining.

e) Impermeable lining:

When the water permeable threatens the stabilization or the normal conditions of the excavation and/or the tunnel, the appropriate impermeable lining is needed. If no dangerous leakage should be worried, the lining is usually formed by the suitable geotechnical fabric/membrane. When the confining condition around the excavation and/or the tunnel is not sufficient, in order to prevent the leakage of the vicinity rock mass, the impermeable lining structure must be formed by concrete or concrete encased steel linings for an adequate permeable capacity of the whole lining structure [76].

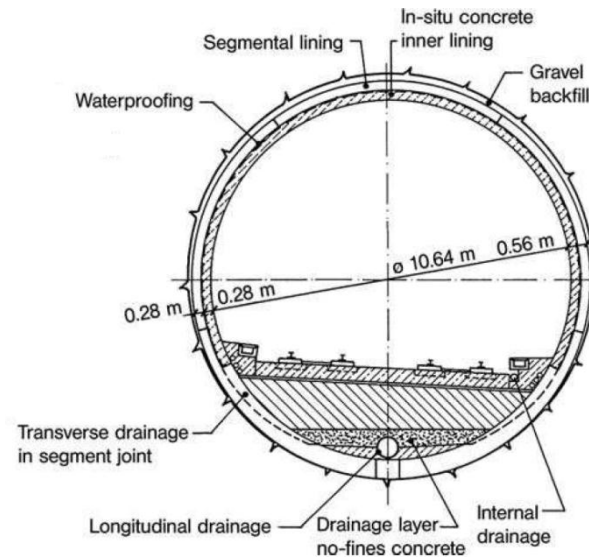


Figure 1.3.4: Structure of drained double-layer tunnel linings of Murgenthal tunnel (Switzerland) in hard rock (sourced from [81])

There are two special tunnel structures that are capable to deal with the presence of water in the ground [81]:

- Watertight structure: the impermeable lining completely covers the entire tunnel boundaries and the lining structure system is designed to resist water under pressure.
- Drained structure: The tunnel vault is made watertight to protect the interior from water by the use of waterproof layers or grouting. The groundwater flows around the technically waterproof tunnel lining into the drains at the sides, where it is collected and carried away. The tunnel lining system is designed to resist ground pressure.

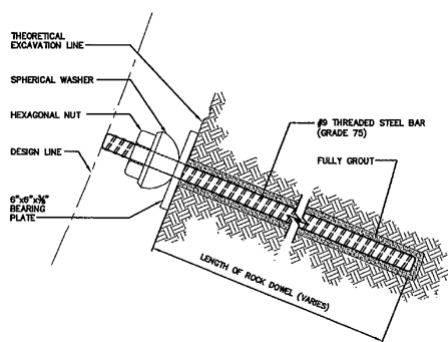
1.3.1.2. Rock strengthening

Rock strengthening objects are installed on the rock faces in the periphery of the excavation during the construction phases to fix the loosen blocks that are predicted to fall and/or to create a necessary pressure in the rock medium. The stabilization of those blocks is help to prevent the unfavourable failure caused by the block falling and the domino failure phenomenon that they could lead to. Those blocks which are called the “key blocks” analysed by the “Key block” theory of P.M. Warburton [68]. Moreover, the strengthening objects are used to fix the steel ribs/arches on the boundary of the excavation for providing the support to the opening in the medium. The analysis of the behaviours of the objects

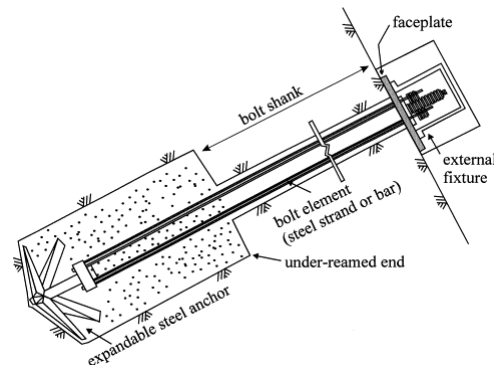
under the normal loading conditions is needed to assure the appropriate strength and the life-service of the objects inside the vicinity medium of the opening and the permanent tunnel. The local failure at the installed location of the object must be taken into account in the analysis.

Sometimes, the name “rock anchor” is used for all type of rock strengthening objects. In fact, two common “rock anchors” which are popular in use are the rock dowels and the rock bolts [80]:

- Rock dowels (or passive rock anchors) are passive reinforcement elements that are only activated after a movement of the surrounding medium. When displacements along discontinuities occur, dowels are subject to both shear and tensile stresses. The grout material filling the annular gap between the dowel and the ground takes part in the shear and tensile strength of the dowels together with the threaded steel bar that is thrust in the rock medium.
- Rock bolts (or active rock anchors) have a friction or grout anchor in the rock and are tensioned as soon as that anchorage is attained to actively introduce a compressive force into the surrounding ground. Rock bolts are normally total bonded to the surrounding medium after tensioning, for long-term load transfer considerations. They may or may not be grouted on their full length. They are activated as soon as they are tensioned. The rock bolts stay in several forms: resin grouted, expansion shell, split set stabilizers, Swellex, self-drilling anchor, Cable-bolt reinforcement, *etc.*



a) A temporary rock dowel
(sourced from [80])



b) A rock bolt for soft rock
(sourced from [82])

Figure 1.3.5: Schemas of rock anchors

1.3.1.3. Steel support structures

Several steel supports are used: steel ribs/arches, lattice girders, spiles and forepoles [80]:

- Steel ribs are often installed with shotcrete instead of wood for support the opening in its medium. When shotcrete is used, it often does not fill absolutely the entire void between steel and rock;
- Lattice girders are support members made up of steel reinforcement bars in a triangular form and rolled to match the shape of the opening. Because their cross-section is typically very small compared to the surrounding shotcrete zone, they do not independently induce a strong support to the opening. However, they provide temporary support to blocks having an immediate tendency to loosen and fall. Furthermore, they provide a ready template for applying a sufficient thickness of shotcrete. Together with shotcrete, lattice girder is very commonly used for the NATM tunnels;
- Spiles and forepoles are used interchangeably to describe support elements consisting of pipes or pointed boards or rods driven ahead of the steel sets or lattice girders. They provide temporary overhead protection while the excavation and the installation of the next set or girder are accomplished.

1.3.2. Structural design approach in tunnel engineering

In general, there are three main groups of approaches that have been widely applied in the structural design in tunnelling: empirical, analytical and observational one [83] or the empirical, calculated and judgemental solution [84]. They are used in tunnel engineering for “the determination of dimensions and quantities of tunnel support and possibly construction procedures” [74].

1.3.2.1. Empirical approach

The empirical approach relies on the past experiences from case histories and the use of the rock mass classification systems in combining with the findings from observation, experience, and engineering judgment for providing a quantitative assessment of rock mass conditions [83]. For a tunnelling application, a rock mass classification has the following purposes [83]:

- Divide a particular rock mass into groups of similar behaviour;
- Provide a basis for understanding the characteristics of each group;

- Facilitate the planning and the design of excavations in rock by yielding quantitative data required for the solution of real engineering problems;
- Provide a common basis for effective communication among all persons concerned with a tunnelling project.

Having no doubt that this group of approach is the most applied in tunnel engineering, as well as rock engineering up to now. Based on the past information of the ground where the future tunnel will take place, the working ground of the future tunnel is qualified by the use of some selected rock classification systems. In another word, the rock mass classification is applied as a design tool in rock and tunnel engineering. H. Stille, A. Palmstrom [84] published a profound introduction of the empirical approach: “The process of rock mass characterisation consists of describing and quantifying the parameters that govern or influence the rock mass behaviour. The characterization can be simplified by classifying them. The result of the characterization process will be used to assess the rock mass quality, according to some pre-defined systems. This procedure is normally given the name “rock mass classification”. It is found to be the most fulfil description of the method, in the scope of our knowledge.

There are many systems for rock mass classifications that had been proposed in rock engineering. By the use of the classification tables, the rock mass can be estimatly divided into different categories. The development “milestones” of the rock mass classification systems are presented followed T. Ramamurthy [4], C. Edelfro [7], Ö. Aydan *et al.* [24]:

- In 1964, Rock Quality Designation (RQD) was proposed by D.U. Deere. In the same year, the earliest formula of Joint Index Methods (JIM) were published by Protodyakonov and Koifman;
- In 1973, Rock Mass Rating (RMR) was suggested by Bieniawski;
- In 1974, Q-system was published by Barton *et al.*;
- In 1975, Mining Rock Mass Rating (MRMR) for mining applications was developed by Laubscher. In the same year, Unified Rock Classification System (URCS) started to be used by the US Forest Service;
- In 1981, Basic Geotechnical Description of Rock Mass (BGD) was established by the International Society of Rock Mechanics (ISRM);

- In 1982, Rock Mass Strength (RMS) was published by Stille *et al.* as the modification of RMR system. In the same year, Modified Basic RMR System was developed for block caving operation in western US.;
- In 1985, Slope Mass Rating (SMR) was proposed by Romana;
- In 1993, T. Ramamurth and Arora suggested their classification system;
- In 1994, Geological Strength Index (GSI) was proposed by E. Hoek and E.T.Brown;
- In 1995, the rock mass number N and Rock Condition Rating (RCR) were published by Goel *et al.* as the new version of the Q-system and RMR;
- In 1996, Rock Mass index (RMi) was developed by Palmström.

Each system classifies the rock mass based on different parameters as in the summary of C. Edelbro [7] cited in the table 1.3.1.

Table 1.3.1: Parameters included in different numerical and function classification systems (sourced from [24])

Classification system												
Parameters	RQD	RSR	RMR	Q	MRMR	RMS	MBR	SMR	*RAC	GSI	N	RMi
Block size	-	-	-	-	-	-	X	-	-	-	-	X
Block building joint orientations.	-	-	-	-	-	-	X	-	-	-	-	X
Number of joint sets	-	-	-	X	-	X	-	-	-	-	X	X
Joint length	-	-	-	-	-	-	-	-	-	-	-	X
Joint spacing	X	X	X	X	X	X	X	X	X	X	X	X
Joint strength	-	X	X	X	X	X	X	X	X	X	X	X
Rock type	-	X	-	-	-	-	-	-	-	-	-	-
State of stress	-	-	-	X	X	-	X	-	-	-	-	-
Groundwater condition	-	X	X	X	X	X	X	X	-	-	X	-
Strength of the intact rock	-	-	X	X	X	X	X	X	X	X	X	X
Blast damage	-	-	-	-	-	-	X	-	-	X	-	-

Researching the four most common rock mass classification systems: RMR, Q, GSI and RMi; S. Tzamos, A.I. Sofianos [85] proposed the common base for all rock mass fabric indices as the combination of four mentioned index. Each rock classification system has its own scope and restriction that need to follow. A. Palmstrom [84] summarised the main application of their systems as in the following table.

Table 1.3.2: Application in tunnel engineering of some common rock classification systems (revised from [84])

System	Application
RQD	Characterization of jointing from drill cores, input to some classification systems
GSI	Indication of the strength of the rock mass, input to engineering applications
RMi	General characterization, input to engineering applications
Terzaghi classification, RQD, RSR	Design of steel support
NATM	Excavation and design in incompetent ground
RMR, Q	Design of tunnel, mine and foundation

Due to the variation of the classification criteria of those systems, the choice of the suitable one for the research of the rock mass is not easy. E. Hoek [75] suggested using at least two systems for a rock mass. AFTES [5] strongly recommended that: “Using a classification system for any particular project presupposes that the designer has first assured himself that the project is truly compatible with the system used”. Bieniawski [83] suggested that when using the rock mass classification systems for tunnel design, it should respect well the guidelines provided by those systems for the selection of tunnel support.

Being the most common approach for the tunnel design, this approach cannot avoid its inherent restriction. The disadvantage of the empirical approach is that basing on case histories and on the classification systems for the new tunnel in new situations is sometimes beyond the experience of the engineers or surpasses the application scope of the guides [86]. Moreover, the categorization of rocks by physical criteria with the tolerance of values or by the description of the appearance of rocks contains always the natural inaccuracies of the method. Furthermore, the precision of the assessment and the appropriation of the designed support structures depend seriously on the experience of the engineers and the rich source of past knowledge on the site of the future tunnel and the existed alike tunnel. The gravest disadvantage of this approach is the “over-conservative designs” that leads to high cost constructions ([77]) due to the recommendation of re-use of the protocol successful

tunnels in similar rock masses. The choice of support structures is preferred to be safe rather than to be appropriate. ITA [77] proposed that the tunnel preliminary supports may be selected based on experience and on the empirical approach of which direct observations are more important than numerical calculations. The application of this approach for large projects in similar ground conditions is possible if the provisions of more intensive measurements had been done in the initial projects to collect sufficient data for the extrapolations in other projects [77].

For a better exploitation of this approach, Bieniawski [83] proposed the downstream methodology for the application of this approach: (1) input data; (2) rock support requirements; (3) influence of stress field; (4) rock mass deformability; (5) strength of rock masses; and (6) emerging new applications". The combination of this approach with the other ones is recommended to be the wise solution and it has been put into practice in almost all current tunnel projects [83].

1.3.2.2. Analytical approach

The approach bases on the application of theoretical and numerical solutions on the input data of the rock mass conditions that came from the *in situ* investigation and past knowledge of the construction zone. At the time of 90s when Z.T. Bieniawski wrote his Report GL-79-19 [83], this approach was rated to be the least used because of the difficulties in the supply of appropriate input data for the numerical procedure rather than the robust capacity of the analytical methods.

In the analytical approach, the real conditions of the rock mass and the designed tunnel structures are replaced by simplified models that aimed to be the representations of the actual objects. Those models are then analysed through manual theoretical calculations, with the aid of reference charts or computers. Even how sophisticated the model is, it can hardly portray the reality but is only a simplification/idealisation of the real conditions of the rock mass and the tunnel structures [84]. Additionally, some typical natural conditions, the development of the rock structure, the exact image of the rock mass are sometimes beyond the limit of the modelling. Before the powerful participation of computer in this approach, the limitation of the manual calculation restricted the quantity of unknown variables and also the complicated geometry of the structures.

USACE [87] proposed that tunnel design is normally tackled by the search of analysable modes of failure, and then apply them to realistic but postulated situations. The failure

modes are defined as the damage situations of the rock mass and the tunnel structures when they lose their ordinary service states or strength states. Those modes can be caused by the natural hazard, the construction and in-service procedures, the degradation of the materials and structures, unexpected risks, *etc.* that are stipulated in relevant technical specifications and from the type and the importance of the future tunnels. They are used for the verification of the calculated models to determine if the medium and the tunnel structures still meet the normal working conditions. During the analytical procedure, the rock mass and its tunnelling structures are placed under the application of assumed loading cases until a failure mode or a failure phenomenon appears. Alternatively, the failure probabilities of analysis objects are searched when the normal conditions of the construction/excavation phases and the service life are set to the models. The failure phenomena are divided into two categories ([24], [88]):

- Local failure: when rock blocks are kinematically movable into the excavation;
- Global failure: when stress and the strength of rock mass surrounding the excavation are at critical state.

If the reinforcement is need, the strengthening of the rock mass and the tunnel structures at risk zones or for the whole medium is described by the supplementation of the relevant mathematical quantities in the initial analytical functions or by the presence of the relevant auxiliary models in the initial model. The new working state of the rock mass and the tunnel structures are then recalculated and assessed for safe probability. With the strong point in the prevision capability of different risk scenarios of the analytical objects during the construction period and during the service life, the analyses assure the safety and durability of the tunnel. This is the dominant advantage of this approach to the empirical one when the design can achieve “the quantification of the degree of safety” [84].

However, some disadvantages of this approach can be found. The reliability of the modelling results and the total analysis is firstly depended on the appropriation of the input data and the selection of the calculation theories and/or the proposed models. The defeat of an analytical works sometimes stays on the preparation step of the analysis works. Besides, the simplification nature of the model in comparison with the reality brings about its inherent inaccuracies. Any set of analytical results is needed to regard in its assumption and the goal of the works. The acceptance of a suitable approximation helps reduce the complication and the volume of calculations. The intention of reaching the absolute model

that totally represents the real conditions of the rock mass and the tunnel structures is not appreciated and practical. Moreover, the robustness of calculation tools (mathematical functions, calculation theories, reference charts and machine or computer) authorises in some way how far the complication of the model can be and the obtained behaviours of the analysis. The last but not least, somehow the most important attention, is the interpretation of the calculation/modelling results. This step should be done by the professional judgements of qualified engineers. A good set of obtained responses of the analysis objects means nothing if it is not used for the assessment of safety and/or strength/resistance and/or reliability of the projects from the specialists. The quotation from Peck (1980) that A. Palmstrom, H. Stille used in [84] is found to be stronger than any comments: “Judgement is the intelligent use of experience. It is the recognition of the limitations of the methods one uses, and of the limitations and uncertainties of the material one works with”.

For answering the given demand, to be able to ensure of the obtained analysis results, the validity is always required for any analysis. The analysis results of the mechanical behaviours of the excavation, the tunnel and the boundary rock mass in each construction phase, for the whole project and in the service life of the tunnel are recommended to be cross-checked with another parallel analysis procedure or with different analysis tools. The referencing with the similar tunnel projects is also a useful operation. Moreover, the professional experiences of the working team and the consultant office with experimental judgements act as a necessary quality-control of the design and construction procedure. The combination of the pure analytical analysis and the numerical method is a smart solution that has been more and more required in almost all construction projects. The checking of a numerical model should be first carried out on simple models or with simplified boundaries conditions. All given hypotheses of the models must be checked whether they are appropriate and well applied in the models. Once the basic models are valid, the more complex models can be analysed and the results compared with existing field data and analytical solutions where possible. All of the significant input data should be varied systemically over their credible ranges in a series of runs, so that the influence of each parameter on the results can be determined [76].

There is a large application scope for the analytical approach: a simplified one adapts the preliminary design when not-too-high accuracy is demanded; comprehensive one suits the detail design with high accuracy with the analysis in depth; a minute local research needs

for a narrow but profound verification of particular doubts. The state-of-the-art of the available numerical methods in rock engineering has been presented in the section 1.2.

1.3.2.3. *Observational approach*

The observational approach in geotechnics is defined in EuroCode 7 as the method of which “the design is renewed during construction” on the updated geotechnical behaviours of the medium obtained by the monitoring and observation works [89]. This approach is inherent with the New Austrian Tunnelling Method (NATM) and the “build/learn as you go” philosophy: the support structures of the tunnel are adjusted by the construction time to meet the ground conditions [83], [84], [90]. In fact, this approach can be classed as the combination of the two above approaches and the immediate interpretations of *in situ* measurements [77].

During the tunnel excavation process, a detailed and strict *in situ* monitoring is carried out. The geodesic convergence on the excavation faces, the deformations and stresses of the tunnel and support structures are measured automatically and/or manually. The data are read with the frequency based on by the importance of the structures and the location of the measurements. The content and procedure of the monitoring in a NATM-based tunnel are complicated and strongly influence the construction progress, the stability of the excavation and the success of the project. From the recorded responses of the tunnel and its structures, the resistance of the tunnel supports (temporal and permanent ones), the deformation of the tunnel on the tunnel faces and along the tunnel axis, the movement and settlement of the bottom surface, *etc.* are carefully checked in comparison with initial designed values and with the previous behaviours of the same measure objects. If the monitoring is considered to be an important task in the whole tunnel construction, the interpretation of the obtained data is placed to be vital. It is then used as the base for the assessment of the initial design and if need for the decision of the modification. The “design - monitoring - recalculation - adjustment routine” is repeated along the construction procedure until the tunnel is done and is regarded as the integral part of the design [77]. The monitoring is continued even after the finish of the excavation and takes place “at longer intervals after the tunnel” [77].

Originally, the NATM was suggested to be suitable for only weak or squeezed ground [84]. Many tunnels were constructed successfully and economically by the observational tunnelling approach and the NATM. Later, NATM in medium and strong rock has been persuaded their conformation. With the many continuous endeavours of the Austrian

National Committee of the International Tunnelling Association in particular and the tunnel engineering society, NATM and the observation approach have gained their weighty positions.

The controversy of the liaison between the observation approach in tunnelling and the NATM is always a topic of interest. There are some opinions that refused the concurrence of NATM and the observation approach and [90] is a typical example. By showing the incompatible points between the original idea of the observation approach from R.B. Peck in his Rankine lecture in 1969 [91] and the principles of the NATM, the two authors proposed that “NATM as an observational method can be disregarded” and the approach itself has had independently a long development in civil engineering even from 480B.C [90]. Moreover, the current observation approach that has been applied in NATM and lately in CIRIA approach [92] was clearly distinguished from the observation approach of Peck by [91]. The former adopted a “progressive modification” of the design by moderately conserve the initial parameters based on the monitoring procedure to achieve the most probable conditions [92]. Whereas, the later embrace the “most probable” design and modify it to “moderately conservative” parameters [92]. The authors also mentioned about the shortcomings of the EuroCode 7 and the relevant European specifications in descriptions of the observation approach in geotechnics in general.

1.3.3. Conclusion

Through a short introduction of three main approaches for structural design in tunnel engineering, their basics are found with their own inherent points. Depending on the historical moment, one replace another to be the most applied. Furthermore, each one has its advantage in different phases of the total construction project of a tunnel. For the extension of the scale and the complication of the real demands with the stricter requests in technics, economy, society and ecology, the application of a multi-approach solution is normally found in a tunnel project. The development of the technology knowledge in civil engineering, in rock engineering and in tunnelling as a specific case facilitates and satisfies that wise direction. Hence, we emphasize that the structural design and analysis as a combination of empirical, theoretical, and numerical approaches is likely to ensure a safer design and the success for the future tunnel as the recommendation of Z. Gurocak, P. Solanki, M.M. Zaman [94]. A presentation of this combination can be found in the recommendation of H. Stille, A. Palmstrom [93] that was concreted into the figures 1.3.6 and 1.3.7.

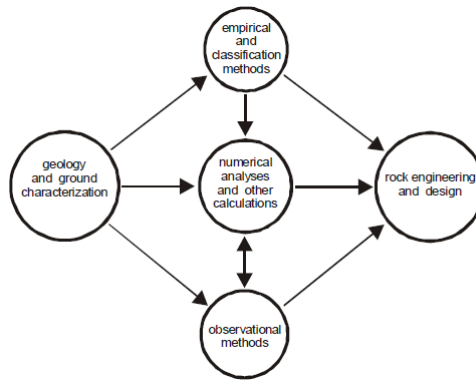


Figure 1.3.6: Main principles in the process of ground characterization and rock engineering (sourced from [93])

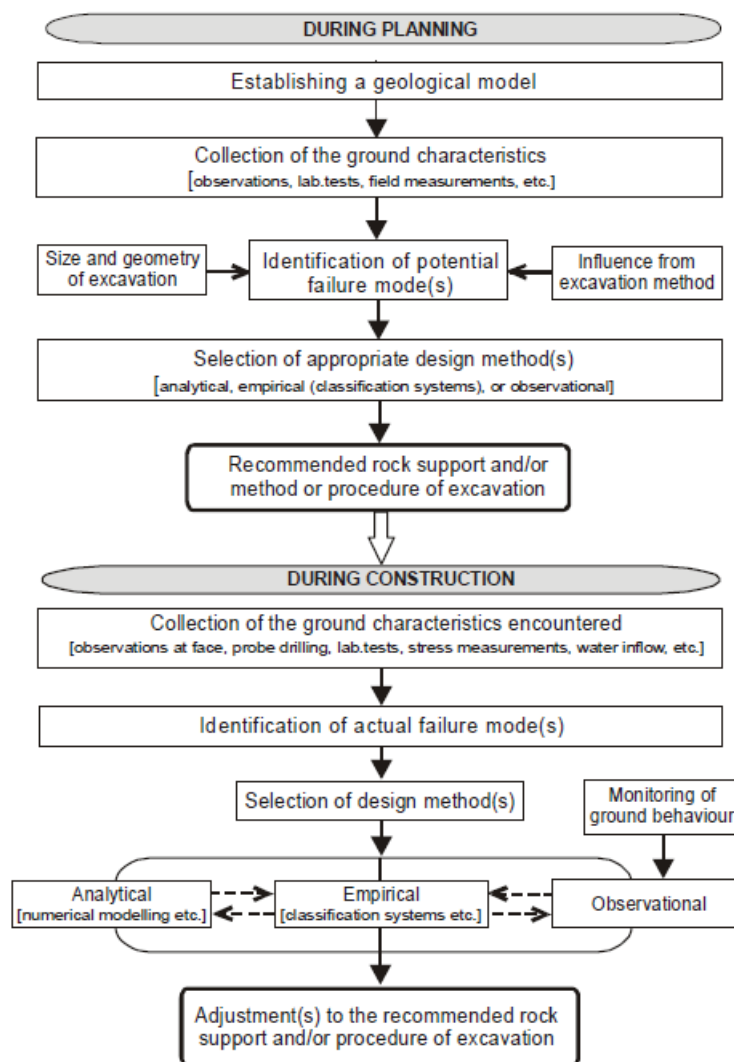


Figure 1.3.7: Principles of the design process for underground constructions in rock including the use of classification systems as an empirical design method (sourced from [93])

The development of the rock classification systems has gained its successful achievement by the numerous of available systems and their undeniable role in all tunnel design work. The analytical approach has also become more and more robust with the puissance of numerical computer codes based on classic mathematical and mechanical theories. The observation approach and the NATM has been rewarded their position in tunnel engineering with its strict technical and construction procedures and the state-of-the-art monitoring technics. The harmonious combination and control of the participation of the three approaches, in more or less contributions, is another challenge in tunnel engineering. The British Tunnelling Society [76] recommended that “in all tunnel designs, because of the uncertainty and complexity involved in the problems, more than one design method should be used to provide independent checks”.

1.4. Forward a new methodology for the modelling of rock tunnels

1.4.1. Introduction

As discussed in the section of the analytical approach for tunnel engineering, the numerical models have been widely used in the design and construction procedures of not only tunnel projects but also for nearly all other construction projects. The numerical analysis acts either as an independent operation for the validity of other analysis solutions or as a constitutive part of the comprehensive and assured scheme for the project. Conversely, the results of the numerical analysis must be cross-checked with other expert analytical works and with the experimental data from the experiments and monitoring of the real rock mass. The numerical analysis and modelling has become now a trend in many research domains. It is an in-door work that brings out the verification for the real data that have been obtained in history, the alternative solution for experimental works (when the working conditions of the conventional method is not adapted or out-of-reach), the ability of predicting the behaviours of the research objects.

A tunnel construction project is always expensive and presents some levels of risk. The behaviours of the rock mass where the future tunnel is located are difficult to predict with unexpected hazards. Even the application of the same design of an existing tunnel in the similar ground condition cannot be a completely risk-free insurance for the construction project. Furthermore, due to the increasingly severe requirements of environment and social impacts on a construction project, the working schedule is shortened with higher quality demands. The numerical analysis and modelling have shown the robust capability in the

domain and have demonstrated their own advantages over other conventional analysis solutions. The British Tunnelling Society [76] proposed that the numerical analyses offer the ability to model explicitly complex structures, including adjacent structures, different geological strata, complex constitutive behaviours, transient and dynamic loading, and construction sequences. It provides an unparalleled capability for simulating ground-support interaction and has led to the replacement of the numerical methods to the other methods of analysis [76]. The mentioned solution has overcome the limitation as a part of the analytical approach when proposing the capability of cooperation with the other approaches. The complementation of the computer modelling to the observational approach has been proven in many tunnel projects and is always recommended. The “over-conservative designs” disadvantage of the empirical approach that leads to high cost constructions ([77]) can be limited with the consultation of the parallel modelling results. Once the “strongest” philosophy in tunnelling support design is preferred to be replaced by the “optimal” one, the given combination of analysis seems to be a smart choice.

Return to the modelling in fractured rock, along the development of the domain, various types of models and related computer tools have been proposed and tested. Each has obtained its own strong points, based on its particular hypotheses and the scope of application. The British Tunnelling Society [76] suggested the quick guide for the choice of a reasonable model:

- For tunnels in soft ground: Since the soft ground is normally considered as continuum, the FDM, FEM hybrid FEM/BEM and FEM/FDM are proposed;
- For tunnel in fractured rock mass: When the medium is lightly fractured with small number of discontinuities, the FEM, FDM and hybrid FEM/FDM are favourable. Else, the BEM and DEM are more suitable, DEM for deformable and rigid blocks while DDA for rigid blocks and contacts.

The dominant effect of the rock material or of the rock structure on the rock mass is an important factor to the decision of the continuous or discrete models. Each has its own characteristics and its relevant mathematical solutions for the solving of the basic mechanical equations. The decision of the 2D or 3D modelling is also needed to be consideration and a further discussion is presented in the section 1.4.3. Otherwise, the combination of some numerical methods to form hybrid solutions is the recent tendency for the amelioration of the existing tools and heading to the optimal use of them.

1.4.2. Application of the numerical methods on the block generation and the tunnel modelling

Besides the references and citations that have been mentioned in the previous parts, a bibliographical study on the application of the numerical methods mentioned in the section 1.2 on the block generation and tunnel modelling was executed. It gave us a general understanding on the domain and guided us to a proposition of a methodology for the tunnel modelling that will be presented after this section.

1.4.2.1. Block generation solutions

M. Elmouttie *et al.* [67] developed an algorithm for the identification of rock blocks generated from the partial or complete intersection of large numbers of both planar and curved rock mass discontinuities based on the DFM. The generated blocks were able to connect with FEM-based codes with the limitation of planar discontinuities and finite element mesh with sensitive quality and density.

D. Heliot [64] proposed a theory for the generation of the blocky rock mass by splitting the initial rock mass by the discontinuity network into an assemblage of small blocks. Each component (vertex, edge, face, and block) was defined by the necessary information for the generation. The development of the rock structure was also considered. The Block Generation Language (BGL) is the computer language of this theory for the numerical modelling of the rock masses.

V. Merrien-Soukatchoff *et al.* [12] introduced the RESOBLOK code based on the theory and the BGL of D. Heliot. It was a downstream solution for the 2D and 3D block generation and the quick stability analysis based on the Key block theory of P.M. Warburton.

1.4.2.2. Tunnel modelling

- FEM-based researches:

S.C. Moller and P.A. Vermeer [95] used the 2D FE-mesh with six-node-triangular elements for the modeling of the installation of a tunnel in medium-weak heterogeneous ground.

S.Y. Wang *et al.* [96] studied the failure mechanism for a circular tunnel in transversely isotropic rock using a 2D FEM-based numerical code to obtain the stress fields in the mesoscopic elements. Elastic damage mechanics, the maximum tensile strain criterion and the Mohr–Coulomb criterion was applied.

R.E. Hammah *et al.* [14] applied the SSR method on Rocsience for the 2D simulation of the distribution of major principal stress around a circular hole in a homogenous intact rock mass and in a two-family-fractured rock mass.

H. Mashimo *et al.* [97] carried out a 2D FEM analysis using the monitored crown settlement and convergence data to evaluate the modulus of elasticity, the coefficient of lateral pressure of the ground, and the load acting on the tunnel supports during the construction phases. A NATM tunnel in large and small overburden condition was modelled.

H.Y. Liu *et al.* [98] realized the 3D FE calculations coupled with elasto-plastic material models, which took into account the tunnelling procedure, the interaction between the shotcrete lining and rock mass, the interaction between the rock bolts and rock mass, and the elasto-plastic behaviour of the rock mass, the shotcrete lining and the rock bolts.

G. Swoboda and A. Abu-Krishanumerical [99] analysed 3D FE coupled linear flow for Tunnel Boring Machine (TBM) tunnelling in saturated porous medium and to simulate explicitly the behaviour of excess pore water pressure mobilization and its dissipation in time.

H. Mroueh and I. Shahrour [100] created the simplified 3D FE model with the twenty-node-hexahedral-element-mesh for the prediction of soil movement induced during tunnel construction using TBM to a shallow tunnel in soft soils. The modelling was done by the use of a sparse storage scheme for the stiffness matrix, and the bi-CGSTAB iterative method coupled to the Successive Symmetrical Over-Relaxation preconditioning operator for the solution of the resulting linear systems.

C. Yoo [101] conducted a 3D FE analysis on a number of tunnelling cases with different face advancing sequences of multi-faced NATM tunnelling in soft ground. The eight-node isoparametric-solid-element-mesh was used for the tunnel and the eight-node-trilinear-displacement-element-mesh for the ground and the shotcrete lining. The tunnel excavation sequences were simulated by adding and removing corresponding elements at designated steps.

G. Galli *et al.* [102] realized a 3D FE model to simulate the conventional procedure of tunnel excavation and lining. The technics of activation/deactivation of the structural elements was used to simulate the simple procedure for the excavation phases through different analysis steps.

J. Bartak *et al.* [103] realised a simulation of the construction of the jet-grouting curtain and of the subsequent utility tunnel excavation in overburden condition using PLAXIS – a FEM-based software with an automatic fifteen-node-triangular-element-mesh generator.

- FDM-based researches:

M. Barla [104] used FLAC – a FDM-based numerical tool for the modelling of a tunnel in two conditions: i) plane strain: The excavation of the tunnel was simulated by reducing the normal internal pressure at the tunnel contour from the *in situ* state of stress to zero, in undrained conditions; ii) total stress condition: The tunnel excavation was simulated by removing elements inside the tunnel in sequence in the longitudinal direction.

G. Barla [105] published the analysis of a large diameter TBM tunnel in complex hydro-geological conditions by using FLAC to compute the bending moments and axial forces in the primary lining have. The lining and the rock mass were discretized by rectangular elements. A relaxation of the traction forces at the tunnel perimeter was allowed to simulate the excavation process and activating for the computational step chosen.

- FVM-based researches:

J. Maryska *et al.* [106] set up a numerical model of groundwater flow and transport in fractured rock using the mixed-hybrid FEM with the lowest-order Raviart - Thomas elements on tetrahedra, triangles and line segments on three hydraulically connected domains; and the FVM for the transport on the same mesh that had used for the calculation of the flow field, due to the direct calculation of the inter-element fluxes in the mixed-hybrid FEM.

- BEM-based researches:

R. Adey and A. Calaon [107] applied BEM to calculate the stress distribution and the stability of underground mines for disposal of chemical waste. A modelling technics using the Engineering disturbed zone (EDZ) was developed to investigate the stability in the presence of a large number of fracture zones and to determine the stress near the mine during the time.

M. Cerrolaza and R. Garcia [108] used the BEM direct formulation based on the Somigliana identity on a 2D model in plane strain for several tunnels in different rock masses by a code written in Pascal language.

- DEM-based researches:

J. Guittard *et al.* [109] applied the geo-statistics on the in-situ-collected discontinuity data and RESOBLOK – a DFN-based software to 3D model a cubic rock mass in which a circular

opening was situated. Primary analyses were realised. A cross-check on the equivalent 2D model for UDEC – a DEM-based software was also executed.

M.J.M. Maynar and L.E.M. Rodriguez [110] published the determination of the thrust and torque needed by the Earth Pressure Balance (EPB) machine to excavate the tunnels; and the soil stability at the tunnel face by the use of the DEM on the PFC30 code. A 3D model constituted of circular bond particulars was employed to reproduce the combined movement of the cutting head in the EPM. The simulations of the tunnelling were carried out both by filling the whole space between the tunnel and the ground surface with clumps and by substituting the upper part of this depth with an equivalent vertical load.

N. Hataf and M. Baharloo [15] constructed a DEM-based model that took into consideration of the large displacements and the behavior of highly fractured rock masses. On the edge-to-edge and the vertex-to-edge contact, two springs were assumed at each contact point. Their relative displacements generated the normal and shear forces in the springs. The rock bolt was assumed to be anchored at both ends without the side friction. The model took into account the effect of ground water in reducing normal pressure on the surface of discontinuities.

A. Rafiee *et al.* [72] generated a rock mass by using the statistical expression of the discontinuities families. The discontinuities were planar surfaces with different orientation. The joint spacing and the orientation data were assumed to follow an exponential and a normal law, respectively. The model of tunnel and its vicinity which was constructed on AutoCAD was immersed into LMGC90 for the DEM-based analyses.

V. Merrien-Soukatchoff *et al.* [12] applied the RESOBLOK for the modelling of an excavation in rock. Many cases of generation were created and the stability analysis based on the Key Block theory of P.M. Warburton was executed by the integrated module in the code for the determination of the critical cases.

- DDA-based researches:

S. Chen *et al.* [111] applied the DDA for the analysis of the displacements and stability of an excavation in the clean cobble-gravel deposits. Different sizes of 2D polygons of 12 vertices and 12 sides in elliptic shape were used to simulate the cobble-gravel particles. The deposits of particles were formed by gravity with the long axis laying either primarily in horizontal or vertical direction. The direct shear tests were performed to demonstrate the anisotropic characteristics of the rock mass. Open excavations on both deposits were simulated to

investigate the influence of anisotropic characteristic and to observe the performance of gravel mass around the tunnel.

J.H. Wu *et al.* [112] studied on the stress distribution an inclined layer rock mass by DDA and compared the numerical results with the results of the equivalent laboratory tests. He proposed to use the DDA to explain the mechanical behaviours of tunnel, such as arching phenomenon, non-symmetrical earth pressure distributions acting on the trap door, and the surface settlement profile in the jointed rock masses.

1.4.3. Recommendation of the 3D modelling and analysis

The selection between 2D and 3D analysis and modelling does not seem to be difficult. One knows the obvious advantages of the latter over the former in the detail of the models, the appropriation of the modelling, the visual interaction and demonstration, *etc.* However, on the same problem, the 2D analysis is simpler, less time consuming, simple requirement of the calculation tool and memory space. In fact, the strong point of a solution is the weak point of the rest. It is found that the 2D solution is good for simplified and quick analyses, in local zones of the rock mass or when the calculation can be discretized in two orthogonal spaces: one goes along the longitudinal axis, the other passes the cross-section of the medium. This is the conventional resolution that has been widely applied but the calculation must be repeated in various cross-sections perpendicular and/or parallel with the longitudinal axis. The volume of calculation is thus heavy. Moreover, simplifying of the spatial stress tensor composed of three normal components and three tangential components into the plane stress composed of a normal component and a tangential component, the natural state of the of the rock mass is far from being true. Followed [113], another weak point of the 2D simulation is that it is impossible to observe rotations of the blocks in the medium. By considering only some important sections, the task can be lighten but it is possible to underestimate the real behaviours of the medium. The 3D analysis is recommended for comprehensive analysis, with the demand of an explicit redistribution of the stresses and deformations on the tunnel structures and the vicinity medium. However, while the discontinuity mapping technics is still limited in 2D, the representation and converting functions for 3D is needed with the application of the geo-statistics.

1.4.4. Conclusion

In this research, we do not aim at paying attention to all the details of a tunnel construction project, but we want to examine the benefit of a reasonable fast solution for any *in situ*

engineers or a not-well-equipped designer/researcher to be handled for tunnelling design in rock. The terminology “opening” is used instead of “tunnel” because the tunnel support structure is not, at the moment of this redaction, presented in our models. The thought of replacing them by the appropriate loads acting on the rock face of the excavation at assumed locations was considered but it is not the priority of our research. The proposed methodology is hoped to be comprehensive since it covers the main procedures of a classical tunnel project from the *in situ* investigation, through the in-door data processing to the 3D geometrical simulation until the analysis and modelling in 3D. This methodology can be used as independent analysis tools or as a cross-checking solution for the validity of the results of other approaches. Besides, it can be equipped for a structural and/or geological engineering in the working team of the tunnelling project as a simple computation of the behaviour-control of the opening during the construction project. The detail of this research are presented in the next chapter and followed by the real applications related to a tunnel construction project in Haute Garonne, France.

CHAPTER 2:
**COMPREHENSIVE METHODOLOGY
FOR THE MODELLING OF ROCK MASSES:
FROM GEOLOGICAL SURVEYS
TO DEM-BASED MODELLING AND ANALYSIS**

In the scope of our research, a comprehensive methodology from the *in situ* investigation and test, through the in-door data processing to the 3D geometrical simulation until the 3D mechanical simulation and analysis is proposed to satisfy the demand of a quick and accuracy-accepted solution for the rock mass modelling. This is a downstream procedure that is composed of three main tasks which are concretized in small steps. The summary of the main contents of the methodology is given as follows:

Task 1: Geometrical modelling in 3D

- *In situ* measurements on exposed rock faces by the scan-line method:
 - The scan-lines are surveyed on exposed rock faces representative for the rock medium of interest;
 - The data obtained from each discontinuity: type, intersection with scan-line, orientation, persistence, extension, opening, filling, *etc.*
- Discontinuity data processing:
 - The discontinuities are grouped into main families by the clustering methods;
 - The variability of discontinuities in each family is analysed to find out the geo-statistical distribution laws of the family in the space and the centre of the family by the geo-statistical and statistical processing.
- Model generation in 3D by RESOBLOK:
 - The configuration and direction of the model are decided;
 - The centre and the distribution laws are used to defined each family;

- The different scenarios of the intersection between the discontinuity families in the rock mass are assumed;
- The rock structure is defined by its discontinuity families and isolated fractures, the generation of the 3D model is created by the use of RESOBLOK based on the DFN method;
- The preliminary selection of critical cases of generation is done by the stability analysis of RESOBLOK based on the Key block theory.

Task 2: Mechanical modelling of the rock mass

- Choice of the models of the mechanical behaviour of the rock blocks: rigid or deformable (elastic, plastic or viscous, *etc.*);
- Choice of the contact laws between rock blocks;
- Choice of the mechanical parameters of the intact rock and the rock mass:
 - Natural stresses in the rock mass are obtained from the *in situ* measurements;
 - The geotechnical data of the intact rock are obtained from laboratory tests.

Task 3: Numerical simulation analysis in 3D

- Simulation setting:
 - Boundary conditions;
 - Loading conditions:
 - Theoretical combinations of earth pressures;
 - Application of *in situ* stresses in the rock mass.
 - Numerical simulation and calculation parameters: the length of time step, the parameters of the Non Linear Gauss-Siedel resolution algorithm, the convergence criteria.
- Discrete analyses are realised based on the NSCD method with the implicit discretization of time and the integration of the meshing of the FEM by the use of LMGC90;
- Post-processing processing on obtained numerical responses of the modelling:

- Evolution of displacements;
- Distribution of forces and stresses in the medium;
- Numerical stabilisation analysis.

The organisation of the methodology is illustrated in the flowchart presented in the following figure.

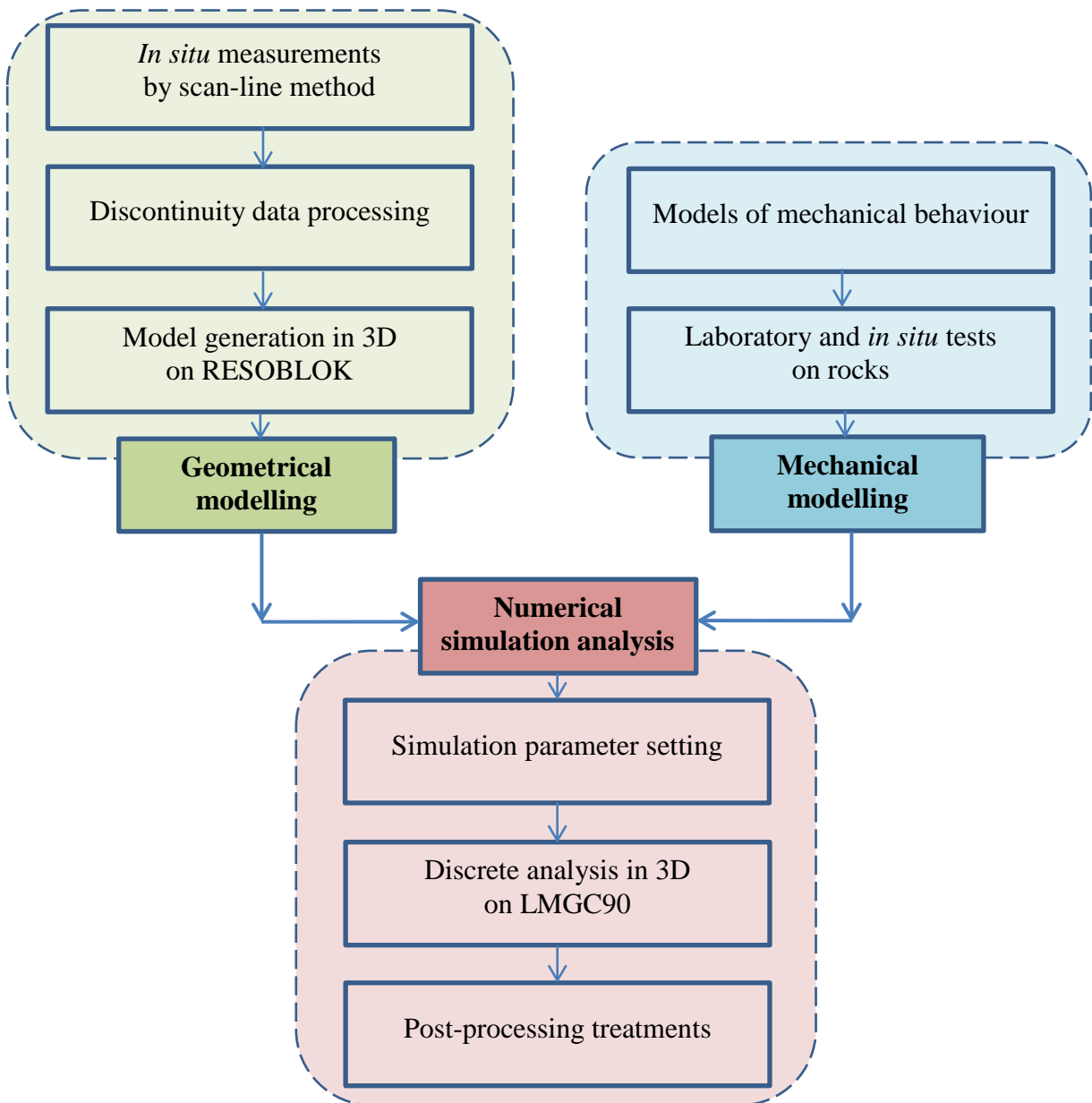


Figure 2.0: Flowchart of the proposed methodology for the modelling of rock masses

The following parts of this chapter are dedicated to the details and the applications of the methodology.

2.1. *In situ* discontinuity measurements

The data collection of the rock structure is an important task that constitutes the first step of our methodology. By the realisation of the *in situ* measurements at the investigation site, the comprehensive discontinuity data gathering of the rock mass is aimed: orientation, size, frequency, surface geometry, genetic type and infill material, *etc.* [1]. Many measurement methods have been proposed in rock engineering. They can be classified into two groups:

- The manual or direct methods: the measurements are carried out directly on the exposed rock faces or on the borehole core. They are the scan-line, the window and the borehole sampling methods [1], [2], [3].
- The digital image or remote sensing methods: the image of the rock medium is first captured and then analysed to reconstruct the structure of the real rock medium [4], [5], [6], [7]. There are several mapping technics such as the aerial photography and mapping, radar, volumetric surveys, digital mapping, contour mapping, topographic mapping, land mapping, photogrammetry, digital terrain models and other 3D aerial surveys.

The first group, which is classical and more common, is characterised by some typical features:

- Advantages:
 - Simple requirements for the measurements: the two most important instruments are the geological compass - inclinometer and the measuring tape;
 - Common technics requirements: the technics of the measurement is quite simple and easy to be handled; the post-processing processing on the obtained data is quite simple and not time consuming;
- Disadvantage:
 - Labour requirement: At least two workers are needed for any simple measurement;
 - Time-consumption: it is due to the manual realisation of the *in situ* measurements. Moreover, severe *in situ* working conditions sometimes limit the speed of the work;

- Large sources of errors: the data quality strongly depends on the working tool error (the equipment bias), the experience and the concentration of the workers (the human bias), the influence of the climatic, working conditions and rock face features (the environment bias). The measurement can only be realised on finite zones of the studied rock mass where the scan-line, the sampling window or the borehole are located (the local bias);
- Safety risk: there is always a high probability of unsafe actions that can happen at working sites. Besides, some rock surfaces of interest are inaccessible or out of human reach limits.

The measurements by the second group of methods are normally based on the geodesy, the laser scanning and the imaging or aero-photographical technics. The second group has been progressively more popular in the field of geology mapping thanks to the capacity of the technics to avoid the defaults of the first group. The permutation between the advantages and disadvantages of the former group can lead to those of the latter.

- Strong points:

- The measurements can be taken on site or realised from a certain distance that helps to overcome the natural obstacles of the *in situ* works;
- The application of the aero-photography can offer the multi-target mapping images that can be also exploited for geological purposes;
- The capacity of large captures in each measurement without long delays helps to promote the rate of the work and to provide the alternative data collection to avoid the bias due to small number of data;

- Weak points:

- Modern and expensive equipment, highly technical requirements for labourers and the mastery of complex data processing are needed;
- The image processing is time consuming;
- High risk of missing small and micro traces of discontinuities in small scaled captures. The confusion or errors are risked when the mapping capture and the image processing are separately realised;

- The data quality is based on the quality of the captured images that can be biased due to external impacts (weather, capture conditions), personal biases (the labourer experience and the concentration during the campaign) and notably by the machine precision;

Whatever the method is, the investigation location takes an important role to the whole work. For a tunnel modelling, the *in situ* measurements on several exposed rock faces are conducted in the investigation site of the future tunnel. The most ideal rock faces is located at the exact location of the tunnel. If not possible, the investigation site can be remote from the site but must be in a zone with similar geological conditions with the actual site of the tunnel. However, the impossibility of the direct observation or measurement can happen due to the limitation of the space inside a tunnel. This thought is well illustrated by the figure of A. Palmström [120], quoted in the next figure.

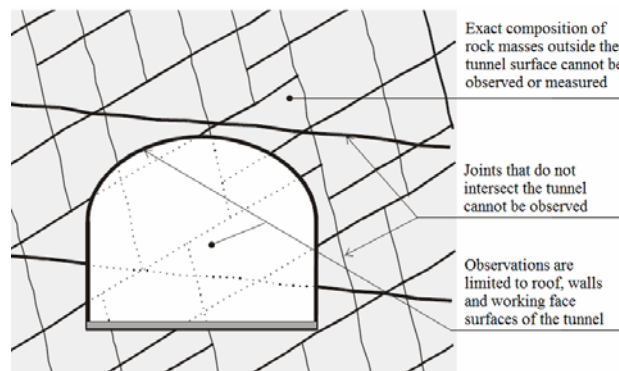


Figure 2.1.1: Limitation of the observation and the measurement
of the properties of the rock mass inside a tunnel (sourced from [120])

Measuring work is simple or complicated, in short or long periods of time depending on technology and resources but discontinuity properties are the necessary required data. Other geological indices can be extracted from previous investigation documents. To this step much attention should be paid because it will supply input data for all succeeding procedures and because of its possible arbitrary characteristics due to the probabilities of bias.

In the scope of our research, the two first manual methods were proposed to fulfil the first step of our methodology. In fact, the latter can be considered as the special case of the former when the measurement on the scan-line is replaced by the one on an area of rock face.

2.1.1.1. Scan-line method

The scan-line method, which is until now the most widely applied one, is done by the mark of an artificial line on the study rock face and the collection of all discontinuities that intersect it. The line can be created simply by a measuring tape and visible markers at every regular interval along it, giving us fracture information as follow: type, intersection with scan-line, orientation, persistence, extension, opening, filling, *etc.* The instruction of this method can be found in [6], [9], [121].



Figure 2.1.2: Trace of a scan-line on an underground rock face

For a good scan-line survey, the selected rock face should be safe, convenient for working and show representative characteristics of discontinuities and rock materials. S. Priest [6] has suggested the rock faces that “contain at least 150 to 350 discontinuities of which 50% should have at least one end visible”. We found that it is a reasonable recommendation in relation to the future data processing that will be done in the next step. On the chosen rock face, a good location of the scan-line should be at the convenient reach of the workers and satisfy one of the definitions given by A.K. Manda and S. B. Mabee [115] as follows:

- perpendicular to the planes of a specific discontinuity family;
- perpendicular to the bisector of the acute angle between two discontinuity families;
- parallel to the direction of maximum frequency of multiple families.

However, the measurement on a single straight scan-line is under-sampling the fracture structure of the rock face [117] when only discontinuities that cut the line are taken into account. That is why some other configurations other than a simple horizontal line have been proposed:

- multiple lines [115];
- curve [114], [122];
- or circular line [123].

They are considered as special cases of the scan-line technics.

2.1.2. Window sampling

This method is called by several names as the window sampling [6], the cell mapping [116] or the aerial survey [9]. The same technics as in the scan-line method is used but the scan-line is replaced by an area of rock face, of which each side should intersect from about 30 to 100 discontinuities [6]. The latter can be treated as the extension of the former, as suggested by [9].

P.J. Pahl [124] has classified three types of discontinuities in a sampling window traces: those which are contained in the window, those which intersect the window and those which cross the window. The discontinuities that exist on the selected rock face are collected in three mentioned groups. However, there are always inaccessible zones on the rock face (when they are out of the human reach or in dangerous conditions) that bring difficulty to the measurement and affect the data quality. In order to remedy these disadvantages, the combination of the first and the second method has been recommended by Laslett [125], E. Villaescua and E.T. Brown [126]. A. K. Manda and S. B. Mabee [115] used a simplified version of the window sampling method that they called “the selection method”. In the comparison with the single scan-line, multiple scan-line and “the selection method on layered dolomitic rocks, the authors [115] suggested that the scan-line method is “more preferable for smaller outcrops and/or when the worker is not pressed for time” and on a FEM-based model built on the obtained fracture data, the authors proved that the good positioned scan-line measurement was the best performed in the recreation of the natural fractures.

2.1.3. Conclusion

The rock geological surveys, which can only be realised in limited areas, are far from being representative of the real rock mass. Taken in a short or long period of time, a fracture data collection based on the single scan-line measurement “reflects only the finite length properties, which are bias and cannot be representative for large rock mass”, as mentioned by Q. Feng [127]. The under-sampling of the orientation and the spacing of discontinuities is the common bias [117]. The discontinuities of which the spacings are longer than the adopted length of the scan-line cannot be observed [128].

An important attention is needed to be paid to the impact of the errors on the investigation results coming from [129]:

- the insufficient quantity of measurement within a small area that cannot “ensure a reliable estimate of the relative abundance of joints in the area”;
- the interaction angle of the discontinuities and the scan-lines.

R.D. Terzaghi [129] proposed to reduce those errors to a tolerable level by “making observations in an adequate number of appropriately orientated boreholes, and by plotting the results of the survey in polar diagrams”. A factor which was suggested to correct the under-sampling of the discontinuities on a straight scan-line is introduced in the section 2.2.1. This bias correction has been widely applied for geological sampling engineering.

The combination of several methods or one method of the first group with one of the second group can be a solution for the minimization of bias and improvement of the obtained data. S. Priest [6] recommended the colour photo images of the investigation rock mass as the reference for the data processing. For the window sampling method, those images are suggested to be the best implementation for indoor data processing [6]. It is aimed at ensuring the quality result of the surveying work.

As the first step of our proposed methodology, the discontinuity measurement is recommended to be realised by the scan-line method thanks on the simplicity of the enrolling procedure and the least restricted requirements of working tools that any field engineer can supply. This task can be a part of the geotechnical investigation procedure of the related construction project or can be independently conducted for the purpose of research or for the validity of other methods. It does not mean that the other methods are less efficient or less suggested.

2.2. Discontinuity data processing

Because of the complex distribution of discontinuities on a rock face, it is nearly impossible to treat and analyse each of the separated discontinuity as their natural appearances. It is practical to group them into main families (or main clusters) and to use the mean orientation and the closest theoretical geo-statistical laws of distribution of each family to represent them. By the use of the geo-statistical laws, with the probabilistic functions, the data from the discontinuity investigation on the limited area of the rock mass can be used as the representation of the whole rock mass since “it is not necessary to consider the number of samples” [64].

2.2.1 Geological and graphical presentation of discontinuities

The line or plane to which the discontinuity belongs is chosen to define its orientation by some couple of angles: plunge and trend for the first case, dip and dip direction for the second. Some other names of these angles can be used instead. Short definitions of these angles are as follows:

- Dip (or dip angle) is the angle measured in a vertical plane between the steepest line of the plane to which the discontinuity belongs and the imaginary horizontal plan. Its value varies from 0 to 90° if there is an additional letter that shows the direction (N, S, E, W representing north, south, east and west) or from 0 to 180° (or -90° to 90°) if there is not any addition.
- Azimuth is the angle between the North and the horizontal intersection of that plane and the imaginary horizontal plan. Its value varies from 0 to 180° if there is an additional letter that shows the direction (N, S, E, W) or from 0 to 360° if there is not any addition (right hand law). It can be called by another name as strike.
- Dip direction is the angle between the descending direction of the steepest line of the plane to which the discontinuity belongs and the horizontal plane. It is perpendicular to the strike so that its value is 90° off the strike or azimuth.
- On a plane, the trend and the plunge of the steepest line is referred to be the dip direction and the dip angle of the plane. Azimuth of a plane is the trend direction of a horizontal line on it [129].

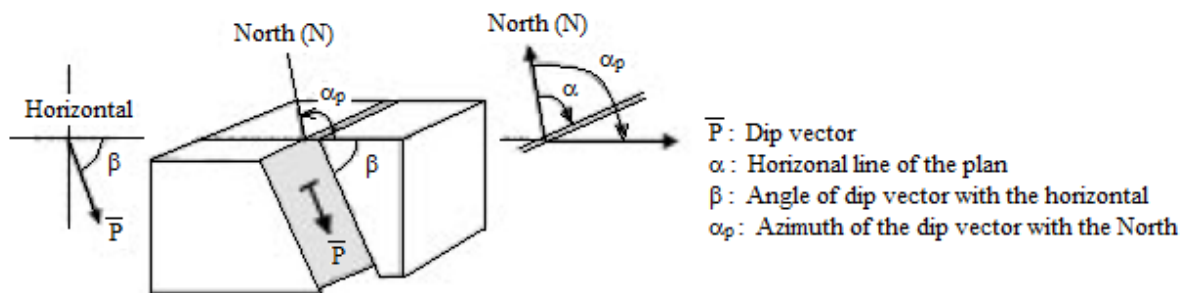


Figure 2.2.1: Orientation of the discontinuity in space (sourced from [131])

It should be noticed that there is a slight difference between geographical and magnetic value of each angle due to the different position of the geographical North and the magnetic North. Furthermore, there are some different ways to present these angles: the French convention versus the American one and the right hand law versus the left hand one [186]. So a careful note with clear explanation or illustration at the site when collecting the

surveying data is recommended to apply the internal data processing more easily and correctly.

The orientation of a discontinuity can be expressed by its directional vector (the vector that runs parallel with the discontinuity) or by its unit normal vector (the vector that runs perpendicularly with the discontinuity). As in the case of angle conventions, we have found some various ways to calculate the value of a normal vector from the direction vector of a discontinuity but the formula of S. Priest [6] was chosen:

$$\alpha_n^i = \alpha_d^i \pm 180^\circ$$

$$\beta_n^i = 90^\circ - \beta_d^i$$

With:

α_n^i, β_n^i : orientation of the normal vector of a discontinuity

α_d^i, β_d^i : orientation of the directional vector of a discontinuity

This discontinuity can be situated on a spherical space and its normal vector is then expressed in a 3D Cartesian coordinate system:

$$x_1^i = \cos(\alpha_n^i) \cdot \cos(\beta_n^i)$$

$$x_2^i = \sin(\alpha_n^i) \cdot \cos(\beta_n^i)$$

$$x_3^i = \sin(\beta_n^i)$$

With:

α_n^i, β_n^i : orientation of the normal vector of a discontinuity

x_1^i, x_2^i, x_3^i : Cartesian coordinate of the normal vector of a discontinuity

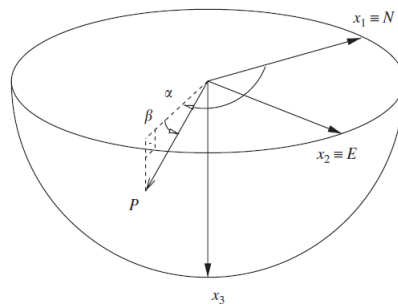


Figure 2.2.2: 3D Cartesian coordinate system (sourced from [130])

In another hand, this discontinuity can be also represented on a plane and its normal vector

is then expressed in a 2D Cartesian coordinate system on the lower or upper hemisphere with the equal angle (Wulff) or equal area (Schmidt) projection. In our knowledge, the lower hemisphere is more widely applied and it is used in all related projections in our methodology. The coordinates of the discontinuity is calculated as in the Table 2.2.1.

Table 2.2.1: The x, y Cartesian coordinate of a point representing a line of trend/plunge α/β on a lower hemisphere projection of radius R (sourced from [129])

Projection	x	y
Equal angle	$R * \cos(\alpha) * \tan\left(\frac{90^\circ - \beta}{2}\right)$	$R * \sin(\alpha) * \tan\left(\frac{90^\circ - \beta}{2}\right)$
Equal area	$R\sqrt{2} * \cos(\alpha) * \cos\left(\frac{90^\circ + \beta}{2}\right)$	$R\sqrt{2} * \sin(\alpha) * \cos\left(\frac{90^\circ + \beta}{2}\right)$

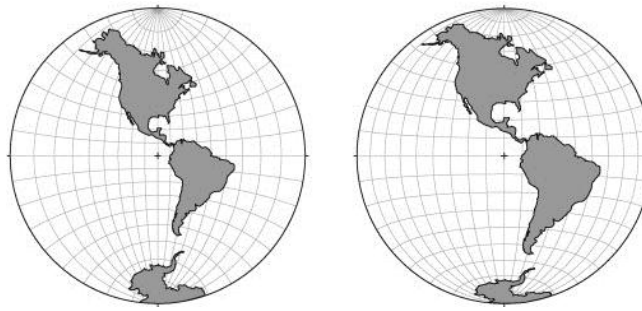


Figure 2.2.3: Equal angle and equal area projection of the Americas and Antarctica
(sourced from [131])

Sampling on a linear scan-line can produce orientation bias. R.D. Terzaghi in 1965 had first worked on this problem and proposed a correction of the angle of intersection between the discontinuity and the drill holes or exposed faces [129]. This theory has been widely applied ([129], [114], [132]). For a straight scan-line, the correction factor is the invert value of cosine of the angle δ between the scan-line and the normal vector of a discontinuity on this scan-line [114]:

$$w = \frac{1}{\cos(\delta)}$$

S. Priest [6] also researched on this problem and proposed to calculate the angle δ according to the following equation:

$$\cos(\delta) = |\cos(\alpha_n - \alpha_c) * \cos(\beta_n) * \cos(\beta_c) + \sin(\beta_n) * \sin(\beta_c)|$$

With:

α_n, β_n : Orientation of the normal vector of the discontinuity

α_c, β_c : Orientation of the directional vector of the scan-line

The author recommended the maximum value of 10 for w to avoid the domination of discontinuities to the overall results of a scan-line sampling. The weighting w is then multiplied with all Cartesian coordinates of the unit normal vector of each discontinuity.

$$x_1^{i*} = w \cdot \cos(\alpha_n^i) \cdot \cos(\beta_n^i)$$

$$x_2^{i*} = w \cdot \sin(\alpha_n^i) \cdot \cos(\beta_n^i)$$

$$x_3^{i*} = w \cdot \sin(\beta_n^i)$$

With:

α_n^i, β_n^i : Orientation of the normal vector of a discontinuity

$x_1^{i*}, x_2^{i*}, x_3^{i*}$: Corrected Cartesian coordinate of the normal vector of a discontinuity

w : Weighting of sampling bias

It is suggested to use the coordinates (x_1^*, x_2^*, x_3^*) to replace the initial ones in all geological processing afterward [129].

2.2.2 Discontinuity clustering into main families

As mentioned above, clustering takes an important part in rock discontinuity engineering. In some words, clustering is the task of changing a complicated system of discrete discontinuities into a few main groups (or families/clusters) scattered in the rock medium according to their laws of distribution. R. E. Hammah and J. H. Curran [133] wrote that “Clustering, in the language of pattern recognition, is an unsupervised learning procedure for classifying objects or patterns”. This issue of research has been of interest for many researchers and can be applied in many other domains. R. Jimenez-Rodriguez and N. Sita [130] have classified two groups of clustering methods: one only based on discontinuities orientation; another based on discontinuities orientation and other information such as planarity, weathering, spacing or roughness. R. E. Hammah and J. H. Curran [133] have used two other groups: the hierarchical one of which members in a group have a non-equal relationship (as a family tree) and the partitive one that clusters objects into mutually exclusive sets.

Many algorithms have been adopted and in the limitation of our work, we have paid attention to three algorithms of the first group which had been published by R. Jimenez-Rodriguez and N. Sita [130], R.E Hammah and J.H. Curran [133], and S. Priest [6].

2.2.2.1 The spectral method of R. Jimenez-Rodriguez and N. Sita

Based on the similarity between normal unit vectors of discontinuities in the spherical space, the two authors proposed a clustering method based on the orientation of discontinuities. The algorithm of this clustering method can be shortly introduced as follows [130]:

Each discontinuity is represented by its normal vector in a 3D Cartesian coordinate system. Before starting the clustering work, a predicted number K of main families in the space is required. This pre-assignment should be firstly based on the geological observation at site or on existing documents of the researched rock mass. However, it is only an assumption that needs to be verified by a geo-statistical analysis on the distribution of the discontinuities in their assigned family [129].

Then, the acute angle between unit normal vectors of two random discontinuities in the space is calculated by the dot (or scalar) product operation:

$$\delta = \arccos \left| \frac{x_1^i \cdot x_1^j + x_2^i \cdot x_2^j + x_3^i \cdot x_3^j}{\sqrt{(x_1^i)^2 + (x_2^i)^2 + (x_3^i)^2} \cdot \sqrt{(x_1^j)^2 + (x_2^j)^2 + (x_3^j)^2}} \right|$$

and the sine-based similarity measure between them is calculated as:

$$d^2(x^i, x^j) = 1 - \cos^2 \delta$$

With:

x_1^i, x_2^i, x_3^i : Cartesian coordinate of the normal vector of the discontinuity i

x_1^j, x_2^j, x_3^j : Cartesian coordinate of the normal vector of the discontinuity j

The kernel of this method is the transformation of N discontinuities in the Cartesian spherical space into K dimensional space. The clustering procedure is given in several steps:

- Compute the affinity matrix NxN with $A^{ij} = \frac{-d^2(x^i, x^j)}{2 \cdot \sigma^2}$ and $A^{ii} = 0$, σ is the decay parameter, $\sigma = 0.1 \div 0.15$ recommended by the authors;
- Build the diagonal matrix D with $D^{ii} = \sum_{j=1}^N A_{ij}$ and the normalized affinity matrix

$$L = D^{-1/2} \cdot A \cdot D^{-1/2};$$

- Compute the K largest eigenvalues and their corresponding eigen vectors v_i ($i = 1, K$) of the matrix L to form the matrix $V = [v_i]$ then normalise each line of V to achieve the matrix U;
- Consider each row of the matrix U as a point in K directions and execute the K-mean algorithm on the matrix U to cluster N points into K sets.
- A discontinuity in the Cartesian spherical space x_i is assigned to the k^{th} set if and only if the row i of the matrix U belongs to the k^{th} set.

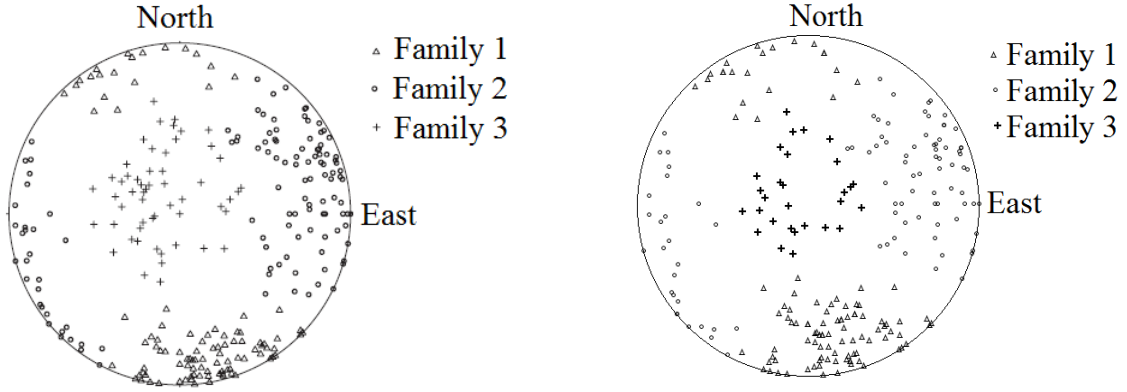
The mentioned K-means is an algorithm to classify N objects into K groups by minimizing the sum of the square of the distance between an object to its corresponding clustering centre [134]. First published by J. MacQueen in 1967 [134], this is a simple but robust algorithm that has been developed and extensively applied in many domains of research.

The basic K-means algorithm that has been applied on the matrix U to cluster N points into K sets was executed by iteration. The contents of a loop [134], [135] were given as follows:

- First, K random points are selected to be the centres of K sets. By calculating the Euclidean distances to K centres, a point is assigned to the set which is nearest to it.
- Second, after classifying N points into K set, the coordinate of the new centre of each set is given as the average value of the coordinates of its members.

The new centres of K sets at the end of the previous iteration were used as the input data for the next one. Some loops are required until the new and the old centre is coinciding.

After an effort to develop this algorithm on Excel with only the required expressions and conversions, we found that this clustering method is a robust one with not too complicated steps that bring out an explicit result of clustering families. No supposition is required except the value of K (i.e. the desired number of families). Nevertheless, the calculation of the affinity matrices becomes quickly harder as the number of observed discontinuities increases. With the kind help of Professor R. Jimenez-Rodriguez on giving us the permission of using the input data of San Manuel copper mine that had been treated on his paper [130], we reached nearly the same result with their published one that confirms the validity of our Excel program. However, in our research, the value of the decaying parameter has been followed by the two authors and further study is only being produced in order to find out a suitable value adapted for each case of application.



a) Results of R. Jimenez-Rodriguez and N. Sita (results from [130]) b) Our results by using spectral method of R. Jimenez-Rodriguez and N. Sita [130]

Figure 2.2.4: Clustering results on the discontinuities data of the San Manuel cooper mine (data sourced from [130])

2.2.2.2 The Fuzzy K-means method of R.E Hammah and J.H. Curran

R.E Hammah and J.H. Curran [133] applied a modified K-means algorithm with the criterion of highest density region to classify discontinuities into main families. The term “fuzzy” mentions that one discontinuity can belong to more than one family with different degrees of membership. This is the important difference with the previous clustering method in which a discontinuity belongs only to a unique family. Otherwise, this method shares some basics with the previous one. They are:

- The number K of main families must to be assumed before starting the clustering procedure.
- N discontinuities are treated as N points on the 3D spherical space and the distance between two points is calculated by the dot product of two vectors.

The membership value of the discontinuity as the distance from the centre of K family is defined as:

$$u_{ij} = \frac{\left(\frac{1}{d^2(x^j, x^{ci})} \right)^{1/(m-1)}}{\sum_{k=1}^K \left(\frac{1}{d^2(x^j, x^{ck})} \right)^{1/(m-1)}}$$

With:

x^j : Cartesian coordinate of the normal vector of the discontinuity j

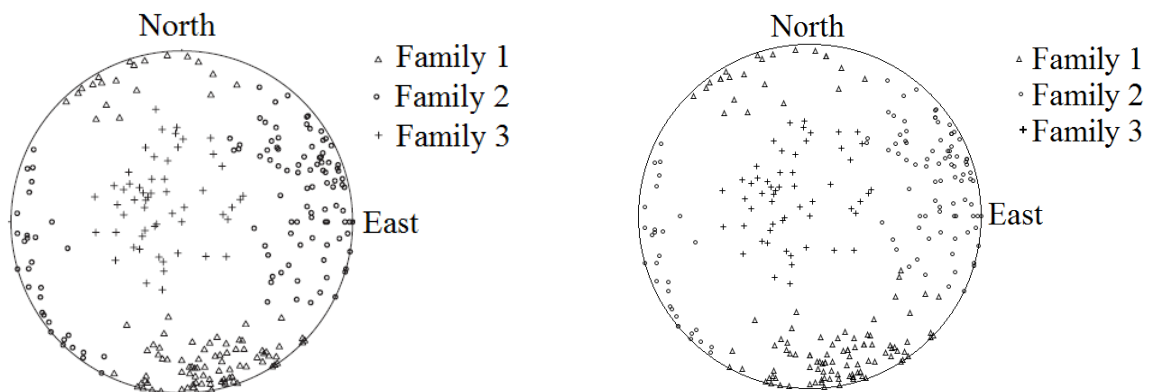
x^C : Cartesian coordinate of the normal vector of a family centre

m: weighting exponent, greater than 1. The value of 2 was proposed by the two authors of the method for clustering discontinuity orientations

A basic loop of this method was carried out in some steps as followss:

- Compute the modified orientation matrix for each family;
- Compute the three largest eigenvalues and their corresponding normalized eigenvectors. The normalized eigenvector of which the eigenvalue is the largest is then assigned as the new centre of family;
- Recalculate the distance between all discontinuities to the new centres and update the membership value.
- A discontinuity is assigned to a family of which its value of the updated membership value is maximal in comparison with other families. If there are more than one family that have the same membership value, the discontinuity belongs to the least-numbered family.

The condition for starting a new iteration is the absolute value of the difference between the new and the old membership value. If it is smaller than the criterion, recommended to be 0.001 by the two authors [133], the iterations continue.



a) Results of R. Jimenez-Rodriguez and N. Sita
(results from [130])

b) Our results by using Fuzzy K-mean
method [133]

Figure 2.2.5: Clustering results on the discontinuities data of the San Manuel cooper mine
(data sourced from [130])

Rebuilding this algorithm on Excel and doing the same task on the data of San Manuel

copper mine (sourced from R. Jimenez-Rodriguez and N. Sita [130]) as with the previous method, we have found that they bring out not-too-much-different results that presented in the figure 2.2.5. However, in our limitation of knowledge, the number of loops for this method is bigger with a longer computing time in comparison with the previous one.

R. Jimenez [136] proposed in 2007 a combination between these two methods which is called “the Fuzzy spectral clustering method”. The K-means algorithm in the first method was replaced by the fuzzy K-means algorithm for transforming the matrix U into K sets. A discontinuity in the Cartesian spherical space x^i was assigned to the k^{th} set when its membership value with the set is highest. The author was convinced that the new hybrid method showed better performance than the two original ones.

2.2.2.3 Method of S. Priest

S. Priest [6] published a technique to identify and delimit sets of discontinuities that was based on the researches of Shanley and Mahtab (1976) and of Mahtab and Yegulalp (1982). A cone with a suitable cone angle α is constructed on the normal vector of a random discontinuity. This discontinuity then becomes an assumed centre of a family in the space. The acute angle δ between this centre and another discontinuity is given by the vectorial algebra methods:

$$\cos(\delta) = |\cos(\alpha_n - \alpha_c) * \cos(\beta_n) * \cos(\beta_c) + \sin(\beta_n) * \sin(\beta_c)|$$

With:

α_n, β_n : Orientation of the normal vector of the discontinuity

α_c, β_c : Orientation of the normal vector of the assumed centre

If the acute angle between a discontinuity and the assumed centre is inferior to the cone angle α , they belong to the same family. The probability when there are t discontinuities of which acute angles with the centre of the family are within the angle α of the cone is calculated:

$$P(t, c) = \frac{e^{-Nc} * (Nc)^t}{t!}$$

With

$$c = 1 - \cos(\delta)$$

N: Number of discontinuities in the space

The probability that more than t discontinuities belonged to a same family is given by:

$$P(> t, c) = 1 - \sum_{j=0}^t \frac{e^{-Nc} * (Nc)^j}{j!}$$

in which j was an integer pointer.

A value of the critical frequency t_{cript} of the Poisson probability associated with random events when the cone is centred on each discontinuity normal is found and used as a density criterion. A dense discontinuity belongs to only one family while the non-dense one may be assigned to several families at the same times or none of the families.

In our knowledge, the technique of S. Priest is simple and visual. However, lacking of a suitable position of cone (on which the discontinuity normal is centred) leads to a not clear result with dispersed families. Hence, placing the cone on the predicted centre of a family is very helpful to reach a clustering result without long time computations. In order to satisfy this objective, using an additional support is required. A. Rafiee and M. Vinches [69] had some success in combining the methods of S. Priest [6] and the method of R. Jimenez-Rodriguez and N. Sita [130] with the cone angle of 25° .

2.2.3. Data processing in each family

After clustering all discontinuities of the rock mass into main families, a data processing is required on each family. This work is aimed at finding out the concentration of the discontinuities in the space and searching theoretical statistical laws that can be used as the mathematical representations of the distribution of each family. The geo-statistics has been widely applied in many domains of engineering, one of which is mine engineering. Among others, S. Priest [6] proved that it can also well adapt to the research of the spatial variability of discontinuity field. D. Heliot [64] also shared the same viewpoint when stating that “the tendency for joints to exhibit a spatially dependent variability and, more particularly, to bunch together, have led to the geo-statistical approach”

It may be useful to recall the scattered nature of discontinuities in a rock medium, even when they have been grouped into some main families. This fact is clearly illustrated in the obtained geo-statistical values. A basic grade is recommended to classify these results into continuous scales of distribution: 0.5 or 1m for the spacing distribution and 10° or 20° for the angle distribution, for instance. Then cumulative distribution functions of real condition in each family are traced and due to the form of each graph, a fitting statistical law is

searched. Numerous admitted geo-statistical and statistical laws with different fitting methods can be found. However, some laws have been recommended due to their high probability of suitability: Laplace – Gauss (called normal), exponential, lognormal statistical laws for the spacing distribution and Fisher distribution for the angle one ([129], [69]).

Demonstrating by the correlation of a rock property and the distance along a line obtained by geo-statistical theoretical basics, S. Priest [6] strongly recommended this application for the research of the discontinuities distribution in the rock mass. In our proposed methodology, the geo-statistical treatment is applied on the distribution of each discontinuity family to know how structure the family is and to find a geo-statistical fitting of the real distribution for the appropriate description of the discontinuity network. The mathematical and statistical processing is also applied on the discontinuities in each family that has been obtained from the clustering work to find out the logical order of the spatial distribution of the discontinuities. The obtained treated data are then used to describe the rock structure in the rock mass. Those results are indispensable for the numerical modelling and analysis in the following step of our methodology.

2.2.3.1. Centre of the family

R.D. Terzaghi [129] found that the mean value of discontinuity data from the *in situ* investigation is one of the complete and accurate information concerning the spacing and orientation of the discontinuities. In a family of discontinuities, each member is represented by its unit vector (normal or directional one) and expressed by its Cartesian coordinates (x_1^i, x_2^i, x_3^i). The centre of a family is calculated as the mean of vector elements of all family's members.

$$\bar{x}_1 = \frac{\sum_{i=1}^n x_1^i}{n}$$

$$\bar{x}_2 = \frac{\sum_{i=1}^n x_2^i}{n}$$

$$\bar{x}_3 = \frac{\sum_{i=1}^n x_3^i}{n}$$

The Cartesian coordinates of the unit vector of the centre of a family (x_1^C, x_2^C, x_3^C) are given by:

$$x_1^C = \frac{\bar{x}_1}{\sqrt{(\bar{x}_1)^2 + (\bar{x}_2)^2 + (\bar{x}_3)^2}}$$

$$x_2^C = \frac{\overline{x_2}}{\sqrt{(\overline{x_1})^2 + (\overline{x_2})^2 + (\overline{x_3})^2}}$$

$$x_3^C = \frac{\overline{x_3}}{\sqrt{(\overline{x_1})^2 + (\overline{x_2})^2 + (\overline{x_3})^2}}$$

The orientation of the unit vector of each centre is calculated as indicated in [129]:

$$\alpha = \text{atan}\left(\frac{x_2^C}{x_1^C}\right) + Q$$

$$\beta = \text{atan}\left(\frac{x_3^C}{\sqrt{(x_1^C)^2 + (x_2^C)^2}}\right)$$

With:

x_1^C, x_2^C, x_3^C : Cartesian coordinates of the centre of the family

x_1^i, x_2^i, x_3^i : Cartesian coordinates of a discontinuity in the family

n: Quantity of discontinuities in the family

α, β : Orientation of the centre of the family (rad)

Q: The quadrant parameter proposed by S. Priest [6]

2.2.3.2. Average semi-variograms of the discontinuity distribution on the scan-line

D. Heliot [64] underlined that the “variogram which characterizes the deterioration between measure data with increase in the distance between the data points” is the basic mathematical tool of geo-statistics. The position of members of a family on the scan-line is studied and on a distance scale of which the unit length is h(m), the number of discontinuities in each h-metre-segment on the scan-line is counted. The average semi-variance at a distance x on the scale shows the spatial dependence between two observations: the quantity of discontinuities and the position on the scan-line:

$$\gamma(h) = \frac{1}{2n} \sum_{i=1}^n [p(x) - p(x+h)]^2$$

With

h: Unit length of the distance scale(m)

n: Number of couples of data at a distance h

p(x): Number of discontinuities that appear at the distance x_i on the scan-line

$p(x+h)$: Number of discontinuities that appear at the distance x_i+h on the scan-line

The empirical average semi-variogram which shows how semi-variance changes as the position of discontinuities changes is then compared to some theoretical ones to find the most fitting representative function for the distribution of discontinuities on the rock face. Four practical theoretical average semi-variograms: spherical; nugget effect; exponential; hole-effect; and the combination of those and other theoretical models were suggested by S.Priest [6].

2.2.3.3. Statistical processing

Although S. Priest [6] showed the capability of geo-statistics for the discontinuity research, he suggested that the semi-variograms based on discontinuity spacing on a scan-line measurement give a clear but fairly weak indication of the spatial correlation. Sharing the same opinion, a more detailed research on the spatial distribution of discontinuities, precisely on 2D and 3D spaces, is recommended after the previous processing.

a) Distance distribution of discontinuities

The aim of this study is to find a statistical distribution that represents the diversity of the distance along the scan-line between members of a family of discontinuities.

The position of discontinuities on the scan-line and the distance between a discontinuity and a similar one on the rock face was studied. By using a distance scale of which the unit length was L(m), the diversity of distances was classified into different groups and the quantity of discontinuities in each group was counted. The probability curve of the empirical distribution of discontinuities was compared with the one of a theoretical statistical law.

Some statistical law were recommended by LAEGO [137]:

- Exponential law:

- Probability density function: $f(x) = \lambda \cdot e^{-\lambda \cdot x}$

- Cumulative distribution function: $P(x) = 1 - e^{-\lambda \cdot x}$

- Log-normal or Laplace – Gauss law:

- Probability density function: $f(x) = \frac{1}{\sigma\sqrt{2\pi}} * e^{-0.5*\left(\frac{x-\mu}{\sigma}\right)^2}$

- Cumulative distribution function: $P(x) = \frac{1}{2} \left[1 + \operatorname{erf} \left(\frac{x-\mu}{\sqrt{2}\sigma} \right) \right]$

- Uniform law:

○ Probability density function:
$$f(x) = \begin{cases} \frac{1}{b-a} & \text{for } x \in [a, b] \\ 0 & \text{otherwise} \end{cases}$$

○ Cumulative distribution function:
$$P(x) = \begin{cases} 0 & \text{for } x < a \\ \frac{x-a}{b-a} & \text{for } x \in [a, b] \\ 1 & \text{for } x \geq b \end{cases}$$

- Fractal law, power-law:

○ Probability density function:
$$f(x) = k * x^k$$

Based on the comparison results, the most fitting statistical law is chosen to be the representation of the distance distribution of discontinuities in each family.

b) Orientation distribution of discontinuities

The analysis and representation of rock discontinuities in a spherical space has been widely applied. Hence, the distribution of researched discontinuities on a spherical space is essential.

The knowledge foundation for our research was the clustering method of S. Priest [6]. In his method, discontinuities in the space are divided into families by the magnitude of acute angles between them and the centre of the family of which they were assigned to. In other words, if a cone is constructed on a family centre, all member of this family must be located inside this cone by having the acute angles between discontinuities and the centre not bigger than the angle of the cone.

First, by assuming a cone with the cone angle of α on the centre of each family, the acute angles δ of all members of a family and their centre are calculated with several cases of different values. Next, the diversity of the angle magnitude is studied by classifying them into a variation scale of which the unit length was $\delta(^{\circ})$. Then, the probability curve of the empirical distribution of discontinuities was compared with the statistical law of Fisher. Published by the author in 1953 [138], this statistical law was firstly proposed for the measurement of object position on a sphere. With the concurrence of two distribution theories of Von Mises and Fisher, it was called the von Mises – Fisher (vMF) distribution with the probability density function [139]:

$$f(x | \mu, K) = C_p(K) * e^{K\mu \cdot x}$$

With:

μ : Mean direction

K: Dispersion parameter

C_p(K): Concentration parameter

The vMF distribution as a criterion for clustering objects on a sphere has been confirmed and applied by many other researchers ([140], [141], [142], [127]). S. Priest [6] proposed a simple form of the probability density function:

$$f(\alpha) = \frac{K \cdot \sin(\alpha) \cdot e^{K \cdot \cos(\alpha)}}{e^K - e^{-K}}$$

and an approached function of angle:

$$\cos(\alpha) = 1 + \frac{1}{K} \cdot \ln(1 - P)$$

With:

α : Angle between a discontinuity and the centre of the family (rad or degree)

K: Dispersion parameter of Fisher law

P: Cumulative distribution value

The latter was used in the RESOBLOK code [137] for the calculation of the dispersion parameter of the distribution of discontinuities in the space. Moreover, they have demonstrated on a Fisher distribution of discontinuities orientation that, in a family, there are 95% of discontinuities for which the angle with the centre of the family is inferior to 20° [137].

2.2.4. Conclusion

The complex distribution of the discontinuities on the research rock mass has been synthetized by the procedure of discontinuity data processing. The discrete discontinuities are clustered into main families and each family is represented by its centre and its laws of distribution in the space. The procedure is executed in the following sequence:

- Firstly, the clustering is realised to group the discontinuities into main families. Within the three methods that have been presented above, the spectral method proposed by R. Jimenez-Rodriguez and N. Sita [130] is recommended thanks to its clear and robust methodology with the quick convergence in low time consumption. In this research, this methodology was rewritten on EXCEL and it was validated by the comparison with the published results of R. Jimenez-Rodriguez and N. Sita on the discontinuity data of the San Manuel cooper mine [130].

- Secondly, all the discontinuities in a family are represented by its unit normal vector and the centre of the family is given as the mean vector of all family members.
- Thirdly, the positions of discontinuities in each family on the scan-lines are represented by the semi-variogram and the obtained curve is compared with theoretical curves. The theoretical semi-variogram that is closest to the empirical distribution of discontinuities is taken as representative.
- Fourthly, the distance between two discontinuities of a given family on the rock face is studied by classifying the distance into different groups of length and the quantity of discontinuities in each group was counted. The statistical law that best fits to the empirical distribution of discontinuities is taken as the representative law.
- Fifth, the angle between discontinuities in each family and the centre of the family are calculated and the diversity of the angle magnitudes is classified into different groups. The probability curve of the empirical distribution of discontinuities is compared with the statistical law of Fisher and the closest function is taken as the representative law.

The achievement of this procedure is that the random allocations of discontinuities on the scan-line, the diversified distribution of each discontinuity family in the space are synthetized by the family centres and by the representative theoretical geo-statistical laws of distribution. Hence, the natural complex distribution of discontinuities in the rock mass is replaced by a series of logical operations that can be easily described by mathematical functions. This is an indispensable processing for the numerical modelling of the rock mass with the consideration of the presence of the rock structure. The combination of the first step of the *in situ* discontinuity measurements and the second one of the geological and geo-statistical processing can be called “the rock fracture mapping” that was described by Q. Feng [127] in three tasks:

- Capturing the fracture measurements in the field;
- Quantifying and analysis geometrical parameters of the fractures;
- Documenting and presenting the mapping results.

With the results from the first and the second steps of the methodology, the third step of the geometrical model generation on a DFN-based code can be started.

2.3. Geometrical modelling in 3D on RESOBLOK

At the end of the previous task, the rock structure of the rock mass has been replaced by the main families of discontinuities and represented by the family centres and the theoretical geo-statistical laws of distribution in the space. The results of those geological and data processing are used as the input data for this task. The DFN method is applied for the generation of the geometrical models of the rock mass by the use of the theory of D. Heliot [64] and the Block Generation Language (BGL) using on the RESOBLOK code.

In this part, the fundamentals of the block generation theory of D. Heliot [64] are presented. Next, the procedure of the creation of the 3D geometrical models is introduced as a step in our methodology on the RESOBLOK code. Then, this procedure is concretised in two specific cases in rock engineering:

- Geometrical model generation of a cylindrical specimen for triaxial compression tests;
- Geometrical model generation process of a multi-phase-excavated tunnel.

2.3.1. Block generation theory of D. Heliot

A discontinuity is analysed on two levels [64]:

- At a morphological level: a discontinuity is represented by a volume and the morphological variables are taken into account by only specifying the mechanical properties of discontinuities;
- At an architectural level: a discontinuity is represented by a line which is composed of small straight segments (for 2D generation) or small planar facets (for 3D one). There are, thus, two kinds of discontinuities: few isolated well defined ones and numerous statistically distributed ones.

The generation of a “blocky rock mass” according to D. Heliot [64] is the splitting of the initial block into new smaller blocks by the interaction of the isolated discontinuities and/or the main families of discontinuities. The generation of the rock mass by the simulation of discontinuities families, one after another, aims at taking into account the chronology of tectonic episodes that gave birth to their related discontinuities families. However, the final result of the generation of the rock mass, with the presence of all families, might be not really dependant on their appearance orders. The mentioned chronology is only important when a principal family takes influence on a minor family by the termination or

continuation of the latter after the intersection with the former. The professional observations of the geologists during the sampling investigation should be thus paid attention to, for giving and supporting the judgements on the hierarchical organization of the discontinuities on the rock mass.

2.3.1.1. “Block database”

The block generation is based on the construction of the “block database” that contains the definition of the zone of interest, the block geometry and the discontinuity properties of the rock mass. The zone of interest is defined in the form of a rectangular parallelepiped of which the 3D perpendicular global reference is given with respect to the geo-reference of the X axis from West to East, the Y axis from South to North and the Z axis opposite to the gravity direction.

A rock block is represented by a convex polyhedron that is defined by:

- the coordinates of a point inside the polyhedron (called the centroid of block);
- the sub-zone of the zone of interest to which the block belongs;
- the list of vertices of the polyhedron;
- the list of faces of the polyhedron;
- the group to which the block belongs;
- and the state of the block: active, inactive or to be removed.

A face of a polyhedron is the contacting face between two neighbouring blocks or between a block and the boundary of the zone of interest. A discontinuity is described by:

- the plane to which the face belongs;
- the family or the isolated discontinuity to which the face belongs;
- two related blocks;
- and the state of the face: on the boundary of the zone of interest or not, on the external boundary of the block or inside a non-convex block.

Meanwhile, a plane is defined by the indices (a, b, c, d) that are expressed by the equation of $ax + by + cz = d$ of which $a^2 + b^2 + c^2 = 1$ and $d > 0$. A plane separates the space into two half-spaces H_i^{Q+} and H_i^{Q-} .

A vertex of a polyhedron, a point, is defined either by its coordinates or by three planes of which it is the intersection. The vertices that belong to a same edge of a polyhedron have two common indices. This feature helps to quickly detect all the vertices of a face or of an edge. A vertex belongs to the upper half-space H_i^{Q+} if and only if:

- the distance from the vertex to the plane that created the half-space is null;
- or the sign of this distance is identical to the one of a vertex that does not belong to the plane.

A vertex belongs to the lower half-space H_i^{Q-} if and only if the sign of the distance from the vertex to the plane is opposite to the one of a vertex that does not belong to the plane.

The clustering of discontinuities is realised on the classification of their names and the mechanical properties which are described by specific values of the weight (for specifying the importance of the family), mean and dispersion (for specifying the distribution of the family).

The excavation is generated by the definition of “blocks of air” (proposed by [64]) in the relevant zone and configured by the convex polyhedral sub-zone of which the participant polyhedra are switched from the normal blocks to the “blocks of air”. The excavation is determined by the list of boundary planes and a point inside the sub-zone.



Figure 2.3.1: 3D model of a rectangle excavation and its vicinal blocky rock mass
generated on RESOBLOK

2.3.1.2. Algorithm for the block splitting

The basic algorithm for the splitting of the initial block into two new smaller blocks is given as follows:

- The initial block is defined by n planes P_i and a point Q . The plane P_0 (a_0, b_0, c_0, d_0) represents the discontinuity that will split the initial block;

- The polyhedron of the initial block is separated into three sub-polyhedra: the upper-polyhedron H^+ is described by vertices on the upper half-space H_i^{Q+} , the lower-polyhedron H^- is described by vertices on the lower half-space H_i^{Q-} and the middle-polyhedron H^0 is described by vertices on the plane P_0 that separates the two half-spaces;
- The cardinality calculation of the three polyhedral is executed. If $\text{Card}(H^-) = 0$ or $\text{Card}(H^+) = \text{Card}(H^0)$, the plane P_0 is concluded not to split the polyhedron. If else:
- All pairs of vertices that belong to both sub-polyhedra H^+ and H^- and have two common indices are found and the common edge between them is achieved. Hence, a new vertex is created between two initial vertices and belongs to the two new smaller blocks;
- The coordinates of the new vertex and of a point inside each new polyhedron are computed;
- The common vertices and faces of the two new polyhedra are duplicated;
- The list of vertices and the list of faces that described the faces of the new smaller blocks are rebuilt.

2.3.1.3. Algorithm for the discontinuity generation

The discontinuity network is simulated by the following algorithm:

- From the reference point $O(0, 0, 0)$ along the orientation of the central vector of the family, the succeeding perpendicular sampling of which the magnitudes are described by the law of spacing distribution of the family is created to define the local discontinuity plane;
- The centroids of each group of blocks are projected onto the orientation of the central vector of the family at a random distance from the reference point;
- The extent of discontinuity is generated by the splitting of all blocks in groups at the same time.

The random distances from the reference point in the projection of the centroids of blocks in the generation of discontinuities in the model are then controlled by the number of scenarios that is defined by the users. Each scenario which is initiated giving to a specific distance creates a specific generation of rock blocks in the model.

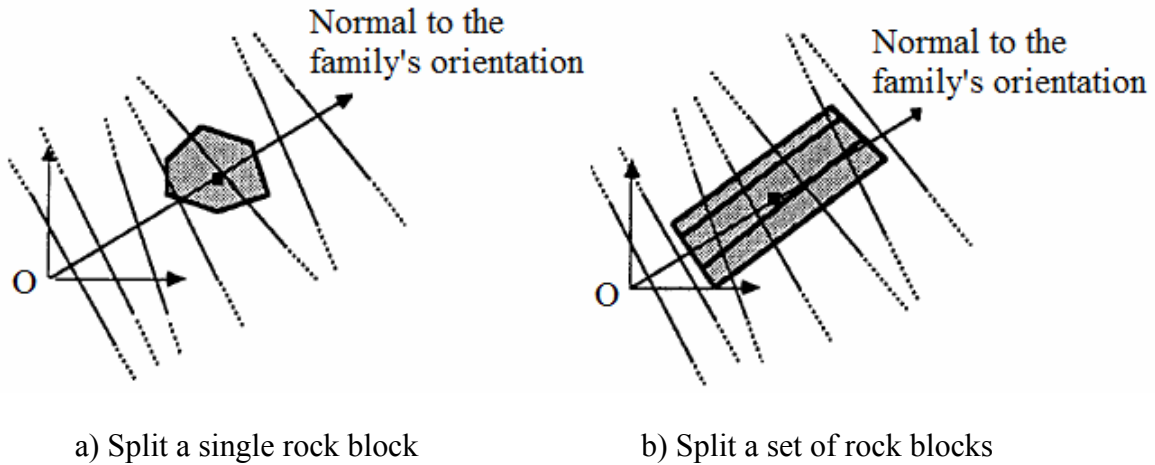


Figure 2.3.2: Simulation a family discontinuity (sourced from [64])

2.3.2. BGL written on RESOBLOK

BGL is the numerical tool for writing the rock database and the generation algorithms in a scenario and then interpreting by the computer language C to generate the geometrical models of the rock mass. Written on BGL and belonging to LAEGO (Laboratory of Environmental Geo-mechanical Works) and INERIS (National Institute of Industrial Environment and Risks) at the “*Ecole des Mines de Nancy*”, France, RESOBLOK is a code dedicated to fractured rock media and integrates the capacities of 2D and/or 3D geometrical model generation and stability analysis.

The display of the created geometrical model of the rock mass is executed by [64]:

- Firstly, the zone of interest is displayed with three visible faces;
- Then, three cross-sections that are perpendicular to the three axis of the global reference are projected on those three faces. The positions of those cross-sections on the relevant axis may be different.

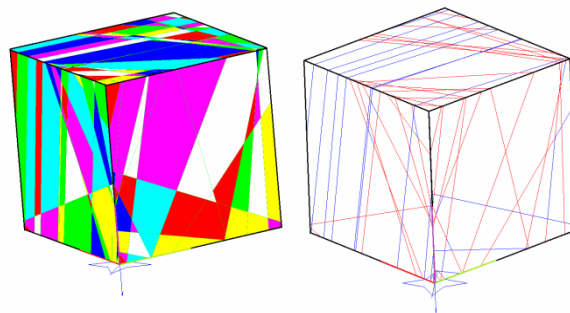


Figure 2.3.3: Display of the 3D model and three perpendicular cross-sections of a rock mass on RESOBLOK

In our knowledge, RESOBLOK is a robust code that can generate either 2D or 3D fractured rock models. It is also a smart choice for a quick stability analysis of a rock mass including the rock strengthening (rock dowels or rock bolts) for the medium. For the demand of further analysis with higher accuracy, it is recommended to export the initial results of modelling and analysis to a more specialized mechanical analysis code.

2.3.3. Geometrical modelling in 3D of a fractured rock object

Based on the experiences obtained during our research, a procedure for creating 3D geometrical models of the rock masses using RESOBLOK is proposed.

2.3.2.1. Model generation

The configuration of the model and its geological characteristics are written in BGL in a scenario file *.sc. By executing the BG module on this file, a 3D model of the rock mass is created. The order of presentation in this sub-section follows the typical architecture of our scenario files. All relevant syntaxes and their details can be found in [64], [137].

a) Configuration of the rock mass

First, the dimension of the total rock mass is required. At this moment, the total rock mass is always in the form of a rectangular parallelepiped whose dimensions are given by three perpendicular coordinates. The smaller the medium is, the limited zone of the real rock mass can be modelled. Hence, the numerical representation of the discontinuity distribution on the modelled rock mass is probably less precise which can lead to the underestimation of the stability of the medium but helps to reduce the computing time. The selection of the dimension of the model must also take into account the presence of the future tunnel situated in the numerical rock mass. Normally, the thickness of the surrounding medium in the vicinity of the tunnel should be about 5 times of the radius of the future tunnel. However, when the model size augments, the time consumption and the required robustness of the calculation may become a challenge. The orientation of the rock mass is set by giving the orientation of the X axis.

Next, one needs to assign the minimal volume of rock blocks that can be generated inside the rock mass. By default it is set to be null by the code, the smaller it is, the more rock blocks appear. A suitable large value of this parameter helps to reduce the “powder clouds” in the rock mass and lightens the analysis afterwards.

Then, if the rock mass is not homogenous, it can be divided into various zones separated by

flat boundaries. In general, a domain must be convex. Otherwise, it must be created by an assembly of convex sub-zones.

Once the configuration of the rock mass has been fixed, the structure of the rock mass is described by the main families of discontinuities or by the isolated fractures. Each discontinuity family is statistically declared as follows:

- The family centre: represented by the directional vector $\{\beta_d, \alpha_d\}$ of the centre with $\beta_d = [0, 90^\circ]$, $\alpha_d = [0, 360^\circ]$;
- The orientation distribution of the family: represented by the dispersion parameter K of the Fisher law;
- The distance distribution of the family: represented by a statistical law among the Laplace-Gauss, the exponential, the uniform, the lognormal and fractal laws;
- The extension of the family at the intersection with other families: “SET” for maintaining the discontinuities after intersecting all other families; “BLOCK” for the interruption of the discontinuities after the intersection with all other families; “FAMILLE_x” for stopping the current family when crossing the family x .
- There is only one tendency of development in the family. Otherwise, several families with the same orientation but different tendencies should be declared.

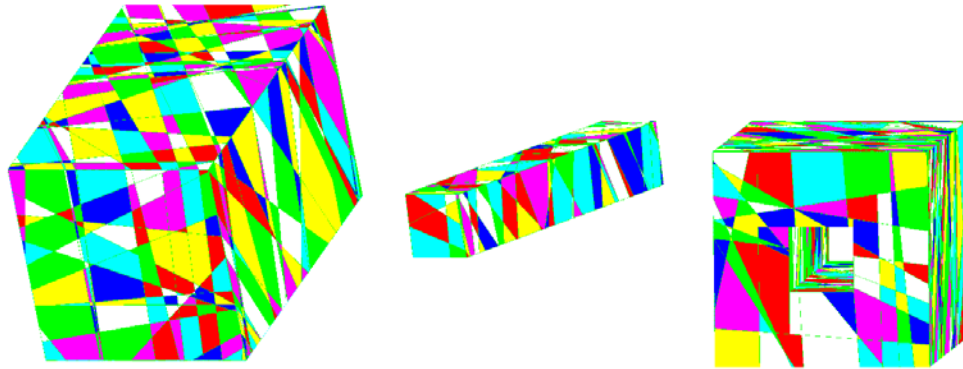
A free or isolated fracture can be defined as a polygonal line that is declared by their configuration or represented by a statistical law or the Poisson process. For a clear graphical representation, each family or isolated fracture should be assigned a specific colour.

b) Configuration of the tunnel

The tunnel is created as an “excavation” inside the rock mass that has been defined in the previous part. The cross-section of the tunnel, convex, is created by a set of straight plans (for simple configuration) or polygonal lines (for complex one). Segments in arc of a polygonal plan are the connexion of tangential planes of the inscribed circle. On the longitudinal direction, the configuration should be regular in each segment. However, if the model has the shape of a rectangular box, it will be more simple to directly define it as a rock mass as in the sub-section a.

The model of the created “excavation” can be exported separately from its rock mass. Hence, by selecting the target object for the data exportation, three different models can be generated from the same scenario file from which an excavation is declared. They are:

- the total rock mass without the excavation;
- the excavation;
- the rock mass that is holed by the excavation.



a) The rock mass “without hole” b) The excavation c) The rock mass “with hole”

Figure 2.3.4: Three models exported from a scenario file in RESOBLOK

c) Geotechnical characteristics of the model

Because RESOBLOK is applied in our methodology at the step of the geometrical modelling creation, the geotechnical characteristics of the model are not necessary. However, for exploiting the quick stability analysis capacity of RESOBLOK as the criterion for selecting an interested generation of the rock mass following a given criterion, this task is recommended. (A detailed presentation of the selection of wanted simulations is placed in the sub-section 2.3.2.3).

The geotechnical parameters of the rock structure (the friction angle, the cohesion and the stiffness of the discontinuities and the isolate/free fractures, *etc.*) and those of the rock material (the density, Young modulus *etc.*) are needed. Among them, some are required and some are optional. The nature of the given parameters is declared as a Boolean, entire, real value or represented by a statistical distribution. If the statistical distribution form is chosen, the Kernel function is applied for the declaration. Each parameter is then chosen to be active on the whole model, in some zones of the model or with certain families of discontinuities or free fractures.

2.3.2.2. Various simulations of a model generation

By choosing the simulation number $N > 0$ before executing the model generation in the module BG, various cases of the structure of rock blocks inside the model are created. RESOBLOK “uses a series of random numbers to generate different block assemblies from the same scenario file” [12]. The bigger the simulation number N is, the more comprehensive the generation is. The limitation of the computer is suggested to be taken into account. When the generation is fulfilled, N different simulations of a model are achieved. Moreover, even in a simulation, by changing the extension conditions of a family of discontinuities or a free fracture in the model, many “sub-simulations” can be obtained:

- when all families are continued after the intersections with other families;
- when all families are terminated after the intersections with other families;
- when a family is blocked after the intersection with another family.

As aforementioned, each discontinuity family is often linked by a specific tectonic episode. The predomination of a family over another might be a consequence of a stronger geological action with longer effects in comparison with the rest. Hence, the data reference to the structural geological conditions and historical documents of the region where the *in situ* investigation was carried out and to the professional judgements about the measurement works are needed to well select the appropriate cases of simulation.

2.3.2.3. Selection of a representative simulation by the stability-analysis-based statistics

By declaring the simulation number N in the model BG, numerous simulations of the same scenario file are created. When only a limit number of geometrical models of this step can be used as the input data for the next step, how to choose a “good” simulation is a challenge. A strong advantage of RESOBLOK is the speed in the stability analysis of the fractured rock model by the limit equilibrium computation [12]. For this reason, a quick stability analysis for N simulations of a scenario file is proposed for the preliminary selection of generated geometrical models. The aim of this task is, based on the stability analysis results, to find out the special cases among the generated simulations followed a given criterion and to use them as the representative models of the rock mass for the next steps of the methodology.

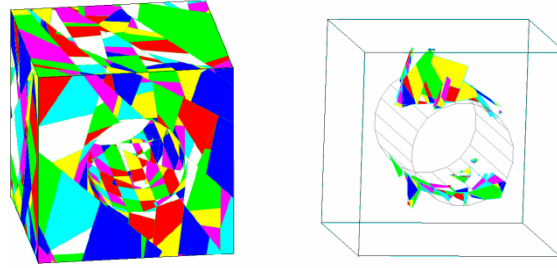
The stability analysis on RESOBLOK is the application of the Key Block theory of P.M. Warburton [20] for the kinematic analysis of the rock mass and the vicinity of the tunnel

inside the medium. Four main phenomena of failure of a rock mass are needed to be checked: the falling under the gravity, the plane sliding, the wedge sliding, and the toppling instability. The stability analysis procedure in RESOBLOK is realised in two stages as published by V. Merrien-Soukatchoff *et al.* [12]:

- Geometrical analysis: the geometry of each block is examined under the kinematic criteria of four mentioned failure phenomena to determine two groups of blocks:
 - o Irremovable blocks (or kinematic non-feasibility): blocks that cannot be removed due to their geometry and the direction of the driving forces;
 - o Removable blocks (or kinematic feasibility): blocks can possibly move. The removable blocks are checked in rotation by using the vectorial conditions proposed by D. Lin and C. Fairhurst [143].
- Mechanical analysis: this stage is executed on the stable blocks after the rotation check of the previous stage. Three types of the potential movements of rock block are examined:
 - o Free falling due to the gravity;
 - o Movements parallel to one or two faces of blocks: A limit equilibrium analysis is realised with the need of the following parameters: the cohesion, the friction angle of the discontinuities and the block density;
 - o Movements parallel to more than two faces of blocks: An energy-based analysis is realised with the additional need of the normal and shear stiffness of the discontinuities.

Two modules BSA and BSAH of RESOBLOK are used for the stability analysis of N generated simulations. Assuming a zero tensile strength of the discontinuities, the stability of the medium is checked with the consideration of four mentioned phenomena of failure. A block in the vicinity of the tunnel is considered to be unstable when it is:

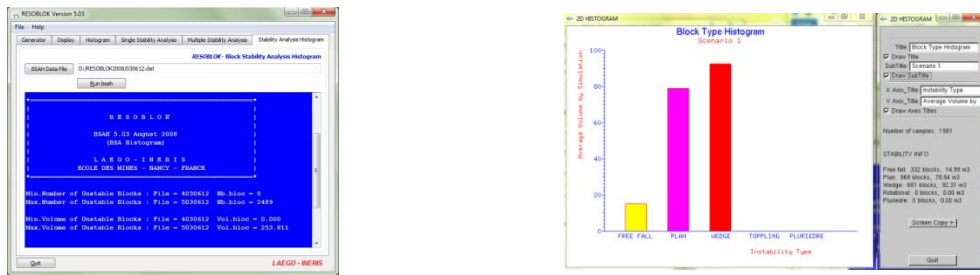
- free falling due to the gravity;
- sliding on one or two faces;
- rotation check failed;
- limit equilibrium analysis failed (alternative);
- energy-based analysis failed (alternative).



a) Rock mass b) Unstable rock blocks around the opening

Figure 2.3.5: Stability analysis of a rock mass with its opening on RESOBLOK

The analysis is continued by the replacement of new adjacent blocks into the empty zones caused by the falling of the unstable blocks until no more unstable blocks are found and the analysis results are obtained. With the integrated statistics option of the code, the results can also be presented as statistical data in graphs (histogram, correlation curves) and data output.



a) Critical simulations and their details b) Histogram of unstable blocks

Figure 2.3.6: Statistical data of the stability analysis of a rock mass using RESOBLOK

Among them, the variation in the average number and volume of unstable blocks versus the number of simulation was underlined since V. Merrien-Soukatchoff *et al.* [12] recommended taking the simulation when the gradient of those curves became quasi-null as the last simulation that needs to be realised. The quantity of 50 simulations was proposed for a reasonable analysis of the rock slopes [144]. Followed the suggestion of the authors, with the geological data of the white marble at Saint B  at (Haute Garonne, France), we generated several scenarios of a numerical rock mass with a circular opening and analysed them in 100 simulations on RESOBLOK. The mentioned curves of variation obtained from this analysis were built and the Figure 2.3.6 is an example.

The other curves are presented in the Appendix B. From those curves, we found that:

- At the 50th simulation, the gradient of the curves were not stable so that it was needed to continue the simulation;
- From the 70th simulation, the two curves became stable. The value of their gradients was nearly unchanged.

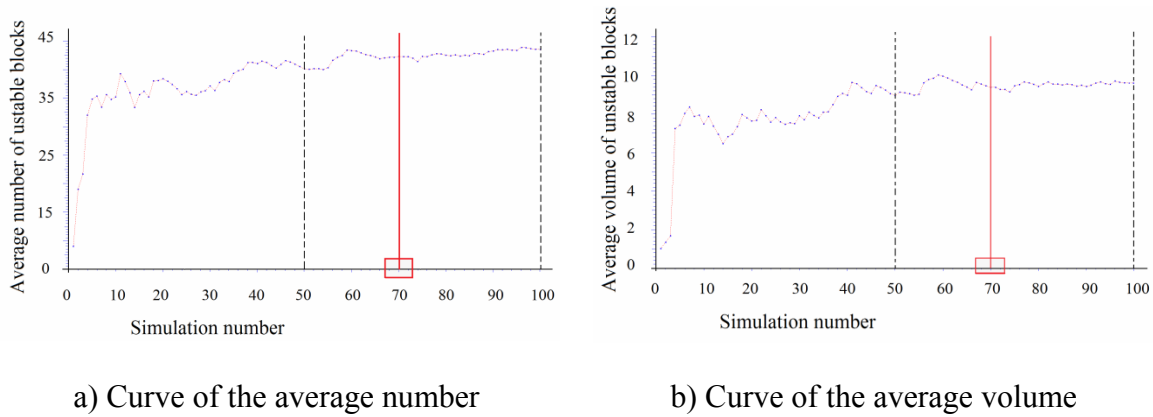


Figure 2.3.7: Variation in the average number and volume of unstable blocks versus the number of simulation of a modelling for the marble of Saint Beat on RESOBLOK

The quantity of about 70 simulations was thus more reasonable for the tunnel analyses on RESOBLOK than the suggested value in [12], [143]. However, when repeating the task with the quantity of 20 simulations for each rock mass, nearly the same critical simulations were found (refer the section 3.4.5 in the next chapter). Due to the limitation of the real data for the reliable validity of this phenomenon, the final judgement of the suggested number of simulation for a reasonable generation in RESOBLOK was not given.

After the determination of the sufficient quantity of simulations for the analysis, the stability analysis of the generated simulations is realised and compared on the statistically treated data. On those statistical results, some critical cases of N simulations can be found such as:

- the maximal and minimal quantity and/or volume of total unstable blocks;
- the maximal and minimal quantity and/or volume of unstable blocks in a specific phenomenon of failure.

It is recalled here that in the scope of the 3rd step of our methodology, the stability analysis is not the final goal. This stability calculations and their statistical summary serve as a criterion of the selection for the critical cases of the composition of rock blocks of the model following the theory of P.M. Warburton [20]. It is worth noting that this selection

may lead to the inappropriate stability analysis of the model since the selected cases are critical but not necessary to be the closest to the observed behaviours of the real rock mass. Hence, further research is hoped to be continued to head for a selection guide for the “right” representative models of the real rock mass.

Since “kinematics” is the study of movement without considering the cause of the motion, the stability analysis on RESOBLOK is limited to the application of the gravity. The consideration of the rock natural stresses in the vicinity of the tunnel in the analysis is possible but after the first iteration, their influence is nearly ignorable due to the redistribution of stress in the model [12]. In the scope of our knowledge, this is a limitation of the analysis capacity of REOBLOK for tunnel applications. It is thus needed to study more precisely and in a more detailed way on the mechanical behaviours of the model. Friendly interacted with different DEM-based codes (UDEC, 3DEC, HYDRO and LMGC90, more precisely) and with a popular graphical tool such as AutoCAD, the results of geometrical models, preliminary stability analysis from RESOBLOK can be exported and exploited by other more comprehensive codes for the discrete simulation and mechanical analysis.

In the following step of the methodology, the generated models, which have been created by RESOBLOK and exported as the files *.dat, are immersed in the Pre-Processor of LMGC90 as the input data for a comprehensive DEM-based analysis of the mechanical behaviours of the models.

2.3.3. Geometrical modelling in 3D of a cylindrical specimen for the triaxial compression tests

Aimed to simulating a conformed monotonous classical triaxial compression test in rock mechanics, we referred to [145], [146] [147] and [148] for the generation of the specimen. The cylinder is the most regular shape of conformed specimens but no specific parameter was required except the slenderness ratio (*i.e.* the ratio between the height H and the diameter D of the specimen) must be between 2 and 2.5. For a real test in laboratory, concrete parameters of specimen are chosen due to the capability of available rock core drilling and testing machines. For instance, the MST 816 Rock test system (Regional Laboratory of Bridges and Roads of Toulouse, France) can test rock cores up to $H = 100$ mm and $D = 50$ mm [149]; or the triaxial Hoek cell TS 708/NX for a rock core of $D =$

54.75 mm [150]. Hence, the generation of a cylindrical rock core with $D = d$ (m) and $H = 2d$ (m) was our goal.

For the creation of that specimen, a rock mass in the rectangular parallelepiped zone of interest $2d \times 2d \times 2d$ (m) was declared. The characteristics of the rock material and the rock structure where the target rock specimen had been found were assigned. In the middle of this model, a cylindrical excavation with the diameter $D = d$ and the length along the longitudinal axis $L = 2d$ was created. The longitudinal axis of the excavation was the vertical axis of the specimen. The procedure of the model generation followed the aforementioned principals given in the previous part.

It is noted that the stability analysis of RESOBLOK is executed at the vicinity of the excavation to check if the rock blocks outside the excavation are unstable due to the “disappearance” of the rock block inside the excavation. For this application, one only needs the rock core that is generated by all blocks situated inside the excavation. Since the stability analysis of the external zone does not take sense to our target model, the preliminary selection of the generated models is neglected. The zone inside the excavation of the model is exported to LMGC90 in a file *.dat and immersed into the Pre-Processor of this code to reconstruct the generated model on RESOBLOK before the realisation of detailed mechanical analyses.

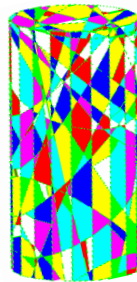


Figure 2.3.8: Model of a conformed cylindrical specimen generated on RESOBLOK

2.3.4. Geometrical modelling in 3D of the excavation process of a tunnel

The procedure of fractured rock model generation in the previous sub-section is concretized with the aim of the modelling of a tunnel excavation process. Assuming that the future tunnel will be excavated in K phases versus time with the length of the i^{th} segment is L_i (m). K , i are positive real numbers and i is varied from 1 to K . The excavation length L_e^j (m) at a moment j of time is given by:

$$L_s^j = \sum_{i=1}^j L_i$$

The total length of the tunnel $L(m)$ is given by:

$$L = \sum_{i=1}^K L_i$$

Three approaches for generating the geometrical model of an in-progress tunnel excavation are proposed:

2.3.4.1. Approach 1

A rectangular parallelepiped rock model was created with the characteristics of the rock material and the rock structure of the rock mass. The model “without hole” was exported in a files *.dat and imported in the Pre-Processor of LMGC90.

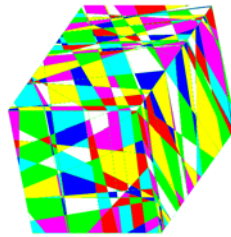


Figure 2.3.9: Model “without hole” of a fractured rock mass

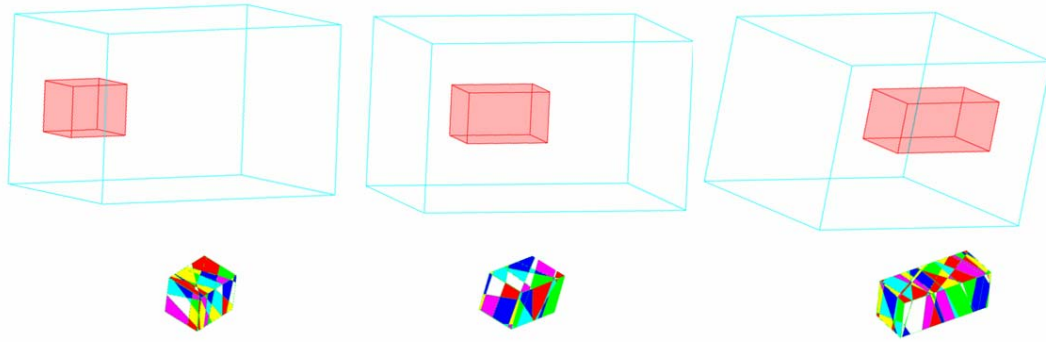
2.3.4.2. Approach 2

In the first scenario file, a rectangular parallelepiped rock mass with the characteristics of the rock material and the rock structure of the rock mass was generated. An L_1 -metre-long-excavation was generated in the middle of the rock mass. It was situated along the longitudinal axis of the future tunnel with the coordinated $Y_1 = [0, L_1]$. The rock mass was holed by the presence of the L_1 -metre-long-excavation and becomes the model 0 “with hole”. Two zones of the rock mass were exported to LMGC90 in two files *.dat: inside the excavation (model 1) and the surrounding medium (model 0 “with hole”).

In the second scenario file, a same rock mass as in the first one was created. An L_2 -metre-long-excavation was generated in the middle of the rock mass. It was situated along the longitudinal axis of the future tunnel with the coordinated $Y_2 = [L_1, L_2]$. Only the model of the excavation (model 2) was exported to LMGC90 in a file *.dat. The task in the second scenario file was repeated in some scenario files until the L_K -metre-long-excavation which

was situated along the longitudinal axis of the future tunnel with the coordinated $Y_K = [L_{K-1}, L]$. Those 3^{th} to K^{th} excavation models were exported in K-2 output files *.dat for immerging in the following step in LMGC90.

In total, there were one model of the rock mass “with hole” (model 0) and K models of the excavation with the length of L_i , $i = [1, K]$.

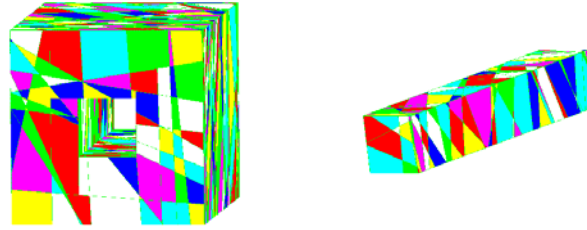


a) In the 1st scenario file b) In the 2nd scenario file c) In the 3rd scenario file

Figure 2.3.10: Excavation models in three continuous scenario files of a 3-phase-excavation

2.3.4.3. Approach 3

The first model was a rectangular parallelepiped rock model with the characteristics of the rock material and the rock structure of the rock mass. The second model was an excavation that was located in the middle of the first model. It had exactly the same configuration with the future tunnel. With the presence of the second model inside the first model, the first model became holed and the total rock mass is divided into two zones: inside the tunnel (model 2) and the surrounding medium (model 1 “with hole”). The length along the longitudinal axis of the future tunnel of the second model was $L(m)$. The generation data of the model 1 “with hole” and the model 2 were exported as two output files *.dat for immersion in LMGC90 at the following step. It is easily understood that the tunnel model (model 2) in the 3rd approach is the sum of K excavation models of the 2nd approach. So the excavation algorithms of these two approach are nearly the same except the segmentation procedure is done in the geometrical modelling step by RESOBLOK (in the case of the 2nd approach) or in the advanced simulation and analysis step by LMGC90 (in the case of the 3rd approach). The excavation algorithm of 1st case will be totally done by LMGC90. The excavation progress will be designed in LMGC90 and the details of a typical assumed construction sequence are presented in the section 2.4.



a) Model 1 (the rock mass “with hole”) b) model 2 (the excavation)

Figure 2.3.11: Model 1 and model 2 of a fractured rock mass from a scenario file

2.3.5. Conclusion

The block generation theory of D. Heliot [64] is based on the splitting of the initial zone of interest into an assemblage of rock blocks by the intersection of the main discontinuities families and the isolated fractures. It was considered as a polyhedral detection algorithm incorporating with the statistical representation of the rock structure [67]. The data treatment on the distribution of the discontinuities in the rock mass permitted the representation the rock structure on the whole rock mass by using the collected data of some limited regions of the rock mass. The probabilistic and statistical forms of the distribution laws of the discontinuities took into consideration the spatial organization of the discontinuities families. Another strong point of this methodology is the proposition of the participation of the tectonic history of the rock mass in the generation of its model aiming at the maximum use of the collected data of the discontinuities [65] and geologist observations. The BGL is the transformation of the theory into a computer language. It was used to build the rock generations in RESOBLOK code dedicated to the generation of the 2D/3D graphical representation and stability analysis of the fractured rock mass. We utilised the version V5.03 of RESOBLOK with several different sub-versions on Window and Ubuntu environment to create the 3D geometrical models of the rock mass in our methodology. The quick stability analysis based on the “Key blocks” of P.M. Warburton [20] on RESOBLOK helped to preliminarily select the most critical cases among the generated simulations of the same scenario. They are exported to be more accurately and comprehensively analysed by some other DEM-based codes: among them we choose LMGC90. The generated models on RESOBLOK were exported to be reconstructed on LMGC90 for the comprehensive simulation and analysis of the mechanical behaviour of the modelled rock. The combination of the two codes was found to be relevant.

2.4. Mechanical modelling of the rock mass

Through the brief introduction of the nature of the rock mass in the first chapter, the complexity and diversity of the mechanical behaviour of the rock mass were presented. However, even in the most serious research on a rock mass, one cannot ensure that the rock behaviours are properly controlled. Rock engineering is an interesting but difficult task when the objects of study possess unexpected characteristics, or exhibit accidental phenomena that might be challenging. The determination of an appropriate model of the mechanical behaviour of rock is thus an important task for the rock study. This is an important segment of the characterization of the rock mass that has been mentioned in many guides and technical specifications of the construction in rock media.

M. Potsch *et al.* [151] suggested executing the relevant task as a two-step procedure:

Describe the geological model and define the important geotechnical relevant parameters for each model. Several models of the rock mass were set on the difference of selection of those parameters and on the specific conditions on the construction procedure.

- Evaluate the potential rock mass behaviours considering each model of the rock mass to define the specific behaviour types of the rock mass.

The authors [151] also proposed a procedure for the determination of behaviour models based on the Austrian guideline for the geo-mechanical design in 2001, for tunnel purposes, as follows:

- Set up the basic structure of the computational model: The 3D geological model is cut into slices along the considered tunnel alignment. The key geological parameters, the boundary conditions and the important factor are assigned to the each slice. The analysis is realised on each slice with respect to the response of the current model of the rock mass to tunnel excavation under the corresponding important factor. Different analytical calculation models are simultaneously applied.
- Probabilistic data processing: In probabilistic simulations the deterministic values of the input parameters are replaced by statistical distributions. The results are also obtained in terms of statistical distributions.

The excavation and support methods of the tunnel are decided based on the rock behaviour model of the project. The monitoring during the excavation and its data evaluation are also based on the type of the selected models.

In the previous step of our methodology, the 3D geometrical model has been generated. It will be immersed into the Pre-Processing of the LMGC90 for the targeted simulation and analysis. The downstream procedure can only be continued after the choice of the equivalent mechanical model which is the objective of this step. Based on the own features of the generated geometrical model and the NSCD-based solutions for the analysis, we proposed the following procedure:

- Choose the mechanical models of the rock;
- Select the contact laws between the discontinuities and blocks;
- Determine the relevant geotechnical parameters.

The first and second steps are based mainly on the theories in rock engineering; on the documents of case histories of the similar rock masses and projects; and on the pretensions of the research. The laboratory and *in situ* measurements were required for executing the third one. The research on the case histories and the collection of the technical data related to the object of study were also involved.

2.4.1. Models of the mechanical behaviours of the rock

The mechanical behaviour of rocks depends firstly on the nature of the rock and its real existence conditions; and strongly on the loading conditions (*i.e.* pressure, temperature and strain-rate). The terminology “mechanical model” can be understood as the representation that can appropriately account for the mechanical behaviours of the object. The “mechanical model” can reflect several aspects: the mathematical expression, the principal mechanical characteristics following a specific criterion, *etc.* Hence, some groups of mechanical models can be found. They can be used either independently or in the combinative form according to the purposes and the scope of the research.

2.4.1.1. Classification based on the deformation capability of rock

This category is based on the deformation capability of rock in its natural state and/or under the load applications. There are two bulk behaviours that can be used for characterizing a rock mass:

- The rocks are considered as rigid (or incompressible) when there is no deformation of the rock under the application of external loads. They always have their rotational and/or translational displacement but their configurations (surface, volume) do not change during or after the loading period.
- The rocks are deformable (or compressible) under the application of external loads. Their responses are characterized by the displacement and the alteration of the configuration.

2.4.1.2. Classification based on the restitution capability of rock

This category is based on the restitution of the rock mass under the application of the loading conditions. Hence, one can find the link between this category and the deformable behaviour that is mentioned above. In general, a rock can show one of four main models of the mechanical behaviour as follows [152]:

- When the temperatures and the applied pressures are low with the rapid strain-rates, most rocks show the elastic behaviour. The stress-strain relation is linear. The slope of the stress - strain curve is the elastic modulus E of the rock;
- When the temperatures and the applied pressures are more elevated, the rocks show the plastic behaviour. The deformations are large while the stresses exceed the yield point of the rocks. The strain is not recoverable and the deformation is permanent;
- When the rocks behave as flowing fluids, the rate of deformation or strain is controlled by the applied pressures, the rocks show the viscous behaviour;
- The elasto-plastic behaviour of rocks is considered as the combination of the elastic and plastic behaviours. This model of material behaviour is widely the most applied to characterize rocks.

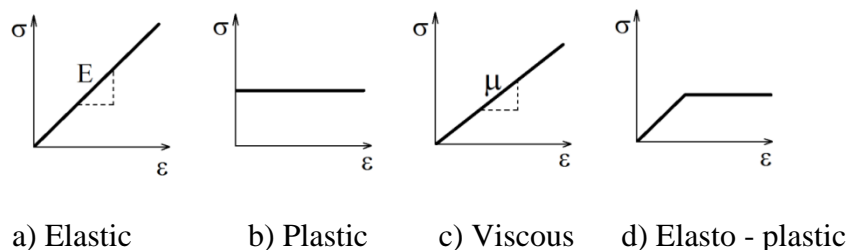


Figure 2.4.1: Stress-strain curves of the four deformable models of rock

2.4.1.3. Classification based on the characteristics of the stress-strain relation curve

Based on the correlation between the elastic and non-elastic strain of the rock and the tendency of the stress-strain curve during the loading, the mechanical behaviours of rock can be categorised into two classes [154]:

- Class I: when the increasing rate of the non-elastic strain is faster than the decreasing rate of the elastic strain. The gradient of the stress-strain curves are positive in the post-failure region.
- Class II: in the opposite case of the type I. The gradient of the stress-strain curves are negative in the post-failure region.

C. He *et al.* [155], through the unloading-reloading uniaxial compression tests conducted in the post-failure region, concluded that the biggest difference between the two classes is the increasing rate of non-elastic strain. However, the elastic strain decreases in the post-failure region while the load-bearing capacity reduces in both two types of behaviour. In general, the non-elastic strain increases with the confining pressure while in the uniaxial compression tests, at the confining pressure, the non-elastic strain increases rapidly while the elastic strain decreases in the post-failure region. The rock behaviour thus changes from class II to class I at higher confining pressure.

2.4.2. Contact laws between the discontinuities and the rock blocks

Considering the presence of the rock structure in the rock mass, the generation of the rock model as an assemblage of rock blocks has been admitted. The contact between the neighbouring blocks is specified by the contact laws that are influenced by many aspects: the presence of water (dry or wet); the morphology of the wall (rough or smooth); the presence of the filling (friction and/or adhesion); the restitution of the contact; the contact nature (smooth or shock, elastic or non-elastic, with or without interpenetration); *etc.* The consideration should be paid to the observation of the real rock mass, the results of the *in situ* investigations, the research of the case histories on similar rock masses and projects. The pre-intentions of the research, the adaptation with the modelling tools, the correlation and combination with the geometrical models, *etc.* are also taken into account. Some mechanical theories can be also used to characterize the contact interaction between the neighbouring blocks [156]: Newton restitution law, Coulomb's friction law, derived Signorini Coulomb law, Mohr Coulomb law, Lennard Jones law, Hertz law, Moneri Acary Cangemy, *etc.*

With the intention of using the LMGC90 code for the simulation and analysis in our methodology, we suggested to apply the available contact laws proposed in the library of the code or to construct a new adapted law based on the exist laws for the declaration of the interaction laws in the model. There were the capacity of the coupling of some basic theoretical phenomena and the addition of the reinforcement structures in the rock mass by some special contact laws.

2.4.3. Measurements of *in situ* stresses of the rock mass

Once the mechanical model of the rock and the interaction laws between its constitutive blocks had been selected, the laboratory and the *in situ* measurements were required on the demanded parameters which characterised the rock mass. For instance, for the simplest definition of a rigid rock mass the density is necessary while at least the density, the modulus of Young and the Poisson ratio are needed for a deformable medium. Normally, the geotechnical characteristics of the rock material and the parameters of the rock structure can be measured by the laboratory tests on the rock cores drilled in the rock mass. However, the behaviour of the rock mass has been proven to be more complicated than the combination of the behaviours of the rock material and the rock structures. Furthermore, some geological aspects cannot be simply determined or estimated by laboratory tests due to the limitations of the specimen extraction, the capacity of the test machines and notably the separation from the natural location of the rock mass. Hence, the *in situ* measurement on rock masses is always considered as a key operation in almost all projects related to the rock media.

In general, one can classify the *in situ* measurement methods into three groups [157]:

2.4.3.1. Indicative methods

These methods are realised with the borehole drilling. In fact they are only stress estimation methods while one is not capable to directly measure the stress/strain inside the rock mass, at a large scale.

- The core dishing [158]: the cut of the horizontal drilling core into curve disks for the measurement of the horizontal stresses. It is normally realised during the overcoring procedure. The core disks are aligned with the direction of the maximal horizontal *in situ* stress. Several hypotheses on the mechanism of this measurement have been published, one of which is “the combination of the micro-crack formation parallel to the horizontal stress and unloading of the core in the vertical direction”.

- The borehole breakouts [158]: the imaging record of the borehole by dipmeters or borehole viewers to observe the breakout direction that is assumed to be coincident with the minimal horizontal *in situ* stresses. Hence, the orientation of the critical horizontal principal stresses and their orientation variation with the depth of the borehole can be estimated, but not the magnitude of the *in situ* stresses.

2.4.3.2. Field-based methods

The *in situ* stresses are measured by the disturbance of the *in situ* rock conditions with the induction of strains or with the opening of pre-existing fractures [157]. They are direct measurement methods for the stresses in the rock mass. They are based on the assumption that the rock mass is linearly elastic, homogeneous and isotropic in the zone influencing the measurement. There are some typical methods:

- Borehole relief methods: The *in situ* stresses are liberated by the relaxation of the vicinity of the measurement borehole bottom and measured by special tools (called “cell”) fixed there. There are two solutions:
 - Borehole slotting/doorstopper [159]: for measuring the 2D *in situ* stress in the borehole. The measuring cell is inserted in the flattened bottom of a borehole. A smaller core is drilled around the cell for isolating it from the rock mass in order to relief the stress in the bottom of the borehole. The core and the cell are then removed from the borehole.



a) Installation of the equipment



b) Rock cores removed from the big borehole

Figure 2.4.2: Overcoring measurement for *in situ* stress realised in the Cap du Mount (France) by INERIS on 04/10/2011

- Overcoring [159]: for measuring the 3D *in situ* stress in the borehole. In the flattened bottom of the big borehole, the smaller borehole is drilled. The measure cell is inserted and fixed into the smaller borehole. A core is drilled around the smaller borehole for isolating the cell from the rock mass in order

to relief the stresses at the boundary of the bigger borehole. The core and the cell are then removed from the borehole.

- Flat jack method: the cutting slots are created on the rock faces of underground opening that produce the deformations on the rock mass. The deformations are recorded and then the equilibrium of the rock mass is restored by inserting a flat jack in the slots. It is pressurized until all deformations vanish [158]. The method can be used only in the walls of the underground opening after the opening has been made, and it measures the induced stresses from which the *in situ* stresses are calculated [160].
- Hydraulic methods: A fluid pressure (normally water) in a test section is applied in a borehole isolated by packers until the rock fails in tension [157]. It can be carried out in vertical holes drilled from the surface or underground in holes drilled from tunnels (vertical, inclined or horizontal). The borehole direction is assumed to be coincident with the direction of a principal stress and the vertical stress is assumed equal to the overburden stress [160].

2.4.3.3. Core based methods

They are laboratory tests realised on the drill cores when they are removed from the boreholes. In fact they are indirect stress measurement technics. There are two main methods:

- Strain recovery methods [158]: based on the monitoring of the rock responses of the drill cores, the *in situ* stresses are inferred from the observed strains on the rock cores. In the inelastic strain recovery method, the direction of the principal recovery strain is assumed to be coincident with the direction of the principal stresses. The mechanical model of the rock is assumed to be viscoelastic in the unloading period. In the different strain curve analysis method, a hydrostatic pressure is applied on the cubic specimen created from the boring core. The responses of the specimen are measured and the principal *in situ* stresses are determined based on some assumptions.
- Kaiser effect methods: The mechanism of the methods is based on the stress memory effect of rock (or called Kaiser effect) [157]. The *in situ* stresses are estimated through the determination of the magnitude of the preceding normal

stresses applied on the rock cores in various directions [78]. There are two main solutions: the acoustic emissions and the deformation rate analysis.

2.4.4. Conclusion

The mechanical modeling of the rock was built by the selection of the mechanical model of the rock mass and the interaction laws of the rock structure. The required geotechnical parameters for the modeling are obtained from the data collection from the case histories and the related technical documents of the targeted rock mass; from the laboratory tests and from the *in situ* measurements. The last option has been always recommended for the research of rock media and is necessary for the design of the rock structures. It is realized directly on the targeted rock mass and supplies the specimens for many laboratory tests.

In our methodology, once the mechanical model of the rock mass was obtained in this step, it was used to describe and fulfil the geometrical model that had been created in the previous step to generate a full model of the rock mass. This model was ready for the simulation and analysis on LMGC90 to obtain the mechanical responses of the numerical rock mass. The success of the following task was strongly influenced by the appropriation of the two aspects of the model: the geometry in 3D and the mechanical behaviours. The proposed methodology was expected to be comprehensive and steadfast when the realisation is based on three main operations:

- Generation of the geometrical model in 3D;
- Definition of the mechanical model;
- Simulation and analysis of the discrete solution.

They were executed, with a strict correlation between them, while any assignment affect to not only its own operation, but also the following operations. In turn, the decision about any action was continued by the other actions. The final aim was suitable models of the rock masses that well represent the two phases of the medium and their mutual influences. The next part of this chapter is devoted to the presentation of the third operation of the methodology.

2.5. Discrete simulation and analysis in 3D on LMGC90

The previous steps have provided us the 3D geometrical models and the mechanical model of the rock mass with the consideration of the rock structure. The geometrical models which had been generated and preliminarily selected on REBOLOK were exported to LMGC90 under the form of data files *.dat to be immersed as pre-created models in the Pre-processor part of LMGC90. In this step, the use of LMGC90, a DEM-based code built on the NSCD method, for the discrete simulations and analysis of the rock masses is presented. The code imported the geometrical models from RESOBLOK to rebuild the objects, and then the mechanical data of the rock mass are given to set up the simulation for the analysis. Our research has been carried out using the Python interface of the development version of LMGC90, using the Fortran compilation – the open and not-for-profit LMGC90 platform.

2.5.1. LMGC90 – a robust DEM-based solution for discrete media

Developed at the LMGC laboratory and belonging to CNRS (National Centre for Scientific Research, France) and the University of Montpellier 2 (France), the LMGC90 code (“*Logiciel de Mécanique Gérant le Contact*” in French) is dedicated to the modelling of various kinds of interacting objects (in 2D or 3D) with complex mechanical behaviours. Written in Fortran, C/C++ and Python languages, LMGC90 is based on the NSCD method proposed by J.J. Moreau and M. Jean [38]. The method which has been introduced in the section 1.2.4 of the first chapter has been applied to the mechanical analysis of masonry structures and rock mass stability [161]. The principal of the discrete analysis of LMGC90 was interpreted by F. Dubois *et al.* ([162], [163], [164]) as the combination of:

- the Non-Smooth Dynamics framework;
- the implicit time integration;
- the implicit contact solver.

But it is also able to implement other complicated tasks such as the molecular dynamics, the explicit time integration and quasi-static evolution, *etc.* The fundamentals of the LMGC90 code can be expressed by the correlation between the components of the analysis procedure [164]:

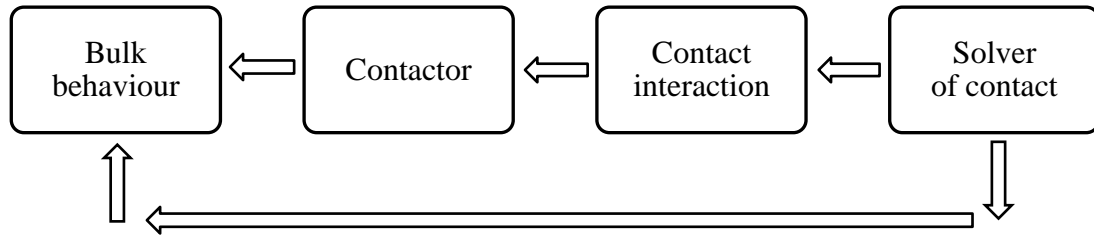


Figure 2.5.1: Analysis philosophy of LMGC90

A basic model on LMGC90 is characterised by ([162], [163], [164]):

- The shape: The objects of the model are 2D or 3D in the convex forms of various types that can be selected from the dictionary of the code. Each prototype is defined by its specific contact detection.
- The bulk behaviour: The objects are rigid or deformable. If they are deformable, they can be elastically linear or non-linear: hyper-elastic, viscous, plastic, *etc.* There are some other options: meshless, lattice, *etc.*
- The interaction laws: The basic frictional contact laws used in LMGC90 are, Signorini unilateral conditions involving the gap and the normal relative velocity, and Coulomb law. Besides, there is a choice of available laws in the dictionary of the code. The choice of a law is depended on the bulk behaviour of the contact couple (rigid-rigid, rigid-deformable, and deformable-deformable). These laws are expressed by the application of the Convex Analysis theory proposed by J.J. Moreau [39].
- Multi-coupling and multi-physics nature: The complex behaviours of the objects can be described by the combination of the thermal, fluid dynamic, hydraulic effects for normal or mixed objects.

Each object is hence defined by five necessary features: the material parameters, the physical model and the behaviour law, the interaction law, the visibility table of the contact and the avatar (physical object) [165].

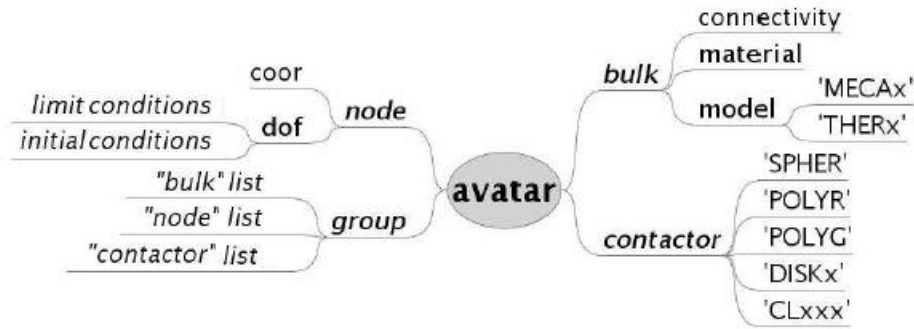


Figure 2.5.2: Description of a physic object on LMGC90 (sourced from [165])

The bulk behaviour of the object is assigned either by its inertia centre and its volume mass or by the mesh that is attached to the object. The fact that the objects in the analysis model need to be meshed in LMGC90 is the exploitation of LMGC90, a DEM-based solution on an advantage of the FEM. The surface or volume mesh created by this integrated option helps to compute the inertial mass of the objects. The meshing is required for the deformable objects and optional for the rigid ones. LMGC90 proposed several solutions for meshing an object:

- directly in LMGC90;
- via the integration of the GMSH code.

The configuration diversity of the contactors is one of the most remarkable advantages of LMGC90 over other DEM-based codes. This option helps the user to freely describe the object as its real appearance. For the rock masses, we proposed the polyhedron to be the representation of the constitutive rock blocks of the medium. It helps to well generate the vertices and the non-regular configuration of the rock blocks. One of the code strong points is its capacity to deal with thousands of objects, not necessarily convex, in dynamical detections.

The contact detection between two neighbouring objects (which are called the candidate and the antagonist) is described by:

- Contact locus;
- Local frame;
- Gap between two objects;
- Contact force and other options, if any.

The contact detection is a process consisting in three operations [53]:

- Neighbourhood construction: the determination of a space for the contact detection. It is based on the sort of closed bodies using the surrounding box or the tessellation method;
- Rough detection: the research of the neighbouring objects in the space determined from the neighbourhood construction;
- Accurate detection: the research of the contact points on the objects in the list of the neighbouring objects from the rough detection.

Different iterative solvers of contact are available in the LMGC90 [162]:

- Non-linear Gauss-Seidel (NLGS): use of all shapes of objects (2D or 3D) and supports all types of interaction law;
- Conjugate Projected Gradient Algorithm (GPCP): use of all shapes of objects (2D or 3D) but only supports some types of interaction law;
- Bi-potential: very close to the NLGS solve;
- Interface with the external solvers from other analysis codes.

Once the simulation has been set up correctly, the analysis and post-processing of the results can take place. According to the demand, the related commands which can be chosen from the library of commands and post-processing demands are written and organised on three downstream command files of which the 1st and the 2nd are necessary while the 3rd is optional:

- The first one generates the model configuration, meshes it if need, defines the limit and loading conditions, contact conditions, *etc.* The limit conditions of the model are declared by the definition of imposed values of the DOFs and the loading conditions are defined by two options: initial velocity and initial force. They can be assigned as a constant value, described by a function of time or by an evolutionary data file. This command file works on the data from the Pre-Processor.
- The second file executes the simulation and analysis, and records the demanded results. In this file, the parameters of the iterative solver and of the analysis are declared and the analysis targets are defined with the relevant commands. This command file works on the results of the 1st file.

- The third file performs some specific analysis at certain time intervals with a new, user defined, time scale (different from the one of the 2nd file) or allows to continue the tasks of the 2nd file for a new working period, without the need to rerun the 2nd file. It works on the output of the 2nd file.

Here, another feature of the FEM exploited on LMGC90 is the characterization of the 3D objects (*i.e.* element nodes, blocks) by the setting of its DOFs: a thermal object has 1 DOF, a deformable object has 3 DOFs, a porous object has 4 DOFs and a rigid object has 6 DOFs.

It should be noted that the time consumption of the analysis, the robustness of the calculation tool with its available memory is dependent with the complexity of the analysis, the object quantity of the model, the parameters of the iterative solver of contact and other calculation parameters. Once the simulation and analysis are realised, the mechanical responses of the objects in the model are recorded into two categories:

- Algebra data in multi column text files *.dat for data processing can be dealt with any spread sheets;
- Graphical visualization files *.vtk for 3D displays by the PARAVIEW code.

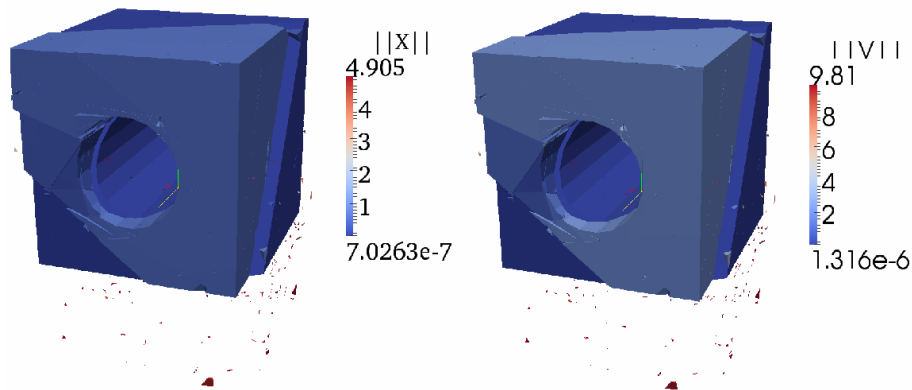


Figure 2.5.3: Failure mechanism of a numerical tunnel simulated on LMGC90

Notation of Figure 2.5.3:

$||X||$: Displacement (m)

$||V||$: Velocity (m/s)

In our methodology, the LMGC90 model setting up began with the processing of the *.dat exported files from the RESOBLOK code into the Pre-Processor after the meshing by GMSH. The skin of each block that constitutes the medium was automatically meshed by this integrated script to obtain a meshed rigid polyhedron [166]. In the scope of this

research, the rock blocks were rigid and the rock mass was fractured in 3D space, without the presence of hydraulic, thermic or multi-physics coupling conditions. The most fundamental contact type to be applied was the dry friction contact following the law of Coulomb. The contact detection was PRPRx and was solved by the NLSG solver. The following results of the simulation and analysis were initially obtained:

- Displacement and velocity of the objects and their evolution;
- Forces (external force, contact force, inertia force) of the objects and their evolution;
- Redistribution of the contact forces and the contact stresses between the objects;
- The failure of the model due to the sliding threshold of the friction contact;
- Variation of contact conditions during the simulation.

2.5.2. The connection between RESOBLOK and LMGC90

The fractured rock model that had been created by RESOBLOK was exported to LMGC90 as the data file *.dat. The rock mass was an assembly of many rock blocks that were generated by the intersections of the discontinuities network inside the rock mass. Each block was formed as a polyhedron of n vertices. In the data file *.dat, the coordinates of vertices and the formation of edges as the vertex combinations, the formation of faces as the edge combinations, and the formation of blocks as the face combinations were listed respectively. The connection of RESOBLOK and LMGC90 was executed by the script GMSH that has been integrated in LMGC90.

Some parameters needed to be declared before the connection:

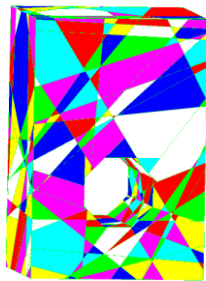
- Objects to be taken into account: only physical objects or all objects.
- The size of mesh elements: $L_{\min} \leq L_c \leq L_{\max}$;
- The 3D meshed algorithm: 1=Delaunay, 4=Frontal, 5=Frontal_Delaunay, 6=Frontal_Hex, 7=MMG3D;
- The mesh optimization to improve the quality of the tetrahedral elements: 0=deactivate and 1=activate.

First, the vertices, edges and faces that had been created by RESOBLOK were detected. By the calculation of the barycentre of all faces and their normal vectors, the orientation of faces is checked. If one face is oriented badly, it is turned to the right position.

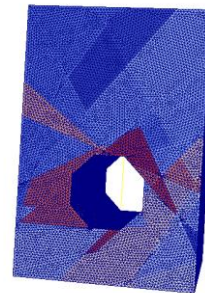
Next, an empty mesh object was created. The vertices were added to the mesh as “NO3xx” nodes and the faces were added to the mesh as “T3xxx” elements. A 3D rigid avatar for a surface meshed object in 3D was built by computing its mass and inertia. The elements of the mesh were triangles. If the inertia of an object is positive, it is added as a rigid block of the model. A 3D rigid block was defined by some features:

- The material of block: type “RIGID” with density (kg/m^3);
- The rigid model of object: type “MECAx”, element “Rxx3D”, dimension = 3.

Last, all the vertices, edges and faces from RESOBLOK were transformed into rigid meshed blocks by the GMSH script integrated into LMGC90. The model was ready for the declaration of loading conditions and boundary conditions in the next step of LMGC90



a) Generated on RESOBLOK



b) Surface meshed on LMGC90

Figure 2.5.4: Numerical model of the rock mass on the vicinity of an opening

2.5.3. Simulation setting

Once the model has been reconstructed on LMGC90 with all the required features, the simulation was started with the declaration of the simulation conditions:

- Boundary conditions;
- Loading conditions;
- Numerical computational parameters.

They are briefly introduced here while the specific conditions for the two application cases of the methodology are presented in the following parts of this section.

2.5.3.1. Boundary conditions of the model

The boundary setting of the model is the declaration of the imposed DOF of the constitutive blocks, especially those on the boundaries of the model. Since the bulk behaviour of object

was rigid in the scope of this research, the 6 DOFs (3 translational and 3 rotational) of an object were assigned. However, due to the splitting of the initial rock mass into discrete blocks by the intersection of the discontinuities families, there were a large number of blocks on the boundaries that takes time to determine them. We proposed to use an intermediate rigid object placed on the boundary of the model and contacted with all the blocks on that boundary. The contact configuration between this object and the blocks of the model was the same with the contact configuration of the model. The DOFs of those intermediate objects (also called the boundary rigid plates, rigid plates or plates) were then defined according to the purposes of the simulation.

2.5.3.2. Loading conditions of the model

The gravity was defined as a three-component (G_x , G_y , G_z) and was applied to all the blocks of the model. The nature of this acceleration can be:

- Constant: defined by a real number with the sign of the application direction;
- Time-dependent: defined by a mathematical function of the simulation time;

The consideration of the real location of the rock mass is realised by:

- Application of an equivalent force representing the ground layers above the rock mass;
- Assignment of the initial value of the gravity force.

The external forces of the model were not recommended to be directly applied on the boundaries of the model. Since the surfaces of the bounding blocks were greatly different, the actual values of the external forces to be applied on those surfaces were diversified. The preparation of the details of the actual forces and their applied positions was complicated and error-risked. Hence, the external forces of the model were directly imposed on the boundary rigid plates attached on the boundaries of the model. The forces were declared to be constant or time-dependent by a mathematical function of time or by a data file of the evolution during the simulation time. Through the contact between those plates and their contacting blocks, the forces were transferred to the contact blocks of each plate and then to the other blocks in the medium. The mechanism of the transference of the applied forces was the redistribution of an external force of a block to its neighbours. This distribution of the external forces on the rock mass was strongly influenced by the contact map of the

model. It is considered, at this moment, as a limitation of the numerical simulation of our proposed methodology. This limitation is further discussed in the next section.

2.5.3.3. Numerical simulation and calculation parameters

The contact detection of the model is characterized by the value of the frequency of the rough detection “n” for the research of the neighbouring objects in the neighbourhood contact space around an object. The research is executed every “n” time steps while the accurate detection is automatically operated in each time step.

Once the Non-Linear Gauss-Seidel solver has been used for solving the contact detection in the model, the following numerical parameters are needed to be assigned:

- The parameter θ of the Crank-Nicholson method: This method is used to evaluate the integral of the forces applied on the objects and the integral of its velocity in an interval of time, the value of the parameter θ is suggested to be 0.5 for the conservation of the integrals over the time step for smooth evolution problem. Besides, if $0.5 \leq \theta \leq 1$, the computation of the integral is implicit and stable unconditionally. If $\theta = 0$, the scheme is explicit.
- The time step dt : It is depended on the mechanical parameters of the model (*i.e.* the mass and the stiffness) and can be computed by:

$$dt = \frac{1}{N} \sqrt{\frac{m_{eff}}{K_n}}$$

With:

N: Time step discretization

m_{eff} : Effective mass of the model

K_n : Normal component of the local stiffness

dt must be small enough to ensure the numerical stability and to describe with accuracy the contact.

- The convergence norm: The convergence of the NLGS solver is considered to be achieved and the iteration is stopped when the following condition is satisfied:

$$\frac{\|x^{k+1} - x^k\|}{\|x^{k+1}\|} < tol$$

With:

x^{k+1} : Computed value from the current iteration

x^k : Computed value from the previous iteration

tol: Tolerance of the iteration

The value of the tolerance is suggested to be small enough to ensure the acceptable accuracy of the analysis. A tolerance of 10^{-6} was generally used.

The parameters of the NSGS solver in the command file of the LMGC90 are:

- The maximal number of calculations in an iterative loop: `gs_it1` is suggested to be not smaller than the number of the blocks inside the model;
- The convergence norm of the iteration: `gs_it2` belongs to the interval of [10, 100].

The analysis is normally suggested to be executed with the minimized time step length in the maximised quantity of time step. However, the time consumption will rise up quickly as well as the virtual memory requirement for the process. The Gauss-Seidel iteration has been widely applied because of its fast convergence capacity and the auto-update of the solutions right when it is computed but not until the whole iteration is executed. The quality of the computation lies on:

- The respect of interaction laws;
- The number of iteration performed;
- The free evolution of bodies;
- The time step.

However, in the scope of this research, no study of the influence of those parameters on the analysis results was done due to the time limitation. This is a research topic that we do hope to realise in the near future.

2.5.4. Limitation of the RESOBLOK – LMGC90 coupling

The connection between RESOBLOK and LMGC90 was achieved thanks to the contribution of the CALAMI team of CNRS at LMGC laboratory (University of Montpellier 2, France). The results from the initial applications showed the good potential interaction between the two codes. However, there were some limitations that need to be dealt with in the future for a more convenient connection.

The biggest obstacle of the connection, up to now, stayed in the transformation of the generated geometrical model from the RESOBLOK to the LMGC90 code. It was caused by the different conventions of the model construction used in the two codes. Firstly, the sign convention of the generation order of object (*i.e.* vertices, edges, faces and blocks) was not mentioned [64]. Meanwhile, for the detection of a face of an object, the order and the direction of the declaration of the relevant edges and vertices must follow the right-handed rule on LMGC90 code so that the normal vector of the face was always pointing to the exterior. Hence, the faces created on RESOBLOK which were considered to be “non-conformed” by LMGC90 cannot be detected between the neighbouring contacts. Even when LMGC90 supplied a command for the auto-correction of those “non-conformed” faces, the contact detection was still difficult and time consuming, and some rare cases can be rejected by the detection algorithm of the LMGC90 code. Secondly, in the models generated on RESOBLOK, the vertices which were attached to the common edge of a block had not always the matching vertices on the common edge of the adjacent block with the first block. In another words, the composition of vertices on the common edge of the first block was not the same with the composition of vertices on the common edge of the second block. Contrarily, the matching of all adjacent objects (vertices, edges or blocks) was strictly required on LMGC90. Neither the surface nor the volume meshing was thus possible to be achieved on the relevant faces or blocks where the matching errors were found. The bulk behaviours of those objects cannot be determined. The simulation was thus not performed. This was considered to be the most important handicap of the current connection between the RESOBLOK and the LMGC90 codes.

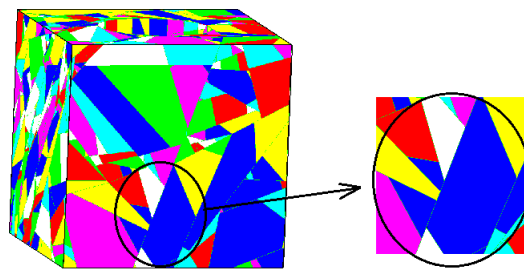


Figure 2.5.5: Example of a matching error on the common edge
between two adjacent blocks of the model generated on RESOBLOK

Another limitation of the coupled modelling-analysis by the combination of the two codes was the load distribution in the model. Given that any cross-section of the model can be constituted of many faces of the relevant blocks, a force which was applied directly to the

cross-section contacted only with the rock block that was situated at the point of contact. As aforementioned, the forces that needed to be applied to the whole rock face were applied on the force-transferring-objects (the rigid plates). The applied forces were imposed on the centre of inertia of those special objects and transferred to all rock blocks that contacted with them. Depending on the contact surfaces of the bounding blocks with the force-transferring-objects, the initial force was actually replaced by various forces that were linked to the contact surfaces. The initial force was distributed as the combination of “n” forces on “n” contact surfaces of n blocks under the special object. Those bounding blocks continued to transfer their forces to their neighbouring blocks and the “n” forces were distributed as “m” forces. With the same mechanism, the initial force that applied on the intermediate object was transferred in the rock mass with the dependence of the contact map in the model. Hence, the “non-regular” distribution of the forces on the model was one of the main features of our model. This fact is well illustrated on the following figure where the external axial pressure which applied on top the model was distributed on all rock blocks of the model. The force value on each constitutive block is represented by a vector of which the magnitude is expressed by the colour on the colour scale and by the shape of the vector.

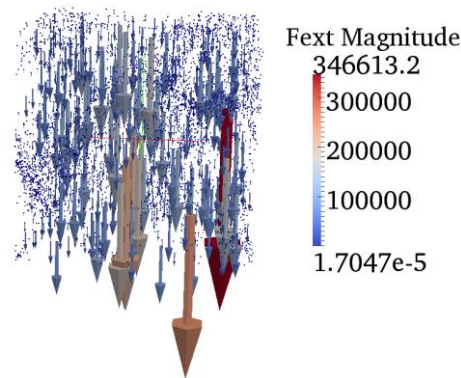


Figure 2.5.6: Non-regular distribution of a vertical pressure applied on a cubic rock model to the constituted blocks in the model

Notation of the figure 2.5.6: The magnitude of the pressure applied on a block was represented by the size and the colour of the vector placed at the inertia centre of the block. The values were in N.

The diversity of the colour and of the size of those vectors is the representation of the non-regular nature of the force distribution in the model. The amelioration of the force distribution network on the rock models is one of the coming tasks of our future research.

2.5.5. Simulation of a conformed triaxial compression test in rock engineering

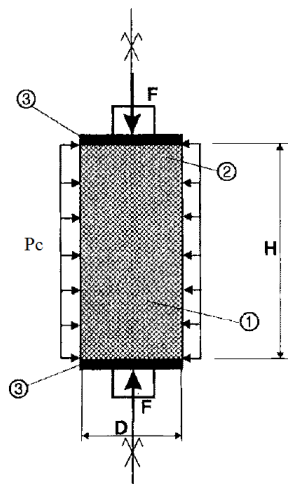
With this simulation, we hoped to achieve:

- An equivalent ideal rock (with its recorded numerical mechanical behaviour) that can be replaced the real fractured marble of Saint Béat;
- The verification of the simulation system and the loading charge system by the use of the rigid plats for transferring the applied load on the boundary of the model to all rock blocks of the model;
- The numerical modelling capacity of the proposed methodology for the typical tests in rock mechanics.

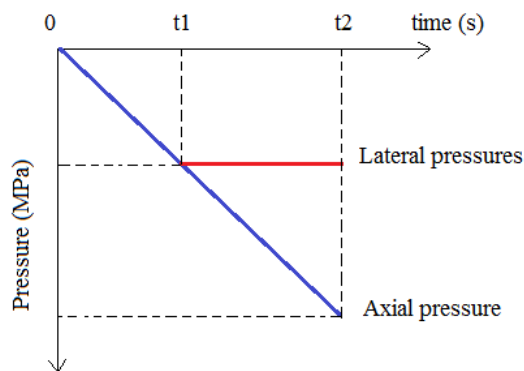
2.5.5.1. Fundamental notion

A monotonous classical triaxial test in rock engineering is realised as followss: The conformed cylindrical specimen ([145], [146], [147], [148]) is placed under a compression in 3D by an axial pressure σ_1 along the longitudinal axis and two lateral pressures $\sigma_2 = \sigma_3$ on the periphery. The loading path is divided into two periods:

- Confining pressure: The axial pressure σ_1 and lateral pressures σ_2, σ_3 are set to be equal and applied on the rock specimen with a same velocity during t_1 seconds;
- Deviator: The axial pressure is then applied with a regular increase while the confining pressure is kept constant until the destruction of the specimen at t_2 seconds.



a) General sketch (sourced from [145])



b) Typical loading path

Figure 2.5.7: Principals of the triaxial compression test for rock and soil specimen

Notation:

1: Cylindrical specimen

2: Covering membrane

3: Plates for the application of the axial pressure

H: Height of the specimen

D: Diameter of the specimen

F: Axial pressure

Pc: Lateral pressure

This test was simulated on LMGC90 on the conformed cylindrical specimen that had been created on RESOBLOK. After the DEM-based analysis, the mechanical responses of the numerical specimen were recorded and treated for understanding the behaviours of the created numerical rock.

2.5.5.2. Simulation setting

After the model generated on RESOBLOK has been reconstructed on LMGC90, the boundary conditions of the model were defined:

- All the blocks of the model were set to be free in all 6 DOFs;
- The 1st big rigid plate of $D \times D \times d$ (m) was attached under the bottom of the model. D is the diameter of the model. The thickness of those plates d was suggested to be small enough to not cause a considerable weight on the model. Its 6 DOFs were totally fixed for the stability of the model;
- The 2nd big rigid plate was attached on the top of the model;
- There were “ n ” rings of “ m ” small rigid plates of $A \times B \times d$ (m) regularly positioned on the height of the model. On each ring, “ m ” plates were symmetrically placed on the periphery. In total, there were $p = n \cdot m$ small plates regularly attached on the periphery of the model. The values of n , m , A , B are selected for aiming at the best distribution of the confining pressures on the model.
- The DOFs of the 2nd big plate and p small plates were assigned by some cases: all-DOF liberation, rotational-DOF fixation, translational-DOF fixation or all-DOF fixation.

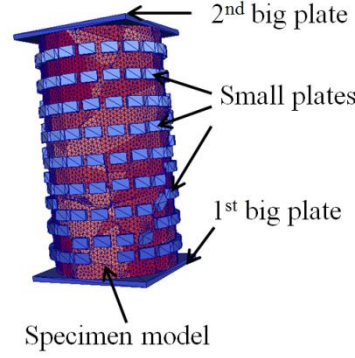


Figure 2.5.8: Arrangement of the boundary rigid plates around the numerical specimen of the triaxial compression tests

The details of the boundary condition of this application on the real data of the marble of Saint Béat are presented on the third chapter of this redaction.

The loading scheme of the simulation was constructed following the loading path presented in the previous part. The pressures were converted as the external forces by:

$$F_{\text{ext}}^j = \sigma_i \cdot A^j$$

With:

F_{ext}^j : External force applied on the j^{th} rigid plate (N)

σ_i : Pressure (N/m²)

A^j : Area of the j^{th} rigid plate (m²)

The increase rates of all external forces were the same. They were characterized by:

- Lateral force on the small rigid plates F_{lateral} :
 - When $t = [0, t_1]$, F_{lateral} was increased regularly from 0 to $F_{\text{lateral}}^{\text{max}} = \sigma_2^{\text{max}} \cdot (A.B)$
 - When $t = [t_1, t_2]$, F_{lateral} was constant at $F_{\text{lateral}}^{\text{max}} = \sigma_2^{\text{max}} \cdot (A.B)$
- Axial force on the 2nd big rigid plates F_{axial} :
 - When $t = [0, t_1]$, F_{axial} was increased regularly from 0 to $F_{\text{axial}} = \sigma_2^{\text{max}} \cdot D^2$
 - When $t = [t_1, t_2]$, F_{axial} was increased regularly from $F_{\text{axial}} = \sigma_2^{\text{max}} \cdot D^2$ to $F_{\text{axial}}^{\text{max}} = \sigma_1^{\text{max}} \cdot D^2$

They were assigned to the model as the time-dependent forces described by the relevant evolution files. The NLGS was chosen to solve the contact detection of the model. The numerical parameters of the solve were selected following the suggestion presented in the section 2.5.3.3. The different cases of the boundary conditions led to the equivalent models. After the simulation was executed during t_2 (s), the obtained results of the mechanical responses of those models were compared for the final decision. The responses of the models during the loading time were recorded and the post-processing treatments on the obtained data were realised. Beside the stress-strain relation, some other behaviours of the model and the numerical rock were interesting:

- Evolution of the deformation;
- Variation of the contact;
- Formation of the sliding planes and their tendency of development;
- Failure: type and time of appearance.

2.5.6. Simulation of a multi-phase-excavation in rock masses

With this simulation, we hoped to achieve:

- The modelling of the massif of the fractured marble of Saint B  at;
- The simulation of a supposed tunnel in the numerical massif and a complex tunnelling procedure that included different periods: before, during and after the excavation of the tunnel;
- The stability analyses of the tunnel and the massif during the tunnelling procedure;
- The numerical modelling capacity of the proposed methodology for the rock tunnel engineering.

2.5.6.1. Simulation of the excavation progress

The simulation of the multi-phase-excavation of a tunnel was created by the disappearance of the relevant blocks inside the zone of the tunnel according to a supposed excavation schedule. During the simulation progress, the disappearing length of the rock core inside the tunnel was developed to represent the actual construction phases. Assuming that the future tunnel will be excavated in K phases with the length of the i^{th} segment is $L_i(\text{m})$. K , i were positive real numbers, i varied from 1 to K .

The total length of the tunnel $L(\text{m})$ was given by:

$$L = \sum_{i=1}^K L_i$$

In the previous steps (see the section 2.3.4), three approaches for the geometrical modelling generation of the tunnel excavation process had been proposed. The three corresponding algorithms for the excavation are provided here:

a) Excavation algorithm 1

This algorithm was applied on the geometrical modes that had been generated by RESOBLOK with the modelling approach 1 presented in the sub-section 2.3.4.1. The geometrical model was a fractured rock mass “without hole”. After immersing it into the Pre-Processor of LMGC90 and meshing all surfaces of the blocks in the model, the declaration procedure for a rigid 3D in LMGC90 was carried out. Assuming that the tunnel was located at the middle of the rock model in the cross-section zone that defined on the Cartesian coordinates by:

$$x_{\min} \leq x \leq x_{\max}$$

$$z_{\min} \leq z \leq z_{\max}$$

With the longitudinal axe of the future tunnel is Y, the K phases of excavation were mathematically represented by the y coordinate during the time of excavation:

- At the 1st phase (1st excavation segment): $0 \leq y \leq L_1$;
- At the ith phase (ith excavation segment): $L_{i-1} \leq y \leq L_i$;
- At the last phase (Kth excavation segment): $L_{K-1} \leq y \leq L$;

When the inertia centre of a rock block was situated in the zone that was defined at a phase of time, it was excavated.

Table 2.5.1: Coordinates of excavation blocks during the excavation times

Coordinate	X	Y	Z
1 st excavation segment	$x_{\min} \leq x \leq x_{\max}$	$0 \leq y \leq L_1$	$z_{\min} \leq z \leq z_{\max}$
i th excavation segment	$x_{\min} \leq x \leq x_{\max}$	$L_{i-1} \leq y \leq L_i$	$z_{\min} \leq z \leq z_{\max}$
Last excavation segment	$x_{\min} \leq x \leq x_{\max}$	$L_{K-1} \leq y \leq L$	$z_{\min} \leq z \leq z_{\max}$

By executing the command “RBDY3_GetBodyVevctor” for the calculation of the inertia centre of all rigid rock polyhedra in the model, the list of wanted rock blocks was obtained. They were then “disappeared” by the command “RBDY3_SetInvisible” at the i^{th} time phase corresponding to their position in the i^{th} excavation segment. The excavation procedure started at the 1st segment, developed along the longitudinal axis of the tunnel and finished at the K^{th} segment.

b) Excavation algorithm 2

This 2nd algorithm was applied on the geometrical models that had been generated by RESOBLOK with the modelling approach 2 presented in the sub-section 2.3.4.2. From the data files *.dat of RESOBLOK, they were immersed in LMGC90, meshed all the surfaces of the constitutive blocks and numbered as follows:

- 1st segment of tunnel with the coordinate $Y_1 = [0, L_1]$ (model 1): n_1 objects RBDY3;
- i^{st} segment of tunnel with the coordinate $Y_i = [L_{i-1}, L_i]$ (model i^{th}): n_i objects RBDY3;
- Last segment of tunnel with the coordinate $Y_K = [L_{K-1}, L]$ (model K): n_k objects RBDY3;
- Rock mass “with hole” (model 0): m RBDY3 objects.

The K-phase-excavation was carried out following the procedure given by:

- 1st phase: n_1 objects RBDY3 of the model 1 were excavated;
- i^{st} phase: n_i objects RBDY3 of the model i were excavated;
- Last phase: n_k objects RBDY3 of the model K were excavated.

The excavation was done by the command ““RBDY3_SetInvisible””.

c) Excavation algorithm 3

This 3rd algorithm was applied on the geometrical models that had been generated by RESOBLOK with the modelling approach 3 presented in the sub-section 2.3.4.3. Two models exported from RESOBLOK were two zones of a rock mass: inside the tunnel (model 2) and the surrounding medium (model 1 “with hole”). Two files *.dat were immersed respectively in the Pre-Processor of LMGC, their surface meshed and numbered from 1 to n (model 2) and from $n+1$ to m (model 1 “with hole”). At the initial simulation time $t = 0(s)$, they formed the total rock mass as illustrated in the Figure 2.5.9.

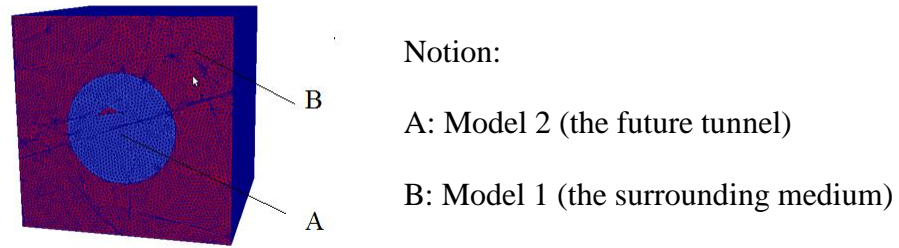


Figure 2.5.9: Model of the numerical rock mass of the 3rd excavation algorithm at $t = 0(s)$

An assumed excavation procedure was executed in K time phases. It was mathematically represented during the time of construction along the longitudinal Y axis of the future tunnel:

- At the 1st phase (1st excavation segment): $0 \leq y \leq L_1$;
- At the i^{th} phase (i^{th} excavation segment): $L_{i-1} \leq y \leq L_i$;
- At the last phase (K^{th} excavation segment): $L_{K-1} \leq y \leq L$;

When the Y coordinate of the inertia centre of a rock block numbered from 1 to n meet the excavation condition, it was affected by the command “RBDY3_SetInvisible”. Hence, n objects RBDY3 of the model 2 were “disappeared”, according to their Y coordinates in the rock mass.

By designing a suitable time sequence of the excavation, a real construction rhythm can be approached simulating as the composition of many different working phases. For instance, in a K -phase-simulation of N time steps, the excavation works were carried out in each a_1 time steps, the preparation time took a_2 time steps and the finishing works took a_3 time steps, a simple relation formula was obtained:

$$N = a_2 + K \cdot a_1 + a_3$$

During the a_1 time steps, a basic cycle of the tunnel construction was organised with multiple continuous tasks such as the rock face preparation, excavation, pause, tunnel structure construction, tunnel facilities assembly, *etc.* It is noted that the excavation segment was required to finish in 1 time step. Due to that, if the real excavation segment is long, it is recommended to be divided into several sub-segments which can be excavated in 1 time step.

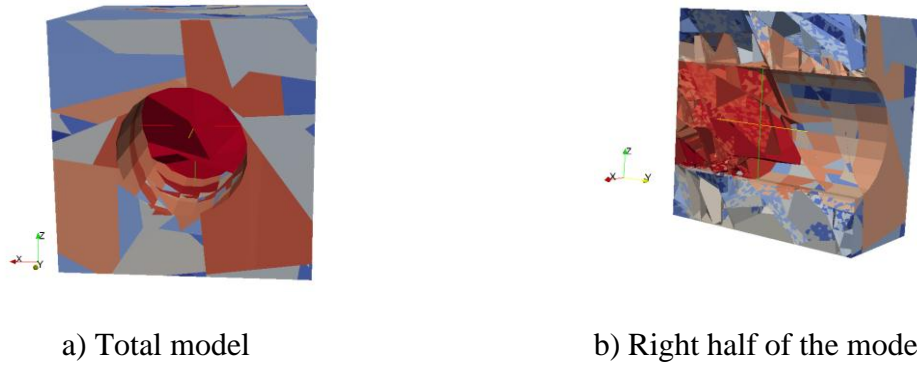


Figure 2.5.10: Simulation of a tunnel in its excavation process

2.5.6.2. Simulation setting

After the model generated on RESOBLOK has been reconstructed on LMGC90, the boundary conditions of the model were defined:

- All the blocks of the model were set to be free in all 6 DOFs;
- N rigid plates of $A \times B \times C$ (m) were attached regularly with the centre-to-centre distance of D (m) to fully cover each external boundary of the model. The actual values of A, B, C and D were decided with the consideration of the size of the model and the medium size of the constitutive blocks so that the external force applied on the boundaries was regularly distributed on the whole model.

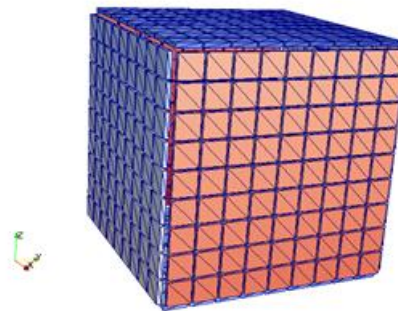


Figure 2.5.11: Arrangement of the boundary rigid plates around the cubic model of a tunnel

The DOFs of those rigid plates were assigned as follows:

- The plates that were situated on the bottom boundary of the model: 6 DOFs were totally fixed for the stability of the model;
- The plates that were situated on the other boundaries of the model: due to the conditions of the vicinity of the rock mass in its real location and due to the

intention of the analysis, some cases were to be considered: all-DOF liberation, rotational-DOF fixation, translational-DOF fixation or all-DOF fixation.

Different cases of the boundary conditions were then applied and the obtained results of the mechanical responses of the equivalent models and their tunnels were compared. The details of the boundary condition of the first real tunnel application of the methodology are found on the third chapter.

The ITA [167] suggested five successive cases of the geological loads on a tunnel and its vicinity:

- Initial state of stress;
- Initial stress relief;
- Excavation support by shield;
- Excavation support by grout segments;
- Long term deformation.

The loading conditions of the model were assigned by two approaches:

a) Theoretical approach

The loading conditions were set up following the theories of loads on the tunnel that can be found in most manuals related to the tunnel engineering. The ITA [77] proposed several plane-strain loading schemes for tunnels at different depths and ground stiffnesses:

- 1st case for shallow tunnels and tunnels in soft ground: the overburden layers on top of the tunnel are computed as the principal load of the tunnel without the allowance of the tension bedding at the crown of the tunnel. The stress released due to pre-deformations of the medium was neglected.
- 2nd case for moderately stiff medium: the ground stiffness is employed by assuming a continuum model and a complete bond between the lining and the medium.
- 3rd case for medium-hard rock or highly cohesive soil: some stress release is assumed to be caused by deformations that occur before the lining. The ground may be strong enough to allow a certain unsupported section at the tunnel face. Also, for high overburden tunnels, a reduction of the acting crown pressure ($h < H$) is taken into account.

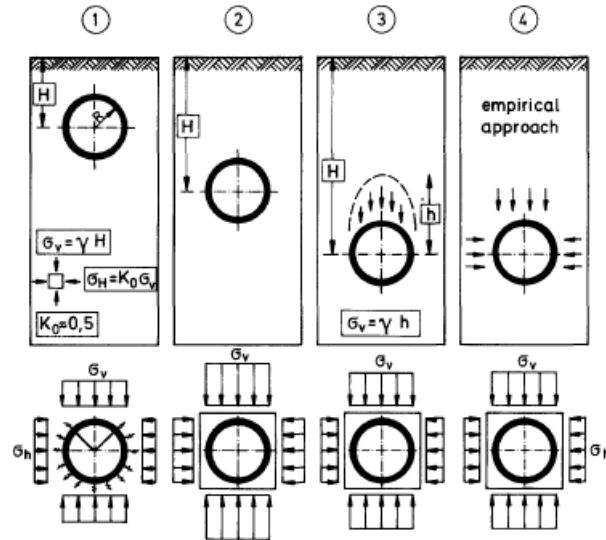


Figure 2.5.12: Alternative plane-strain design models for tunnels
in different depths and ground stiffnesses (sourced from [77])

The 1st case is not suitable for the mountain tunnels when the locations of the tunnels are normally deep. The 2nd case leads to the use of an equivalent medium of the rock mass where the total rock column on top of the tunnel is taken as the vertical pressure of the model. This case is suitable for the tunnel at medium depths. The 3rd case can be applied for almost all tunnels in rock masses, the calculation of the reduced rock columns on top of the tunnels has been proposed by the many tunnel theories (the theory of Protodyakonov, for instance).

Among the loads that are applied on the tunnel, the earth pressures are considered to be the most important permanent load. Based on the solutions for considering the real location of the tunnel in the rock medium, the tunnel theories of earth pressures can be classified into two groups [168]:

- Neglecting the real location of the tunnel in the rock medium: proposed by many theories of which the theory of Protodyakonov is the representation;
- Taking into account the real location of the tunnel in the rock medium: proposed by many theories of which the theory of Bierbäumer and Terzaghi are two representations.

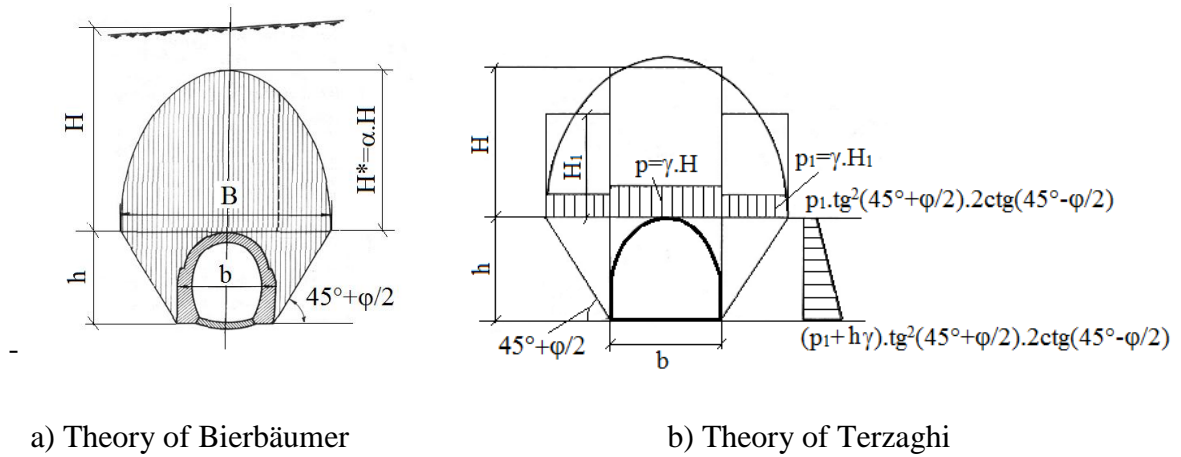


Figure 2.5.13: Two typical schemas of the theoretical earth pressures on the tunnels
(sourced from [168])

Based on the direction of the earth pressures, they are classified as:

- Vertical pressures: the pressures that are caused by the rock strata above the tunnel. They are calculated as the weight of the vertical column on top of the tunnel (the classical theory), the vertical column on top of the tunnel and the two adjacent triangular polyhedra (the theory of Terzaghi), the parabolic polyhedron above the tunnel and the inverse truncated cone around the tunnel (the theory of Bierbäumer, Protodyakonov),
- Lateral pressures: are caused by the sliding of the vertical rock polyhedra above the tunnel and are normally defined as the multiplication of the vertical pressure by the coefficient of lateral earth pressure [167].

The determination of the load combination is an important task for the design of any tunnel. The application of the load combination is normally considered as the superposition of the component loads. Each load is applied on the model with the specific characterization of its nature (constant or time-dependent), value, direction, position. Those operations can be fully executed on LMGC90 with the principal aforementioned in the section 2.5.3.2.

However, the tectonic application on the rock masses is the most difficult load to be quantitatively determined as a specific load. The earth pressures are fairly underestimated when being converted to the plain state as the combination of the vertical and lateral pressure. Moreover, the combination of different loads on the rock mass is not easy to define the “real” loading conditions. Except the loads included by the support structures or the influences of man-made operations (during the investigation, the construction phase and

the service life of the tunnel), the total combination of the geological loads of the rock mass can be represented by the *in situ* stresses of the rock mass that are measured during the important “milestones” of the tunnel construction and/or collected from the empirical approach.

b) Empirical approach

It is noted that the two empirical approaches, one for the tunnel support design that have been introduced in the section 1.4.2.1 of the 1st chapter, another for the tunnel loading conditions which is presented here were not the same. While the first involves the complex procedure that lies with the whole project of a tunnel construction, the second only relates to only the determination of the loading condition on the tunnel and its vicinity. The principal of this empirical approach was quite close to the observation approach of the tunnel structure design in the section 1.4.2.3 of the 1st chapter.

In brief, the empirical approach for the determination of the loading combination for the tunnel modelling was the proposition of the use of the collected data of the natural state of rock mass. This approach was equivalent with the 4th case of the plane-strain loading schemas for tunnels in different depths and ground stiffnesses proposed by ITA [77] and presented in the Figure 2.5.12. The sources of those data were from the case histories of the equivalent media and tunnels, the laboratory and *in situ* measurements on the target rock mass. Followed them, the stresses acting on the tunnel were determined by the study of case histories of the rock media and tunnels with the similar geological conditions and structural design, on the natural stresses from the *in situ* measurements on the target rock mass, on the monitoring of the real excavation progress of the tunnel and from the continuous update of the model. This approach was in fact closer to the fundamental of the NATM.

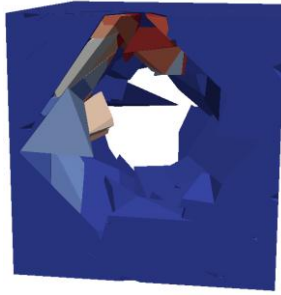
In the tunnel application of our methodology, we proposed the use of the natural stresses of the rock mass for the definition of the geological loading condition of the model. The input data were obtained from the *in situ* measurements at the site of the target tunnel. The relevant measurement technics has been presented in the section 2.5.3. An *in situ* stress was characterized by three normal components and three tangential components presented on the geo-reference or the global reference. The six components of the natural stress were applied respectively on the rigid plates attached on the equivalent boundaries of the model.

Hence, the 3D natural state of the earth pressures including the tectonic influences was well expressed and assigned to the model.

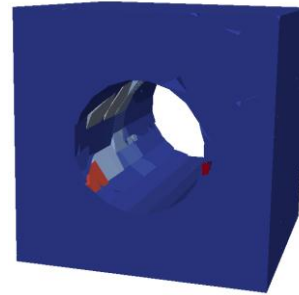
2.5.6.3. Commentaries on the proposed solutions of the excavation simulation

On the same scenario file of a virtual rock mass with a tunnel inside, three proposed excavation algorithms and their corresponding geometrical models were simulated and analysed on LMGC90 with the same excavation procedure. From the obtained results, it was found that:

- Because the excavation simulation of the 1st approach based on the position of the inertia centre of blocks, the boundary of the numerical tunnel was not smooth, especially when the rock blocks in the excavation zone were big. The achieved cross-sections of the tunnel were often smaller than the targeted one. If the rock medium is slightly fractured, this approach is not recommended. However, the initial rock mass before the excavation was in the closest stress state compared with the measured stress state.
- Pre-generating all the excavation segments of the tunnel on the geometrical model of the rock mass, the 2nd approach proven to best simulate the configuration of the future tunnel. The excavation shape was created as in the design: the tunnel front faces were always perpendicular to the longitudinal axis. However, the pre-existence of the tunnel boundaries in the rock mass even at the initial time before the construction may affect the natural state of the rock mass and the re-distribution of the stress field inside the rock mass. Further studies on this effect might be undertaken in another research project.
- The periphery of the future tunnel using the 3rd approach was also pre-determined on the geometrical model of the rock mass. The final state of the numerical tunnel was the same with the results of the 2nd approach. In fact, the 3rd approach is the combination of the 1st and the 2nd one. Therefore, the resulting geometry tunnel has smooth periphery but rough front faces. This scenario helped to reduce the time simulation with a reasonable geometrical configuration state of the excavation work.



a) By the 1st approach



b) By the 2^{sd} and 3rd approach

Figure 2.5.14: The final state of a tunnel simulated by three mentioned algorithms

Once the discrete analysis started, using the NLGS iterative solver of LMGC90, the response of initial rock medium and the redistribution of stress around the tunnel during and after each phase of construction, or at the final state, were required for the post-processing. The final goal was a stability assessment of the rock medium in three phases: (a) before the excavation; (b) during the excavation; and (c) at the permanent state of tunnel during its service life.

2.5.7. Conclusion

LMGC90 is a comprehensive DEM-based simulation and analysis code that is based on the NSCDs method. We have used the developing version LMGC90v2_dev with the Python interface on the Ubuntu environment of this code for the discrete simulation and analysis in our methodology. The 3D geometrical models that had been generated by RESOBLOK were immersed in the Pre-Processor of LMGC90. After redetecting the assemblage of rock blocks inside the model, their surface meshing using the triangle element grids was realised by the integrated script GMSH in LMGC90. Once the geometrical model was reconstructed, the simulation was set up through the assignment of the boundary conditions, the loading conditions of the model, and the parameters of the numerical calculations. The mechanical model of the target rock mass was fully integrated in the numerical model. The detection of contacts between neighbouring blocks was carefully controlled with the suitable iterative solver. The mechanical responses of the model during the simulation time were recorded into two forms: the algebra and the visualization data. They were used into the post-processing treatments for aiming at a better assessment of the numerical behaviour of the simulated rock mass. By comparison with the behaviours of the equivalent natural rock behaviours obtained from the laboratory and/or *in situ* measurements and tests, from the case histories of the similar conditions, from the continuous updated monitoring on the

target rock mass or by the comparison with a confirmed methodology, the validity of the modelling and simulations were assessed.

In this research, the combination of the RESOBLOK code for the geometrical modelling and the use of the LMGC90 code for the simulation and analysis of the rock masses was published for the first time. The initial results showed the auspicious ability of the combination as the backbone of the proposed comprehensive methodology in rock engineering. However, some limitations of the RESOBLOK-LMGC90 couple were also listed: the difficulties in the generation order and directional convention, the vertex matching on the common edges of blocks, the meshing problem of the model and the load distribution on the rock mass. We aim at further studies on those problems and heading for the amelioration of the connection between the two codes.

Two first application cases of the methodology were realised:

- Simulation of a conformed monotonous classical triaxial compression test;
- Simulation of the multi-phase-excavation progress in a rock mass.

In each case, the suggestions of the simulation and analysis setting were given after the successful generation of its geometrical model on RESOBLOK. In the first case, following the loading path and the exact requirement of the real conformed test, we aimed at finding an equivalent rock as the representative for the fractured marble of Saint B  at and also at reproducing the test in the numerical environment as the alternative beside the real ones. In the second case, three simulation algorithms of the tunnel multi-phase excavation progress were proposed paying attention to the continuous change of the tunnel shape and its vicinity during the excavation under the application of the natural stresses in a 3D state, the simulation was hoped to generate a realistic modelling of the targeted objects including their real characteristics. The mechanical responses of the numerical models were obtained and initial comments were expressed.

Those two applications were executed on the real data of the white marble of Saint B  at rock mass (Haute Garonne, France) with the idea of use in the preparation phase of the construction project for a new tunnel to underpass in this town. The realisation is introduced in the next chapter.

CHAPTER 3: APPLICATIONS OF THE METHODOLOGY ON THE MARBLE OF SAINT BEAT (HAUTE GARONNE, FRANCE)

3.1. Marble of Saint B at and the construction project of the Saint B at tunnel

3.1.1. Saint B at town and the marble of Saint B at

Saint B at is a small town in Haute Garonne department of the Midi-Pyr n es region of France. Along the French national road N125, Saint B at is only 10.6 km from the frontier between France and Spain.



Figure 3.1.1: Satellite view of Saint B at town in its region (sourced from [169])

Saint B at is located in a narrow valley between the Cap du Mont (1207m) and the Ri  mountains (1128m), along the Garonne river, in an internal metamorphic zone of the Pyrenees chain. Limited by two sub-vertical crustal accidents, the internal zone is tightened between the Upper primary chain in the South and the northern Pyrenean massif of the Barousse in the North. It is constituted of secondary metamorphic terrain (from Triassic to Upper Albian) and is situated in the Northern Pyrenean Fault (NPF) zone [170].

The town is famous for its high quality marble that has been used from the antique time for many historical monuments, of which two typical examples are the Versailles and the

Fontainebleau palaces. There are three main deposits of the marble in Saint B  at: the Lavigne, the Mafonne and the Marignac ones. They are deposited from the North East – South West toward the East – West direction with a dip of 70-75  . The factory OMG in Saint B  at has exploited the marble at the Lavigne and the Mafonne deposits [171]

The marble of Saitn B  at was formed from the Jurassic age to the early Cretaceous age. There was a series of the thermal metamorphism during 92 to 102 million years. The formations of the marmoreal metamorphic limestone of the internal Pyrenean zone created a narrow region representing the tectonic sedimentary axis of the Pyrenean chain. Strongly folded and unfolded, they formed steep reliefs that can be easily identified in the region [170].

In 2006, M. Renard *et al.* [172] realised a research on the marble of Saint B  at and found that the colour of rock depended on the presence of the pyrite and the graphite in the mass. The very bright marble was poor in graphite but relatively rich in pyrite. The bright types were rich in graphite but very poor in pyrite. The medium coloured and black ones were rich in both pyrite and graphite.

F. Hadj-Hassen [173] had summarized in his report that the marble of Saint Beat had medium sized grains and their discontinuities were relatively smooth, not really rough with a medium extension from 3 to 10m. The filling inside discontinuities, if any, was composed of clay or calcite with the thickness smaller than 5mm. There was water inside the exploiting quarry of the factory OMG under the form of seepage at the level of the most important discontinuities. The marble in the Mafonne deposit was found to be less fractured than in the Lavigne one. He also noticed that the diversity of the orientation of the discontinuities, as well as the presence of iron oxidant (represented as the colour of yellow or orange on rock faces) and the filling of clay in the discontinuities were three main causes of the instability of the exploitation site.

The conditions of the regional geotechnical stresses of the region were analysed in a geotechnical report on the exploitation site of the OMG factory by A McCracken *et al.* [171]: The nature of the tight folding of the Pyrenean chain had provoked the regional stress inside the rock mass. The major fault between the younger mineral metamorphic (Jurassic – Cretaceous) and the Trias acted as a damping in transferring stresses inside the rock mass. This regional geological stress strongly depends on the position in the folds: the maximal stresses in traction might be found in the crest of the folds. In contrary, the

maximal stresses in compression were situated in the middle of the folds. On the site of the exploitation site of the OMG factory, regional stresses were smaller, in general.

A research on the earthquake risk in the region of Saint B  at was conducted by CETE M  diterran  e (Mediterranean Research and Technical Centre for and Public Works, France) in October 2006 [174]. The records of earthquake in the circle of 150km around the Saint B  at town have not passed the magnitude of 5.9 in the historical document of earthquake of the region. The maximal acceleration of the ground in Saint B  at was smaller than 1.3m/s^2 and the return period of this phenomenon is estimated to be about 1000 years. The most recent quake was happened in 4/10/1999 with $A_{cc}^{\text{max}} = 260\text{ cm/s}^2$, the magnitude of 4.8 and the epicentre was nearly 4km from Saint B  at, the hypocentre was superficial (inferior to 15km). However, this event did not have any clear effects on Saint B  at and the northern Pyrenean fault. In the segment action of the fault near the town, there were no historical earthquake records.

3.1.2. The construction project of the Saint B  at tunnel

3.1.2.1. General introduction

There are two important transportation lines that run through Saint B  at: the national road N125 and the departmental road D44. They connect the town with other regions of France but also bring inconveniences to the calm atmosphere of the town.

The national road N125 is an important French national road toward the Spanish frontier. Opened from 1824, the road had passed under several modifications until the latest one in 2006 that brought the up-to-date journey from Montr  jeau to Pont-du-Roi in 28km [175]. Being one of the few roads passing through the central Pyrenees at a medium altitude, the road is nearly the most heavily-travelled corridor between France and Spain [170].

The part of the N125 that runs through Saint B  at is tightened by the Cap du Mont and the Ri   mountain which are steep reliefs with the threatening of rock falls. Furthermore, the Garonne river which is at one side of the road sometimes brings inundation to the valley of the Garonne. For improving the traffic of the N125 in this region and for the reduction of the traffic flows, in particularly heavy transports, passing through the town of Saint B  at, a new tunnel was planned. In 1989, the construction project of a new tunnel as a part of the N125 at Saint B  at started by DREAL Midi-Pyr  n  es (Midi-Pyrenean Regional office of Environment, Development and Accommodation, France), under the supervision of CETE

du Sud-Ouest [170]. This construction is in the framework of the development project of the N125.

The future tunnel will be dual-directional with a length of 1066m, including two security galleries, a transversal ventilation system and a station of smoke ejection on the northern head of the tunnel [170]. It will be on the left side of the Garonne river, go under the Cap du Mont with the northern head on the exploitation site of the OMG factory and the southern head will meet the departmental road D44. The excavation of the future tunnel will be started from both heads [170].



Figure 3.1.2: Illustrational trace of the tunnel of Saint B at in its region
(sourced from [169])

Investigation and research works have been done from 2004 up to now in the preparation phase of the project. Faced with some environmental issues, the excavation of the new tunnel has been postponed until the end of 2012. In august 2012, the deviation of the N125 was started in the plain of Aressec and in the following month, the same works was executed for the D44 [182]

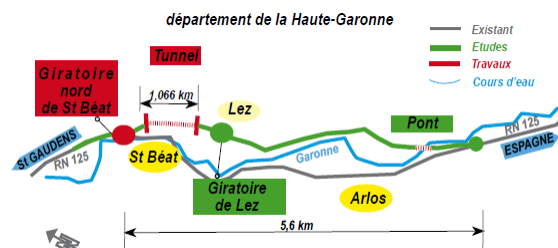


Figure 3.1.3: Deviation in Saint B at town for the construction project of Saint B at tunnel
(sourced from [183])

3.1.2.2. Study on the technical documents of the project

In 2004, the preparation phase of the construction project was realised by DREAL Midi-Pyrénées, LRPC Toulouse (Public Works Regional Laboratory in Toulouse). For the research of the stability of the future tunnel, the technical teams of LRPC Toulouse have carried out many researches by the *in situ* and laboratory tests in three main investigation sites: two heads of the future tunnel and the castle gallery. The castle gallery, an abandoned exploitation site of OMG factory, has been used as the most important investigation site of the construction project. It is about 10m high and 15m wide, 35m above the future tunnel and in shape of the letter Y and in a good condition of stability [176]. Many investigation works of the characterisation of the rock mass of Saint Béat were carried out in this castle gallery.

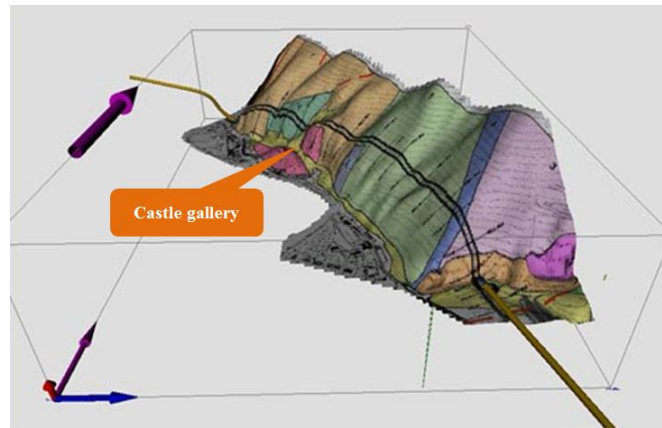
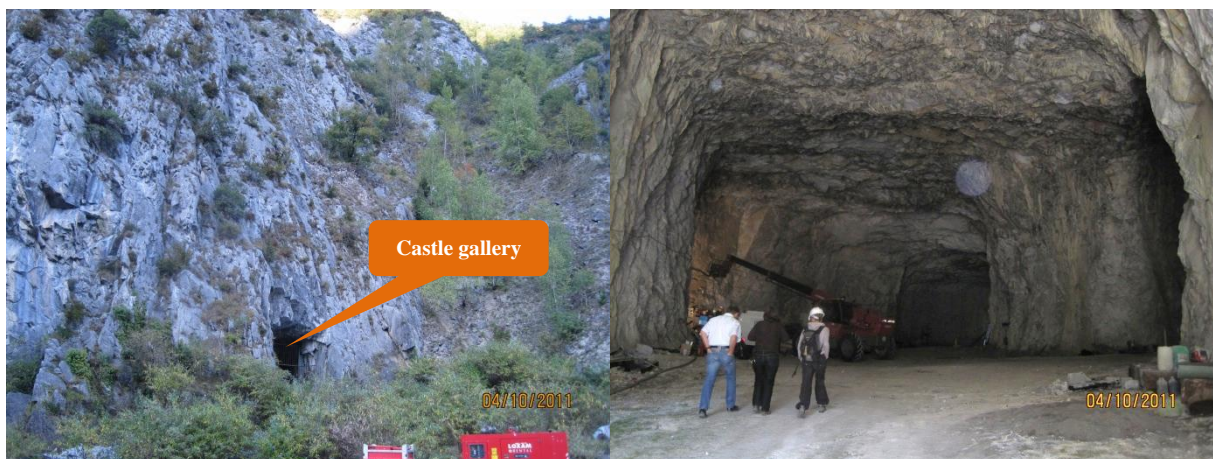


Figure 3.1.4: 3D geological simulation of the tunnel of Saint Béat in its rock mass
(sourced from [177])



a) Exterior

b) Interior

Figure 3.1.5: The castle gallery of the construction project of the Saint Béat tunnel

a) *In situ* stress measurements

The *in situ* stresses of the rock mass of Cap du Mont were measured in the castle gallery by the field-based methods in two campaigns. The first one was in September 2004 by CETE Lyon with the overcoring and the flat jack technics. The second one was in October 2011 by INERIS with the overcoring technics.

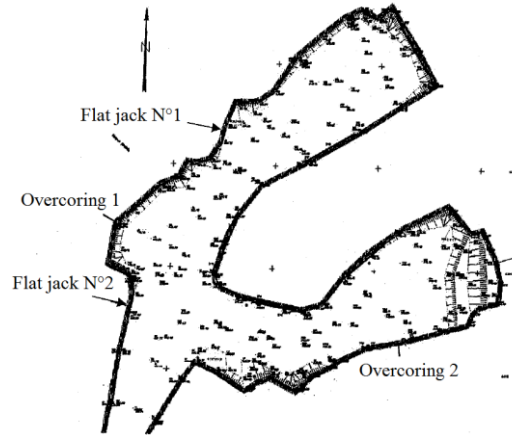


Figure 3.1.6: Aerial plan of the castle gallery and the positions of the measurement realised by CETE Lyon (sourced from [177])

In the first campaign, four overcoring and two flat jack measurements were executed. The results of the overcoring measurements were summarized in the following table.

Table 3.1.1: *In situ* principal stresses measured by the overcoring in the castle gallery by CETE Lyon (sourced from [177])

Measure	Modulus of Young (GPa)	Principal stress (MPa)					
		σ_1	Orientation	σ_2	Orientation	σ_3	Orientation
1	56.9	72.5	Sub-vertical	29.3	Horizontal	-48.7	Oz'
2	58.8	4.3		-1.8		-22.2	
3	61.6	36.1	Oz'	-11.2	Horizontal	-15.6	Sub-vertical
4	61.7	2.0		-1.4		-5.0	Sub-vertical

Notation:

- The negative values represented the compression action and the positive values represented the tension action of the stresses. The tolerance of the measured values

was ± 1.2 MPa.

- Oz' was closed to the longitudinal axe of the future tunnel of Saint B  at.

Based on the results obtained from the coring measurement, CETE Lyon [177] commented that: The presence of strong stresses “presumably of tectonic origin” in the castle gallery were found. The high values of the stresses, which were considered to be high in the approximation of the wall of the castle gallery and also in the whole rock massive, were probably caused by the big size and the local geometry of the gallery and by strong tectonic stresses. Besides, there was a decrease of the stress toward the interior of the rock mass. The fact that the directions of the principal stresses were not aligned with the directions of the stresses on the reference of the borehole was considered to be caused by the local tectonic stress which is not in the horizontal plane and might have the strong tangential component.

In the flat jack measurements, CETE Lyon had pretended four measurements but only two were realised in the conventional conditions due to the strong fractured state of the rock face in the castle gallery. In the 1st measurement, a vertical tension stress was found. In the 2nd measurement, a displacement of 10µm was recorded after the realisation of “la saign  e”. The necessary pressure for which the captures returned to the initial position was 7.5 MPa. The conclusion of the presence of strong stresses “presumably of tectonic origin” in the measurement site was also proposed by CETE Lyon as in the overcoring and flat jack measurements [177].

In the November of 2011, another overcoring measurement was executed by INERIS. Three measurements were carried out but only one was approved. The two failed measurements were considered to be due to the natural fractured condition of the castle gallery and the thermic variation in the rock mass [178].

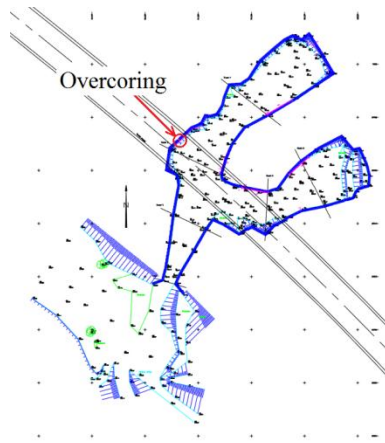
Table 3.1.2: Obtained *in situ* principal stresses (sourced from [178])

Principal stress	Value (MPa)	Orientation (��)		Position with the future tunnel
		Trend α	Plunge β	
σ_1	-4.1 ± 0.5	112	22	parallel with the longitudinal axis
σ_2	-1.7 ± 0.5	355	49	close to the longitudinal axis

σ_3	$+1.3 \pm 0.2$	217	33	perpendicular with the free face of the slope
------------	----------------	-----	----	---

Notation: The negative values represented the compression action and the positive values represented the tension action of the stresses.

The vertical stress which coincided with the vertical axis of the future tunnel was -1.2 MPa.



a) Aerial plan of the castle gallery and the borehole position (sourced from [178])

b) *In situ* measurement

Figure 3.1.7: Overcoring measurement realised by INERIS in the castle gallery in October 2011

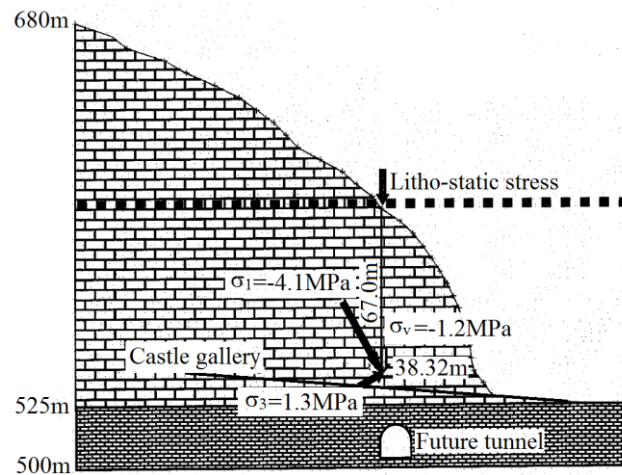


Figure 3.1.8: Profile on the right side of the tunnel project and the graphical representation of the estimated principal stresses (sourced from [178])

A biaxial compression test was realised on the rock core removed from the borehole right after the overcoring measurement. The medium value of 64.8 GPa of the modulus of Young and the coefficient of Poisson of 0.34 were obtained [178]. The results of INERIS in the

November of 2011 showed a weak state of *in situ* stresses in the rock mass and they were highly influenced by the morphology and the topography of the rock slope. The tension action of the minor principal stress was considered by the probably presence of the open fracture near the point of measurement and the free surface of the slope. This value was also suggested not to be important to the future tunnel [178]. In addition, the presence of a lightly high litho-static stress estimated about -2.2 MPa in the zone of the future tunnel and -1.7 MPa at the measurement point were also predicted.

As a consequence of a great diversity of the mentioned values of the *in situ* measurement, the final conclusion about the state of *in situ* stresses of the rock mass under the Cap du Mont was not proposed. However, the influence of tectonic phenomena in the rock mass was confirmed [177], [178].

b) Earthquake research

The research of earthquake of CETE Méditerranée in October 2006 recommended that two heads of the future tunnel would be concerned by the earthquake but no evident risks as rock falls or the sliding of the ground caused by the earthquake would be found. The probability of the return of an earthquake on the fault of Saint B  at was forecasted to be null in the next 50 years [174].

3.2. *In situ* discontinuity measurements

As mentioned in the section 2.1, two conventional methods for an *in situ* collection of discontinuity data of rock masses are the scan-line method and the window sampling method. In addition, the aerial photography and the laser scanning methods are the latest technologies that have been adopted for measuring and describing the exposed rock faces. Among these methods, the first one is the most simple, economic and explicit. Indeed, with the simple requirement of only a measuring tape, a waterproof visible marker (spray-paint as a suggestion), a geotechnical compass and at least two labourers, a working team can be ready for a scan-line investigation. The selection of the research rock face is based on its representation ability for the whole interested rock mass, its security and the convenient working conditions. In addition, a sufficient large rock face that contains at least 150 to 350 discontinuities is suggested by S. Priest [6].

Due to the simplicity of the scan-line methods, it was decided to use it as the investigation method for our geological survey. It should be recalled that in 2004, inside the castle gallery, LRPC Toulouse conducted 7 scan-lines of which the longest one was 10m and the

shortest one was 3m [109]. With the great help of M. Gasc-Barbier (LRPC Toulouse), we had an opportunity to study the discontinuities data of these scan-lines and we tried to do the geological treatments for the clustering of discontinuities into main families. However, the maximal quantity of discontinuities on a line has not been satisfied our demand for a reasonable statistical treatment.

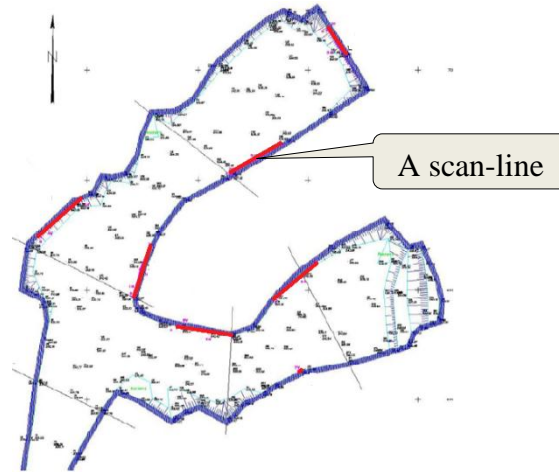


Figure 3.2.1: Plan view of the castle gallery and the position of the scan-lines realised by LRPC Toulouse (sourced from [109])

For the demand of the reliable discontinuity data for the two real applications of our methodology in the scope of this research, the data collection by the scan-line sampling method was decided. Although the castle gallery was the first opportunity due to the good conditions for the investigation, the natural state of its rock faces was fairly destructed by many geological measurements that had been realised for the construction project. Meanwhile, the underground exploitation site of the OMG factory under the Rié mountain, about 1 km from the centre of Saint B  at, 600m from the northern head of the future tunnel, is an ideal place that responds to our demand. The site was composed of one main tunnel and many branches of which the rock faces were in the similar stability condition as in the castle gallery. With the kindly acceptance of the OMG factory, an investigation was realised in November, 2011 by the research team of the “*Ecole des Mines d’Al  s*”, France.

During 2 working days, 3 scan-lines had been realised on three rock faces inside the exploitation tunnel. The longest one is 180.8m, runs along the main tunnel. As the main tunnel was cut by many branches; the scan-line 1 was in fact an assemblage of 9 segments of line that situated on the eastern rock face of the tunnel. The longitudinal direction of this line was nearly coinciding with the longitudinal axis of the future tunnel of Saint B  at. The

total length of this scan-line was measured between two ends of the line but not as the sum of segment lengths. Situated in two branch tunnels that were nearly perpendicular to the main tunnel, a 24.7m and a 26.9m-long scan-lines were also created. More details of these three scan-lines can be seen on the following figures and tables.

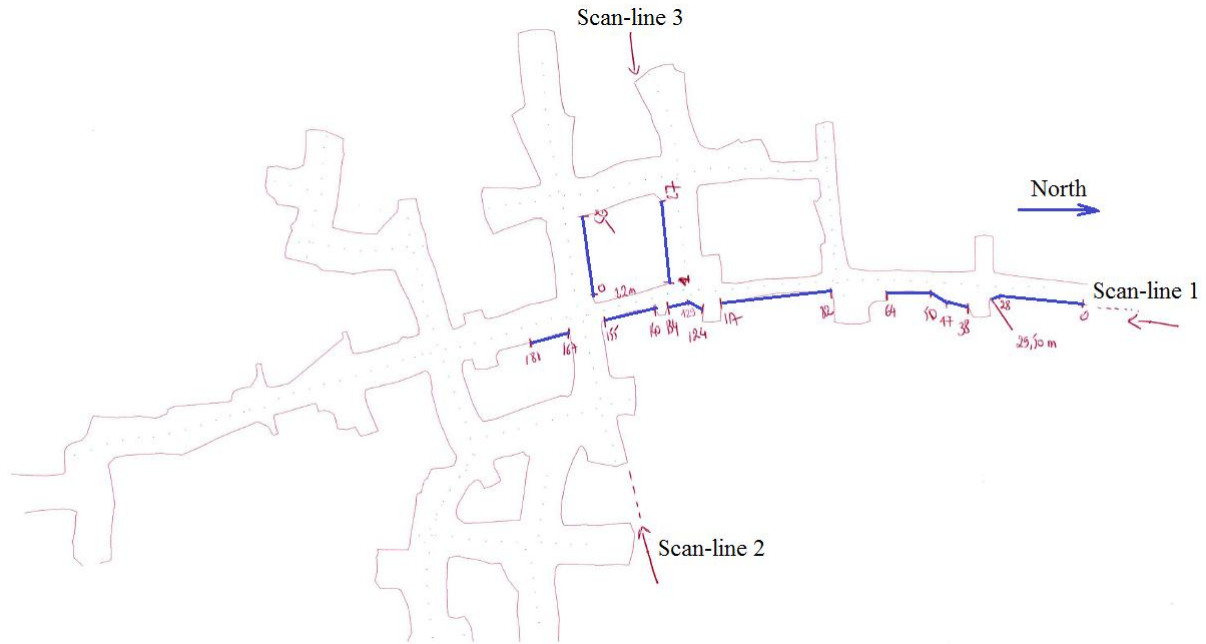


Figure 3.2.2: Sketch of the position of three scan-lines in the underground exploitation site of the OMG factory

Table 3.2.1: Characteristics of the three scan-lines in the underground exploitation site of the OMG factory

Scan-line	Length (m)	Direction	Quantity of discontinuity	Description of rock face
1	180.80	Various	402	Dry and clean
2	24.70	N80°E	22	Wet, covered by rock dust
3	26.90	N75°E	86	Humid, covered by rock dust

Notation: the direction of a scan-line follows the convention of AFTES.



a) Scan-line 1



b) Scan-line 2



c) Scan-line 3

Figure 3.2.3: Surface conditions of the investigation rock faces and their scan-lines

Table 3.2.2: Direction of segments of the scan-line 1 in the underground exploitation site of OMG factory

Segment	Position on the scan-line (m)	Direction
1	0 ÷ 29.84	N25°E
2	38.32 ÷ 44.90	N20°E
3	47.00 ÷ 49.88	N50°E
4	50.10 ÷ 63.80	N5°E
5	82.60 ÷ 116.94	N0°E
6	125.60 ÷ 128.54	N20°E
7	129.08 ÷ 131.82	N170°E
8	139.75 ÷ 154.72	N165°E
9	167.00 ÷ 180.80	N174°E

With the success of the *in situ* investigation by the scan-line sampling method on the rock mass of Saint B  at, the demand of the real and reliable discontinuity data was responded. However, only the data of the 1st scan-line along the main tunnel of the investigation site was proposed to be used because of its great quantity of discontinuities. The obtained data were ready to be immersed in the next step of the geological and geo-statistical processing for the numerical reconstruction of the target rock mass.

3.3. Discontinuity data processing

On the discontinuities data of the longest scan-line realised in the investigation at the underground exploitation site of the OMG factory, a data processing procedure was performed with the following tasks:

- Cluster the discontinuities into main families and determine their centres;
- Study the spatial distribution of the densities of the discontinuities in each family by the geo-statistics;
- Find the fitted statistical laws of the distance and the orientation distribution of the discontinuities in each family by the statistical processing.

With the application of the spectral method of R. Jimenez-Rodriguez and N. Sita [130], four families of discontinuities were found and their centre were determined by the mean vector algorithm. The semi-variograms of the density distribution of the scan-line of the obtained families showed a common spatial characteristic in geology. A Fisher law of the angle distribution and an exponential law of the spacing distribution were assigned for each family. The details of the procedure are presented as following.

3.3.1. Clustering discontinuities into main families

As mentioned in the section 2.2, three typical clustering methods were paid attention to: the spectral method of R. Jimenez-Rodriguez and N. Sita [130], the Fuzzy K-means method of R.E Hammah and J.H. Curran [133] and the method of S. Priest [6]. From the favourable view point of computer-based data processing, we decided to carry out the clustering on 402 discontinuities of the scan-line 1 by the first method. Excel was chosen to be our computer-aided tool with some reasons:

- This is one of a popular office software that can be found in almost all engineering offices;
- Calculations in Excel are clear and nearly identical to any theoretical formula (more precisely “written” ones) so that black-box phenomenon can be avoided.

Most calculations can be executed with the robust data treatment capacity of Excel. Nonetheless, the multi-iterations execution is not a strong point of Excel. We proposed to discretise the iteration into loops, each of which was executed in a separated sheet of calculation. The calculation procedures in all sheets were identified and the obtained results

in the end of the previous sheet were used as the input data at the beginning of the next sheet. Based on the convergence checking situated at the end of each sheet, a conditional function was used to auto-conclude whether a new sheet is needed. It is predicted to be a long procedure of calculations and only semi-automatic since the creation of a new loop must be done by hand. However, the calculations were not heavy because algorithm details in all iterations stayed the same.

Due to the interrupted nature of the scan-line 1, an orientation sampling bias correction was carried out following Terzaghi [129] and S. Priest [130] by calculating the acute angle δ between the unit normal vector of each discontinuity and its sampling segment. The weighting ratio w of the discontinuity was then set as the invert value of cosine of δ . The maximum value of 10 was adopted for w as suggested by S. Priest [130]. This ratio was then multiplied with all Cartesian coordinates of the unit normal vector of each discontinuity.

3.3.1.1. Identification of discontinuity families

Before starting the spectral method for discontinuity clustering into main families, it is needed to assign the number of the main families in the space. Basing on the great diversity of the nature of the discontinuities on the rock faces at the site of investigation, and also in the castle gallery, and referring the clustering results of J. Guittard *et al.* [109], we decided to choose 3 or 4 families. However, only after the total statistical analysis of the distribution of discontinuities, the final conclusion of the number of discontinuities families can be found.

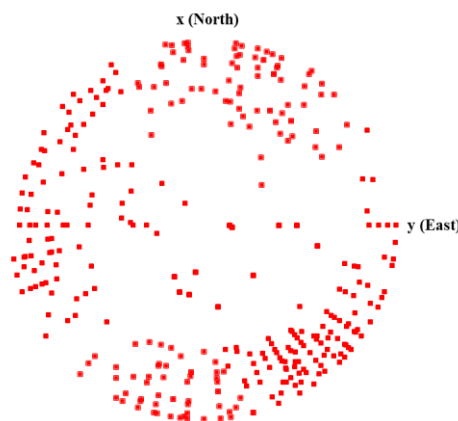


Figure 3.3.1: Equal-area lower hemisphere projection of unit normal vectors
of 402 discontinuities on the longest scan-line

The same clustering procedure was executed for two proposed cases. Before starting the clustering algorithm proposed by R. Jimenez-Rodriguez and N. Sita [130], acute angles between unit normal vectors of any couple of discontinuities and the sine-based similarity measure between them were calculated. Then, the mentioned algorithm was written on Excel to divide 402 discontinuities into 3 or 4 families. Due to the large size (402x402) of the normalized affinity matrix L [130], an additional program was written on Scilab [179] to compute the eigenvalues and the corresponding eigenvectors of L . The decay controlling value σ was set to be 0.12 as suggested in [130].

The clustering results of the two cases were presented on the equal-area lower hemisphere projection of unit normal vectors of discontinuities in the Figure 3.3.2.

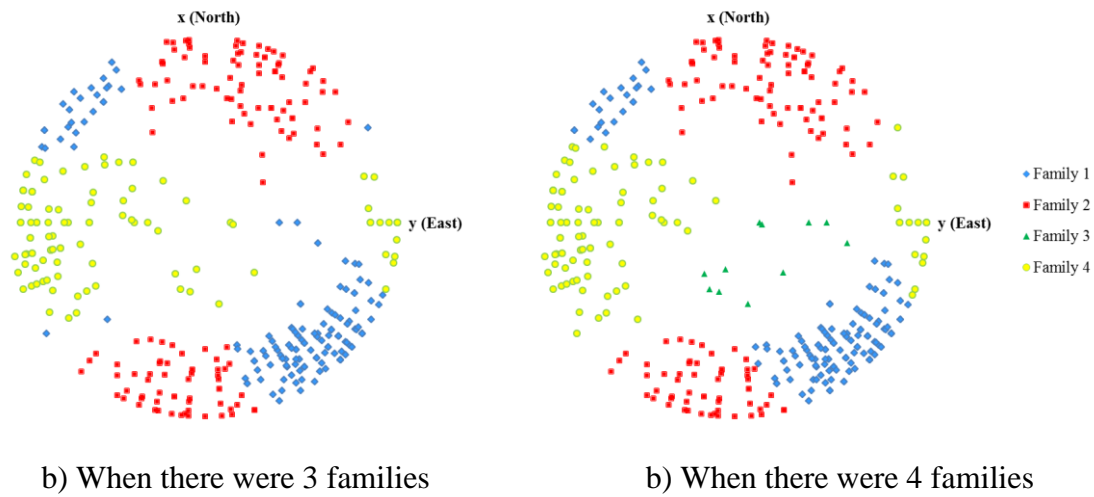


Figure 3.3.2: Equal-area lower hemisphere projection of unit normal vectors of the clustering results by the spectral method

3.3.1.2. Determination of the centre of each discontinuity family

Each discontinuity was represented by its unit vector and expressed by its Cartesian coordinates (x_1^i, x_2^i, x_3^i) . The centre of a family was calculated as the mean of the vector elements created by all family members. From the Cartesian coordinates of the unit vector of the centre of a family (x_1^C, x_2^C, x_3^C) , the orientation of the unit vector of each centre was calculated. The application of the mathematical solution of this geological problem was found simple and effective. However, when a family distributed nearly symmetrically on the two poles of the hemisphere (the family 2 in both cases), the pure mathematical mean - vector calculation for the family centre needed a supplement geological treatment on the obtained results.

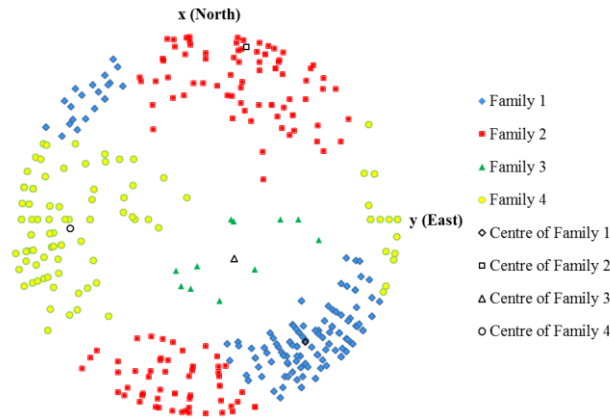


Figure 3.3.3: Equal-area lower hemisphere projection of unit normal vectors of 402 discontinuities in 4 families and their centres

Table 3.3.1: Details of 4 families of 402 discontinuities

Family	Centre of family (directional vectors)		Centre of family (normal vectors)		Quantity of discontinuities
	Trend α_d (°)	Plunge β_d (°)	Trend α_n (°)	Plunge β_n (°)	
F1	321	71	141	19	155
F2	194	81	14	09	138
F3	323	21	143	69	11
F4	86	60	266	30	98

The same work was done for the case when there were 3 families of discontinuities and the results are presented as follow.

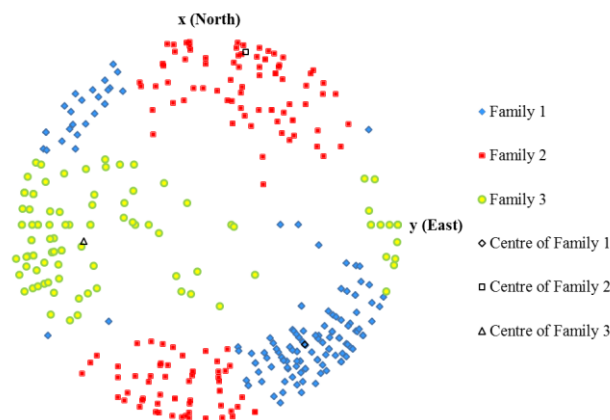


Figure 3.3.4: Equal-area lower hemisphere projection of unit normal vectors of 402 discontinuities in 3 families and their centre by the mean vector calculation

Table 3.3.2: Details of 3 families of 402 discontinuities

Family	Centre of family (directional vectors)		Centre of family (normal vectors)		Quantity of discontinuities
	Trend α_d (°)	Plunge β_d (°)	Trend α_n (°)	Plunge β_n (°)	
F1	320	70	140	20	163
F2	193	81	13	09	140
F3	82	54	262	36	99

3.3.1.3. Geo-statistical processing

In this part, by the use of the geo-statistics, the spatial distribution of the discontinuity densities in each family on the scan-line was studied. The position of members of a family on the scan-line is studied and on a distance scale of which the unit length is h(m), the discontinuity quantity in each h-metre-segment on the scan-line is recorded. The correlation of the quantity of discontinuities and the position on the scan-line was showed on the empirical average semi-variograms of the discontinuity densities with the segment size h of 0.5m, 1.0m and 2m of the scan-line 1. The empirical average semi-variograms showed how semi-variance changes as the position of discontinuities changes. Presented in the following figures and tables, the obtained average semi-variograms presented the same tendency, except for the family 3 of the 2nd case.

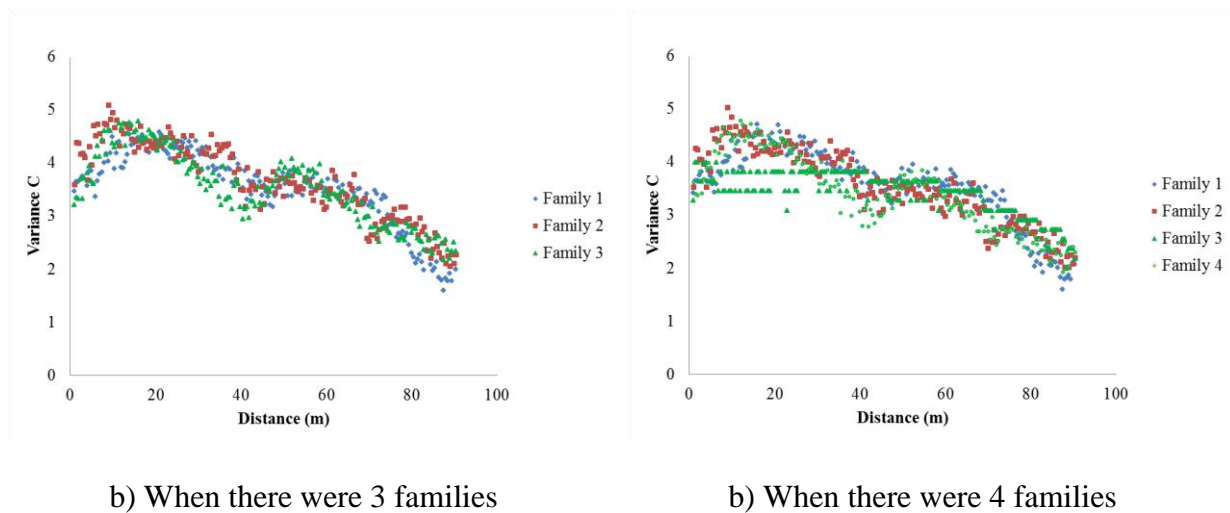
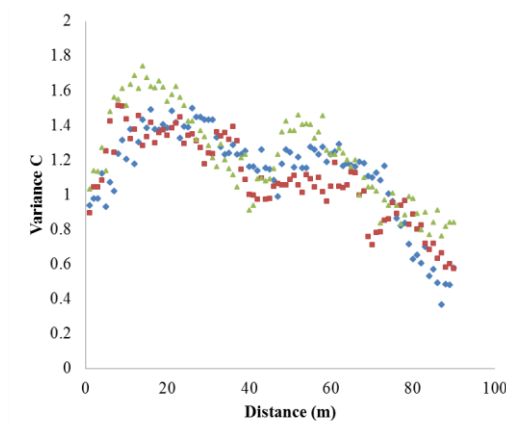
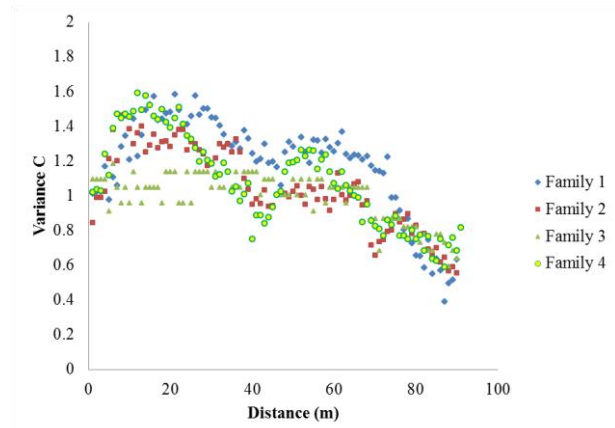


Figure 3.3.5: Average semi-variograms of 402 discontinuities with h = 0.5m

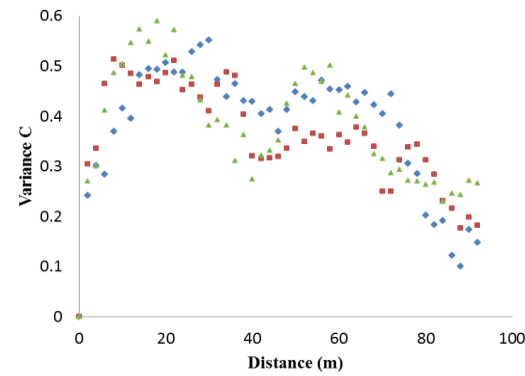


b) When there were 3 families

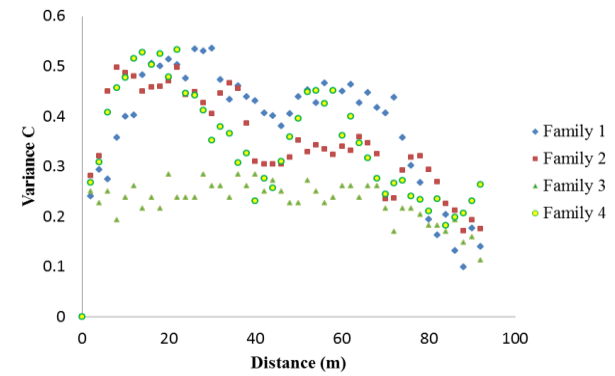


b) When there were 4 families

Figure 3.3.6: Average semi-variograms of 402 discontinuities with $h = 1.0m$



b) When there were 3 families



b) When there were 4 families

Figure 3.3.7: Average semi-variograms of 402 discontinuities with $h = 2.0m$

The form of the obtained curves showed periodic-waved form with the clear hole-effect [6]. Some practical theoretical average semi-variograms were applied on the data of each family. They were then compared with the equivalent empirical average semi-variograms to find the most fitting representative function for the density distribution of discontinuities on the scan-line. Because of the similar forms of the curves of each family with three segment sizes, the work was executed on the case of $h = 2m$ as the representation of the rest. Two most fitted theoretical functions to the curve of each family in two cases of the family number were found and presented.

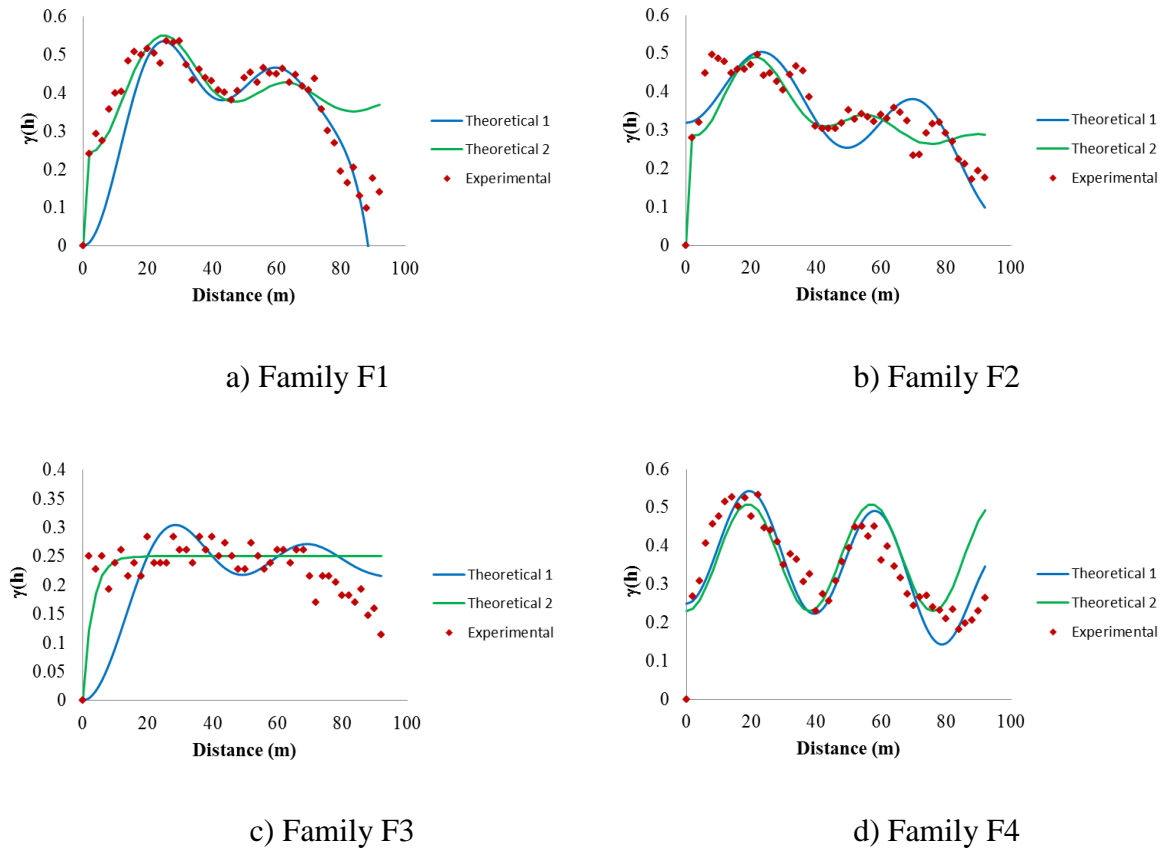
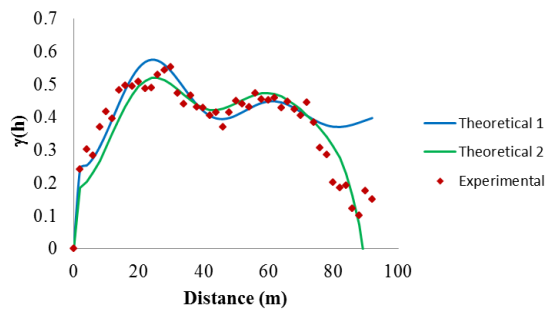


Figure 3.3.8: Experimental and theoretical average semi-variograms
when there were 4 families

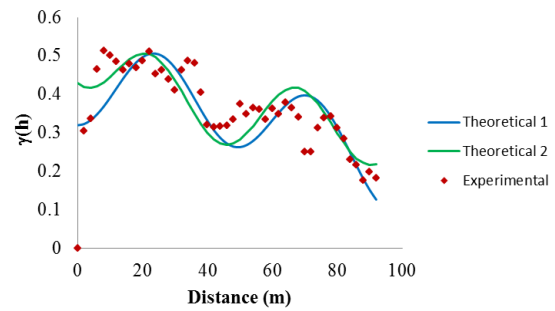
Table 3.3.2: Theoretical average semi-variograms when there were 4 families

Family	Theoretical function 1	Theoretical function 2
F1	$C0+C1*(1-\exp(-(h/a)^2))+C2*(1-\sin(2\pi h/a)/(2\pi h/a))$ <p>Sum of Gaussian and Sinuous hole-effect</p>	$C0+C1*(1-\exp(-(h/a))+C2*(1-\sin(2\pi h/a)/(2\pi h/a))$ <p>Sum of Exponential and Sinuous hole-effect</p>
F2	$C0+C1*(1-\exp(-(h/a)^2))+C2-(1-\cos(2\pi h/a))$ <p>Sum of Gaussian and Cosinuous hole-effect</p>	$C0+C1*(1-\exp(-(h/a))+C2*(1-\sin(2\pi h/a)/(2\pi h/a))$ <p>Sum of Exponential and Sinuous hole-effect</p>
F3	$C0+C1*(1-\exp(-(h/a)^2))+C2*(1-\sin(2\pi h/a)/(2\pi h/a))$	$C(1-\exp(-x/a))$ <p>Spherical</p>

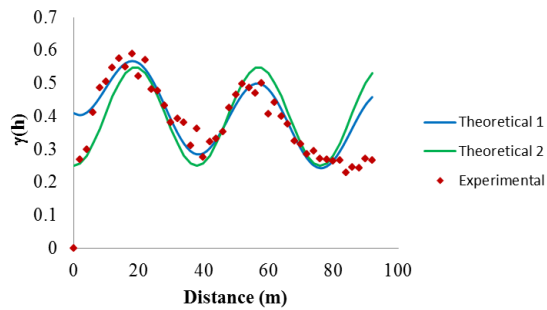
	Sum of Gaussian and Sinuous hole-effect	
F4	$C0+C1*(1-\exp(-(h/a)^2))+C2-(1-\cos(2\pi h/a))$ Sum of Gaussian and Cosinuous hole-effect	$C0+ C1(1- \cos (2\pi h/a))$ Cosinuous hole-effect



a) Family F1



b) Family F2



c) Family F3

Figure 3.3.9: Experimental and theoretical average semi-variograms when there were 3 families

Table 3.3.4: Theoretical average semi-variograms when there were 3 families

Family	Theoretical function 1	Theoretical function 2
F1	$C0+C1*(1-\exp(-(h/a))+C2*(1-\sin(2\pi*h/a)/(2\pi*h/a))$ Sum of Exponential and Sinuous hole-effect	$C0+C1*(1-\exp(-(h/a)^2))+C2*(1-\sin(2\pi*h/a)/(2\pi*h/a))$ Sum of Gaussian and Sinuous hole-effect

F2	$C0+C1*(1-\exp(-(h/a)^2))+C2-(1-\cos(2\pi h/a))$ Sum of Gaussian and Cosinuous hole-effect	$C0+ C1(1-\cos(2\pi h/a))$ Sum of Hyperbolic and Cosinuous hole-effect
F3	$C0+C1*(1-\exp(-(h/a))+C2*(1-\cos(2\pi h/a))$ Sum of Exponential and Cosinuous hole-effect	$C0+ C1(1-\cos(2\pi h/a))$ Sum of Hyperbolic and Cosinuous hole-effect

3.3.2. Statistical processing

The distribution of discontinuities in space was verified in two categories: on a plane (2D space) and on a sphere (3D space). The most fitting statistical law that could fit the empirical distributions were searched.

3.3.2.1 Distance distribution

The distribution of distances between all discontinuities of a given family was checked and a statistical law that fitted was searched. After some trials, we found that the statistical exponential distribution fitted well with the empirical distributions of the researched discontinuities. This law is characterised by ([141]):

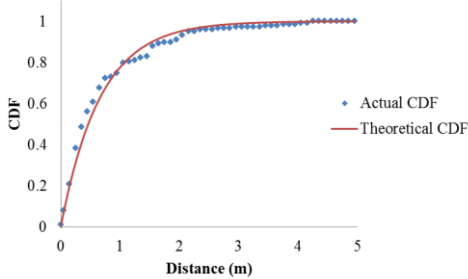
- Probability density function: $\lambda \cdot e^{-\lambda \cdot x}$;
- Cumulative distribution function: $1 - e^{-\lambda \cdot x}$.

The statistical treatment had been realised with the unit scale of distance of 0.1m and the following results were obtained.

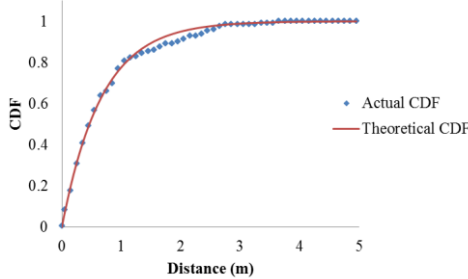
Table 3.3.5: Function of the spacing distribution around the centres of discontinuities families

When there were 3 families	Mean parameter $\mu = \frac{1}{\lambda}$	When there were 4 families	Mean parameter $\mu = \frac{1}{\lambda}$
F1	0.63291	F1	0.66667
F2	0.66667	F2	0.66667

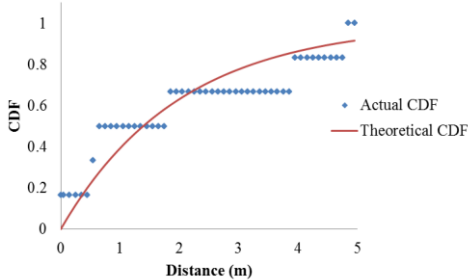
F3	0.72464	F3	2.0
		F4	0.79365



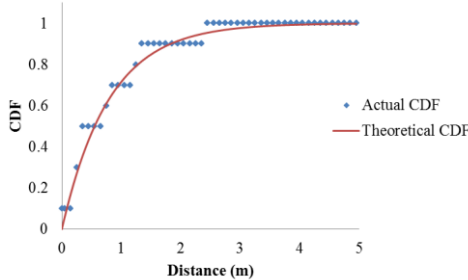
a) Family F1



b) Family F2

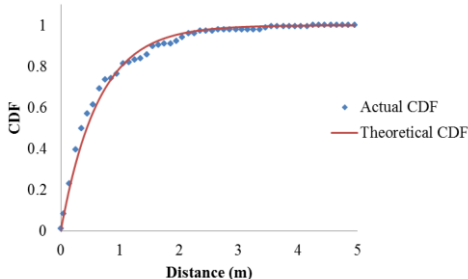


c) Family F3

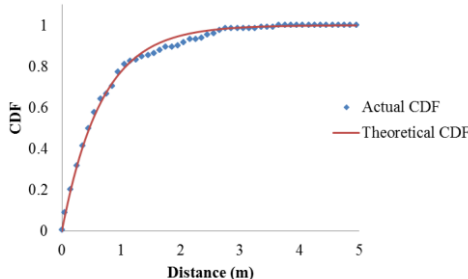


d) Family F4

Figure 3.3.10: Experimental and theoretical cumulative density curves
when there were 4 families



a) Family F1



b) Family F2

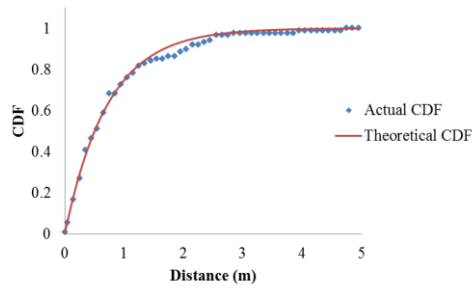


Figure 3.3.11: Experimental and theoretical cumulative density curves when there were 3 families

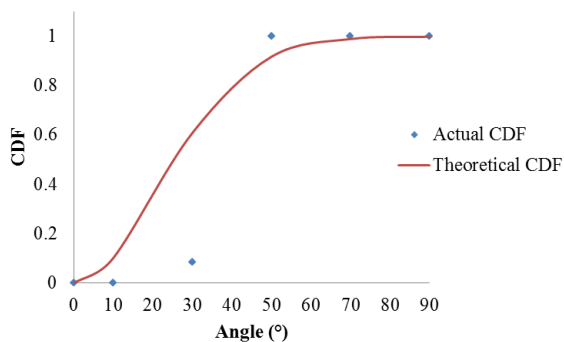
c) Family F3

3.3.2.2. Orientation distribution

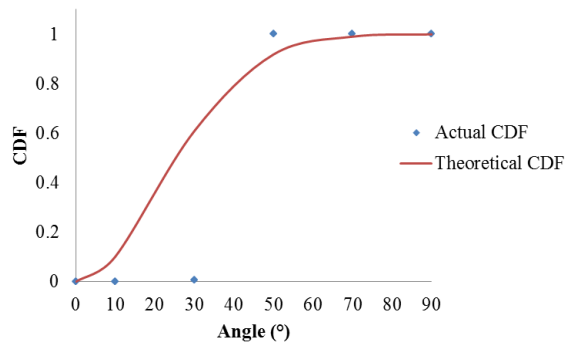
Building a cone on the centre of a family with the assumed cone angle of 20° , it was verified that the distribution on the spherical space of all members of the family followed the statistical law of Fisher. The achieved results are presented in table 3.3.8 and figure 3.3.12 and figure 3.3.13.

Table 3.3.6: The dispersion parameter of Fisher law of 4 families of discontinuities

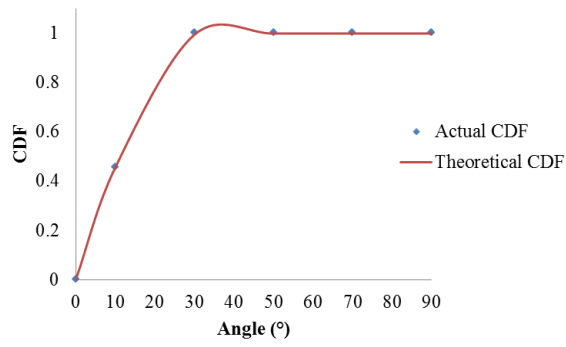
When there were 3 families	Dispersion parameter K	When there were 4 families	Dispersion parameter K
F1	14.5	F1	7.0
F2	22.0	F2	7.0
F3	4.5	F3	40.0
		F4	6.0



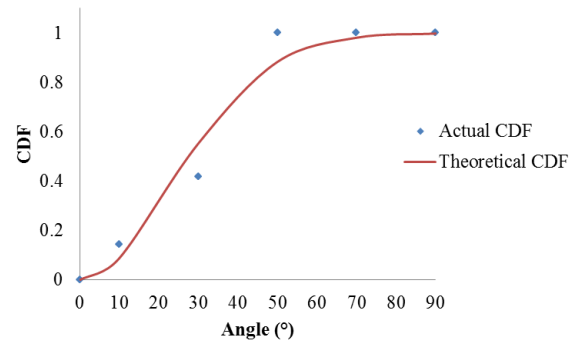
a) Family F1



b) Family F2

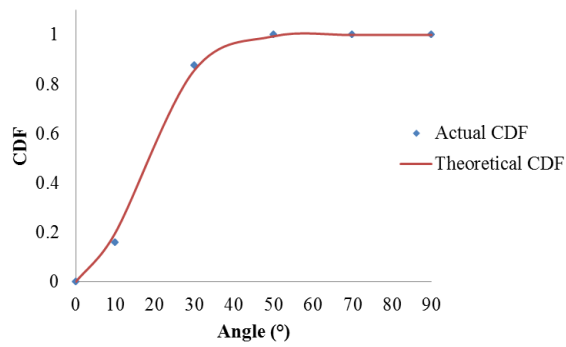


c) Family F3

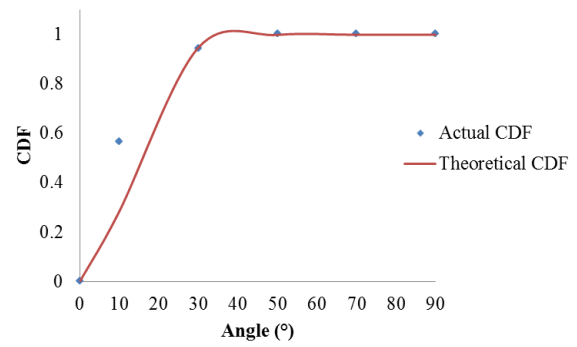


d) Family F4

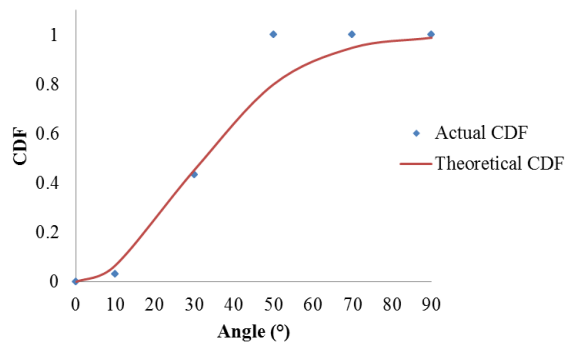
Figure 3.3.12: Theoretical and empirical cumulative distribution curves of the distribution on a spherical space when there were 4 families



a) Family F1



b) Family F2



c) Family F3

Figure 3.3.13: Theoretical and empirical cumulative distribution curves of the distribution on a spherical space when there were 3 families

3.3.3. Commentaries on the obtained results

The geological and geo-statistical processing were executed on the 402 discontinuities of the longest scan-line of the *in situ* investigation presented in the previous part. Two cases of the discontinuity distribution were proposed. Through the geological and geo-statistical treatment procedure of the distribution of the discontinuities on the scan-line, some commentaries on the obtained results were given.

3.3.3.1. Identification of the main families

- In the 1st case when there were 4 main families: On the equal-area lower hemisphere projection of unit normal vectors, the distribution cloud of each family of this case was found to be clear and net. There were a non-equilibrate in the discontinuity quantity of the four families when the third family was quite miner in comparison with the rest.
- In the 2nd case when there were 3 main families: Compared the hemisphere projection of this case with the previous case, no great difference was found. On a quick glance, the family 3 of this case was formed by the combination of the family 3 and the family 4 of the previous case. In details, the family 3 of the 1st case was mobilised into the three other families together with several changes of member between the families. However, the distribution cloud of each family on the hemisphere of this case was found to be less net than the previous case with two regions between the clouds of the three families (see the next figure).

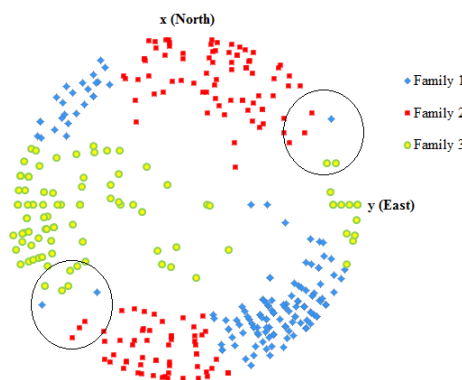


Figure 3.3.14: Distribution clouds on the equal-area lower hemisphere projection of unit normal vectors when there were 3 discontinuity families

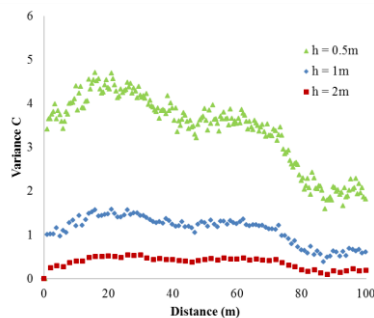
3.3.3.2. Determination of the centre of the main families

The results of the centre of the main families of the two cases enforced the initial conclusion of the difference between the two cases of distribution when the position of the centre of the family 1, 2 and 4 of the 1st case were nearly coincide with the centre of the family 1, 2 and 3 of the 2nd case.

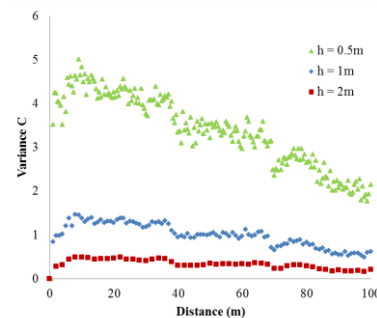
3.3.3.3. Spatial distribution of the discontinuity densities of each family

The average semi-variogram of the spatial distribution of the density of each family in each case was built. It indicated the variation of the family densities when the distance between its discontinuities changed. Three segment sizes h of 0.5m, 1.0m and 2m were used to build the target average semi-variograms. Based on the obtained results, we found that:

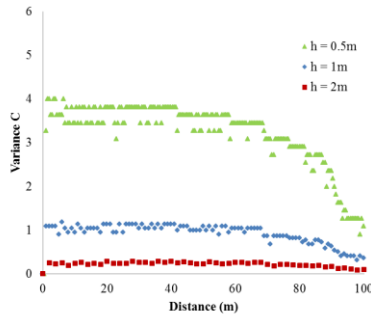
- The periodic-waved form with the clear hole-effect was the structural similarity of the average semi-variograms of all families except the family 3 of the 1st case. This hole-effect structure indicated the periodicity of the distribution of the discontinuities, which is a common and legitimate spatial characteristic in geology [69]. Compared the equivalent curves of each family, the same structure was found which was considered as the stable feature of their density distribution on the scan-line.
- For further understand the variation of the periodic-waved form of the obtained curved with different segment size, the comparison of the 0.5-metre-semi-variogram, the 1-metre-semi-variogram and the 2-metre-semi-variogram of each family was realised. The nugget effect of the curves was considered to be inversely proportional to the segment size: the variance interval in each monotonous-gradient-period of the curve development, the maximal difference between the furthest points.



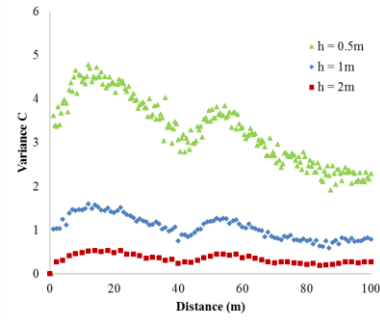
a) Family 1



b) Family 2



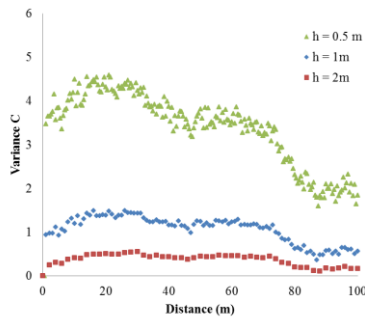
c) Family 3



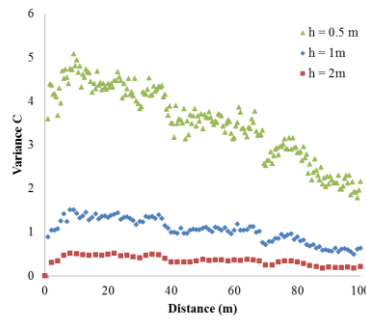
d) Family 4

Figure 3.3.15: Average semi-variograms of the discontinuity densities
for the three segment sizes in the case of 4 main families

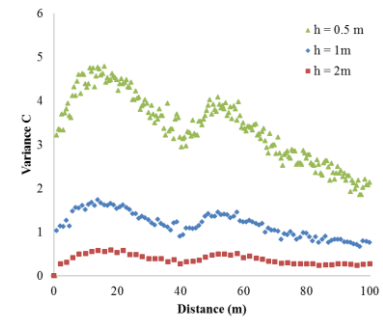
- The forms of the average semi-variograms of the family 3 of the 1st case were different from the equivalent curves of the other families but did not change when the segment changed. Having the same feature of distribution, the separation of the discontinuities in this family with the others was proven.



a) Family 1



b) Family 2



c) Family 3

Figure 3.3.16: Average semi-variograms of the discontinuity densities
for the three segment sizes in the case of 3 main families

In order to verify if the density distribution of each family on the scan-line was geo-statistical conformed, some popular theoretical function of the geo-statistical distribution were built on the data of the family. As the matter of fact that the average semi-variograms of each family with three different segment sizes had the same structure, the processing on the 2-metre-segment semi-variograms were executed as the protocol. Regarded on the two most fitted theoretical functions, the Sinuous/Cosinuous periodic functions of the hole-effect were always presented. This result strongly proved the above judgement on the structure of the curves.

3.3.3.4. Statistical distribution of the discontinuities in their family

The discontinuity distribution in their family was studied: the distance distribution on the scan-lines and the angle distribution on a sphere. The fitted theoretical functions to the empirical curves were searched. The statistical exponential function was applied for the 1st distribution and the statistical Fisher function was applied for the 2nd one. The results showed the statistical conformed distributions of all families and validated the decision of the representative theoretical functions. The distribution of the family 3 of the case of 4 families was not very clear in the distance distribution but contrary in the angle distribution when the empirical curve was nearly coincide with the equivalent theoretical one. It emphasised the specific characteristic of the spatial distribution of this family in comparison with other families.

After the geological and geo-statistical processing, the decision of the family number in 402 discontinuities was proven by the well fitted distribution of the discontinuity densities, the distance and the angle of the discontinuities in each family. Although the results of the 4-family-case was more diversified than the 3-family-case, the specific but reasonable distribution feature of the family 3 of the 1st case did not allow us to decline it. Assured not to wrong conclude on the real distribution of the rock structure in the marble of Saint B  at at our investigation site, we decided to take the both cases in consideration for the generation of the geometrical models of the target rock mass.

3.3.4. Conclusion

On the results of the *in situ* investigation by the scan-line sampling method realised in the underground exploitation site of the OMG factory, the geological and geo-statistical processing were performed. By using the spectral clustering method proposed by R. Jimenez-Rodriguez and N. Sita [130], 402 discontinuities were divided into 4 families (Case 1) and 3 families (Case 2). The mathematical mean-vector algorithm was used to determine the centre of each family. Next, the spatial distribution structure of members of each discontinuity family, in two cases, was studied by the construction of the semi-variograms. Then, the variation of discontinuities position on the space was studied for details on a plane (in 2D) and on a sphere (in 3D). The distribution of discontinuities on the space was researched and presented according to three statistical indicators: the semi-variograms, the distance distribution and the angle distribution.

3.4. Geometrical modelling of the marble of Saint B  at

With the results of the discontinuity processing in the previous step, the complex network of discontinuities had been replaced by the main discontinuities families. Each family was represented by its centre and its spatial distribution laws. Those results were repeated in the two following tables.

Table 3.4.1: Discontinuity data of the rock mass when there were 4 discontinuity families

Family	Centre (Directional vectors)		Spatial distribution law		Quantity of discontinuities
	α_d (�)	β_d (�)	Exponential law λ	Fisher law K	
F1	321	71	1.5	7.0	155
F2	194	81	1.5	7.0	138
F3	323	21	0.5	40.0	11
F4	86	60	1.26	6.0	98

Table 3.4.2: Discontinuity data of the rock mass when there were 3 discontinuity families

Family	Centre (Directional vectors)		Spatial distribution law		Quantity of discontinuities
	α_d (�)	β_d (�)	Exponential law λ	Fisher law K	
F1	320	70	1.58	14.5	163
F2	193	81	1.50	22.0	140
F3	82	54	1.38	4.5	99

The obtained results from the data treatment of the discontinuity distribution on the investigated rock mass were used as the input data for this step for the creation of the 3D geometrical models of the rock mass of Saint B  at on the RESOBLOK code. Two specific models were the first applications:

- the conformed specimen for the triaxial compression test;

- the multi-phase excavation procedure of a tunnel in rock.

The procedure was composed of the generation of the 3D models and the selection of the critical creations was based on the preliminary stability analysis on RESOBLOK. The details are presented in the following parts.

3.4.1. Scenarios of the geometrical modelling

On the *in situ* observations in the castle gallery and in the underground exploitation site of the OMG factory in Saint B  at, the discontinuity intersection on the monitored rock faces was found to be one of the three following cases:

- The discontinuities did not cross each other;
- The discontinuities maintained their continuity after the intersection with other discontinuities;
- One discontinuity was interrupted after the intersection with another discontinuity.

Based on this observation and on the distribution features of the families of discontinuities that have been carefully studied in the sub-section 3.3, five possibilities of the fractured network of the rock mass were proposed and assigned in five scenarios:

- Group 1: when there were 4 families:
 - o Scenario 1: all families maintained their continuities after the intersections with each other;
 - o Scenario 2: all families maintained their continuities after the intersections with each other except the family 3;
 - o Scenario 4: all families were blocked after the intersections with each other;

The family 3 was selected to be blocked after the intersection with other families due to the least structured state of the family distribution shown on the average semi-variogram.

- Group 2: when there were 3 families:
 - o Scenario 3: all families maintained their continuities after the intersections with each other;
 - o Scenario 5: all families were blocked after the intersections with each other;

The details of those scenarios were presented in the Appendix B.

The upper threshold of the simulation number (*i.e.* N_{\max}) of RESOBLOK was taken as the sufficient simulation quantity of each scenario in this research. By the execution of the BGL on the RESOBLOK code, 100 simulations x 5 scenarios of both cases were generated. If an excavation exists in the model, the preliminary stability analysis on RESOBLOK was executed aiming at the determination of the critical cases among the created simulations. This was the case of the approach 2 and 3 of the multi-phase-excavation simulation (see the section 2.3.4). If else, the stability analysis in the scope of this step was skipped and the obtained geometrical models were exported directly to the LMGC90 code. This was the case of the rock specimen for the conformed triaxial tests (see section 2.3.3) and the approach 1 of the multi-phase-excavation simulation (see the section 2.3.4).

3.4.2. Generation of a cylindrical model

For the purpose of a numerical simulation for a triaxial compression test on fractured rock, we prepared a typical model that conformed to some technical standards ([145], [146], [147], [148]) in the scope of our reference. Hence, a numerical cylindrical model with the height $H = 10$ m and the round cross-section with the radius $R = 2.5$ m was created.

A rock mass of $10 \times 10 \times 10$ (m) with the following characteristics was declared:

- The “zone_of_interest”:

$$\begin{cases} x = (-5, 5) \\ y = (-5, 5) \\ z = (0, 10) \\ FO = \{0, 0\} \end{cases}$$

- The medium is homogenous with the density of 2600 kg/m^3 , the friction angle of the discontinuity $\varphi = 22^\circ$ without cohesion ($C = 0$).
- The fracture conditions followed by five scenarios, respectively.

Choosing the big dimension for the model, we aimed at presenting the strongly fractured condition of the marble of Saint B  at. As an example, in the simulation number $N = 14$ of the scenario 4, the big dimension model ($H = 10$ m, $D = 5$ m) was generated from 514 rock blocks while the 10-time-smaller model ($H = 1$ m, $D = 0.5$ m) was constituted of only 3 rock blocks. The obtained models were directly exported to LMGC90 from RESOBLOK using the option “Export only the excavation” as the data files *.dat and then immersed into the Pre-Processor of LMGC90.

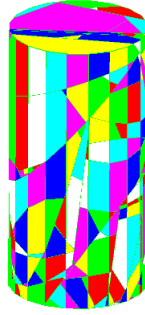


Figure 3.4.1: Cylindrical model generated from the scenario 4 with $N = 14$

3.4.3. Generation of a tunnel excavation model

Geometrical models of a tunnel during the excavation progress were generated with the form of a cylinder $R = 2.5$ m, $L = 10$ m in the middle of a rock mass of $10 \times 10 \times 10$ (m) following the fracture conditions of the five mentioned scenarios. The simulation quantity for each scenario was assigned to be 100 aiming fully embracing the diverse cases of block generation from those scenarios. The tunnel will be regularly excavated in 4 phases, the excavation length in each phase $L_i = 2.5$ m. Since the direction of the tunnel was almost coincide with the direction of the scan-line 1 in the underground exploitation site of the OMG factory at Saint B  at, the direction of the tunnel in the model was neglected.

3.4.3.1 Approach 1

The generation was carried out according to the approach 1 of the geometrical modelling generation presented in the section 2.3.3a. The same rock mass as the modelling of the cylindrical model was declared and then generated with 5 different scenarios. Since the excavation was not existed in the geometrical models created on RESOBLOK of this approach, the preliminary stability analysis cannot be executed. The created models were exported to LMGC90 as the data files *.dat and then immersed into the Pre-Processor of LMGC90.

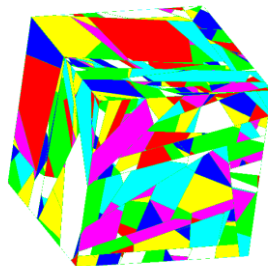


Figure 3.4.2: Models of the rock mass “without hole” of the scenario 4 with $N = 14$

3.4.3.2 Approach 2

The generation was carried out with the principal of the approach 2 of the geometrical modelling generation that is presented in the section 2.3.3b. In the first scenario file, the same rock mass as the modelling of the cylindrical model was declared. A 2.5-metre-long-excavation was generated in the middle of the rock mass. It was situated along the axe of the future tunnel with the coordinated $Y_1 = [0, 2.5]$. The rock mass, with the presence of the 2.5-metre-long-excavation, became “holed”.

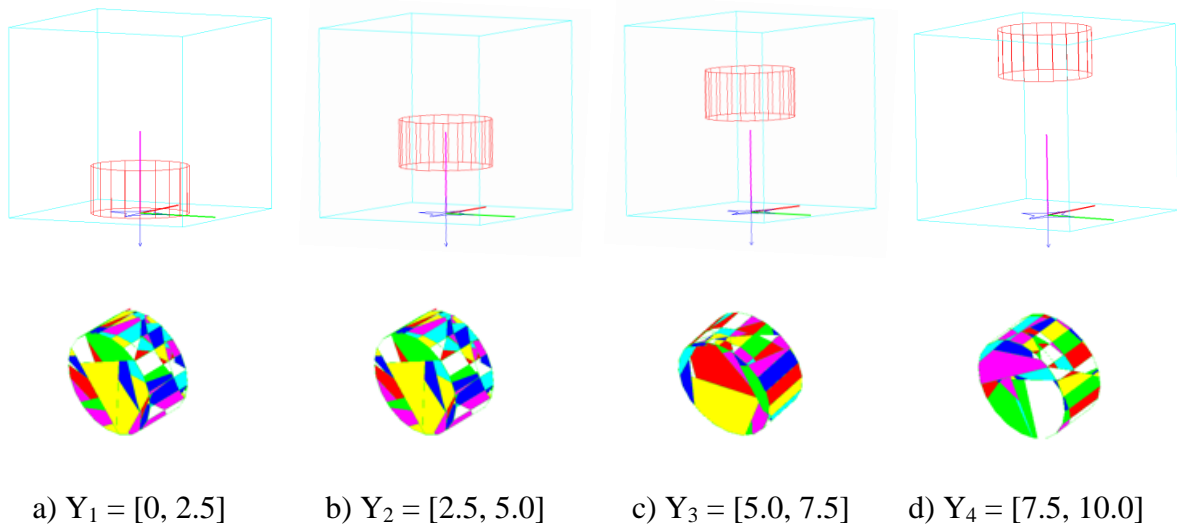


Figure 3.4.3: Excavation segments of the Scenario 4 when $N = 14$

Two zones of the rock mass are exported to LMGC90: inside the excavation (file 1.dat) and the surrounding medium (file 0.dat).

In another three scenario files, a same rock mass as in the first one is created. A 2.5-metre-long-excavation is generated in the middle of the rock mass. It is situated along the axe of the future tunnel with the coordinated $Y_2 = [2.5, 5.0]$; $Y_3 = [5.0, 7.5]$; $Y_4 = [7.5, 10.0]$, respectively. The models of the three excavations were exported to LMGC90 in the file 2.dat, 3.dat and 4.dat, respectively.

3.4.3.3 Approach 3

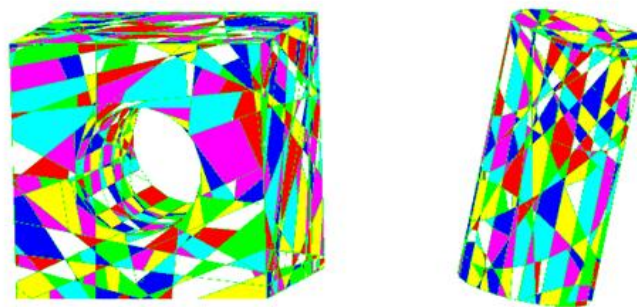
The generation was carried out according to the approach 3 of the geometrical modelling generation that is presented in the sub-section 2.3.3c. First, the same rock mass as in the modelling of the cylindrical model was declared. Then, a 10m-long-cylindrical excavation of which the cross-section formed by 20 tangential planes of the inscribed circle of $R = 2.5\text{m}$ was generated in the middle of the rock mass. The total rock mass was divided into two zones: outside (model 1 “with hole”) and inside (model 2) the excavation. Next, by

setting the simulation number $N = 100$, we obtained 500 combinations of the model 1 “with hole” and the model 2.

With the different values of the minimal volume of an individual block in the models (0m^3 , 0.01m^3 and 0.1m^3 , respectively), the obtained models changed when all smaller blocks were eliminated. Studying the relation between this parameter and the number of blocks in the generated models, the number of blocks was found to be decreased quickly with a light augmentation of V_{\min} . The results of the 1st simulation of five scenarios are shown in the next table as an illustration.

Table 3.4.3: Correlation of the rock block quantity and the minimal block volume of the 1st simulation of five scenarios

Scenario ($N = 1$)	$V_{\min} = 0\text{ m}^3$		$V_{\min} = 0.01\text{ m}^3$		$V_{\min} = 0.1\text{ m}^3$	
	Model 1 (m^3)	Model 2 (m^3)	Model 1 (m^3)	Model 2 (m^3)	Model 1 (m^3)	Model 2 (m^3)
1	5970	1359	3520	906	1971	549
2	9259	2764	3902	1227	1779	527
3	6112	1447	3722	917	2068	592
4	1354	255	1116	204	896	189
5	906	228	777	161	722	190



a) Model 1: the rock mass “with hole”

b) Model 2: the excavation

Figure 3.4.4: Two models of the Scenario 1 when the simulation $N = 1$

3.4.4. Selection of the representative simulations by the preliminary stability analysis on RESOBLOK

Choosing $N = 100$, we had generated 500 simulations in module BG for each approach. The quick stability analyses by using the module BSA and BSAH of RESOBLOK were carried out and the extreme cases were figured out using the following criteria:

- Criterion 1: Maximal quantity of unstable blocks;
- Criterion 2: Minimal quantity of unstable blocks;
- Criterion 3: Maximal volume of unstable blocks;
- Criterion 4: Minimal volume of unstable blocks.

As mentioned above, this task was only executed on the models generated from the 2nd and the 3rd approach of the tunnel simulation.

3.4.4.1. Approach 3

On the 3D geometrical models of the rock mass and its full-length-excavation, the stability analysis were realised and leaded to the results in the Table 3.4.4

Table 3.4.4: Extreme simulations of 5 scenarios following the given criteria

Scenario	Criterion 1	Criterion 2	Criterion 3	Criterion 4
1	$N = 8$ $n = 5736$	$N = 4$ $n = 0$	$N = 5$ $V = 316.02$	$N = 4$ $V = 0$
2	$N = 5$ $n = 5496$	$N = 1$ $n = 0$	$N = 3$ $V = 330.53$	$N = 1$ $V = 0$
3	$N = 8$ $n = 4117$	$N = 10$ $n = 0$	$N = 7$ $V = 341.81$	$N = 10$ $V = 0$
4	$N = 18$ $n = 86$	$N = 14$ $n = 0$	$N = 4$ $V = 24.01$	$N = 14$ $V = 0$
5	$N = 2$ $n = 65$	$N = 17$ $n = 10$	$N = 8$ $V = 29.25$	$N = 14$ $V = 1.08$

Notations of the table:

N: the corresponding simulation number

n: the unstable blocks quantity

V: the unstable blocks volume (m³)

We were interested in three simulations where no unstable blocks were found:

- Simulation 4 of the Scenario 1;
- Simulation 10 of the Scenario 3;
- Simulation 14 of the Scenario 4.

In those simulations, the presence of the excavation did not affect the rock mass and did not lead to any unstable blocks in the model. Based on the stable condition that we had observed in the castle gallery in the Cap du Mont and the underground exploitation tunnel of the OMG factory in the Rié mountain at Saint B  at, we found that the three above simulations had high probabilities to be the best numerical generations of for the future tunnel at Saint B  at. They were proposed to be the representations of 100 simulations that we had created on the fracture data of the investigation site.

3.4.4.2. Approach 2

The same works that had been done with the simulations of the approach 3 were carried out on the generation cases of the approach 2 and the results of the scenario 1 are shown in the next table as an example.

Table 3.4.5: Extreme simulations of scenario 1 following the given criteria

Excavation segment	Criterion 1	Criterion 2	Criterion 3	Criterion 4
1	N = 11 n = 73	N = 0 n = 0	N = 3 V = 18.84	N = 7 V = 0
2	N = 11 n = 41	N = 17 n = 2	N = 2 V = 4.55	N = 17 V = 0.01
3	N = 10 n = 21	N = 9 n = 0	N = 18 V = 1.93	N = 9 V = 0

4	N = 8 n = 3	N = 7 n = 0	N = 1 V = 0.48	N = 7 V = 0
---	----------------	----------------	-------------------	----------------

Notations of the table:

N: the corresponding simulation number

n: the unstable blocks quantity

V: the unstable blocks volume (m³)

It was noted that the generation procedure and its equivalent simulations of a segment did not forcedly coincided with those of the other segments. We did not carry out a research on the correspondence of the simulation number generated in 4 segments of the model. Hence, at the limit of this research, the preliminary stability analysis on RESOBLOK of this approach, if need, was suggested to carry out on the rock mass with the full-length-excavation. The representative simulations of the approach 1 were taken to be the representatives of this approach.

3.4.5. Initial determination of the sufficient quantity of simulations for each scenario of the model generation

For better understanding of the influence of the simulation quantity and the critical cases of the model generation, we decided to execute a parallel procedure from the model generation to the stability analysis on RESOBLOK on 5 given scenarios of which only 20 simulations for each scenario were created. The results of the stability analysis of the 20-simulation-case were compared to the equivalent results of the 100-simulation-case. The results of the 1st scenario were presented in the Table 3.4.6 as an example.

Table 3.4.6: Critical simulations of 1st scenarios followed the given criteria in two cases

Case	Criterion 1	Criterion 2	Criterion 3	Criterion 4
20-simulation-case	N = 8 n = 5736	N = 4 n = 0	N = 5 V = 316.02	N = 4 V = 0
100-simulation-case	N = 8 n = 5736	N = 4 n = 0	N = 99 V = 352.92	N = 4 V = 0

Notations of the table:

N: the corresponding simulation number

n: the unstable blocks quantity

V: the unstable blocks volume (m^3)

Studied on those results, the critical simulations following the four criteria in the 20-simulation-case and in the 100-simulation-case were nearly identic. The other scenarios were showed the similar phenomenon. As a matter of fact, the extension of the generated simulations until 50 (followed [12]), 70 (following our proposition in the section 2.3.2.2) or until 100 (the maximal threshold of the code) for each scenario was considered to be not necessary. Generating 20 simulations of each scenario, we did not totally record the same critical simulations as the 100-simulation-case but the difference was not really considerable. Hence, this value was advised to be sufficient for the quick but assured generation of the geometrical models in our methodology. However, the probability of the hazardous coincidence in the obtained results from those two parallel generation procedures was taken. Underlined that the above cross-checking was only realised on the specific rock mass of Saint B  at, the commentary on the sufficient quantity of simulation for a scenario was given only on the obtained results by this validity approach. More scenarios of the diversified rock masses are needed to be realised on the same approach presented in this section, before giving the final conclusion of the matter.

Further details of the comparison between the 20-simulation-case and the 100-simulation-case were presented on the Appendix B.

3.4.6. Conclusion

With the use of RESOBLOK on the data of the previous step, the geometrical models of the rock mass and the tunnel in many scenarios and rock blocks assembly were achieved. The statistical distribution in number and in volume of blocks associated with each individual simulation and summarised in each scenario were also obtained. They were used as a reference for the selection of the representative models that were exported afterward to LMGC90. In case of the numerical specimens for a conformed triaxial compression test, after the generation of the geometrical models, they were exported directly to LMGC90 for the next steps of the simulation and analysis. In the case of the multi-phase-excavation, aiming a comparison between three proposed excavation approaches, the same assembly condition of rock blocks inside the model was recommended. The preliminary stability analysis on the generated models was carried out and the criterion of the extreme quantity and the extreme volume of the unstable blocks were applied to select the representatives of

the generated simulations. The study were realised on the model generated from the 2nd and the 3rd approach of the excavation simulation. On the obtained results of the block generation of both case of the discontinuity distribution in the rock mass (when there were 3 discontinuity families and when there were 4 discontinuity families), three simulations without the presence of the unstable rock blocks were interested:

- Scenario 1, N = 4;
- Scenario 3, N = 10;
- Scenario 4, N = 14.

This state of generation was close to the stable condition that we had observed in the castle gallery (see section 3.1.2.2) and in the underground exploitation site of the OMG factory under the Rié mountain (see section 3.2) at Saint B  at. For this reason, the three simulations were recommended to be more likely representative of the real fractured and geological conditions of the massif at Saint-B  at. However, due to the restriction of our computer machine, only the last case (Scenario 4, N = 14) which was composed of fewest blocks was chosen to be the representative for the next steps in our methodology.

3.5. Mechanical modelling of the marble of Saint B  at

The mechanical modelling of the marble of Saint B  at was realised as the introduction in the section 2.4 of the previous chapter. The real data sources of this work were taken from the technical documents in the preparation phase of the construction project of the future tunnel of Saint B  at and the related publications ([149], [168], [169], [170], [176], [177],

[178]). Besides, since the obtained mechanical models in this step combined with the geometrical models generated in the previous step for the simulation and analysis of the problems of interest by the use of the LMGC90 code, the selection of the mechanical characteristics and their required parameters was take into consideration of the relevant algorithms and the syntaxes stipulated by LMGC90 ([53], [162], [163], [164], [165]).

This work was concretized into three tasks:

- Choose the mechanical model of the rock mass;
- Select the contact law between the discontinuities and blocks;
- Select the relevant geotechnical parameters for the models.

a) Mechanical models of the rock mass

Two bulk mechanical behaviours of the rock mass for the simulation of the marble of Saint B  at were proposed:

- Rigid behaviour: All rock blocks were assigned to be rigid. They had the rotational and/or translational displacement but their configurations did not change during or after the loading period. The most important parameter for this model was the density of the rock mass $\gamma = 2600 \text{ kg/m}^3$.
- Deformable behaviour: The rock mass and all its constituted blocks were assigned to be deformable under the application of external loads. Three most required parameters for this model were the density of the rock mass $\gamma = 2600 \text{ kg/m}^3$, the modulus of Young $E = 70 \text{ GPa}$, the Poisson coefficient $\nu = 0.3$. The rock was considered as anisotropic with the medium anisotropic index 3.6 %.

b) Contact law between the discontinuities and blocks of the rock mass

On the observations on the rock masses in the castle gallery (the main investigation site of the tunnel project) and on the underground exploitation site of the OMG factory (the *in situ* measurement site of this research) and the related technical documents of the marble of Saint B  at, the discontinuities of the marble of Saint B  at were considered to be very light rough, small or closed opening, very light in-filled or no filling, the presence of the water in the discontinuities was minor. The unilateral Coulomb's law of contact was proposed for the definition of the contact interaction between rock blocks of the model. Two types of contact were suggested for the modelling of the rock mas

- When the discontinuities were closed without filling: The contact was dry and the cohesion was neglected. The dry friction Coulomb's law of contact was used. Two most required parameters were the internal friction angle of the rock $\varphi_m = 22^\circ$ and of the discontinuities 42.8° [149].
- When the discontinuities were opened and in-filled: The cohesive zone models were defined at the contacts between the contact objects. The non-frictional cohesion Mohr-Coulomb's law of contact was used. The required parameters were the aforementioned internal friction angles and the cohesion parameter of 35MPa [149].

c) In situ stresses of the rock mass of Saint B  at

Because the two measurements of the *in situ* stresses of the rock mass of Saint B  at realised by CETE Lyon and INERIS for the tunnel construction project were different in the obtained values, it was difficult to find out the appropriate values. Hence, the *in situ* stresses from the latest campaign of measurement by INERIS [178] in November 2011 were selected and their values were presented in the next table.

Table 3.5.1: *In situ* stresses of the rock mass of Saint B  at

Normal stresses (MPa)		Tangential stresses (MPa)	
σ_x	-2.7	τ_{xy}	1.7
σ_y	-0.7	τ_{yz}	-0.8
σ_z	-1.2	τ_{xz}	-1.6

Notation:

- The negative values represented the compression action and the positive one represented the traction action;
- The coordinates of the stresses in this table followed the reference given in the following figure:

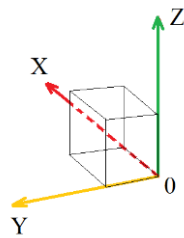


Figure 3.5.1: Reference of the *in situ* stresses of the rock mass of Saint B  at

The litho-static stresses in the vicinity of the tunnel were also taken into consideration as an independent loading case for the mechanical behaviour comparison of the rock mass under the application of the measured *in situ* stresses and the theoretical stresses.

d) Proposed the bulk behaviours of the numerical rock mass of Saint B  at

In the scope of this research, some mechanical models of the target rock mass were proposed:

- The rock mass and its constituted blocks were rigid and the law of contact was the dry friction Coulomb;
- The rock mass and its constituted blocks were rigid and the law of contact was the non-frictional cohesion Mohr-Coulomb;
- The rock mass and its constituted blocks were deformable and the law of contact was the dry friction Coulomb;
- The rock mass and its constituted blocks were deformable and the law of contact was the non-frictional cohesion Mohr-Coulomb;

Referred from the technical documents in the preparation phase of the construction project of the future tunnel of Saint B  at and the related publications ([149], [168], [169], [170], [176], [177], [178]), the proposed geo-technical parameters of the rock mass of Saint B  at for the modelling of the rock mass of Saint B  at were presented in the Appendix 1.

Due to the limitation of this research, only the first proposed mechanical model was combined with the geometrical models generated in the previous step for the simulation and analysis on LMGC90 in the two first applications of our methodology. The other models were hoped to be soon taken into account.

3.6. Study of the mechanical behaviours of the marble of Saint B  at under a numerical triaxial compression test

With the 3D geometrical model created on RESOBLOK with the fracture conditions of the rock faces in the underground exploitation site of the OMG factory, a simulation of a triaxial compression test was realised. In rock and soil engineering, triaxial compression is an important test to determine some geotechnical characteristics of rock such as the Young modulus, Poisson ratio and the triaxial compression strength in laboratory. The uniaxial compression test can be considered as a special case of the triaxial one when the confining pressure is set to be null. Principle of this test can be found in related manuals and standards. [145], [146], [147], [148] were used as our knowledge basis for the simulation. During the test, axial and lateral displacements of the specimen and corresponding pressures are recorded. In a conventional triaxial compression test, the point where the force – deformation curve of the test reaches its peak is most wanted. Sometimes, when no peak can be observed, other equivalent moments can be replaced [145]. The contact responses of the model during the simulation were also our interest and we decided to pay

attention also to the variation of the contact features. Based on the responses of rock core under the compression, some mechanical behaviours of tested rock were studied. Then, a failure criterion was looked for to further analyse the behaviour of the modelled rock mass.

The goals of this simulation, as mentioned in the section 2.5.5, were repeated here:

- Finding equivalent ideal rock (with its recorded numerical mechanical behaviour) that can be replaced the real fractured marble of Saint B  at;
- Verifying the simulation system and the loading charge system by the use of the rigid plats for transferring the applied load on the boundary of the model to all rock blocks of the model;
- Demonstrating the numerical modelling capacity of the proposed methodology for the typical tests in rock mechanics.

The details of the simulation, the obtained results and the commentary were presented in this part.

3.6.1. Modelling and simulation

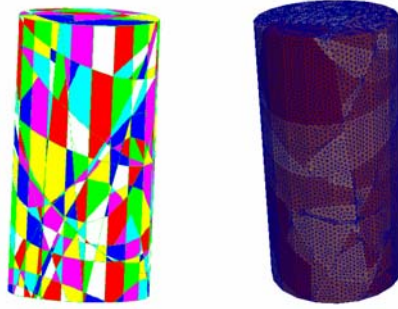
The numerical rock specimen was a cylinder with the height $H = 10\text{m}$ and the diameter $D = 5\text{m}$ (slenderness ratio of 2). Choosing such big size for our specimen, we aim at an acceptable representation of all the families of discontinuities in the rock mass, as monitored *in situ*. The geometrical model of the rock core was generated on the RESOBLOK code (refer the section 3.4.2) and its mechanical model was assigned (refer the section 3.5). As the result, the numerical rock core which had been built on the RESOBLOK code was used as immersed into the Pre-processor of the LMGC90 code as an assemblage of rigid blocks with the dry friction Coulomb's law of contact between them.

3.6.1.1. Reconstruction of the geometrical model in LMGC90

The script GMSH integrated in LMGC90 reconstructed the model from the data of the generation in the input file *.dat and then surface meshed each blocks in the model. The geological conditions of rock mass were defined by the mass density and the contact law between the blocks:

- Based on the almost homogeneous geological condition of the surveyed rock face, only one rock medium was considered with the density $\rho = 2600 \text{ kg/m}^3$;
- There are 514 rigid blocks composing the numerical specimen;

- A rigid block contacted with its neighbours using the IQS_CLB interaction law. This is a combination of the inelastic quasi shock and the dry Coulomb's law ([156]) with the friction coefficient $\mu = \tan(\varphi) = 0.4$ and no cohesion ($C = 0$) of the rock material.



a) Generated by RESOBLOK b) Surface meshed by LMGC90

Figure 3.6.1: Numerical specimen before and after the surface meshing

3.6.2.2. Simulation setting

a) Boundary conditions

All 514 rigid blocks of the model were set to be free in all 6 degrees of freedom (DOF). Ignoring the real position of the rock core in nature, the gravity was neglected in the calculation. They were numbered from RBDY3 number 183 to RBDY3 number 696 in our model.

The loading conditions of a monotonous classical triaxial compression test were simulated by a loading system composed of 182 rigid plates attached to the rock specimen:

- A big square plate with a 5-metre-long-edge was attached under the bottom of the specimen. Its 6 DOFs was all fixed.
- The same big plate was attached to the top of specimen. It was fixed for all its rotational DOFs and free for the 3 translational DOFs. Axial pressure was then applied on the inertia centre of this plate.
- There were 9 rings of 180 small plates of 0.6x0.2x0.4m regularly positioned on the height of the specimen with a centre-to-centre distance of 1.04m. On each ring, 20 plates were symmetrically placed on the periphery. In total, 180 small plates were

fixed in rotation and free in 3 translational DOFs. Lateral pressure was then applied on the inertia centre of each small plate.

Since the rock core is complete dry, no membrane for fluid isolation under the compression is needed. The arrangement of small plates around the periphery of rock core was aimed at evenly distributing the lateral pressure on the specimen. In total, the modelling model was constructed by 696 RBDY3 objects with 7319 contacts PRPRx by IQS_CLB interaction law.

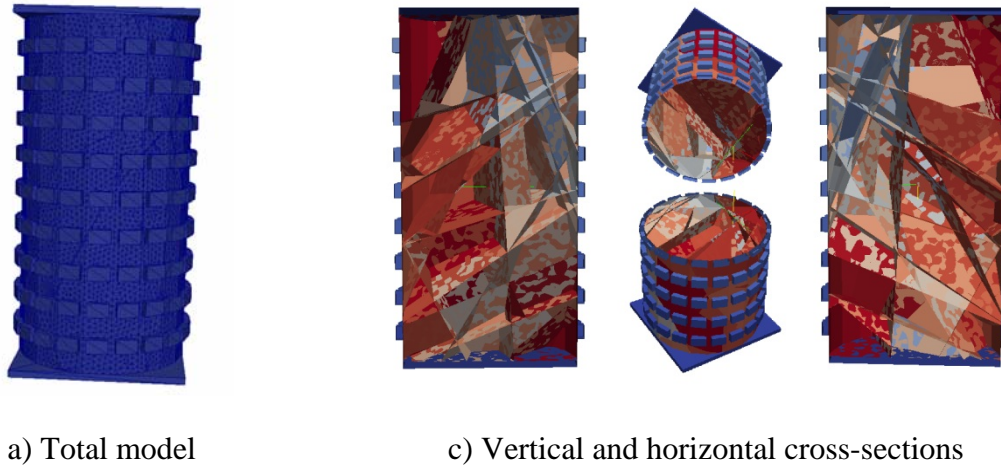


Figure 3.6.2: Numerical model of the simulation

b) Loading conditions

The loading paths for the simulation were based on the principal shown in the section 2.5.5.1 and the Figure 2.5.7. By selecting a load-driving procedure for this simulation, six loading paths were set up. A typical loading procedure can be divided into 4 periods:

- First, the specimen was stabilized during t_0 seconds with no pressure application;
- Second, the axial pressure σ_1 and lateral pressures $\sigma_2 = \sigma_3$ were applied with the same loading velocity v_σ until t_1 seconds;
- Then, all pressures were kept constant $\sigma_1 = \sigma_2 = \sigma_3$ until t_2 seconds;
- Last, lateral pressures $\sigma_2 = \sigma_3$ were maintained while the axial pressure σ_1 was continuously raised with the loading velocity v_σ until the end of the simulation where the axial deformation of the specimen reached 50%.

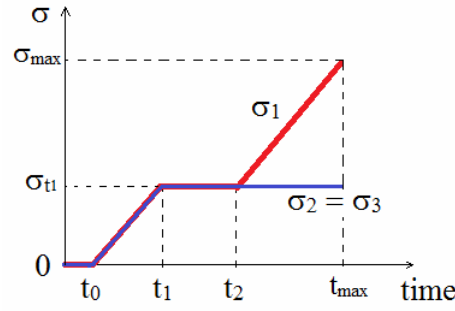
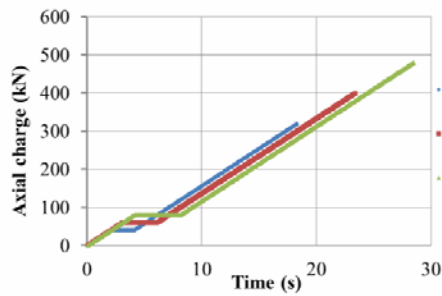


Figure 3.6.3: Scheme of the six loading paths for the simulation

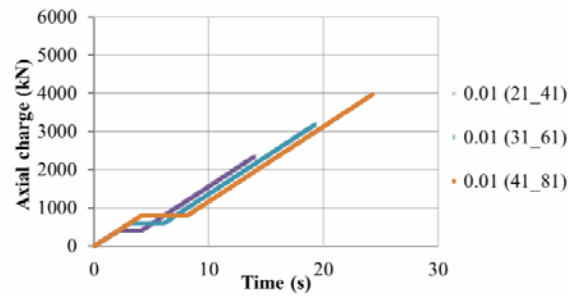
The parameters of the loading paths are listed in the next table of which the positive sign of the velocity of pressure represents the compression action.

Table 3.6.1: Parameters of the six loading paths

Case	v_{σ} (MPa/s)	t_0 (s)	t_1 (s)	t_2 (s)
0.001 (21-41)	0.001	0.1	2.1	4.1
0.001 (31-61)	0.001	0.1	3.1	6.1
0.001 (41-81)	0.001	0.1	4.1	8.1
0.01 (21-41)	0.01	0.1	2.1	4.1
0.01 (31-61)	0.01	0.1	3.1	6.1
0.01 (41-81)	0.01	0.1	4.1	8.1



a) Three first loading paths



b) Three last loading paths

Figure 3.6.4: Sketch of the loading paths of the simulation

The corresponding loading schemas of the loading paths were constructed followed the approach given in the 2.5.5.2. The applied equivalent loads for axial and lateral pressures were determined as follow:

- Axial external force:

$$F_1 = \sigma_1 \cdot S_1$$

And

$$S_1 = \pi R^2$$

With:

F_1 : Axial external force (N)

σ_1 : Axial pressure (N/m²)

R: Initial radius of the cross-section of the specimen (m), R = 2.5m

S_1 : Loading area under the top big plate (m²), $S_1 = 19.64\text{m}^2$

- Lateral external force:

$$F_3 = \sigma_3 \cdot S_2$$

And

$$S_2 = \frac{2\pi R H_0}{n}$$

With:

F_3 : Lateral external force (N)

σ_3 : Lateral pressure (N/m²)

R: Initial radius of the cross-section of the specimen (m), R = 2.5m

H_0 : Initial height of specimen (m), H = 10m

n: Quantity of small plates, n = 180

S_2 : Loading area under a small plate (m²), $S_2 = 0.87\text{m}^2$

c) Selection of the simulation parameters

The NLGS solver (referred the section 2.5.1) was used for solving the contact detection in the model and the relevant numerical parameters were assigned as in the

- Parameter θ of the Crank-Nicholson method: $\theta = 0.5$;
- Time step: $dt = 0.1$ s;
- Convergence norm: $tol = 10^{-6}$;

- Maximal number of calculations in an iterative loop: $gs_it1 = 7000$;
- Numbers of loops in the iteration for each convergence check: $gs_it2 = 20$.

Once the simulation and analysis was started, the mechanical responses of the model was recorded each 10 time steps as the algebra data and as the graphical visualization displays by the PARAVIEW code.

3.6.3. Results and interpretation

The simulation of each case of the loading path was executed until the axial deformation of specimen approached 50%, *i.e.* the axial displacement reached 5m. In the following parts, the mechanical behaviours of the numerical specimen were studied. It was noted that the values of loads, pressures were presented as positive for the action of compression and negative for the tension. However, a positive displacement (as well as the deformation) represents an elongation of the specimen and a negative one shows the inverse: a contraction.

3.6.3.1. Deformations of specimen during the time of simulation

Relative axial displacement:

$$dy = Y_{i+1} - Y_i$$

With:

dy : Relative axial displacement of the specimen (m)

Y_{i+1} : Absolute height of the specimen at the time step $i+1$ (m)

Y_i : Absolute height of the specimen at the time step i (m)

Relative lateral displacement:

$$dR = R_{i+1} - R_i$$

With:

dR : Relative lateral displacement of the specimen (m)

R_{i+1} : Absolute radius of the specimen at the time step $i+1$ (m)

R_i : Absolute radius of the specimen at the time step i (m)

Axial deformation:

$$\epsilon_i = \frac{dy}{H_0} \cdot 100\%$$

With

ε_{1i} : Axial deformation of the specimen at the time step i (%)

d_{yi} : Relative axial displacement of the specimen at the time step i (m)

H_0 : Initial height of the specimen (m), $H_0 = 10\text{m}$

Lateral deformation:

$$\varepsilon_{2i} = \varepsilon_{3i} = \frac{dR_i}{R} \cdot 100\%$$

With

ε_{2i} and ε_{3i} : Lateral deformation of the specimen at the time step i (%)

dR_i : Relative lateral displacement of the specimen at the time step i (m)

R : Initial radius of the cross-section of the specimen (m), $R = 2.5\text{m}$

Absolute positions and relative displacements of the rigid plate on the top of the specimen in all time steps were assigned as the axial displacements of the specimen. In the same way, the average absolute positions and the average relative displacements of twenty small plates

at the middle of the specimen (at $H = \frac{H_0}{2} = 5\text{m}$) in all time steps were obtained as lateral displacements of the specimen. Then, the variations of two types of displacement during the simulation in six cases of loading path were plotted together in the same figure. The results are presented in the figure 3.6.4 with the following notations:

- The left side of the figure is dedicated to the variation of the axial displacement and corresponds to the left column of the legend.
- The right side of the figure is dedicated to the variation of the lateral displacement and corresponds to the right column of the legend.

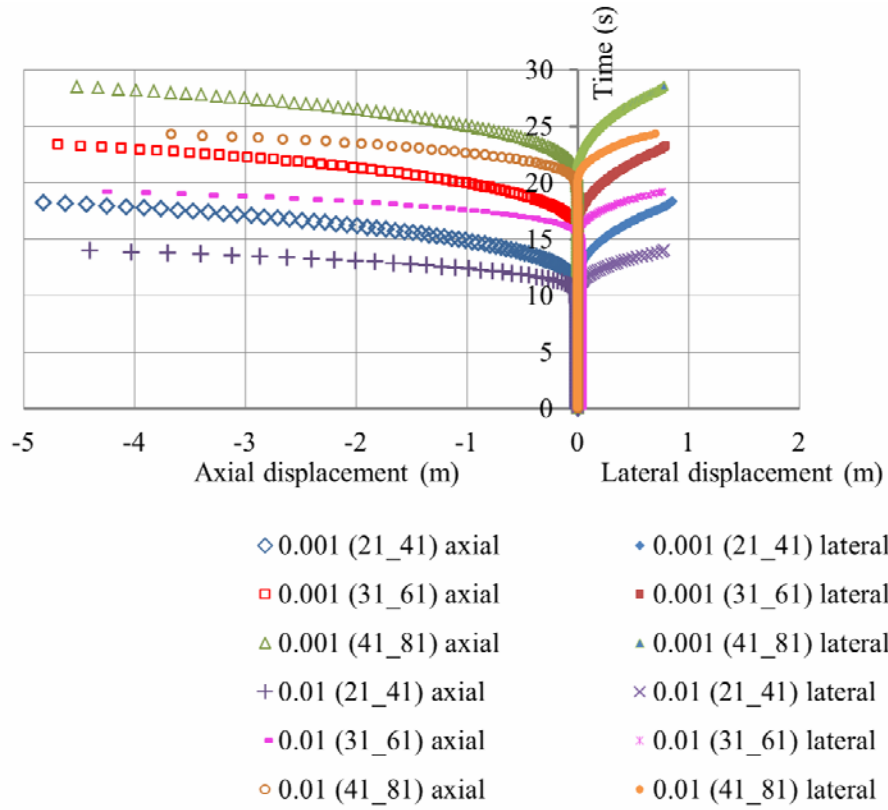


Figure 3.6.5: Variations of axial and lateral displacements during simulation time of six cases of loading path

According to the configuration of those six curves, the same tendency of responses of the specimen clearly divided into two periods:

- Stable state: during this state, displacements of the specimen were nearly null represented by the first segments of curves which were nearly coincident with the vertical axis. The rock mass has not evidently deformed yet.
- Deformed state: after the stable state, displacements of the specimen became obvious corresponding with the second segment of the curves as hyperbola of which the starting points were identic for each loading path. The rock specimen began to deform in two directions. With the same velocity of pressure, lateral displacements rose more quickly than axial ones. With the same procedure of loading path (21_41 or 31_61 or 41_81), the curve of higher velocity (0.01 MPa/s) developed more quickly and gaped more with the horizontal axis, for a given time of simulation than the one of smaller velocity (0.001MPa/s).

3.6.3.2. Relation between pressures and deformations

The relation between pressures and equivalent deformations was researched for the six cases of the loading path and the representation of this variation was obtained.

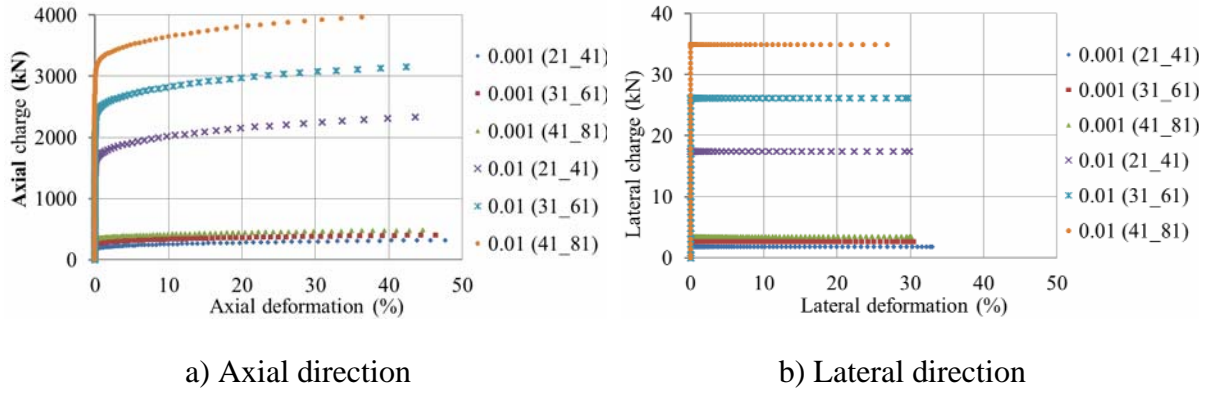


Figure 3.6.6: Relation between deformations and external loads
of six cases of the loading path

The external pressures were calculated as the ratio between the external loads and the initial cross-section of the specimen [145]. The correlation of the axial pressure and the axial deformation of the modelled specimen were presented in the next figure.

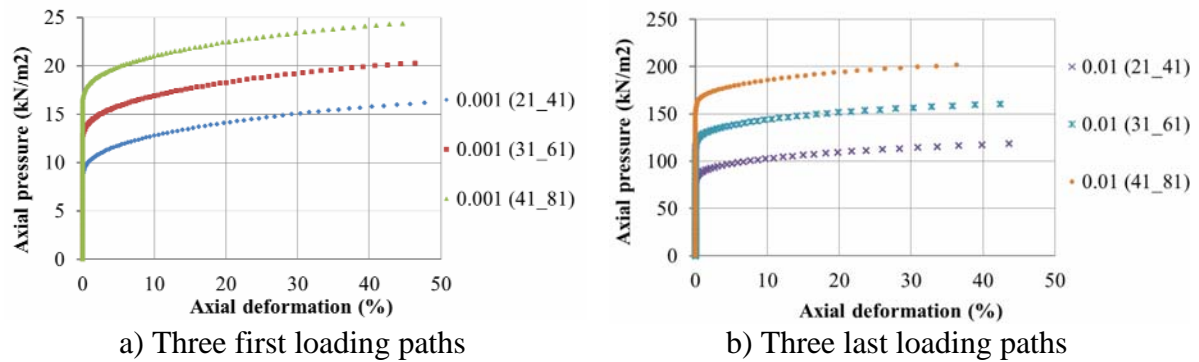


Figure 3.6.7: Relation between axial deformations and axial pressure of the model
under the six cases of loading path

Being divided by the constant value of the initial cross-section of the specimen, the external axial pressure and the axial charge were propositional and the form of the deformation - pressure curve was the same as the load - deformation one. The deformation - pressure behaviours of the model were similar in all cases of simulation with the same shape of the six curves.

The influence of the proportion between the two pressures σ_3 / σ_1 to the axial deformation of the specimen was studied by tracing the correlation curves between the axial deformation and the ratio σ_3 / σ_1 on the figure 3.6.8. Nearly the same behaviour was found in all loading cases when all the curves were nearly coincident. In the first period when $\sigma_3 / \sigma_1 \in]0.25, 1]$, the axial deformation of the specimen were negligible. The specimen was said to be in the stable sequence. The specimen was in the stable condition. The deformation of the specimen began when the ratio was about 0.25. In the second period when $\sigma_3 / \sigma_1 \in [0, 0.25]$, the axial deformation developed quickly with the slight augmentation of the pressures. The specimen was said to be in the deformation sequence. All the curves can be approximated as the two perpendicular-segment polylines of which the first segments were coincident with the vertical axis; the second segments were parallel with the horizontal axis. The change from the stable to the deformation sequence was found to be “brutal”. This fact showed a typical rigid plastic behaviour of the modelled specimen.

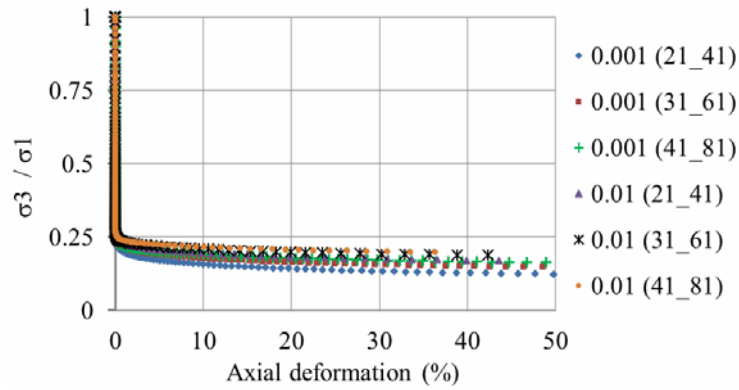


Figure 3.6.8: Relation between axial deformations and the

Given that all deformation – pressure curves were of a regular-rising form, so that we could not find their peak, the triaxial compression strength could not be found. For an intact rock under the same experiment, the moment when the axial deformation ε_1 of the specimen reaches 5% is suggested to be replaced [145]. Once our rock mass is evidently fractured, we did not find a reason for applying this recommendation. This fact also confirmed that the behaviour of any fractured rock mass was completely different from the behaviour of the intact rock cores normally used in the conventional triaxial compression test.

3.6.3.3. Variation of contacts inside the model

During the time of simulation, the contacts inside the model changed. Four parameters were used for monitoring this variation: the total potential number of contacts, the number of sliding contacts, the number of sticking contacts and the number of non-active contacts. The relation between these four parameters for a given time step is expressed as follow:

$$N = n_1 + n_2 + n_3$$

With:

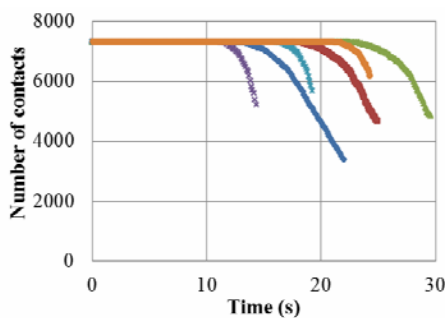
N: Total number of contacts of the model

n_1 : Number of sliding contacts

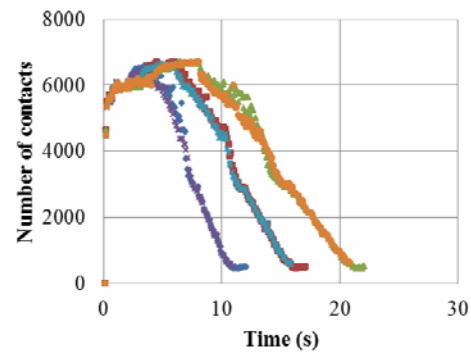
n_2 : Number of sticking contacts

n_3 : Number of non-active contacts

The total number of contacts in a model represents the interaction among rigid rock blocks (the block - block contacts) and between the rigid blocks and the boundary plates (the plate - block contacts). The value of N does not change until the detachment of rock blocks in the model under the axial pressure. It is called the degradation of model. When the tangential force of a contact between two adjacent rigid blocks is smaller than the sliding threshold of Mohr-Coulomb, the contact is called sticking one. The contrary is called a sliding one. A contact became non-active when the distance between two neighbouring polyhedra exceeded the assigned tolerance. The number of non-active contacts increased rapidly when a macroscopic failure plane occurred and the specimen was split into two parts, one sliding on the other.

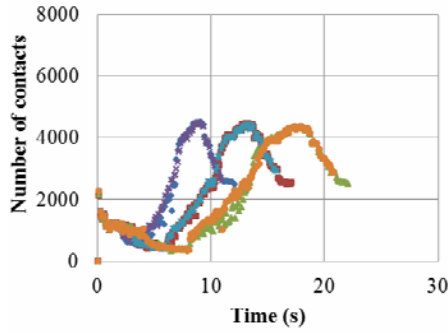


a) Total number of contacts N

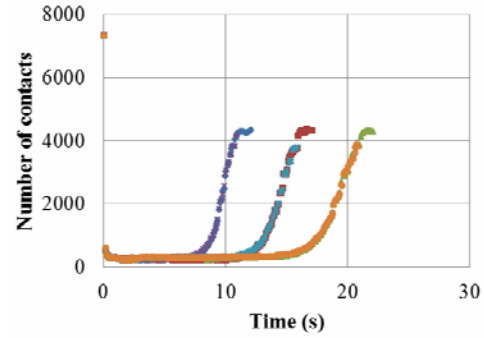


b) Sliding contacts n_1

Figure 3.6.9a: Variation of the contact parameters versus the simulation time
in six loading paths (Part 1)



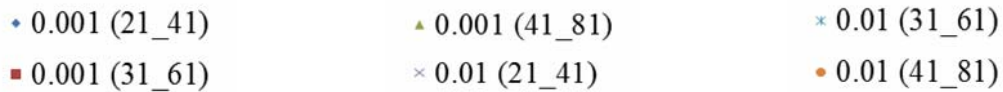
c) Sticking contacts n_2



d) Non-active contacts n_3

Figure 3.6.9b: Variation of the contact parameters versus the simulation time
in six loading paths (Part 2)

Notation of the graphs:



Studying the variation of the contact parameters of the specimen under each loading path, the same trend of the evolution of the contacts in the model was obtained in all the six cases of simulation. The results of the case of 0.01 (31_61) in the figure 3.6.9 is showed as the representative of the six loading paths.

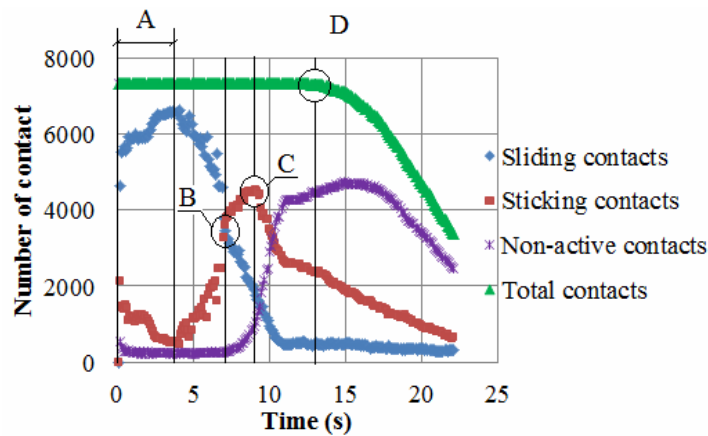


Figure 3.6.10: Variation of the contact parameters versus the simulation time
in the case of 0.001 (21_41)

Studied on these variation graphs, some brief commentaries were given:

- The diffusion of the instability (characterized by the period A in the figure): in this period, the developments of the sliding contacts (n_1) and the sticking contacts (n_2)

were contrary until the critical points were reached. The number of the total potential contacts in the model was constant.

- The contact instable equilibrium point (characterized by the point B in the figure): This point was characterised by the coincidence of the number of the sliding contact n_1 and the sticking contact n_2 in the model. After the diffusion of the instability in the specimen, the development trends of the number of n_1 and n_2 were opposite with the trends in the previous parts. The number of non-active contacts n_3 stayed unchanged until contact instable equilibrium point. After that, n_3 raised quickly. This moment was considered as the occurrence of the sliding in the specimen. Meanwhile, the number of the total potential contacts in the model was constant.
- The restitution after the sliding rupture (characterized by the period between the point B and the point C in the figure): In this period, n_1 and n_2 were continued developed in two contrary trends until the maximal number of the sticking contacts was reached. This peak was quite close to the moment when n_1 and n_3 were coincident. After this moment, the two parameters decreased with the same gradient.
- The degradation of the specimen (characterized by the point D in the figure): The number of N was suddenly decreased. Whereas, after the restitution, the number of non-active contacts n_3 rose quickly and surpass the two other parameters (n_1 and n_2) at the end.

The three important moments in the variation of the contacts of the specimen were interesting:

- The instable equilibrium of the contact number of the model;
- When the number of the sticking contacts in the model were maximal;
- At the start of the degradation of model.

a) The instable equilibrium of the contact number of the model

The model was considered to be in the instable equilibrium when the number of the sliding and the stick contacts were nearly coincident and the number of the non-active contact started to increase. The contact characteristics of the model at this important moment were searched. The results are presented in the next table.

Table 3.6.2: Contact parameters of the model at the contact instable equilibrium of the model under the triaxial pressure

Case	t_1 (s)	t_2 (s)	n_1	n_2	n_3
0.001 (21-41)	7.1	2.9	3459	3588	272
0.001 (31-61)	10.9	4.7	3566	3517	236
0.001 (41-81)	14.0	5.8	3566	3418	335
0.01 (21-41)	7.2	3.0	3449	3527	343
0.01 (31-61)	10.7	4.5	3590	3391	338
0.01 (41_81)	14.4	5.4	3552	3413	354

Notation in table:

t_1 : Moment of interest after the beginning of simulation (s)

t_2 : Moment of interest after the constant confining (s)

n_1 : Number of sliding contacts

n_2 : Number of sticking contacts

n_3 : Number of non-active contacts

Based on the obtained results of the contact variation of the model in the six loading paths, the contact instable equilibrium of the model was considered to be influenced by the procedure of the loading paths but not by the velocity of the applied pressures.

b) Variation of the sticking contacts in the model

The same research method which had been applied in the previous part was applied for the variation of the sticking contacts in the model. The moment when n_2 reaches its maximum value was searched and the relevant contact parameters are recorded in the next table.

Table 3.6.3: Contact parameters of the model for a maximum number of sticking contacts in six simulation cases

Case	t_1 (s)	t_2 (s)	n_1	n_2	n_3
0.001 (21-41)	9.1	4.9	1747	4501	1047
0.001 (31-61)	13.1	6.9	2078	4453	788

0.001 (41-81)	17.9	9.7	1897	4366	1056
0.01 (21-41)	9.1	4.9	1736	4483	1100
0.01 (31-61)	13.1	6.9	2072	4427	820
0.01 (41_81)	17.9	9.7	1855	4368	1066

Notation and units in table:

t_1 : Moment of interest after the beginning of simulation (s)

t_2 : Moment of interest after the constant confining (s)

n_1 : Number of sliding contacts

n_2 : Number of sticking contacts

n_3 : Number of non-active contacts

Once the coincidence of the variations of contact parameters in the same procedure of loading path (21_41 or 31_61 or 41_81) was proven, the same moment of maximum number of sticking contacts was obvious. The value of t_2 was close to the length of the interval for attaining the end of the constant confinement (4.1s, 6.1s and 8.1s, respectively).

c) Degradation of model

In practice, the phenomenon of degradation of the specimen under the triaxial compression test does not exist because the experiment finishes always at the first appearance of a macroscopic fracture in the specimen. As our model was constituted of rigid rock blocks that were interacting only by the dry friction Coulomb's law, the detachment had been anticipated so that the simulation was always executed until the axial deformation of the specimen reached 50%. The moment when the specimen started to be degraded and the relevant number of the contact parameters were searched. The results are presented in the next table.

Table 3.6.4: Contact parameters of the model at the start of the degradation under the triaxial pressure

Notation in table:

t_1 : Moment of interest after the beginning of simulation (s)

t_2 : Moment of interest after the constant confining (s)

n_1 : Number of sliding contacts

n_2 : Number of sticking contacts

n_3 : Number of non-active contacts

Case	t_1 (s)	t_2 (s)	n_1	n_2	n_3
0.001 (21-41)	12.1	7.9	510	2480	4325
0.001 (31-61)	17.1	10.9	486	2534	4295
0.001 (41-81)	22.1	13.9	516	2517	4282
0.01 (21-41)	11.0	6.8	516	2592	4207
0.01 (31-61)	15.9	9.7	586	2928	3801
0.01 (41_81)	20.9	12.7	633	2872	3810

With the same procedure of loading path, the degradation started sooner when the velocity of pressure is higher with larger relevant parameters. With the same velocity of pressure, the longer the confinement was kept, the more slowly the detachment occurred with larger relevant parameters. Furthermore, it was found that the variations of three parameters n_1 , n_2 and n_3 were nearly coincided in the same procedure of loading path (21_41 or 31_61 or 41_81) until the degradation of the model. The higher the velocity of pressure was, the sooner the degradation came. The correlation of these parameters in each loading path before the degradation of model was also studied and presented on the graphs of time versus number of contact of which one was presented as an illustration (refer the Appendix C for the total loading paths).

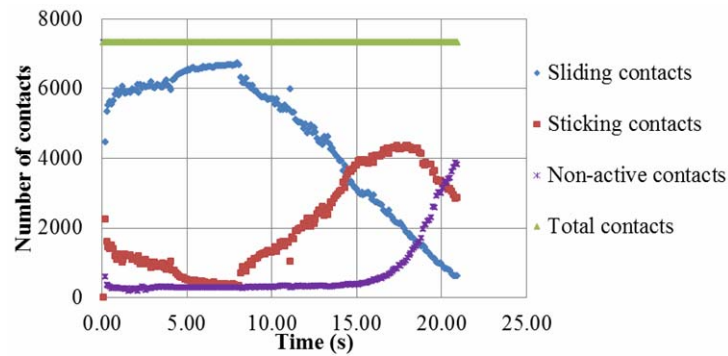


Figure 3.6.11: Correlation of parameters of contact before the degradation of the model
in the case of 0.01 (41_81)

3.6.3.4. Failure procedure of the model

Failure procedures of the model during the simulation were monitored. Under the application of the axial pressure with the constant confining pressure, the specimen was progressively divided into two parts and then slipped on a plane that created by the combination of existing fractures on the model. The Mohr – Coulomb failure criterion [180] was applied on the results of our modelling to know if the failure of the model followed this criterion. According to Mohr – Coulomb, the correlation between normal and tangential stresses on the failure plane of a rock or soil structure is expressed by the formula:

$$\tau = \sigma \cdot \tan(\varphi) + C$$

With:

τ : Tangential stress on the failure plane (N/m² or Pa)

σ : Normal stress on the failure plane (N/m² or Pa)

φ : Angle of internal friction on the failure plane (rad)

C: Cohesion of material

Normal stress occurring on the failure plane:

$$\sigma = \frac{(\sigma_1 + \sigma_3)}{2} + \frac{(\sigma_1 - \sigma_3)}{2} \cdot \cos 2\theta$$

With:

σ : Normal stress on the failure plane (N/m² or Pa)

σ_1 : Axial pressure (N/m² or Pa)

σ_3 : Lateral pressure (N/m² or Pa)

θ : Angle of the failure plane with the horizontal axis (rad)

Tangential stress occurring on the failure plane:

$$\tau = \frac{(\sigma_1 - \sigma_3)}{2} \cdot \sin 2\theta$$

The tangential stress reaches its maximum value when $\theta = 45^\circ$:

$$\tau_{max} = \frac{(\sigma_1 - \sigma_3)}{2}$$

The maximal value of normal stress:

$$\sigma_{max} = (\sigma_1 + \sigma_3)/2$$

As in the previous discussion, the strength of the triaxial compression of specimen could not be found when the deformation – pressure curve had no peak. We were interested in two other moments that took key roles during our simulation:

- The instable equilibrium of the contact number of the model;
- When the number of the sticking contacts in the model were maximal;
- At the start of the degradation of model.

a) The instable equilibrium of the contact number of the model

At the instable equilibrium of the contact number of the model 1, no sliding plane was found in all cases of simulation on the visual results of the simulation procedure recorded in the *.vtu files. Only some small groups of blocks started to move but their absolute values of the displacement and the velocity were very small. The capture of the model at the moment of interest under the loading path 0.01 (41_81) is presented as an example. The similar captures of the other loading paths are presented in the Appendix C.

Notation of the figure 3.6.12:

$\|X\|$: Displacement of rigid rock blocks of the model (m)

$\|V\|$: Velocity of displacement rigid rock blocks of the model (m/s)



a) Translation displacement

b) Velocity

Figure 3.6.12: Moving blocks of the specimen at $t = 14.4s$
of the loading path 0.01 (41_81)

Table 3.6.5: Applied pressures on the model at the instable equilibrium of the contact number of the model

Case	t_1 (s)	σ_1 (N/m ²)	σ_3 (N/m ²)
0.001 (21-41)	7.10	4.95	2.00
0.001 (31-61)	10.90	7.75	3.00
0.001 (41-81)	14.00	9.85	4.00
0.01 (21-41)	7.20	50.50	20.00
0.01 (31-61)	10.70	75.50	30.00
0.01 (41_81)	14.40	102.50	40.00

Once the sliding face was not appeared, the verification of the correlation between the tangential and the normal stresses caused by the applied pressures was neglected.

b) When the sticking contact quantity was maximal

When the number of sticking contacts reached its maximal value, a sliding plane occurred in the specimen. On the visual results of the simulation procedure recorded in the *.vtu files, a sliding plane that made an angle of about 55° with the horizontal line was found in all cases of simulation. The occurrence of this plane was independent from the magnitude and the velocity of the applied pressure and depended only on the structure of the rock mass. The capture of the model at the moment of interest under the loading path 0.01 (41_81) was a good demonstration of the formation of the sliding plane. The similar captures of the other loading paths are presented in the Appendix C.

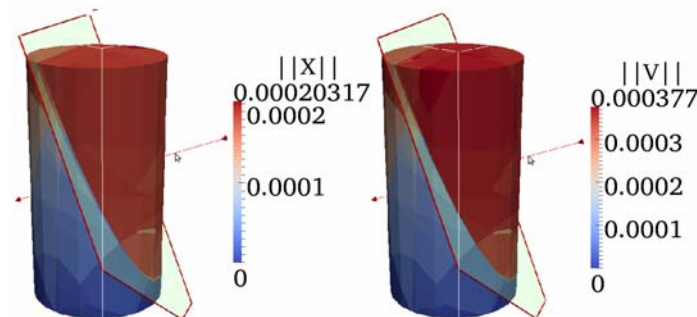


Figure 3.6.13: Sliding plan occurred in the specimen at $t = 18s$
of the loading path 0.01 (41_81)

Notation:

$\|X\|$: Displacement of rigid rock blocks of the model (m)

$\|V\|$: Velocity of displacement rigid rock blocks of the model (m/s)

The similar figures of the other loading paths are presented in the Appendix C.

The calculation of tangential and normal stresses on the discovered plane were realised and the achieved results are presented in Table 3.6.

Table 3.6.6: Tangential and normal stresses on the sliding plane when the number of sticking contacts was maximal

Case	t_1 (s)	σ_1 (N/m ²)	σ_3 (N/m ²)	σ (N/m ²)	τ (N/m ²)
0.001 (21-41)	9.10	6.95	2.00	3.63	2.33
0.001 (31-61)	13.10	9.95	3.00	5.29	3.27
0.001 (41-81)	17.90	13.75	4.00	7.21	4.58
0.01 (21-41)	9.10	69.50	20.00	36.28	23.25
0.01 (31-61)	13.10	99.50	30.00	52.86	32.65
0.01 (41_81)	17.90	137.48	40.00	72.07	45.80

The correlation between the tangential and normal stresses on the sliding plane was studied and the correlation curve was traced. An empirical envelope of the correlation curve $\tau = 0.63\sigma$ was found and the friction coefficient of the total rock mass at the moment of interest was considered to be $\mu = \tan(\varphi_{\text{mas}}) = 0.63$.

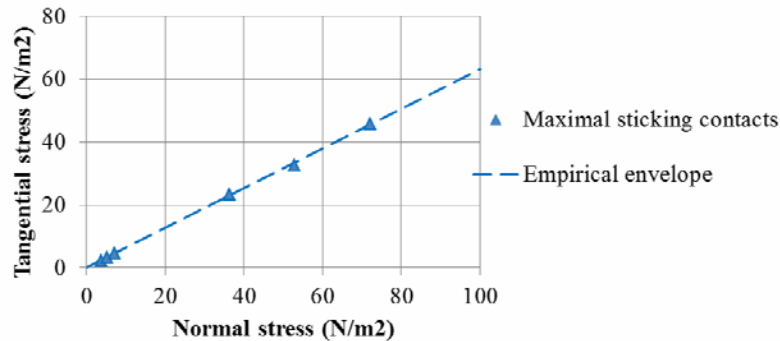


Figure 3.6.14: Relation curve between tangential and normal stress on the sliding plane when the sticking contact quantity was maximal

The maximal values of tangential and normal stresses on the sliding plane were calculated and are given in Table 3.4.5.

Table 3.6.7: Maximal tangential and normal stresses on the sliding plane when the number of sticking contacts was maximal

Case	t_1 (s)	σ_{\max} (N/m ²)	τ_{\max} (N/m ²)
0.001 (21-41)	9.10	4.47	2.47
0.001 (31-61)	13.10	6.47	3.48
0.001 (41-81)	17.90	8.87	4.88
0.01 (21-41)	9.10	44.75	24.75
0.01 (31-61)	13.10	64.75	34.75
0.01 (41_81)	17.90	88.74	48.75

c) At the start of the degradation of model

When the specimen began to degrade, the “old” sliding plane that had appeared on the specimen at the maximal sticking contact time was replaced by the “new” one that made an angle of about 30° with the horizontal line. The latter, similar to the former, was independent from both the magnitude and the velocity of pressure, and depended only on the structure of rock mass. The capture of the model at the start of the degradation of the model under the loading path 0.01 (41_81) was a good demonstration of the formation of the “new” sliding plane. The similar captures of the other loading paths are presented in the Appendix C.

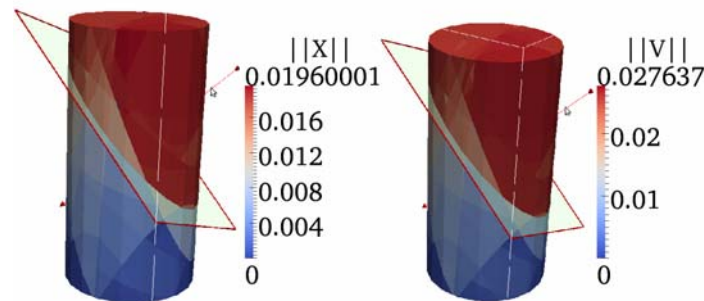


Figure 3.6.15: Sliding plane occurred in the specimen at $t = 21s$
of the loading path 0.01 (41_81)

Notation:

$\|X\|$: Displacement of rigid rock blocks of the model (m)

$\|V\|$: Velocity of displacement rigid rock blocks of the model (m/s)

The same data processing as in the previous part were realised on this case and the obtained results on the following table.

Table 3.6.8: Tangential and normal stresses on the sliding plane at the start of the degradation of model

Case	t1 (s)	σ_1 (N/m ²)	σ_3 (N/m ²)	σ (N/m ²)	τ (N/m ²)
0.001 (21-41)	12.10	9.79	2.00	7.84	3.37
0.001 (31-61)	17.10	13.72	3.00	11.04	4.64
0.001 (41-81)	22.10	17.65	4.00	14.24	5.91
0.01 (21-41)	11.00	86.90	20.00	70.18	28.97
0.01 (31-61)	15.90	125.48	30.00	101.61	41.34
0.01 (41_81)	20.90	164.58	40.00	133.43	53.94

Table 3.6.9: Maximal tangential and normal stresses on the sliding plane at the start of the degradation of model

Case	t ₁ (s)	σ_{\max} (N/m ²)	τ_{\max} (N/m ²)
0.001 (21-41)	9.10	5.89	3.97
0.001 (31-61)	13.10	8.36	5.48
0.001 (41-81)	17.90	10.82	6.98
0.01 (21-41)	9.10	53.45	34.25
0.01 (31-61)	13.10	77.74	48.75
0.01 (41_81)	17.90	102.29	63.75

The correlation between the tangential and normal stresses on the sliding plane was studied and the correlation curve was traced. An empirical envelope of the correlation curve $\tau = 0.4\sigma$ was found and the friction coefficient of the total rock mass at the moment of interest was considered to be $\mu = \tan(\varphi_{\text{mas}}) = 0.4$.

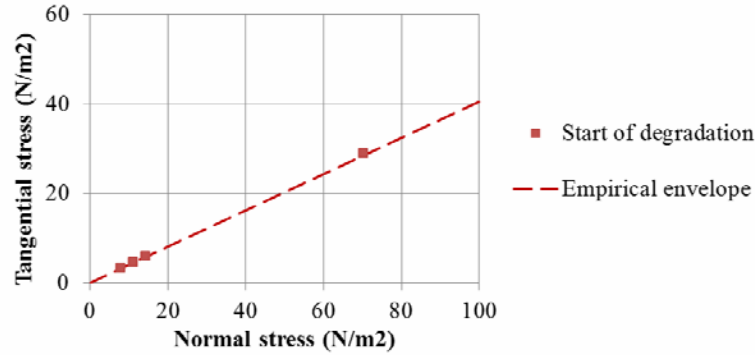


Figure 3.6.16: Relation curve between tangential and normal stress on the sliding plane at the start of the degradation of the model

The obtained empirical envelope $\tau = 0.4\sigma$ was coincident with the theoretical envelope of Mohr written for the rock mass with the internal angle of friction $\mu = \tan(\varphi) = 0.4$. Hence, the start of the degradation of the model was considered as the failure of the model.

3.6.3.5. Evolution of sliding planes occurring in the specimen during the simulation

As presented in the previous part, two sliding planes occurred in the specimen. They are about 55° and 30° , respectively, inclined with the horizontal line. For more understanding of the evolution between these sliding planes, visual results in *.vtu files, recorded in DISPLAY folder were treated. The scanned image of the rock core during the simulation time showed the position of the inertial centre of its 514 RBDY3 blocks. The absolute displacement of a rigid block at a requested time step was represented by a 3D vector placed at the inertial centre of the block: the direction of the vector is coincident with the direction of the movement of the block; and the colour and the shape of the vector presents the magnitude of the displacement. The assemblage of vectors of all the blocks on the specimen formed the sliding flow under the application of external pressures.

The scanned images of the rock core at four milestone times during the simulation were studied:

- at the initial time: $t = 0s$;
- when the number of the sticking contacts was maximal;

- at the start of the degradation of model;
- at the end of the simulation.

At the initial time, three faces created by the arrangement of the rock structure can be predicted.

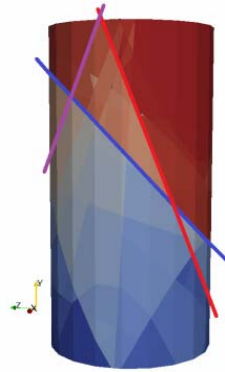


Figure 3.6.17: Pre-existing faces in the rock core

Under the triaxial pressures, different sliding flows occurred on these faces. When the sticking contacts were maximal, the first shift appeared concurrently on the red and the purple faces. They were considered to be dangerous because of their great slopes. The former was predominant both in the evenly distribution and the magnitude of vectors. However, since the two faces did not across the whole cross-section of the rock core, they cannot promptly destruct it. Meanwhile, the displacement along the blue face developed in a stronger way, it disturbed the “continuation” of two other faces and became the principal sliding slope at the beginning of the degradation of the model. Crossed the rock core, the blue face became the prominent among the three faces and the sliding phenomenon on the face were stronger by the time of simulation. This failure plane did not change until the end of the simulation.

Flow movements of the rock core under the loading path 0.01 (41_81) are presented above as an example. The figures of the other loading paths are situated in the Appendix C. It is noted that the colours and the shapes of vectors are different in each scanned image of the rock core and are only appropriate with the magnitude scale placed under the rock core.

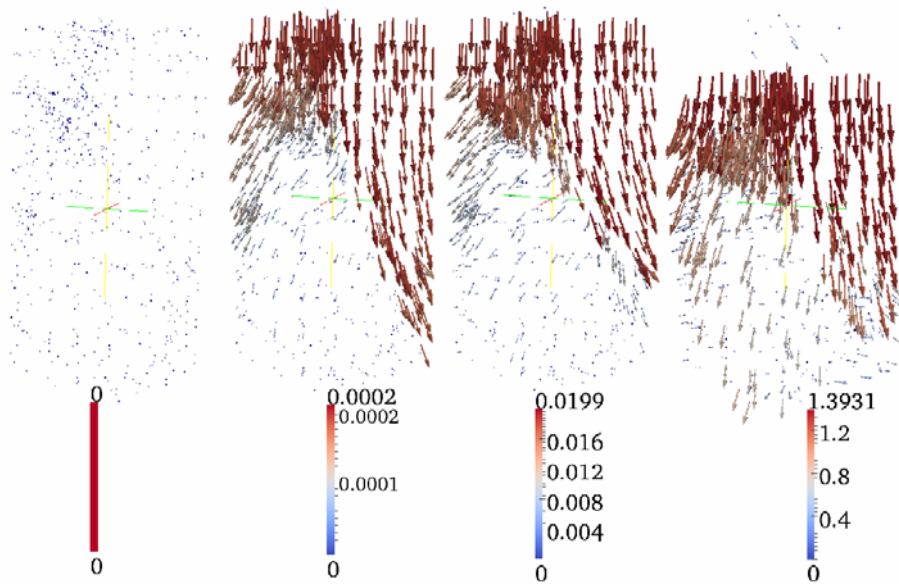


Figure 3.6.18: Flows of movement of rigid rock blocks inside the model
under the loading path 0.01 (41_81)

3.6.4. Conclusions

A monotonous classical triaxial compression test was modelled on a conformed cylindrical fractured rock core with the geological characteristics of the fractured marble of Saint – B  at, under six loading paths. The simulation was executed until the relative axial deformation of the model reached 50%. The mechanical behaviours of the rock core were analysed using the mechanical and visual results. With a model composed of rigid rock polyhedra using a pure dry friction law of contact, the mechanical behaviours that we used were purely rigid without any elastic or plastic characteristics. Once the deformation – pressure relation curves of the simulation had always positive gradients; the classical strength of the rock core under the triaxial pressures was not determined. Monitoring the variation of the contact condition between the rigid blocks of the model, we paid attention to three important moments: a) the contact instable equilibrium of the model; b) when the number of sticking contacts was maximal; c) when the degradation started. On the basis of the combined analyses of data and visual results, the sliding failure phenomenon on an inclined plane was found to be occurring in the model at the two last moments. The scanned images of the rock core showed the failure procedure that had developed in three sliding planes on the specimen during the simulation.

This application was aimed to proving the reality and the performance of the proposed methodology presented in the chapter 2. At the beginning, with this simulation we hoped to find an equivalent ideal rock that can be used to replace the marble of Saint B  at. Since the

behaviour of the numerical rock was quite diversified, the aim was not successful. However, the simulation helped to verify the load application by the use of the attached rigid plates. It also demonstrated the capacity of the methodology in the creation of the numerical rocks for the numerical simulations of the common tests in rock mechanics. With further adjustments, this application is hoped to be used as the verification of the real tests or to stand as the alternative choice for the determination of the geo-technical parameters of the real rocks.

3.7. Study of the simulation of a tunnel excavation in the rock mass of Saint B  at

3.7.1. Introduction

Saint B  at is located on a metamorphic internal zone of the Pyrenees chain, constituted of limestone and dominant dolomite (marble), typical of this zone with steep reliefs with high altitude (Cap du Mont: 1207 metres high, Ri   mountain: 1128 metres high) [1]. The future tunnel of Saint B  at will cross a marble mountain (metamorphic zone) of Cap du Mont, on the right bank of Garonne river. The southern head of the tunnel that runs parallel with the northern Pyrenees fault will cross the French departmental road D44 and the northern head will be located on the exploiting site of the marble factory OMG. A scan-line investigation in the underground exploitation site of the OMG factory under the Ri   mountain was realised in November, 2011 and 402 discontinuities were found on the longest scan-line of 180.8m surveyed on a vertical rock face of which the average direction is N25E.

The fracture conditions that were collected at the site of the future tunnel of Saint B  at were used for an actual application of the methodology for the tunnel modelling in the rock mass that is presented in this research. After the processing on the 402 discontinuities of the mentioned scan-line, two cases of family clustering of discontinuities were proposed. A Fisher law of the angle distribution and an exponential law of the spacing distribution were assigned for each family. Then, five scenarios for the 10x10x10(m) homogeneous rock mass generation were set up in RESOBLOK. The assumed tunnel has a shape of a 5-metre-wide-diameter cylinder in the middle of the rock medium. The generation of the excavation process by three different approaches were carried out. The geometrical models were created from the five scenarios of the rock mass of Saint B  at and the quick stability analysis on RESOLBOK was executed to find out the critical generations. Finally, the

geometrical model created from the simulation of Scenario 4 when $N = 14$ was used as the representative model of the rock mass of Saint B  at and its future tunnel.

The geometrical model generated by RESOBLOK was immersed into the Pre-Processor of the LMGC90 code. Rock mass is assigned with the density $\rho = 2600 \text{ kg/m}^3$. After reconstructing the model in LMGC90 and surface meshing all the blocks using the GMSH script, the dry friction Coulomb's law of contact with a friction coefficient $\mu = \tan(\varphi) = 0.4$ was chosen for the interaction contact of the rock polyhedra. Three cases of loading conditions were tested on the model:

- The gravity and the three normal component of the *in situ* stresses in the region of Saint B  at [178];
- The gravity and the six components of the *in situ* stresses in the region of Saint B  at [178];
- The gravity and a six-component-supposed litho-static pressure.

They were applied through the system of 486 rigid plates attached all around the model fractured rock medium. The tunnel excavation was simulated by phasing out all blocks in the core of the tunnel and all the related plates. The mechanical behaviour of the rock medium in each simulation step was saved for post-processing treatments. The variation of the mechanical behaviour of the rock medium and of the excavation faces of the tunnel before, during and after each construction phase were considered for a stability assessment of the tunnel and its surrounding rock medium. The variations of the contact force and the contact pressure in the rock mass were recorded during the simulation times.

As mentioned in the section 2.5.6, the goals of this simulation were:

- The modelling of the massif of the fractured marble of Saint B  at;
- The simulation of a supposed tunnel in the numerical massif and a complex tunnelling procedure that included different periods: before, during and after the excavation of the tunnel;
- The stability analyses of the tunnel and the massif during the tunnelling procedure;
- The numerical modelling capacity of the proposed methodology for the rock tunnel engineering.

In the limitation of this research, only some results of the mechanical behaviours of the rock mass of Saint B  at and its tunnel are presented. Other details and further results on the stability assessment of tunnel during the construction procedure will be soon analysed.

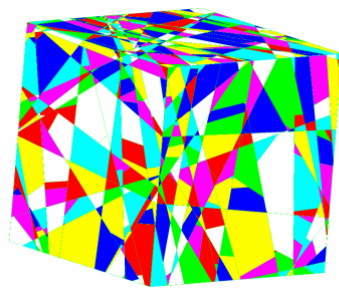
3.7.2. Numerical models

3.7.2.1. Numerical model of the rock mass

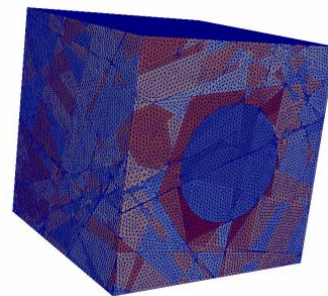
The geometrical model of the three simulation approaches for the multi-phase-excavated tunnel in rock was exported from RESOBLOK to LMGC90. The numerical rock mass was a cube of 10x10x10 (m) and was divided into many rigid blocks by 4 families of discontinuities of which one was blocked after the intersection with another. The rock blocks were declared as the polyhedra and were surface meshed using the GMSH script coupled to LMGC90, the geological conditions of rock mass were defined by the mass density and the contact law between the blocks:

- The rock medium was homogenous with the density $\rho = 2600 \text{ kg/m}^3$;
- The contact between the neighbours was defined by the IQS_CLB interaction law with the friction coefficient $\mu = \tan(\varphi) = 0.4$ and no cohesion ($C = 0$)

The parameter values were referred from [149] with the ignorance of the cohesion in order to represent the dry condition and almost without filling of the discontinuities that we had observed on the monitored rock faces in the castle gallery and in the underground exploitation site of the OMG factory in Saint B  at.



a) Generated by RESOBLOK



b) Surface meshed by LMGC90

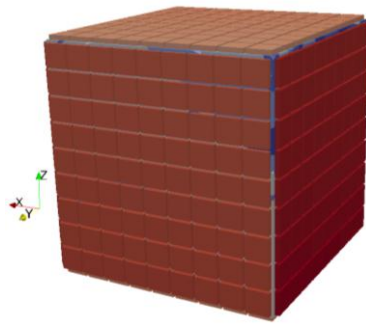
Figure 3.7.1: Numerical rock mass before and after the surface meshing

3.7.2.2. Boundary and loading conditions

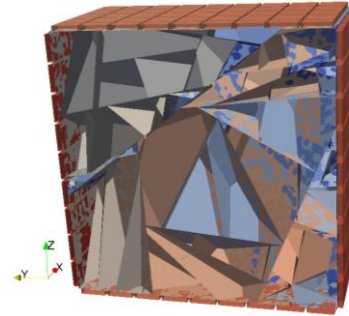
a) Boundary conditions

All the RBDY3 objects of the rock mass were set to be free in all 6 DOFs. The loading conditions of the future tunnel were simulated by a loading system composed of 486 rigid plates of 1x1x0.2 (m) attached to the rock mass. On each face of the cube, 81 plates were arranged as a 9x9 matrix with the centre-to-centre distance of 1 m. The DOFs of those rigid plates are assigned as follows:

- The plates that situated on the bottom boundary of the model and its two adjacent perpendicular boundaries: 6 DOFs are totally fixed;
- The plates that situated on the three other boundaries of the model: 3 rotational DOFs are fixed, 3 translational DOFs are free;



a) Total model



b) One half of the model

Figure 3.7.2: Numerical rock mass and its boundaries plates

b) Loading conditions

The gravity was taken into account in the tunnel simulation. Beside the gravity, the *in situ* stresses in the castle gallery that had been measured in the “Overcoring” test in October 2011 by INERIS [178] were used as the loading conditions for our simulations (see Table 3.5.1 and Figure 3.5.1). The normal stresses were applied vertically on the relevant plates while the tangential stresses were applied horizontally on them. The three loads were assigned as the dead loads in our simulations; it meant that their values and directions did not change during the simulation time.

The models of our simulation were tested under three loading cases:

- Case 1: Combination of the gravity and the normal component of the *in situ* stresses:

Table 3.7.1: *In situ* stresses of the 1st loading case

σ_x (MPa)	σ_y (MPa)	σ_z (MPa)
-2.7	-0.7	-1.2

Notation: The negative values represented the compression action of the stresses.

- Case 2: Combination of the gravity and two components (normal and tangential) of the *in situ* stresses:

Table 3.7.2: *In situ* stresses of the 1st loading case

σ_x (MPa)	σ_y (MPa)	σ_z (MPa)	τ_{xy} (MPa)	τ_{yz} (MPa)	τ_{xz} (MPa)
-2.7	-0.7	-1.2	1.7	-0.8	-1.6

Notation: The negative values represented the compression action and the positive values represented the tension action of the stresses.

- Case 3: Combination of the gravity and the supposed litho-static pressures:

$$\sigma_1 = \sigma_2 = \sigma_3 = \rho \cdot g \cdot 10 \cdot H = 21.72 \text{ MPa}$$

With:

ρ : Density of the rock mass, 2600 kg/m³

g : Gravity acceleration, 9.81m/s²

H : Overburden height of the tunnel, ~82m (see the Figure 3.1.8)

Choosing such an extreme value for the supposed litho-static pressures (10 times bigger than the theoretical litho-static pressures on top of the simulated tunnel), we aimed at studying the effect of the confining stresses on the stability of the numerical rock mass and tunnel.

c) Selection of the simulation parameters

The NLGS solver was used for solving the contact detection in the model and the relevant numerical parameters were assigned as in the

- Parameter θ of the Crank-Nicholson method: $\theta = 0.5$;
- Time step: $dt = 0.1$ s;
- Convergence norm: $tol = 10^{-6}$;

- Maximal number of calculations in an iterative loop: $gs_it1 = 5000$;
- Numbers of loops in the iteration for each convergence check: $gs_it2 = 20$.

Once the simulation and analysis was started, the mechanical responses of the model was recorded each 10 time steps as the algebra data and as the graphical visualization displays by the PARAVIEW code.

3.7.2.3. Numerical models and the excavation algorithms of the excavation process

The future tunnel had the shape of a cylinder with $L = 10$ m along the axis Y and a circle cross-section $R = 2.5$ m on the plane XZ. It was situated in the middle of the rock mass mentioned in the sub-section 3.7.2.1.

In the sub-section 2.3.4 and 2.5.6.1, three types of the geometrical models and their equivalent excavation approach for the tunnelling process were proposed. The models created from the first and the third combinations were chosen to be applied in our simulation. The tunnel modelling was simulated in 100 time steps. The generated tunnelling schedule was assigned as follow:

- The preparation phase: 20 time steps from step 1 to 19;
- The 1st excavation phase: 10 time steps from step 20 to 29. The excavation work was carried out at the step 20, the observation time was from the step 21 to 29;
- The 2nd excavation phase: 10 time steps from step 30 to 39. The excavation work was carried out at the step 30, the observation time was from the step 31 to 39;
- The 3rd excavation phase: 10 time steps from step 40 to 49. The excavation work was carried out at the step 40, the observation time was from the step 41 to 49;
- The 4th excavation phase: 10 time steps from step 50 to 59. The excavation work was carried out at the step 50, the observation time was from the step 51 to 59;
- The finishing phase: 40 time steps from time step 60 to 100.

Two stability criteria for the whole rock mass were applied for the simulation during the tunnelling procedure:

- All rock blocks must not displace outside a limited zone of $25 \times 25 \times 25$ (m) which is 2.5 times larger than the initial rock mass;
- The velocity tolerance of all rock blocks must not exceed the predicted limit of 1m/s.

If an object is not complying with both criteria at the same time, it will be eliminated from the model. The list of the eliminated objects was verified later to understand more the movement of the rock blocks and to predict, if needed, whether a particular strengthening method for fixing them on the rock faces were required. By controlling the extreme movements of the rock blocks inside the model, the numerical simulation was hoped to be closer to the behaviours of the rock mass and its tunnel in reality. It helped also to lighten the calculation procedure and reduce the computing time.

The simulation was executed in two following combinations:

a) Combination 1: The simulation approach 1 and the excavation algorithm 1

The rock mass “without hole” that had been created by RESOBLOK from the Scenario 4 (see 3.4.1), N=14 was an assembly of 1046 rock blocks. Immersed in LMGC90 and meshed its surface using the GMSH script in LMGC90, this model (called “Model 1” here and afterward) was composed of 1046 RBDY3 objects, number 1 to number 1046 in our simulation (called “Simulation 1” here and afterward). The loading system was attached to the boundaries of the Model 1 by 486 RBDY3 plates, number 1047 to number 1532.

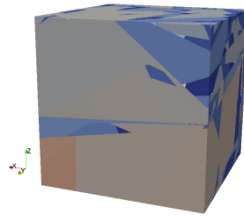


Figure 3.7.3: Model 1

The future tunnel was located in the cross-section zone that was defined on the Cartesian coordinates by:

$$2.5 \leq x \leq 7.5 \text{ (m)}$$

$$2.5 \leq z \leq 7.5 \text{ (m)}$$

Along the axis Y, the 4 phases of excavation were mathematical represented by the y coordinate during the time of construction:

- At the 1st excavation phase: $0.0 \leq y \leq 2.5 \text{ (m)}$;
- At the 2nd excavation phase: $2.5 \leq y \leq 5.0 \text{ (m)}$;
- At the 3rd excavation phase: $5.0 \leq y \leq 7.5 \text{ (m)}$;

- At the 4th excavation phase: $7.5 \leq y \leq 10.0$ (m);

When the inertia centre of a rock block inside the Model 1 was situated in the zone that is defined at an excavation phase, it was eliminated from the rock mass. Besides that, the boundaries plates that were attached on the zone in front of the first cross-section and behind the last cross-section of the excavation were also eliminated in the same time step of the 1st and the 4th excavation phase, respectively.

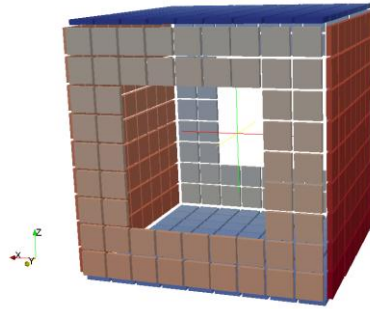


Figure 3.7.4: Phasing out the boundaries plates in front of and behind the tunnel

The tunnelling schedule is given as follows and illustrated in the next figure:

- The preparation phase (time step from 1 to 19) – at time step 1: 1046 RBDY3 objects of the Model 1 and 486 boundaries plates were simulated under the loading conditions;
- The 1st excavation phase (time step from 20 to 29) - at time step 20: 25 boundaries plates in front of the tunnel and 27 RBDY3 objects of the Model 1 in the 1st tunnel segment were eliminated from the model.
- The 2nd excavation phase (time step from 30 to 39) - at time step 30: 22 RBDY3 objects of the Model 1 in the 2nd tunnel segment were eliminated from the model.
- The 3rd excavation phase (time step from 40 to 49) - at time step 40: 52 RBDY3 objects of the Model 1 in the 3rd tunnel segment were eliminated from the model.
- The 4th excavation phase (time step from 50 to 59): at time step 50, 25 boundaries plates behind the tunnel and 62 RBDY3 objects of the Model 1 in the 4th tunnel segment were eliminated from the model.
- The finishing phase (time step from 60 to 100): there were 883 RBDY3 objects of the Model 1 and 436 boundaries plates at the end of the simulation.

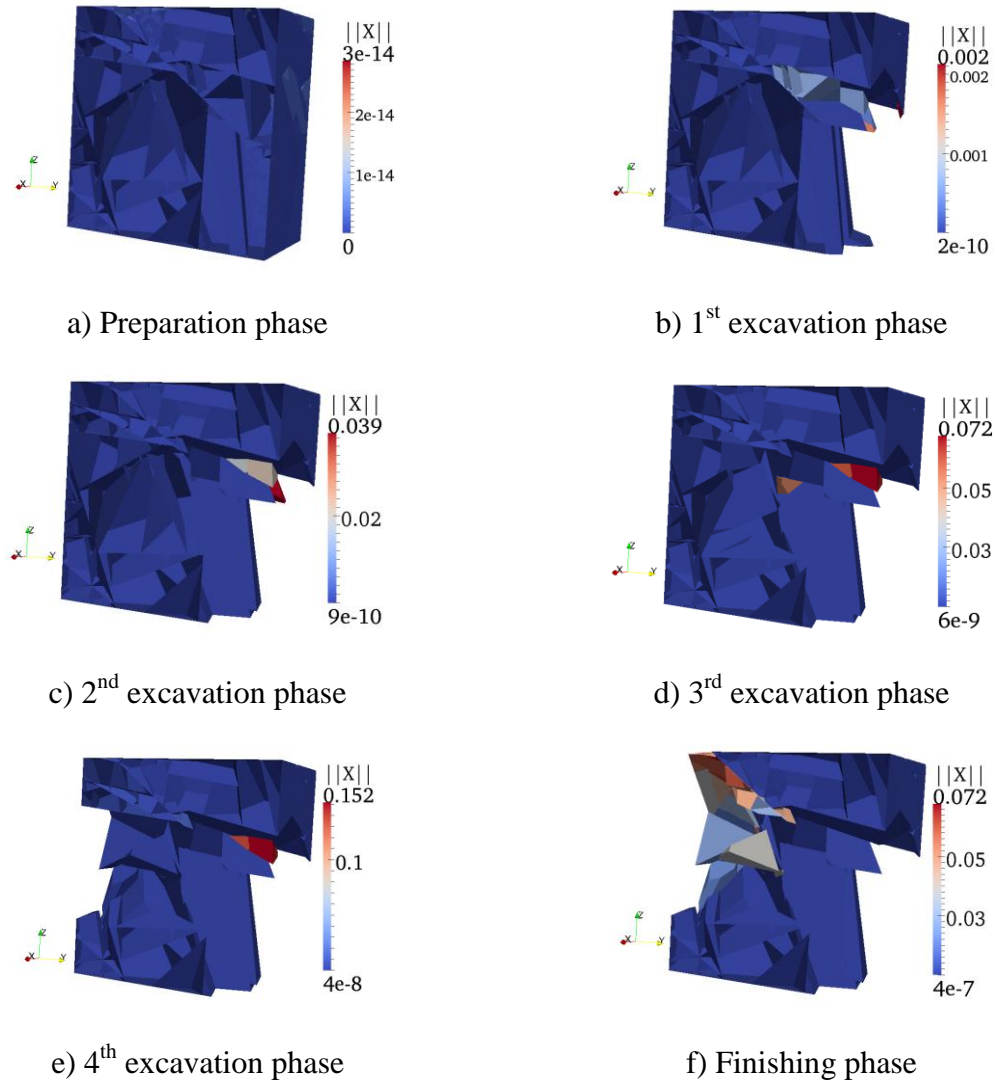


Figure 3.7.5: Change of the left half of the Model 1 during the excavation procedure

Notation of the Figure 3.7.7:

- The direction of the tunnelling is from the right to the left. The images shown a half of the rock mass cut by a vertical plan of view.
- $||X||$ is the absolute displacement of the rock blocks of the Model 4, m. The colour scales indicates the magnitude of the recorded displacements of the rock blocks.

According to the excavation of the Model 1 during the simulation time, it was found that the excavation was not following the targeted configuration. The tunnel boundary was rough and the 1st head of the tunnel was almost “breaking” the rock mass. This is the consequence of the excavation mechanism of the model which eliminated the blocks in the objective zone of the tunnel by their centre of inertia. When a big block that was not totally

situated in the target excavation zone but its centre of inertia satisfied the digging coordinates condition, it was excavated.

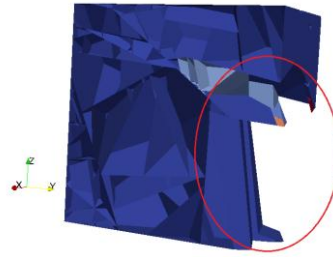


Figure 3.7.6: Pierced rock mass caused by the elimination of several big blocks of Model 1

By the comparison of the two head of the numerical tunnel, it is found that 27 and 62 RBDY3 were eliminated in the 1st and the 4th excavation segment, respectively. The number of removed blocks at the 1st head, equivalent with the 1st excavation segment, was smaller but the broken zone was larger and even reached the bottom of the rock mass. At the 2nd head, equivalent with the 4th excavation segment, more blocks were removed but the concerned zone was closer to the targeted tunnel boundary and the excavation was more symmetrical. The captures of the total excavation at the finishing phase from the front and the back faces are well presenting the irregular development of the tunnel.

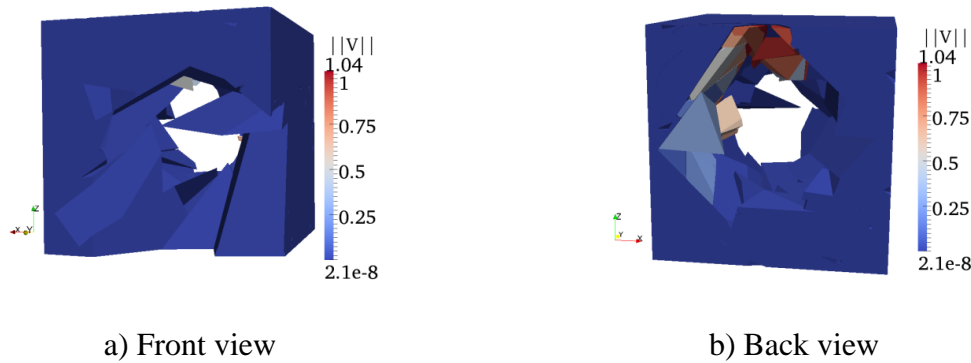


Figure 3.7.7: Model 1 and its numerical tunnel at the finishing phase (at time step 60)

Notation of the Figure 3.7.7: $||V||$ is the absolute displacement velocity of the rock blocks of the Model 4, m/s. The colour scales indicates the magnitude of the recorded velocities of the rock blocks.

As mentioned in the 2.5.6.1b, this simulation approach was recommended for the strongly fractured rock mass of which the constitutive rock blocks were small with regular dimensions. This approach was found not to be suitable for the rock mass of Saint B  at that has been used in our research. Hence, the third approach (see 2.5.6.1c) was recommended.

b) Combination 2: The simulation approach 3 and the excavation algorithm 3

The rock mass “with hole” (called “Model 3” here and afterward) and the excavation model (called “Model 2” here and afterward) that were created by RESOBLOK from the Scenario 4 (see 3.4.1), N=14 produced an assembly of 1258 and 207 rock blocks, respectively. Imported simultaneously in LMGC90, these two models together created a rock mass of 1465 RBDY3 objects (called “Model 4” here and afterward). The rock blocks of the Model 2 were assigned as RBDY3 objects number from 1 to 207 and those of the Model 3 assigned as RBDY3 objects number from 208 to 1465 in our simulation. The loading system was attached to the boundaries of the Model 4 by 486 RBDY3 plates, number 1466 to number 1951.

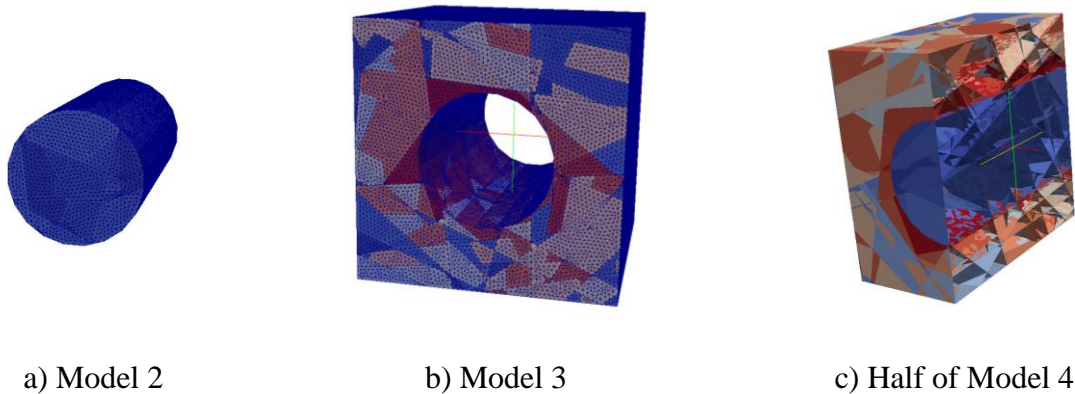


Figure 3.7.8: Three models of the Combination 2

Along the axis Y, the 4 phases of excavation were mathematical represented by the y coordinate during the time of construction:

- At the 1st excavation phase: $0.0 \leq y \leq 2.5$ (m);
- At the 2nd excavation phase: $2.5 \leq y \leq 5.0$ (m);
- At the 3rd excavation phase: $5.0 \leq y \leq 7.5$ (m);
- At the 4th excavation phase: $7.5 \leq y \leq 10.0$ (m);

The RBDY3 objects of the Model 2 of which the coordinate y were fulfilling these requirements were eliminated from the rock mass by the command “RBDY3_SetInvisible”. Besides that, the boundaries plates that were attached to the zone in front the first cross-section and behind the last cross-section of the excavation were also eliminated in the same time step of the 1st and the 4th excavation phase, respectively.

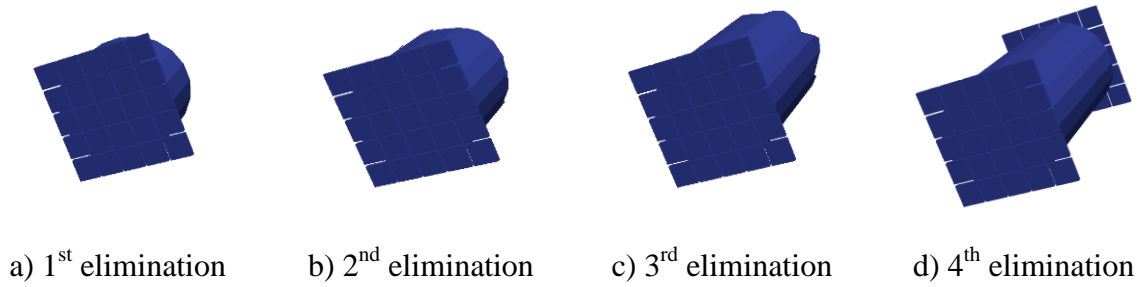


Figure 3.7.9: Eliminated boundaries plates and the excavation segments of the Model 4 during the excavation procedure

The details of the tunnelling schedule is given as follows and illustrated in the figure 3.7.10:

- The preparation phase (time step from 1 to 19) – at time step 1: 1465 RBDY3 objects of the Model 4 and 486 boundaries plates were simulated under the loading conditions;
- The 1st excavation phase (time step from 20 to 29) - at time step 20; 25 boundaries plates in front of the tunnel and 38 RBDY3 objects of the Model 4 in the 1st tunnel segment were eliminated from the model.
- The 2nd excavation phase (time step from 30 to 39) - at time step 30: 31 RBDY3 objects of the Model 4 in the 2nd tunnel segment were eliminated from the model.
- The 3rd excavation phase (time step from 40 to 49) - at time step 40: 68 RBDY3 objects of the Model 4 in the 3rd tunnel segment were eliminated from the model.
- The 4th excavation phase (time step from 50 to 59)- at time step 50: 25 boundaries plates behind the tunnel and 69 RBDY3 objects of the Model 4 in the 4th tunnel segment were eliminated from the model.
- The finishing phase (time step from 60 to 100): there were 1259 RBDY3 objects of the Model 4 and 436 boundaries plates at the end of the simulation.

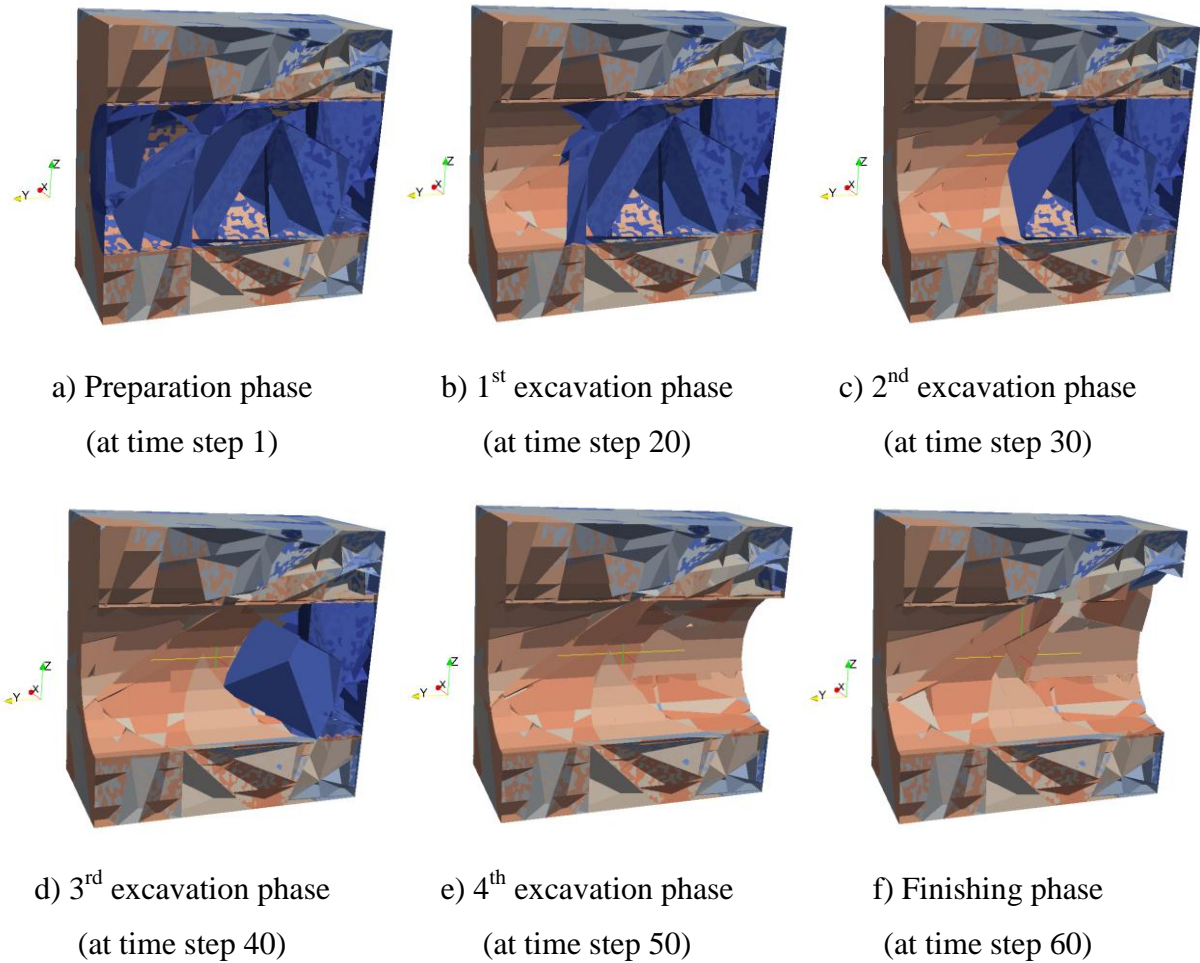


Figure 3.7.10: Change of the left half of the Model 4 during the excavation procedure

Notation of the Figure 3.7.7: The direction of the tunnelling is from the left to the right. The images shown a half of the rock mass cut by a vertical plan of view.

3.7.3. Results and interpretation of the Combination 2 under the 1st loading case

The simulation of each loading case was executed following the equivalent tunnelling schedule. Once all the simulations were launched, the mechanical responses of the models were recorded as algebra data in the *.dat files in the POSTPRO folder and as visual data in *.vtu files in the DISPLAY folder in the Post-Processor of LMGC90. Three categories of responses of the models were examined: the movements of rock blocks inside the models; the contact forces between the rock blocks; and the contact pressures between them. In order to investigation of the redistribution of the contact forces and the contact pressures in the rock mass under the effect of the tunnelling procedure, a 2-metre-thick-slice of the models located on the axis Y with $y = [4, 6]$ (m) was monitored during the 100 time step of the simulation. The following obtained results of some typical moments of the simulation

are presented on the images and on the histograms of the block quantity distribution (refer the Appendix D for the other results).

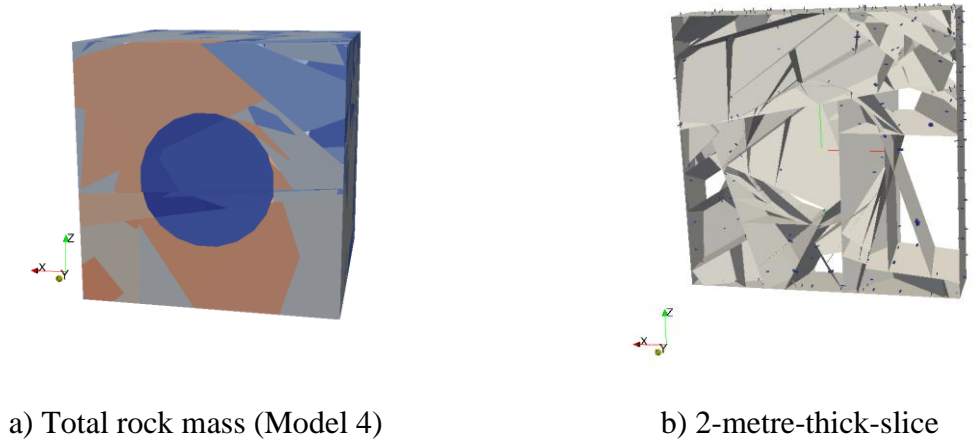


Figure 3.7.11: Total rock mass and 2-metre-thick-slice for the monitoring

3.7.3.1. Movements of rock blocks during the tunnelling schedule

The evolution of movement of the Model 4 under the application of the 1st loading case was studied on the variation of the displacement of blocks in the total model and in the monitored slice at some important moments of the tunnelling schedule.

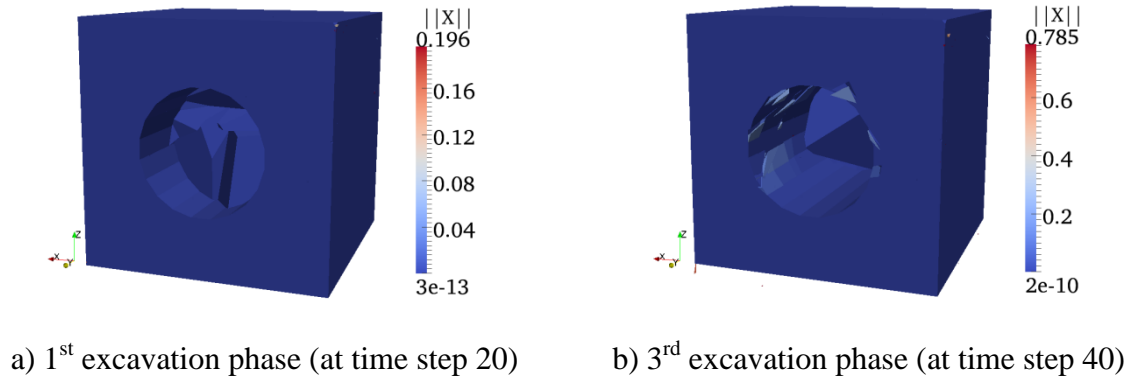


Figure 3.7.12: Moving rock blocks of the Model 4 during its tunnelling procedure

Notation of the Figure 3.7.12: $\|X\|$ (m) is the absolute displacement of rock blocks of the model. The colour scales indicates the magnitude of the recorded displacements of the rock blocks.

The scanned image of the monitored slice in the Model 4 during the simulation time showed the position of the inertial centre of the RBDY3 objects of the model. The absolute displacement of a rigid block at a requested time step was represented by a 3D vector placed at the inertial centre of the block: the direction of the vector is coincident with the

direction of the movement of the block; and the colour and the shape of the vector presented the magnitude of the displacement.

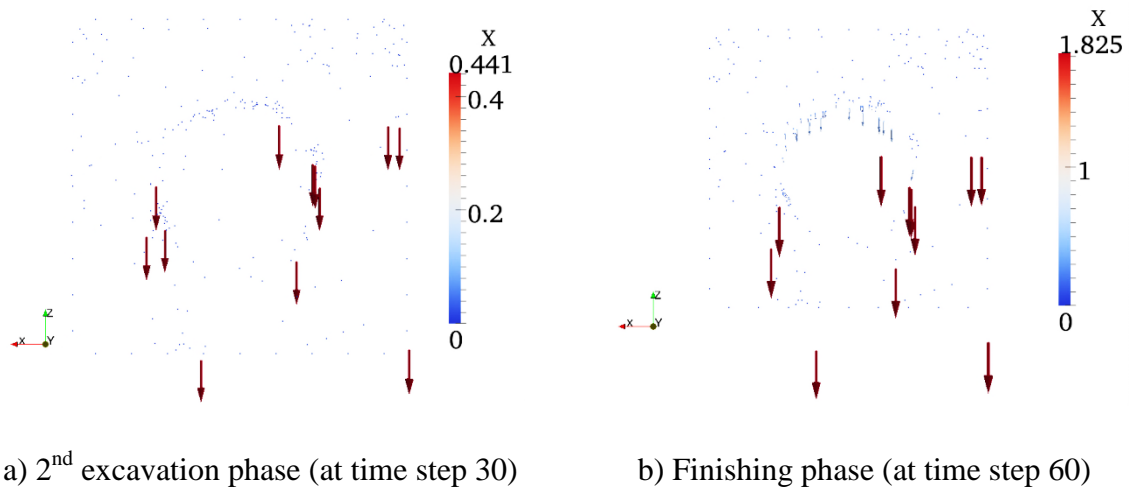


Figure 3.7.13: Flows of movement of rock blocks inside the Model 4 during the simulation time

Notation of the Figure 3.7.13: X is the magnitude of the displacement of the rock blocks of the Model 4, m. The colours and the shapes of vectors are different in each scanned image of the model and are only appropriate with the magnitude scale placed on the right of the model.

The change of the rock mass before and after each excavation was studied on the displacement variation of the rock blocks in the model at the relevant time steps. The results of the 4th excavation are presented as an example. Other results are found in the Appendix D.

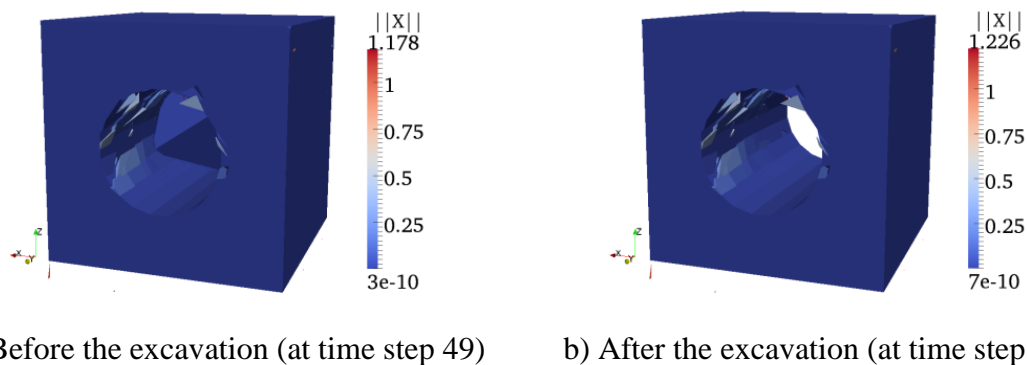


Figure 3.7.14: Change of the displacement of the Model 4 the 4th excavation

Notation of the Figure 3.7.14: $\|X\|$ (m) is the absolute displacement of rock blocks of the model. The colour scales indicates the magnitude of the recorded displacements of the rock blocks.

Studied on the flows of movement of the rock mass on the vicinity of the excavation, some initial conclusions were given:

- The light disturbed movement at the time step 1 was explained as the stabilization of the model under the loading application. The maximum of its absolute values were inferior of 10^{-4} (m) so that this state was proposed to be neglected.
- The numerical flow movements of the rock model was considered to be light perturbed even before the start of the excavation. This phenomenon can be explained as the consequence of the non-equilibrate state of the *in situ* stresses applied on the model. It caused the high absolute displacement of some rock blocks in the model during the excavation procedure but the number of moving blocks was small. Those moving blocks can be fixed by the application of the isolation layers and the shotcrete layer (or the permanent tunnel structures) that will be quickly realised after the blasting of each excavation segment.
- Falling blocks at the tunnel crown after the last excavation phase was observed so that the application of a temporary protection or cover might be recommended on the real structure as a stabilization measure during the construction procedure.

The working states of the tunnel and its rock mass during the tunnelling procedure were concluded to be theoretically reasonable and to be in accordance with the observation of real tunnels in hard rock.

3.7.3.2. Contact forces between the rock blocks

The contact force R between two neighbouring rock blocks in the models is composed of the normal R_N and the tangential R_T components. The variations of the forces were recorded during the simulation time. In order to investigate their redistribution in the rock mass under the effect of the tunnelling procedure, a 2-metre-thick-slice of the models located on the axis Y with $y = [4, 6]$ (m) was monitored during the 100 time steps of the simulation.

a) Variation of the magnitude of the normal contact forces versus the quantity of contact faces

The obtained results are presented on the histograms of the magnitude of R_N versus the number of contacts and on the scanned image of the monitored slice. For a clear presentation, the values of R_N are statistical treated versus three continuous thresholds:

- When $0 \leq R_N \leq 10^3$ (N);
- When $10^3 \leq R_N \leq 10^6$ (N);
- When $10^6 \leq R_N \leq 6.10^7$ (N).

On the scanned images, the contact forces are presented on their contact faces and the magnitudes of R_N are showed by the variations of colour. The colour scales are different in each scanned image of the model and are only appropriate with the scanned image placed on its left. On the histograms, the vertical axis expresses the number of contacts; the horizontal expresses the value of forces.

According to the obtained variations of the normal contact R_N in the monitored slice during the excavation procedure, it was concluded that:

- The number of contact faces of which $10^6 \leq R_N \leq 6.10^7$ (N) was minor in comparison with the rest. The maximal value of contact forces rose lightly during the simulation time.
- At the three first phases, the second interval of forces ($10^3 \leq R \leq 10^6$ (N)) was the most dense but at the three last phases, the first interval ($0 \leq R \leq 10^3$ (N)) and the second one ($10^3 \leq R \leq 10^6$ (N)) were nearly of the same importance.
- The augmentation of the maximal value of R_N during the 6 excavation phases was recorded. The extreme values of the R_N are presented in the following table.

The results are presented in the figure 3.7.15 and in the Appendix D.

Notation of the Figure 3.7.15: R_N is the magnitude of normal contact force of the rock blocks in the monitored slice of the Model 4, N. The colour scales indicates the magnitude of the recorded forces of the rock blocks.

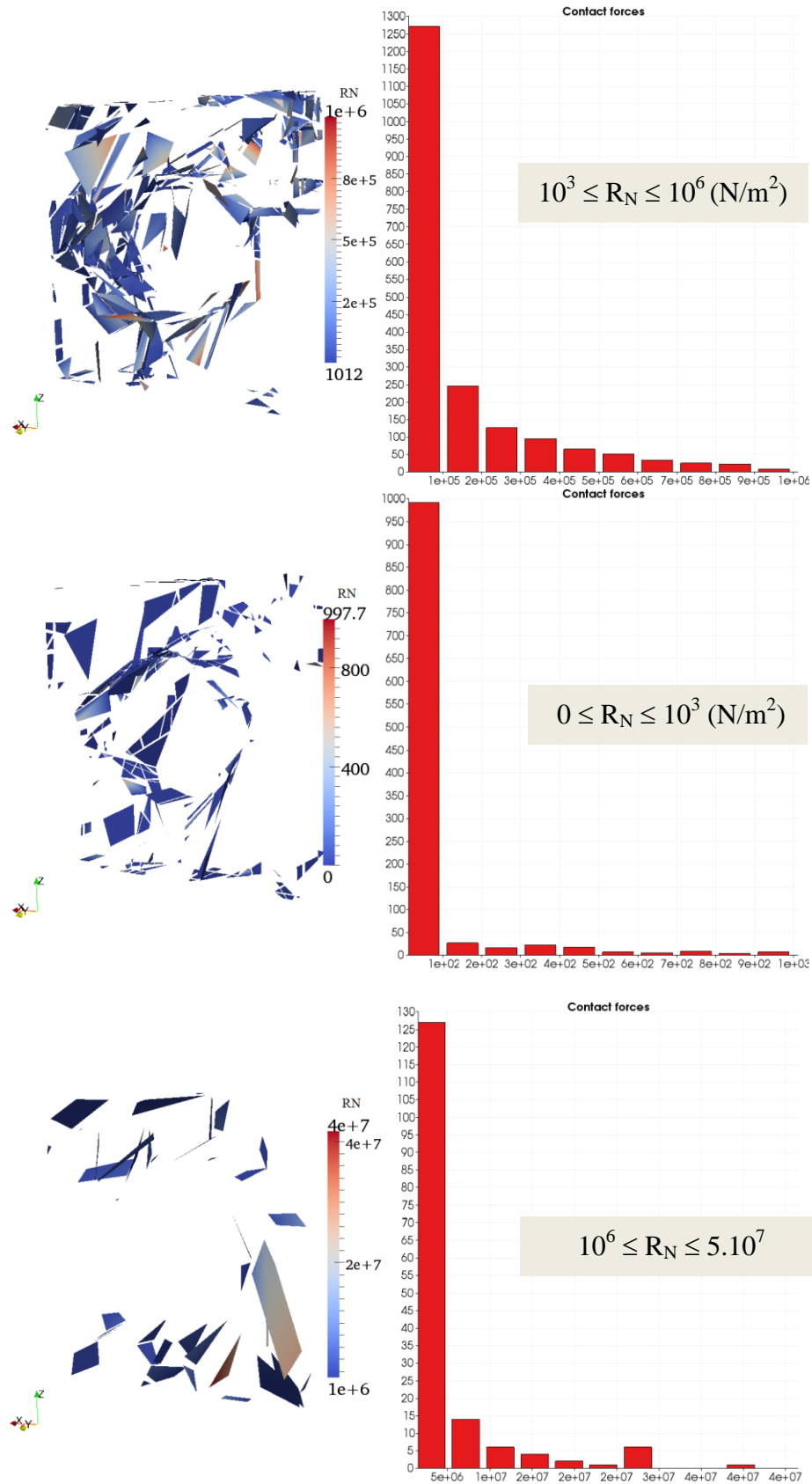


Figure 3.7.15: Variations of the normal contact forces in the monitored slice
at the 2nd excavation phase (at time step 30)

b) Variation of the maximal contact forces in the monitored slice

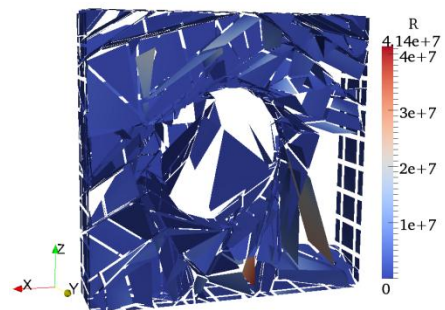
The value of the maximal contact forces in the monitored slice in some important moments of the excavation procedure was recorded and a reduction of the contact forces was observed after the last excavation phase. The obtained results are presented in the figure 3.7.18, in the table 3.7.3, and in the Appendix D.

Table 3.7.3: Maximal values of the contact forces during the excavation procedure

Simulation phase	R_{\max} (N)
Preparation phase (at time step 1)	2.02e+7
Before the 1 st excavation phase (at time step 19)	1.98e+7
After the 1 st excavation phase (at time step 20)	2.85e+7
Before the 2 nd excavation phase (at time step 29)	2.86e+7
After the 2 nd excavation phase (at time step 30)	4.14e+7
Before the 3 rd excavation phase (at time step 39)	4.24e+7
After the 3 rd excavation phase (at time step 40)	4.85e+7
Before the 4 th excavation phase (at time step 49)	5.06e+7
After the 4 th excavation phase (at time step 50)	5.47e+7
Finishing phase (at time step 60)	5.50e+7
Finishing phase (at time step 80)	5.45e+7
Finishing phase (at time step 100)	5.38e+7



a) Before the excavation (at time step 39)



b) After the excavation (at time step 40)

Table 3.7.16: Redistribution of the contact force in the monitored slice
in the 3rd excavation phase

Notation of the Figure 3.7.16: R is the magnitude of normal contact force of the rock blocks in the monitored slice of the Model 4, N. The colour scales indicates the magnitude of the recorded forces of the rock blocks.

c) Sliding threshold of the rock blocks

The correlation between the two components of the contact force influences the stability state of the rock block. With the contact condition of the model being governed by the dry friction law of Coulomb, the sliding threshold of a rock block is the product of $\mu.R_N$. Hence, the mobility of a rock block can be expressed by the stability parameter K that is given by the following ratio:

$$0 \leq K = \frac{R_T}{\mu.R_N} \leq 1$$

With:

K: Stability parameter of the blocks

R_T : Tangential component of the contact force of rock blocs (N)

R_N : Normal component of the contact force of rock blocks (N)

μ : Friction coefficient, $\mu = \tan(\varphi) = 0.4$

$\mu.R_N$: Sliding threshold of rock due to the friction contacts

φ : Internal angle of friction (rad or degree)

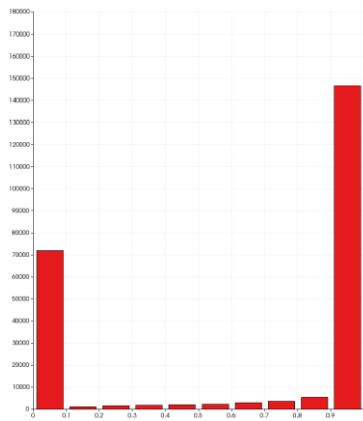
- When $K = 0$, the blocks are completely fixed.
- When $0 < K < 1$, the blocks are stable. The tangential components of contact forces are smaller than the sliding threshold, or the normal components of the contact forces were strong enough to prevent the blocks from moving.
- When $K = 1$, the rock blocks move by sliding on the contact faces between them. The tangential components of contact forces surpasses the sliding threshold of rock.

The variations of the values of K of the rock blocks in the monitored slice in each phase of the excavation process were examined. The obtained results are presented on the histograms of the contact faces distribution versus K of which the figure 3.7.17 is an example (other figures are presented in the Appendix D). The vertical axe expresses the

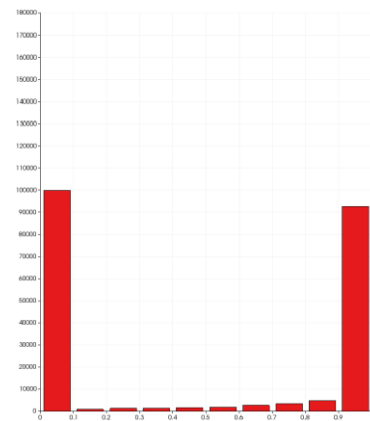
contact face quantity and the horizontal one present the value of K. The extreme values of K and the equivalent numbers of contact faces are shown in the Table 3.7.4.

Table 3.7.4: Quantity of rock faces of which K were critical in the monitored slice

Simulation phase	When K = 0	When K = 1
Preparation phase (at time step 1)	3950	3145
1 st excavation phase (at time step 20)	6618	2641
2 nd excavation phase (at time step 30)	11060	2800
3 rd excavation phase (at time step 40)	14234	2232
4 th excavation phase (at time step 50)	14514	1535
Finishing phase (at time step 60)	12458	1440



a) 2nd excavation phase (at time step 30)



f) Finishing phase (at time step 60)

Figure 3.7.17: Histograms of the stability parameter of rock blocks in the monitored slice

3.7.3.3. Contact pressures between the rock blocks

a) Distribution of the magnitude of the contact pressures versus the quantity of contact

The contact pressure σ of two neighbouring rock blocks was calculated as the ratio between the contact forces and the contact surface between them. It is composed of two perpendicular components σ_N and σ_T equivalent with the two perpendicular components R_N and R_T of the relevant contact force. The variations of the pressures and their redistribution in the rock mass during the tunnelling procedure were monitored on the 2-metre-thick-slice of the rock mass as mentioned in the previous part. The procedure of data treatments that had been realised on the contact forces (see section 3.7.3.2) were carried out on the contact

pressures between the rock blocks in the monitored slice. For a clear presentation, the values of σ are statistical treated depending on three continuous thresholds:

- When $0 \leq \sigma \leq 10^3$ (N/m²);
- When $10^3 \leq \sigma \leq 10^6$ (N/m²);
- When $10^6 \leq \sigma \leq 2.10^8$ (N/m²).

The obtained results are presented as follows. On the scanned images, the contact pressures are presented on the zero-moment-point on their contact faces. Their magnitudes are expressed by the dimension and the colour of the points. The colour scales are different in each scanned image of the model and are only appropriate with the scanned images placed on its left. On the histograms, the vertical axis expresses the number of contacts; the horizontal one expresses the value of contact pressures. The obtained results are found in the figure 3.7.17 and in the Appendix D.

Notation of the Figure 3.7.18: $\|R\|/\text{area}$ is the magnitude of contact pressures the rock blocks in the monitored slice of the Model 4, (N/m²). The colour scales indicates the magnitude of the recorded pressures of the rock blocks.

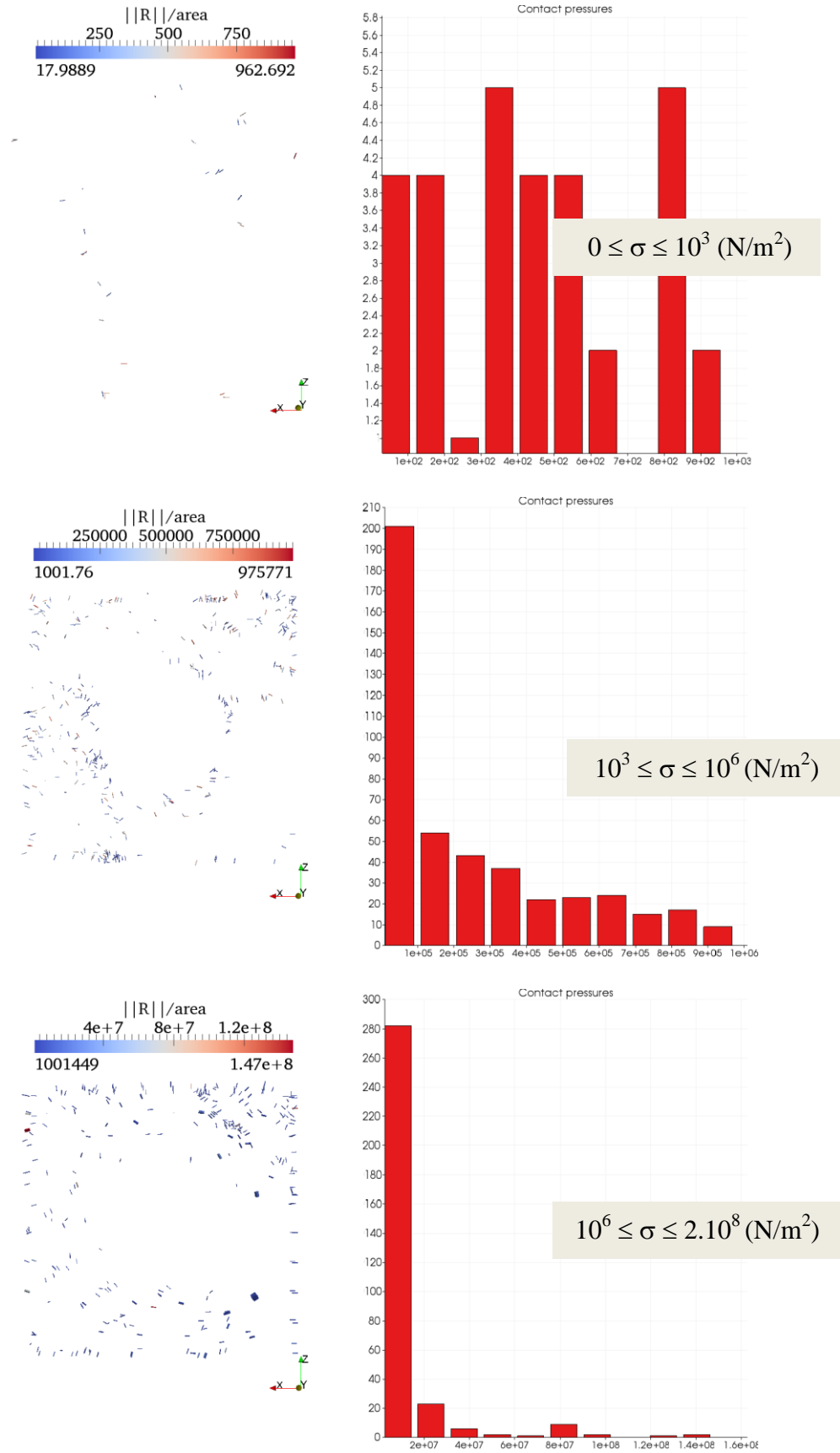


Figure 3.7.18: Variations of the contact pressures in the monitored slice
at the finishing phase (at time step 60)

b) Critical contact pressure in the monitored slice

The value of the critical contact pressures in the monitored slice in some important moments of the excavation procedure was recorded and a reduction of the contact pressures was observed after the last excavation phase.

Table 3.7.5: Extreme values of the contact pressures σ_N during the excavation procedure

Simulation phase	σ_{\min} (N/m ²)	σ_{\max} (N/m ²)
Preparation phase (at time step 1)	4.47e-6	2.97e+8
Before the 1 st excavation phase (at time step 19)	1.85e-5	5.93e+8
After the 1 st excavation phase (at time step 20)	0.0225	7.52e+8
Before the 2 nd excavation phase (at time step 29)	0.0511	3.77e+8
After the 2 nd excavation phase (at time step 30)	0.0002	4.42e+8
Before the 3 rd excavation phase (at time step 39)	0.2106	4.47e+8
After the 3 rd excavation phase (at time step 40)	0.0913	4.91e+8
Before the 4 th excavation phase (at time step 49)	0.0057	5.18e+8
After the 4 th excavation phase (at time step 50)	0.0057	5.20e+8
Finishing phase (at time step 60)	0.0008	5.04e+8
Finishing phase (at time step 80)	0.0008	3.83e+8
Finishing phase (at time step 100)	0.0009	3.72e+8

3.7.4. Results and interpretation of the Combination 2 under the 2nd loading case

The simulation of the rock mass and its tunnel under the 2nd loading case was not in a stable state during the excavation procedure. An oblique failure plane appeared on the rock mass model very soon after the initial simulation step. There was a strong sliding on this plane that developed quickly that at the 6th time step: the model had already lost its initial geometrical configuration.

This failure was explained by the application of the tangential components of the *in situ* stresses on the boundary plates on the three 3-DOF fixed-faces of the cubic model. The plates were pushed out of their initial positions and glided on the relevant faces of the

model soon after some first simulation steps. Once they were not attached to their right places, the model became badly loaded and soon destroyed.

The mechanical responses of the model were theoretically right but were not satisfying our simulation targeted. Hence, this loading case was concluded to be not conformable to our simulation. Its results were kept as references in our research. More suitable boundary conditions of the model will be replaced to adapt this loading case.

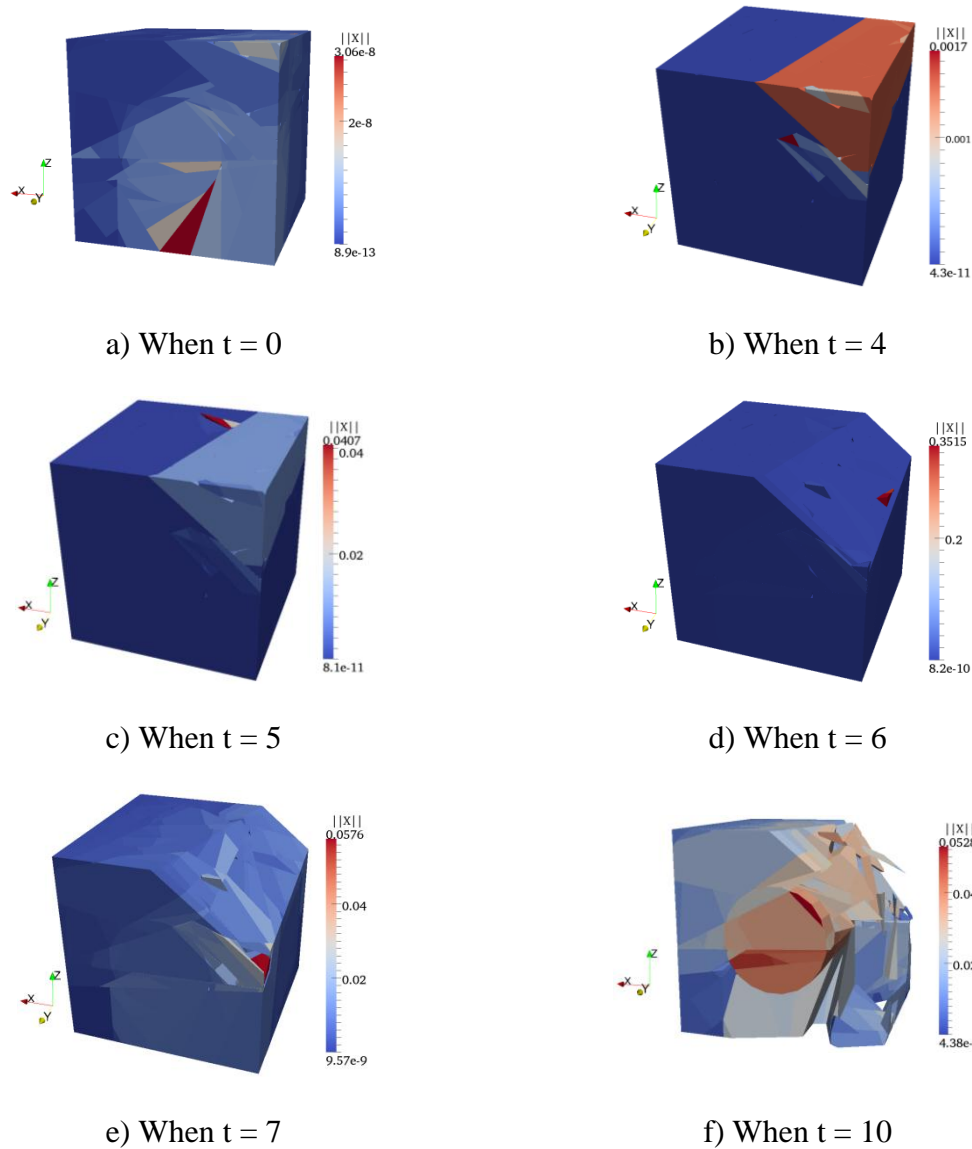


Figure 3.7.19: Destruction procedure of the model under the 2nd loading case during 10 first time steps

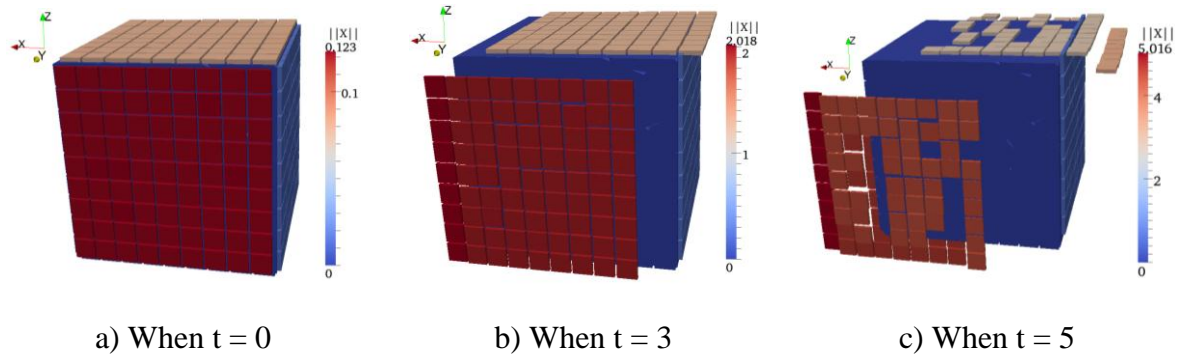


Figure 3.7.20: Faulty displacement of the boundary plates caused by the tangential stresses

Notation of the Figure 3.7.19 and 3.7.20: $\|X\|$ is the absolute displacement of the rock blocks of the Model 4, m. The colour scales indicates the magnitude of the recorded displacements of the rock blocks.

3.7.5. Results and interpretation of the Combination 2 under the 3rd loading case

The presentation on the obtained results of the 3rd loading case shares the same structure of the related part of the 1st loading case in the sub-section 3.7.4. The responses of the rock mass under the combination of the gravity and the supposed litho-static pressures $\sigma_1 = \sigma_2 = \sigma_3 = 21.72\text{MPa}$ were not great different from the ones of the 1st loading case.

3.7.5.1. Movements of rock blocks during the tunnelling schedule

The displacements of rock blocks under the loading condition were recorded and the results of their absolute values and the moving flows of the displacement vectors at some key time steps are presented here in following figures and in the Appendix D.

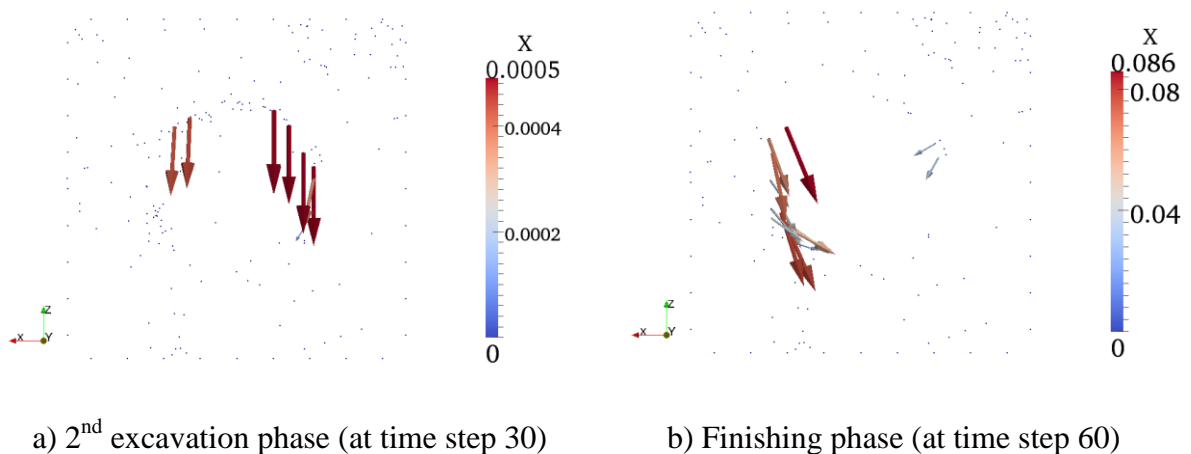
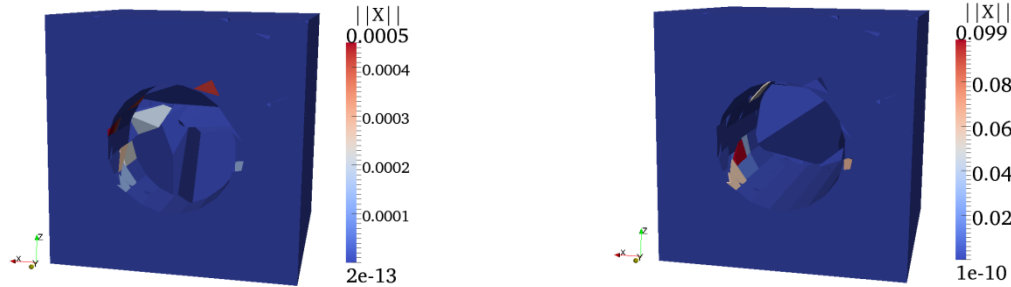


Figure 3.7.21: Flows of displacement of rock blocks of the Model 4 during the simulation time

Notation of the Figure 3.7.21: $X(m)$ is the magnitude of the displacement vector of rock blocks of the model. The colours and the shapes of vectors are different in each scanned image of the model and are only appropriate with the magnitude scale placed on the right of the model.

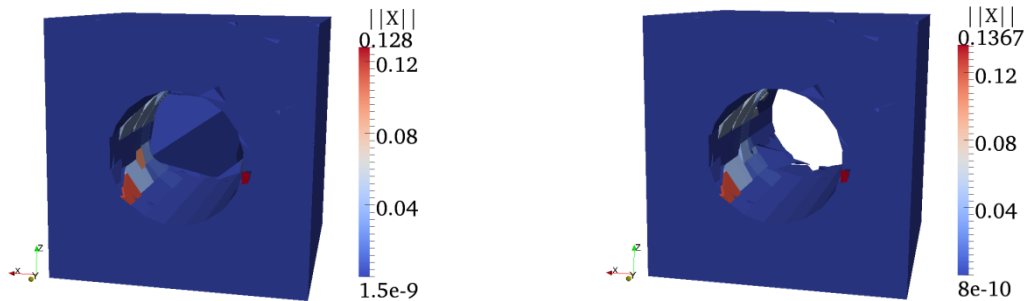


a) 1st excavation phase (at time step 20)

b) 3th excavation phase (at time step 40)

Figure 3.7.22: Moving rock blocks of the Model 4 during its tunnelling procedure

The change of the rock mass before and after each excavation was studied on the displacement variation of the rock blocks in the model at the relevant time steps. The results of the 4th excavation are presented in the figure 3.7.23, other results are found in the Appendix D.



a) Before the excavation (at time step 49)

b) After the excavation (at time step 50)

Figure 3.7.23: Change of the displacement of the Model 4 at the 4th excavation

Notation of the Figure 3.7.22 and 3.7.23: $||X||$ (m) is the absolute displacement of rock blocks of the model. The colour scales indicates the magnitude of the recorded displacements of the rock blocks.

Studied on the flows of movement of the rock mass on the vicinity of the excavation, some initial conclusions were given:

- The light disturbed movement at the time step 1 was explained as the stabilization of the model under the loading application. After the 1st excavation phase, a light

sliding tendency was appeared on the right side above the tunnel crown but then quickly disappeared. The maximum of the absolute displacement of rock blocks in two mentioned cases were inferior of 10^{-9} (m) so that this state was proposed to be neglected.

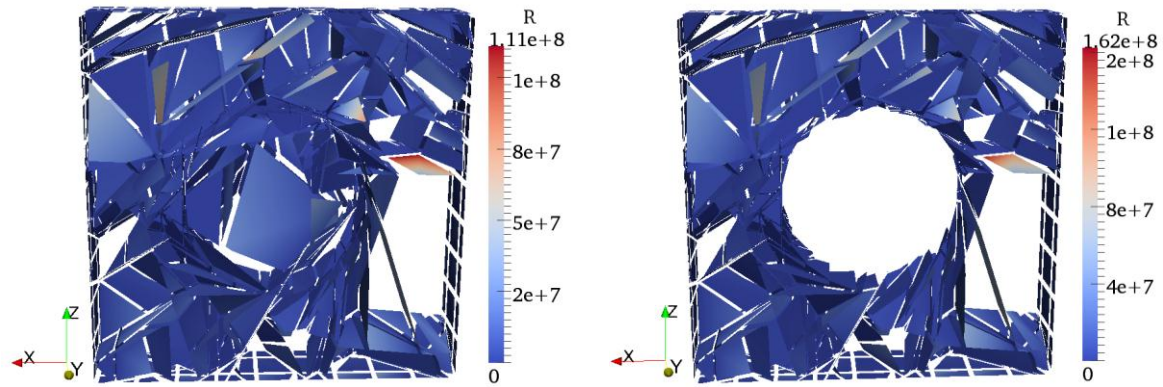
- The numerical flow movements of the rock mass which took place on the boundary of the excavation were reasonable with the actual responses of a real tunnel excavation in hard rock. The other regions inside the model were stable and there were no other sliding zone.
- During the excavation procedure, the absolute values of the displacement of rock blocks were not high in general. In each simulation phase, the number of maximal moving blocks was small. Those moving blocks can be fixed by the application of the tunnel structures that will be quickly realised after the blasting of each excavation segment.
- After the last excavation phase, the block falling was observed at the crown of the furthest tunnel head. The phenomenon created a local deformation at the crown but did not lead to the destruction of the other neighbouring regions in the model. The immediate application of a tunnel structure at the crown after the last excavation case was hence recommended for the stabilization of the whole model.

The working states of the tunnel and its rock mass during the tunnelling procedure were concluded to be more stable than the one of the 1st loading case. This model was considered to be theoretically reasonable and to be able in accordance with the observation of real tunnels in hard rock.

3.7.5.2. Contact forces between the rock blocks

The study approach which has been introduced in the section 3.7.3.2 was applied on the contact forces of rock blocks in the monitored slice of the model 4 during the simulation. The obtained results are presented in the following part and in the Appendix D

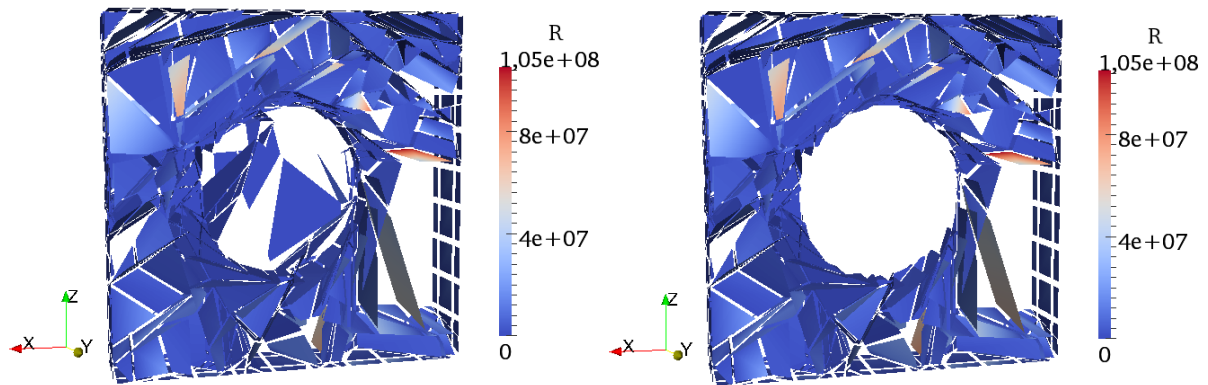
a) Variation of the contact forces in the monitored slice



a) 1st excavation phase (at time step 20)

b) Finishing phase (at time step 50)

Figure 3.7.24: Redistribution of contact force in the monitored slice of the model 4 during the excavation procedure



a) Before the excavation (at time step 39)

b) After the excavation (at time step 40)

Figure 3.7.25: Redistribution of contact force in the monitored slice before and after the 3rd excavation phase

Notation of the figure 3.7.24 and 3.7.25: R is the magnitude of normal contact force of the rock blocks in the monitored slice of the Model 4, N. The colour scales indicates the magnitude of the recorded forces of the rock blocks.

b) Variation of the maximal contact forces in the monitored slice

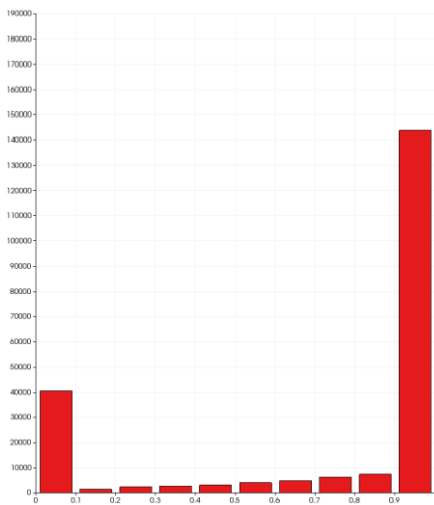
The value of the maximal contact forces in the monitored slice in some important moments of the excavation procedure was recorded and a reduction of the contact forces was observed after the last excavation phase. The obtained results are presented in the table 3.7.6, in the figure 3.7.18 and in the Appendix D.

Table 3.7.6: Maximal values of the contact forces during the excavation procedure

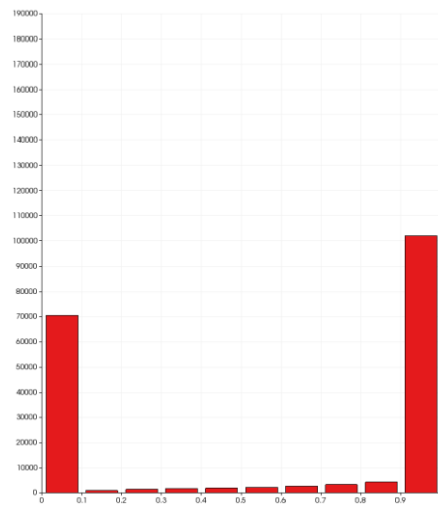
Simulation phase	R_{\max} (N)
Preparation phase (at time step 1)	1.05e+8
Before the 1 st excavation phase (at time step 19)	1.08e+8
After the 1 st excavation phase (at time step 20)	1.11e+8
Before the 2 nd excavation phase (at time step 29)	1.11e+8
After the 2 nd excavation phase (at time step 30)	1.19e+8
Before the 3 rd excavation phase (at time step 39)	1.19e+8
After the 3 rd excavation phase (at time step 40)	1.32e+8
Before the 4 th excavation phase (at time step 49)	1.35e+8
After the 4 th excavation phase (at time step 50)	1.62e+8
Finishing phase (at time step 60)	1.70e+8
Finishing phase (at time step 80)	1.81e+8
Finishing phase (at time step 100)	1+86e+8

c) Sliding threshold of the rock blocks

The histograms of the contact faces distribution versus K were built of which the vertical axes express the contact face quantity and the horizontal ones present the value of K .



c) 2nd excavation phase (at time step 30)



e) 4th excavation phase (at time step 50)

Figure 3.7.26: Histograms of the stability parameter of rock blocks in the monitored slice

3.7.3.3. Contact pressures between the rock blocks

The contact pressures σ of each rock block faces in the monitored slice were studied the same method with the section 3.7.3.3. The value of the critical contact pressures in the monitored slice in some important moments of the excavation procedure was recorded and a reduction of the contact pressures was observed after the last excavation phase.

Table 3.7.7: Extreme values of the contact pressures σ_N during the excavation procedure

Simulation phase	σ_{\min} (N/m ²)	σ_{\max} (N/m ²)
Preparation phase (at time step 1)	2.99e-8	1.15e+9
Before the 1 st excavation phase (at time step 19)	1.11e-5	1.04e+9
After the 1 st excavation phase (at time step 20)	157.24	1.26e+9
Before the 2 nd excavation phase (at time step 29)	164.78	1.27e+9
After the 2 nd excavation phase (at time step 30)	0.0183	1.37e+9
Before the 3 rd excavation phase (at time step 39)	23.266	1.37e+9
After the 3 rd excavation phase (at time step 40)	17.763	1.44e+9
Before the 4 th excavation phase (at time step 49)	1.392	1.45e+9
After the 4 th excavation phase (at time step 50)	14.898	1.41e+9
Finishing phase (at time step 60)	29.677	1.44e+9
Finishing phase (at time step 80)	31.635	1.49e+9
Finishing phase (at time step 100)	15.235	1.9e+9

Further results are found in the Appendix D.

3.7.6. Comparison of the mechanical behaviours of the model under two loading cases

Some mechanical behaviours of the monitored slices of the model in two loading cases were collected to understand more the effect of the two cases on the same model:

- Absolute displacement of the blocks $\|X\|$ (m);
- Absolute velocity of the blocks $\|V\|$ (m/s);
- Position and magnitude (N) of the maximal normal contact forces between the blocks;

- Position and magnitude (N/m) of the maximal normal contact pressures between the blocks;
- Position and magnitude (N/m) of the maximal contact pressures between the blocks.

The results showed that the model and its tunnel were in stable conditions during the excavation procedure. During the excavation phases (from the time step 20 to 49), the evolution of movements of rock blocks around the tunnel boundary in two cases were not strongly different but the absolute values of displacement of the 3rd loading case were evidently smaller. No failure was found in the model during the simulation.

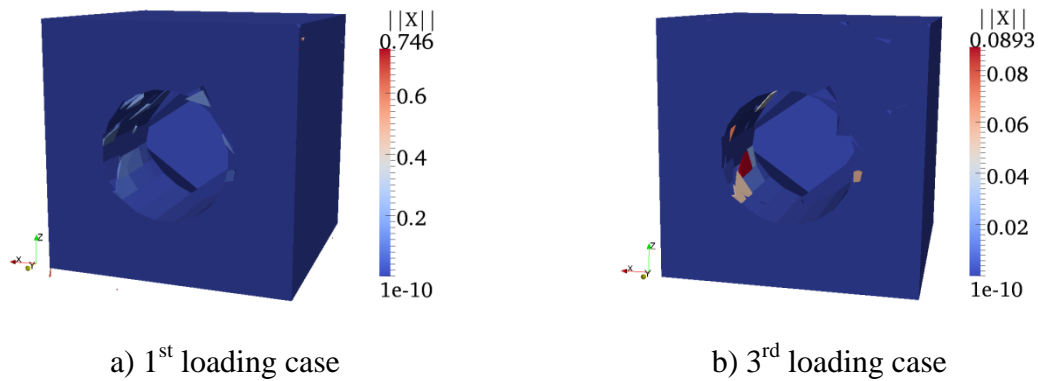


Figure 3.7.27: Falling blocks in the Model 4 in the 1st and 3rd loading cases
at the end of the 3rd excavation phase (at time step 39)

After the last excavation phase (from the time step 50 to 100), the deformation at the tunnel crown of the 3rd loading case was developed more quickly but the absolute displacements of the rock blocks in the model were smaller in comparison with the equivalent values of the model of the 1st loading case.

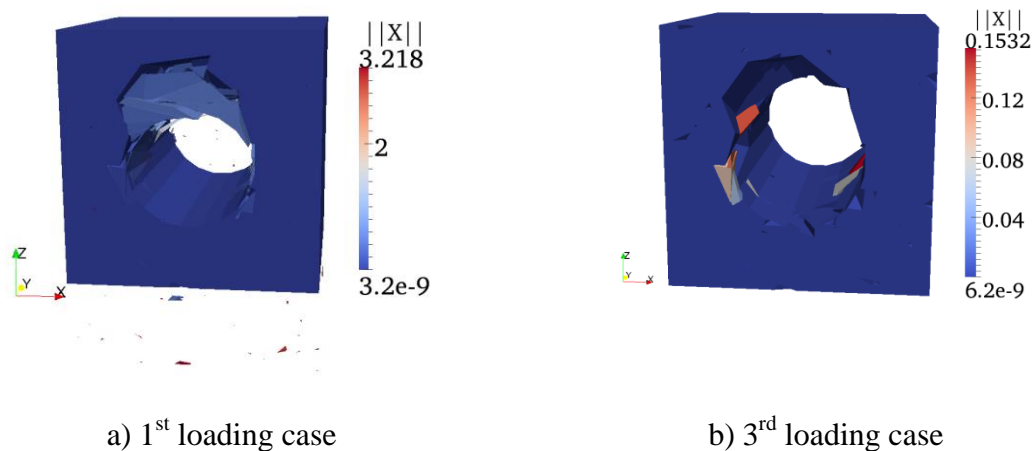


Figure 3.7.28: Deformation at the crown observed from the furthest tunnel head
in the 1st and 3rd loading cases at the finishing phase (at time step 80)

Notation of the figure 3.7.27 and 3.7.28: $\|X\|$ (m) is the absolute displacement of rock blocks of the model. The colour scales indicates the magnitude of the recorded displacements of the rock blocks.

However, observed in the monitored slice, the deformation zone at the tunnel crown of the 1st loading case was more evident than the one of the 3rd loading case. The vicinity of the excavation in the monitored slice of the 3rd loading case was considered to be more stable than the one of the 1st loading case. The obtained results of the model in the finishing phase (at time step 80) under the applications of the two loading cases are presented. The other results are found in the Appendix D.

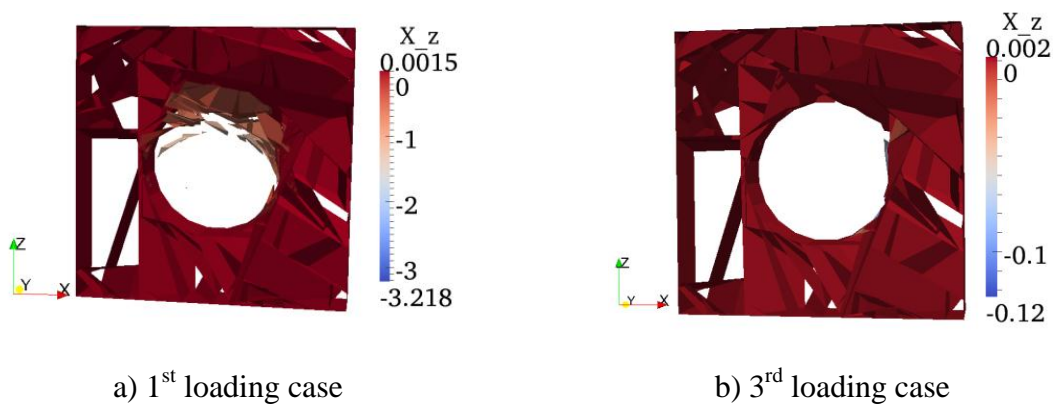


Figure 3.7.29: Deformation zone at the crown of the tunnel observed in the monitored slice in the 1st and 3rd loading cases at the finishing phase (at time step 80)

Notation of the Figure 3.7.29: X_z (m) is the absolute vertical displacement of rock blocks of the model. The colour scales indicates the magnitude of the recorded displacements of the rock blocks.

The values of the contact forces and contact pressures of the 3rd case were bigger than the ones of the 1st case. The zone of the maximal contact force and the maximal contact pressures of the two cases were unchanged during the simulation time. The most critical zone of the model of the 1st loading case was considered to be under the platform of the excavation. The most critical zone of the model of the 3rd loading case was considered to be on the wall of the excavation. The obtained results of the under the applications of the two loading cases are presented in the figure 3.7.31 and 3.7.32 and in the Appendix D.

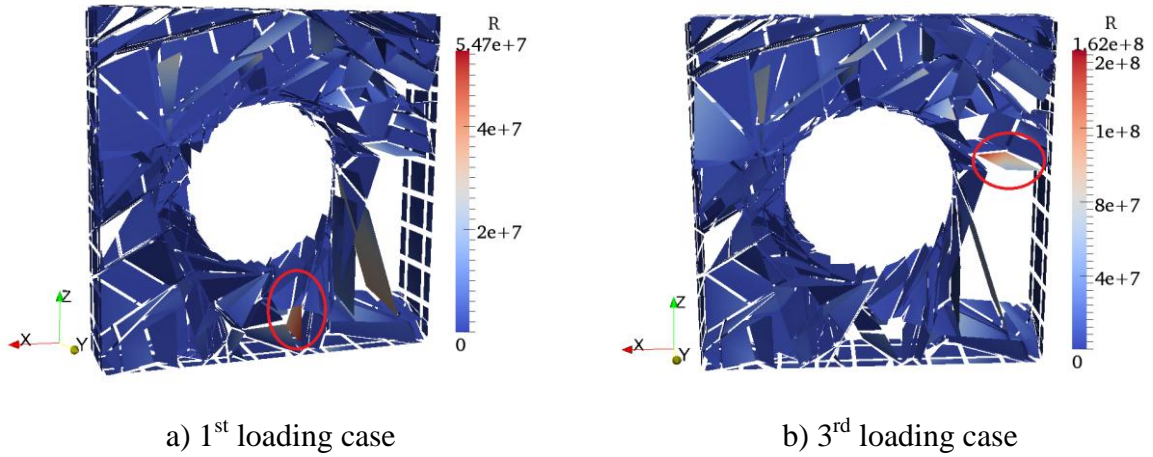


Figure 3.7.30: Comparison of contact forces of the model
in the 1st and 3rd loading cases in the 4th excavation phase (at time step 50)

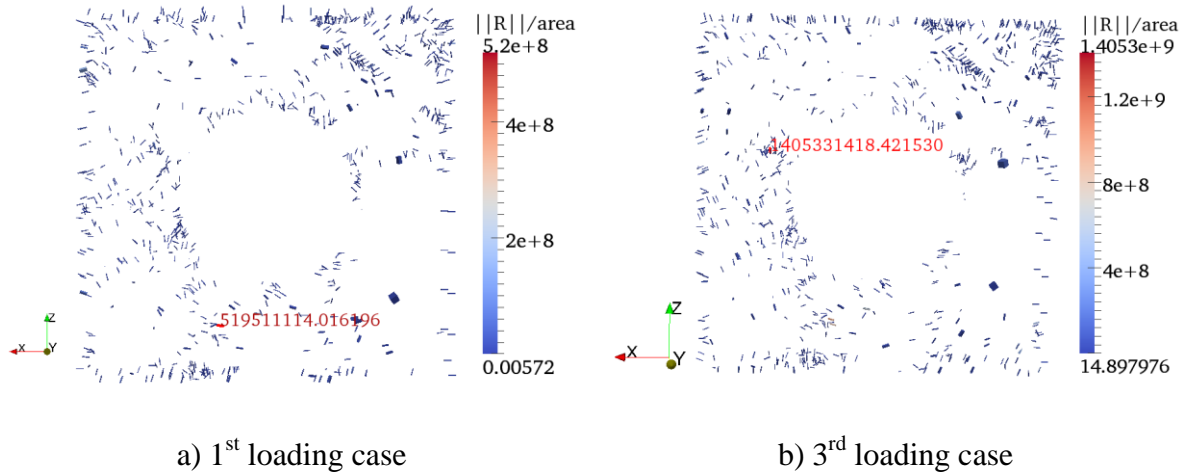


Figure 3.7.31: Comparison of contact pressures in the monitored slice of the model
in the 1st and 3rd loading cases in the 4th excavation phase (at time step 50)

Notation of the Figure 3.7.30 and 3.7.31:

- R is the magnitude of normal contact force of the rock blocks in the monitored slice of the Model 4, N.
- $\|R\|/\text{area}$ is the magnitude of contact pressure of the rock blocks in the monitored slice of the Model 4, N/m^2 .
- The colour scales indicates the magnitude of the recorded values of the rock blocks. The red marks show the position of the maximal equivalent values in the slice.

3.7.7. Conclusions

The methodology that we proposed and presented in the Chapter 2 was applied on the data of the construction project of the future tunnel of Saint B  at. From the *in situ* investigation by the scan-line methods, the discontinuities families and their geo-statistical and statistical laws of distribution were found. The fracture scenarios of the rock mas were set up using the RESOBLOK code for the generation of the geometrical models, and for the discrete simulation and analysis on the LMGC90 code. In the scope of this research, we realised two simulation approaches for the excavation of the tunnel. The assumed tunnel was had the shape of a cylinder with the length $L = 10\text{m}$, and with the diameter $D=5\text{m}$. After importing the equivalent geometrical models of the rock mass and the excavation from RESOBLOK, the GMSH script, coupled in LMGC90, regenerated the rock blocks of the model and meshed their surfaces.

The boundary conditions and the loading conditions of the models were governed by the loading system of 486 rigid plats attached on the six faces of the models. The values of the *in situ* stresses of the Cap du Mont that had been measured by the ‘‘Overcoring’’ test in November, 2011 by INERIS, were applied for our models, together with the gravity. A tunnelling schedule of 6 phases in 100 time steps was simulated and the mechanical responses of the rock mass were recorded during the simulation time. A 2-metre-thick-slice in the middle of the rock mass was taken as the monitoring base. In the limitation of this document, the following behaviours of the rock mass during the assumed construction procedure are presented:

- The movements of rock blocks inside the model (analysis of their displacements and velocities);
- The contact forces and the contact pressures between the rock blocks, the distribution of their magnitude and their positions inside the model;
- The redistribution of the contact forces and the contact pressures fields of rock blocks under the effect of the excavation;
- The sliding threshold due to the dry friction contact of the rock blocks and the stable evolution of the model.

According on the obtained results, the rock mass and the assumed tunnel showed the stability state during the proposed tunnelling procedure. The movement of rock blocks in

the model under the 3rd loading case was found to be smaller than those of the 1st loading case while the contact forces and stresses caused by the 3rd loading case were stronger than those caused by the 1st loading case. In general, the excavation and its boundary rock mass under the 3rd loading case was in a more stable condition than the excavation and its boundary rock mass under the 1st loading case, although the applied pressures in the 3rd loading case was much stronger than those of the 1st loading case. The stronger confining pressures and the equilibrate state of the applied pressures in the 3rd loading case ($\sigma_1 = \sigma_2 = \sigma_3$) were considered to be the main reason for the better stabilization of the model. Some critical zones of the models during the excavation schedule were found. The high value of the contact pressures at these zones was concluded as the consequence of the extreme small contact faces between the constitutive blocks. This localization phenomenon was an inherent default caused by the non-regular loading distribution in the model as mentioned in the section 2.5.4.

In general, the mechanical responses of the numerical models were quite close to the normal states of a real tunnel construction in hard rock that had been found in many related technical documents. In order to take into account the necessary small dimension of the model, the behaviours of the monitored slice in the middle of the rock mass were used as representative of the whole model.

On the obtained results of the numerical behaviour of the modelled tunnel and its numerical rock massif, a normal condition with the general stability was found in both cases of simulation. Even the applied stresses in the 3rd loading case was about 10 times bigger than those of the 1st loading case, the equivalent rock mass was found to be more stable. This fact showed the stabilisation effect of the confining stresses on the rock mass. The massif of the marble of Saint B  at was concluded to be stable with normal rigid behaviour and the supposed tunnelling procedure was not found any grave hazards during the simulation. The results of this simulation can be used as a safe confirmation for the real construction project of the future tunnel of Saint B  at.

CONCLUSION AND RECOMMENDATION

All rock masses are more or less fractured. This statement, strongly acknowledged in rock mechanics, is used as the starting idea of this research. Through the bibliographical study presented in the first chapter, the mechanical framework and the numerical methods applied in rock mechanics have been approached. Simultaneously, three main tunnelling design methods have been recalled. This study has given us the fundamental basis of the research and has led to the choice of a methodology, introduced in the second chapter. To sum up, the methodology is a downstream procedure consisting in:

- The collection of the discontinuity data on the studied rock mass by the scan-line method;
- The geo-statistical and statistical data processing on collected data to define and fit the representative distribution laws of the discontinuities;
- The creation of geometrical models of rock mass and the preliminary selection of suitable models with the application of the Discrete Fracture Network (DFN) method and the block theory using RESOBLOK code;
- The characterization of the behaviour of rock mass through the mechanical responses obtained from in situ and laboratory measurements;
- The modelling of rock mass with the application of the Non Smooth Contact Dynamics (NSCD) method using the LMGC90 code.

The goal of the methodology is to study rock mass with the consideration of the presence of the rock structure (*i.e.* the discontinuity system). It has been applied to two problems in rock engineering:

- The simulation of the triaxial compression test for cylindrical specimens;
- The simulation of the multi-phase tunnel excavation.

The methodology is the combination of the structural geology, the *in situ* investigation and measurements, the discontinuity data processing by the use of the geo-statistics and statistics, the numerical methods in rock mechanics and the use of computer tools. It is aimed at proposing:

- A numerical rock model that can replace or simulate the mechanical behaviour of the natural model in laboratory tests;
- A numerical simulation of a tunnel in the rock medium with a multi-phase excavation schedule.

Direct achievements of the proposed methodology were looked for:

- The replacement of the natural distribution of rock structure by the statistical distribution of the main discontinuity families in the 3D space;
- The geometrical modelling of the rock mass in 3D in many scenarios of creation and a brief selection of interested cases following a given stability criterion;
- The use of natural stresses data in rock mass, obtained from the over-coring test measurements to represent, in the numerical model, the natural loading condition of the rock mass, as well as a means to assess the validity or the limits of theoretical loading cases;
- The simulation of the multi-phase excavation of a tunnel with the consideration of the state of the tunnel and its neighbouring rock medium before, during and after the excavation schedule, and at each excavation phase;
- The implicit discrete analysis of the rock mass, considered as the assemblage of rock blocks in non-smooth contact, controlled by different contact laws.

Some advantages of the methodology can be pointed out:

- The distribution of the rock structure is handled by using the simplest mapping technics and basic geo-statistical and statistical data processing;
- Diversified scenarios of the intersection of the discontinuities in rock mass can be simulated and the rock geometrical representation in 3D is graphically clear and rather friendly interacted with, using different computer codes for the analysis;
- The complex arrangement and precise loading path of classical tests in laboratory condition can be easily simulated;
- Depending on its location in the rock mass, the rock specimen or rock block behaviour is modelled, depending on the value and direction of the gravity, or following a given gravity function in the simulation, so that it is numerically included in or excluded from the model;

- The multi-phase excavation procedure of a tunnel in the rock mass can be modelled by a numerical multi-step schedule in the analysis;
- The tunnelling analysis as a combination of the empirical and numerical approaches is capable of ensuring a safer design and, hopefully, the safe use of the future tunnel;
- The monitoring of the evolution of motion, contact forces and contact stresses of the constitutive rock blocks in the rock mass are straightforward. That helps to predict the failure phenomena in the medium, the creation of the sliding planes, the determination of the weakest plane of the specimen;
- The redistribution of the contact and internal stresses during the simulation schedule is obtained with a clear presentation of the stress concentration zones, of the overloaded blocks and/or contacts;
- The list of the critical blocks and/or contacts in the medium due to some pre-defined criteria (critical values of velocity, displacement, energy, force or stress) can be exported for further analysis, allowing a more efficient design of appropriate reinforcements for those critical zones if necessary. The stability of the opening and of the neighbouring rock mass is thus controlled.

The proposed methodology had been applied on the fractured white marble of Saint B  at (Haute Garonne, France) and introduced in the third chapter for the modelling of a large-scale triaxial compression test and the modelling of a cylindrical four-phase-excavated opening. However, some limitations in the scope of this research are found:

- Only one *in situ* investigation was executed in the underground exploitation site of the OMG factory (the collected discontinuity data might not be fully representative of the general condition of the real 1.1 km long rock mass to be excavated);
- The different scenarios of the block generation in the rock mass by the intersection of the main families of discontinuities are preliminarily selected by the criterion of the number or volume of instable blocks or by a specific failure phenomenon. However, how to choose a particular realisation of those numerical statistically constrained models that is representative of the observed condition of the rock mass is still a challenge;

- The rock blocks are rigid and the contacts between them are governed by the dry friction Coulomb law;
- The morphology of the discontinuity walls is considered to be smooth and the eventual presence of fillings is neglected;
- Only the simplest structure of a tunnel (without its provisional or definitive support structure) is modelled in the second application;
- The published data of the *in situ* stresses in the rock mass of the Cap du Mount are diversified. Due to the proven existence of major tectonic events in the immediate vicinity of the tunnel (presence of the North Pyrenean Fault at the South head of the tunnel), the loading combinations used in the numerical simulation of the tunnel of Saint-Béat are only simplified cases;
- Due to the limitation of the personal computer equipment used, the size of the rock mass in the second application was 10x10x10 (m) and the tunnel diameter was 5 m;
- When the rock mass is strongly fractured with a high number of constitutive blocks, the post-processing for data processing becomes time consuming with the need of an independent processing tool (spread sheet).

For the improvement of the proposed methodology in the future, we aim at:

- Modelling the blocks as deformable and using more relevant contact laws;
- Comparing four cases: i) Rigid blocks and dry contacts; ii) Rigid blocks and cohesive contacts; iii) Deformable blocks and dry contacts; iv) Deformable blocks and cohesive contacts. The obtained results will demonstrate the advantages and defaults of each approach and suggest the scope of application;
- Finding a better solution for transferring the external force applied on the boundaries of the model to all the constituted rock blocks in the numerical rock mass;
- Taking into account the morphology of the walls and the filling of the discontinuities;
- Enlarging the model size of the rock mass for the tunnel excavation process to assess a characteristic length of the stress redistribution around the opening;

- Adding the support structures on the boundary of the opening and in the vicinity zone in the case of the tunnel modelling. Analysing the stabilisation of the rock mass with the presence of those structures and comparing the behaviours of the rock mass before and after the reinforcement.

The proposed methodology is hoped to be comprehensive since it started with the data collection and led to the numerical analysis and the post-processing processing of the rock mass. Its capability of application is not limited to the two examples presented in this document. Many laboratory tests can be simulated, as was done with the triaxial compression test in the first example. The recorded data of the numerical tests need to be compared with the recorded data of the real monitored experiments. With further adjustments and studies, the numerical tests are hoped to be used as the alternative beside the real tests, or to replace them when their realisations are not possible. The second example demonstrates the capability of the modelling of a complex construction procedure for a tunnel. It can be used as a solution for controlling and predicting the behaviour of the tunnel and its vicinity during the construction. It can stand as an independent analysis solution or as a reference for comparison with other analysis approaches.

The excavation phase of the construction project of the future tunnel of Saint-Béat will start in April, 2013. With the help of the in situ geologists and engineers, the rich data source of the real state of the rock mass and its monitored responses during the excavation process are to be obtained. They will be used as the input data for our models, and also as a way to check the validity of the obtained results of the numerical rock mass in our research. The collaboration is hoped to feed our further research, verify and strengthen our proposed methodology and the related models. The input data from other construction projects in different rock masses will also be of interest.

APPENDIX A: FURTHER RESULTS OF THE MODEL GENERATION ON RESOBLOK

A.1 Five scenarios for the model generation in the section 3.5

Basing on the fractured features of the discontinuity families of the rock mass of Saint B  at (see section 3.3 and 3.4), five possibilities of the fractured network of the rock mass were proposed and assigned as five scenarios that are presented in Table B.1 to B.5.

Table A.1: Fracture conditions of the Scenario 1

Family (colour representation)	Centre		Spatial distribution law		Extension of family
	α_d (�)	β_d (�)	Exponential law λ	Fisher law K	
F1 (blue)	321	71	1.5	7.0	Set
F2 (red)	194	81	1.5	7.0	Set
F3 (yellow)	323	21	0.5	40.0	Set
F4 (green)	86	60	1.26	6.0	Set

Table A.2: Fracture conditions of the Scenario 2

Family (colour representation)	Centre		Spatial distribution law		Extension of family
	α_d (�)	β_d (�)	Exponential law λ	Fisher law K	
F1 (blue)	321	71	1.5	7.0	Set
F2 (red)	194	81	1.5	7.0	Set
F3 (yellow)	323	21	0.5	40.0	Block
F4 (green)	86	60	1.26	6.0	Set

Table A.3: Fracture conditions of the Scenario 3

Family (colour representation)	Centre		Spatial distribution law		Extension of family
	αd (°)	βd (°)	Exponential law λ	Fisher law K	
F1 (blue)	320	70	1.58	14.5	Set
F2 (red)	193	81	1.50	22.0	Set
F3 (green)	82	54	1.38	4.5	Set

Table A.4: Fracture conditions of the Scenario 4

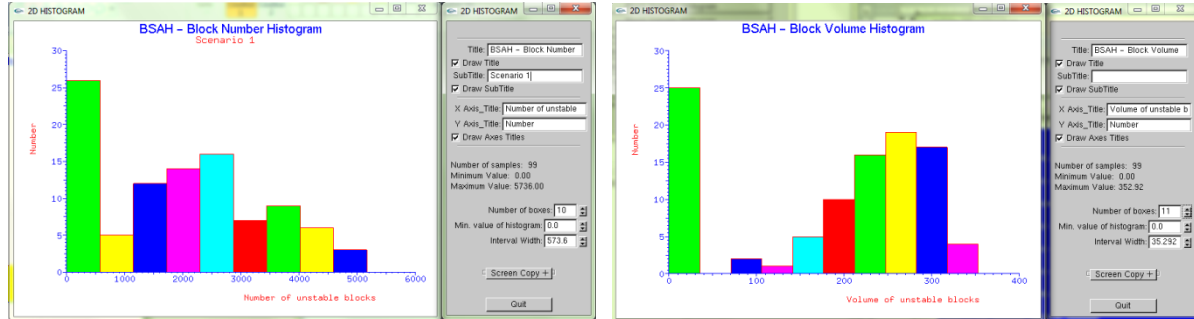
Family (colour representation)	Centre		Spatial distribution law		Extension of family
	αd (°)	βd (°)	Exponential law λ	Fisher law K	
F1 (blue)	321	71	1.5	7.0	Block
F2 (red)	194	81	1.5	7.0	Block
F3 (yellow)	323	21	0.5	40.0	Block
F4 (green)	86	60	1.26	6.0	Block

Table A.5: Fracture conditions of the Scenario 5

Family (colour representation)	Centre		Spatial distribution law		Extension of family
	αd (°)	βd (°)	Exponential law λ	Fisher law K	
F1 (blue)	320	70	1.58	14.5	Block
F2 (red)	193	81	1.50	22.0	Block
F3 (green)	82	54	1.38	4.5	Block

A.2. Statistical representations of the stability analysis on RESOBLOK of the models generated from the approach 2 and 3 of the tunnel simulation

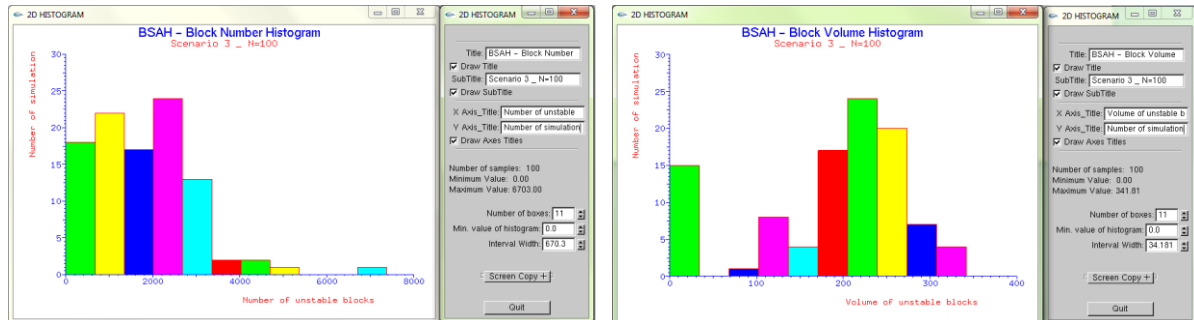
a) Histogram of the unstable blocks in the vicinity of the excavation



a) Unstable blocks number

b) Unstable blocks volume

Figure A.1: Histogram of the unstable blocks in the scenario 1 with $N = 100$ simulations



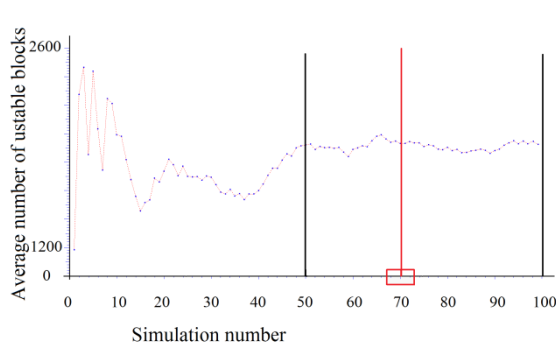
a) Unstable blocks number

b) Unstable blocks volume

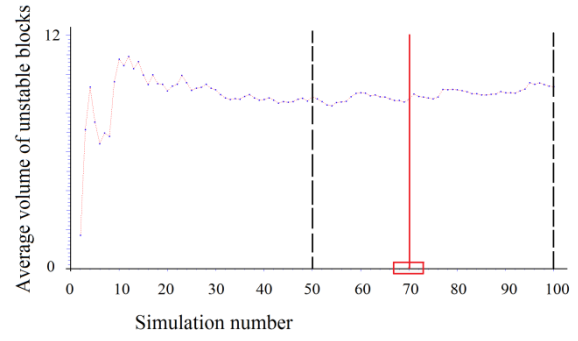
Figure A.2: Histogram of the unstable blocks in the scenario 3 with $N = 100$ simulations

b) Determination of the sufficient number of simulation for each scenario

Based on the graphs of the variation in the average number and volume of unstable blocks versus the number of simulation, the sufficient number of simulation for each scenario was found at the free-gradient segment of the graphs.

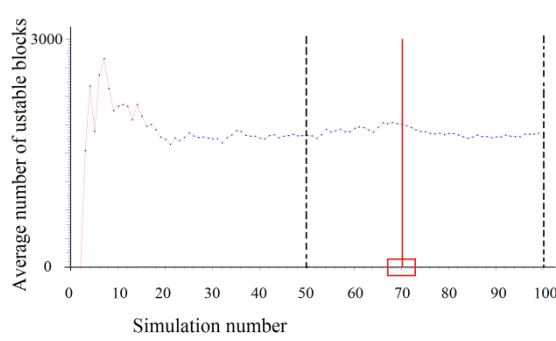


a) Curve of the average number

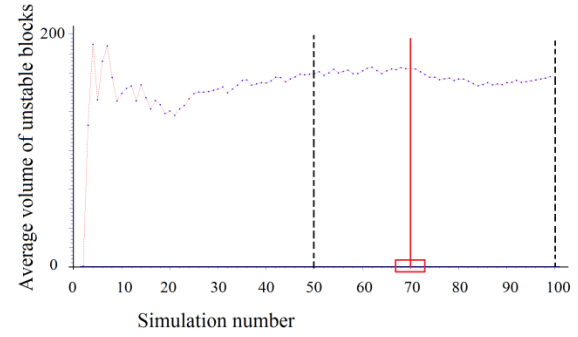


b) Curve of the average volume

Figure A.3: Variation in the average number and volume of unstable blocks versus the number of simulation in the scenario 1 with $N = 100$ simulations

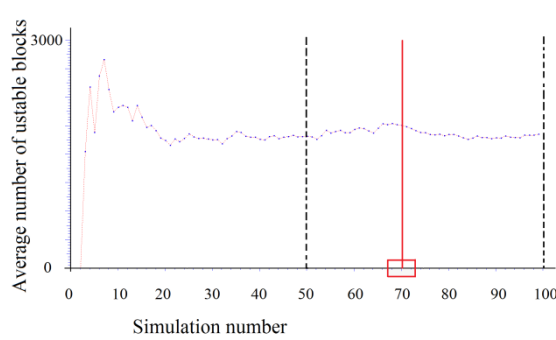


a) Curve of the average number

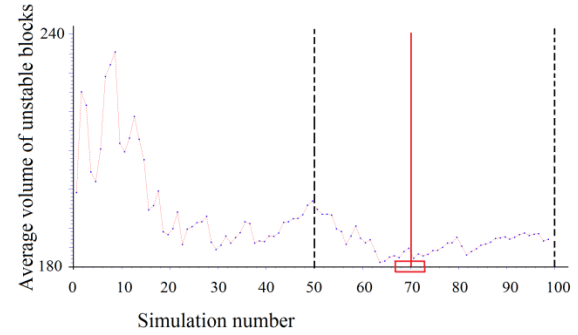


b) Curve of the average volume

Figure A.4: Variation in the average number and volume of unstable blocks versus the number of simulation in the scenario 2 with $N = 100$ simulations

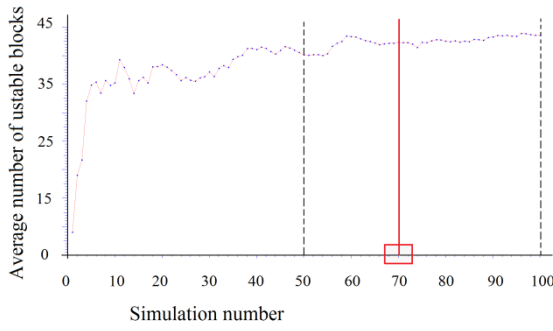


a) Curve of the average number

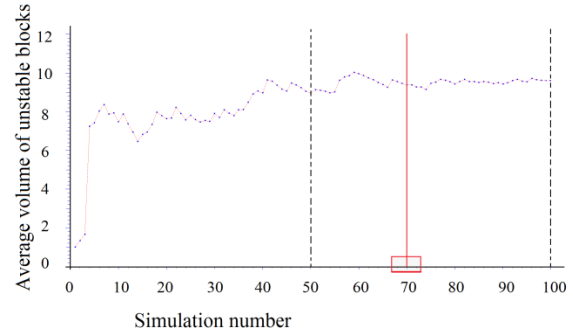


b) Curve of the average volume

Figure A.5: Variation in the average number and volume of unstable blocks versus the number of simulation in the scenario 3 with $N = 100$ simulations

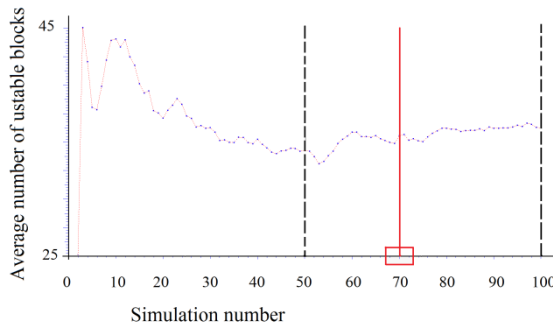


a) Curve of the average number

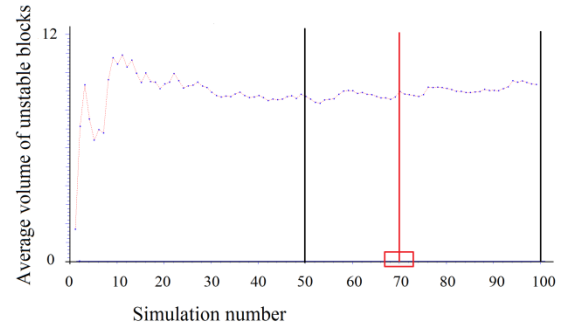


b) Curve of the average volume

Figure A.6: Variation in the average number and volume of unstable blocks versus the number of simulation in the scenario 4 with $N = 100$ simulations



a) Curve of the average number



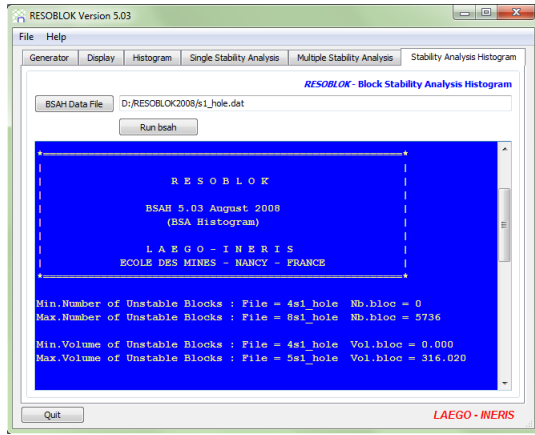
b) Curve of the average volume

Figure A.7: Variation in the average number and volume of unstable blocks versus the number of simulation in the scenario 5 with $N = 100$ simulations

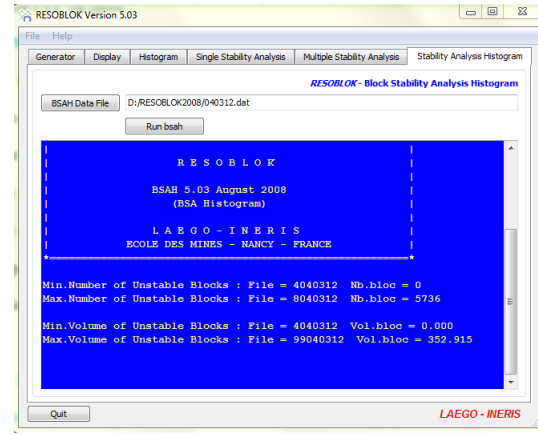
A.3. Comparison between the stability analysis on RESOBLOK of the 20-simulation-case and the 100-simulation-case of the same scenario

For the determination of the reasonable quantity of the simulation generated from a scenario, a comparison between the stability analysis on RESOBLOK of the 20-simulation-case and the 100-simulation-case of the same scenario was executed and the obtained results were presented.

a) Extreme simulations

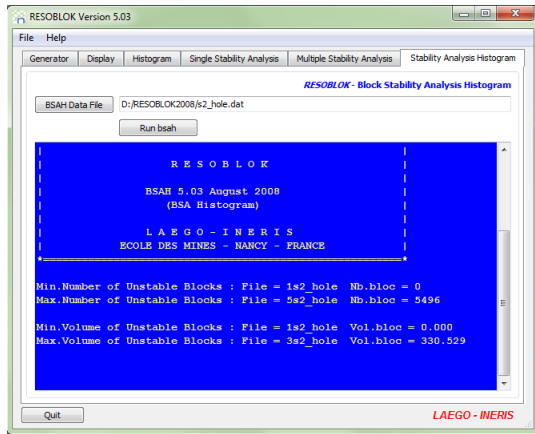


a) 20-simulation-case

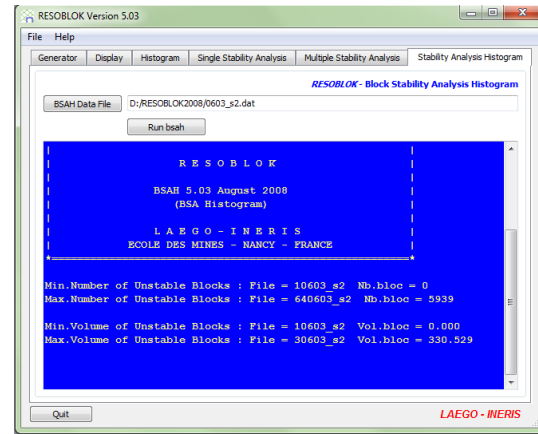


b) 100-simulation-case

Figure A.8: Stability analysis results on the extreme simulations of the Scenario 1 in 2 cases

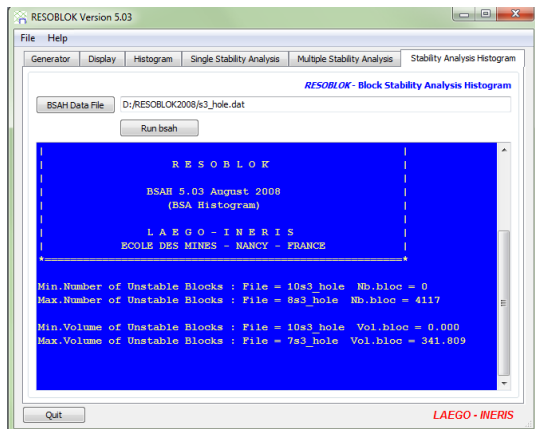


a) 20-simulation-case

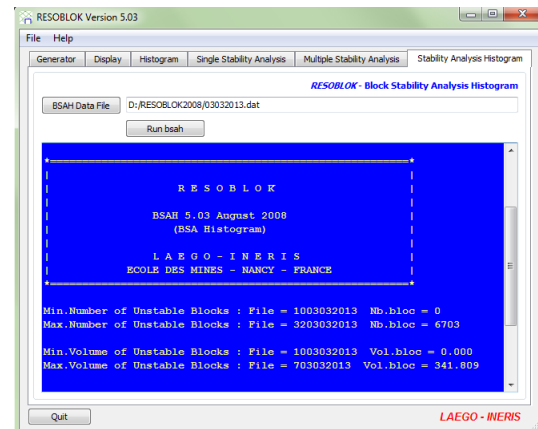


b) 100-simulation-case

Figure A.9: Stability analysis results on the extreme simulations of the Scenario 2 in 2 cases

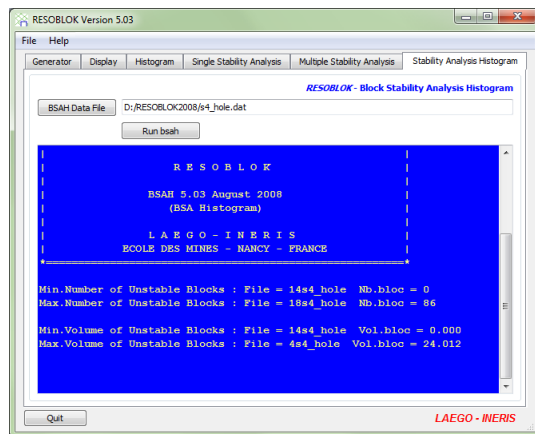


a) 20-simulation-case

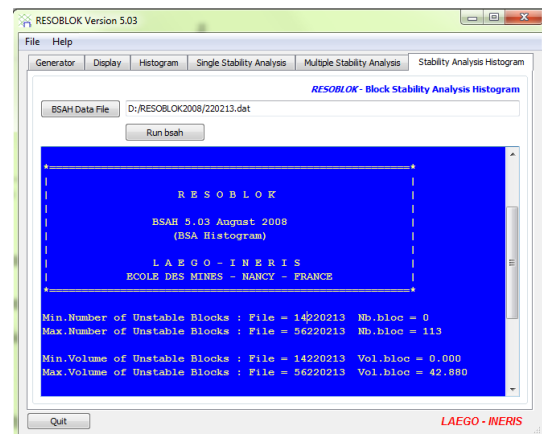


b) 100-simulation-case

Figure A.10: Stability analysis results on the extreme simulations of the Scenario 3 in 2 cases

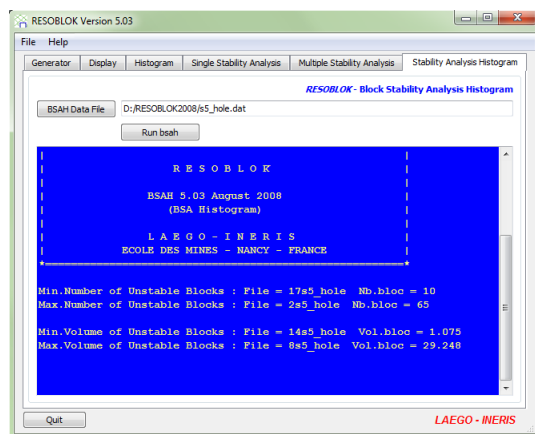


a) 20-simulation-case

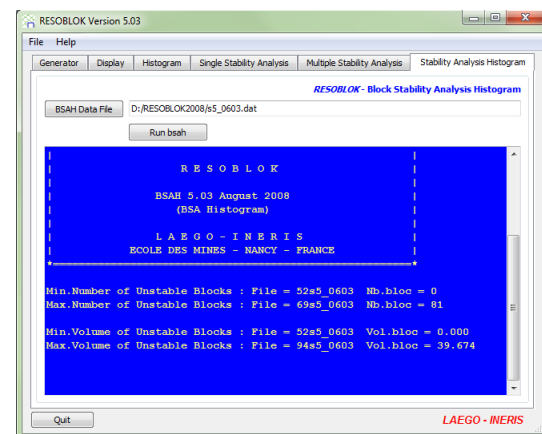


b) 100-simulation-case

Figure A.11: Stability analysis results on the extreme simulations of the Scenario 4 in 2 cases



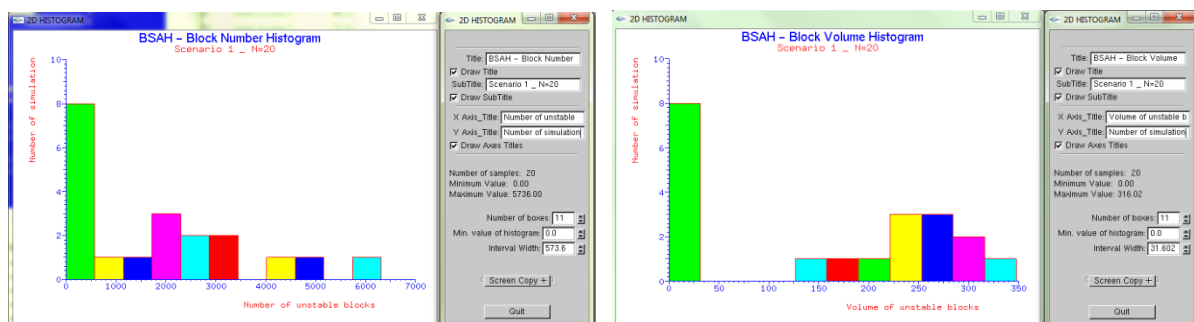
a) 20-simulation-case



b) 100-simulation-case

Figure A.12: Stability analysis results on the extreme simulations of the Scenario 5 in 2 cases

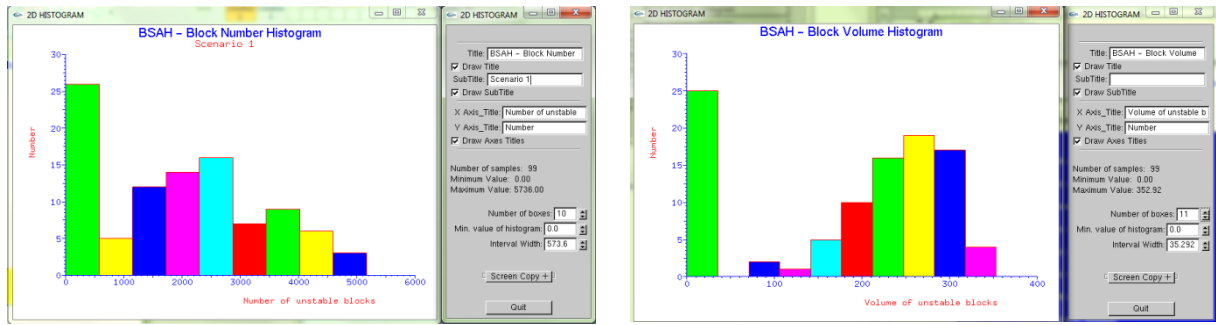
b) Histogram of the unstable blocks



a) Unstable blocks number

b) Unstable blocks volume

Figure A.13. Histogram of the unstable blocks in the scenario 1 with N = 20 simulations



a) Unstable blocks number

b) Unstable blocks volume

Figure A.14. Histogram of the unstable blocks in the scenario 1 with N = 100 simulations

APPENDIX B: FURTHER RESULTS OF THE TRIAXIAL COMPRESSION SIMULATION

B.1 Details of the model listed by LMGC90 at the beginning of the simulation

```

514 RBDY3 found
--
RBDY3::default contact configuration is used
LOAD TACTORS
=====
topo tol= 8.72664625997164739E-002
flatness tol= 1.52304843608730422E-004
=====
[POLYR::read_bodies]: 696 POLYR found
!-----!
! MAX RADIUS POLYR 3.4369478367654787
! MIN RADIUS POLYR 2.91606501697922707E-004
! MEAN RADIUS POLYR 0.71642843872732931
! NB BIG POLYR 2
! Average vertex number 145.36494252873564
! NB tot vertex 101174
! Average face number 204.55316091954023
! NB tot faces 142369
!-----!

```

B.2. Variation of contacts inside the model

The correlation of the contact parameters in the six loading of model were studied and presented on the graphs of time versus the number of the contacts.

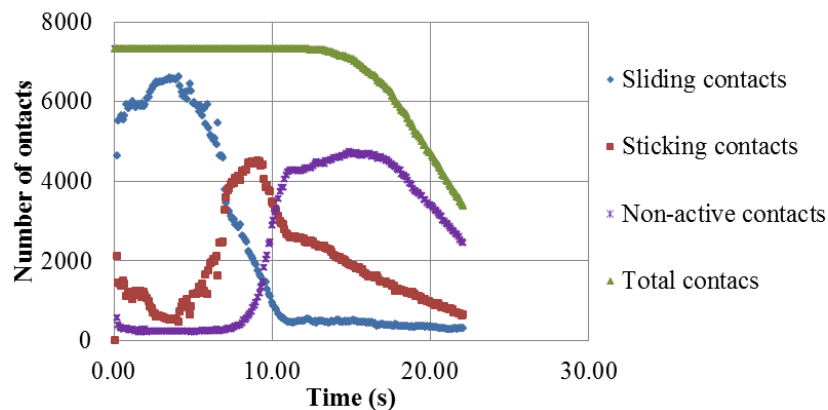


Figure B.1: Correlation of contact parameters under the loading path 0.001 (21_41)

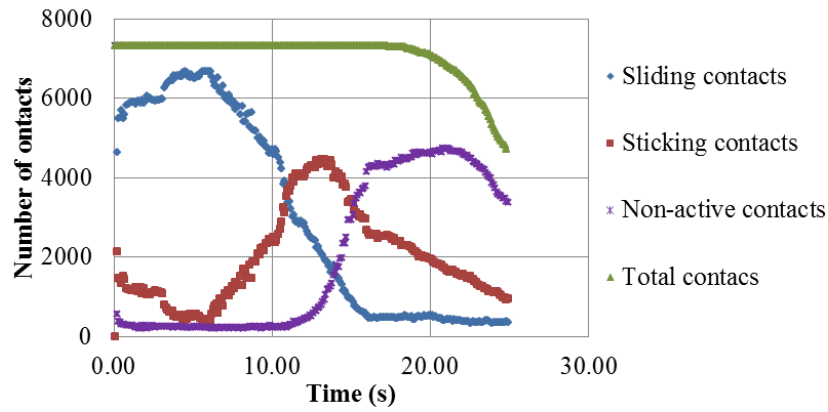


Figure B.2: Correlation of contact parameters under the loading path 0.001 (31_61)

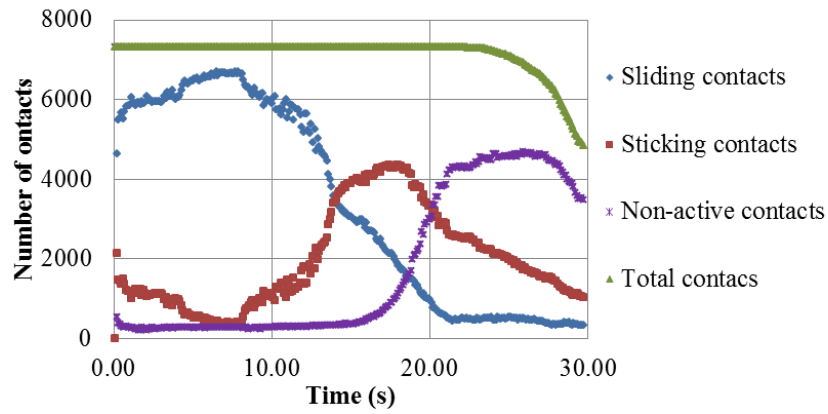


Figure B.3: Correlation of contact parameters under the loading path 0.001 (41_81)

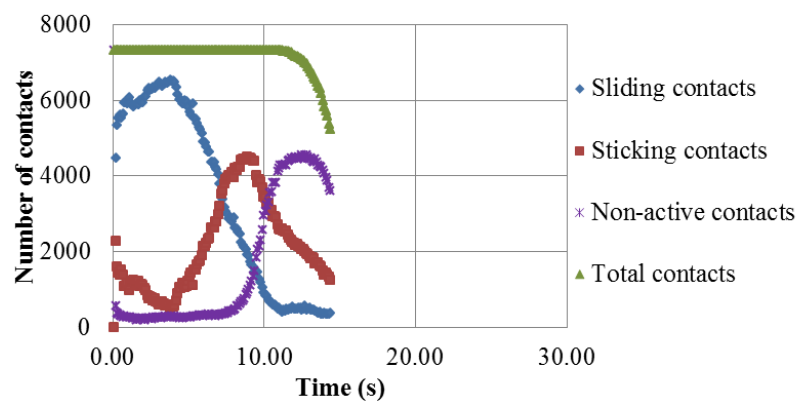


Figure B.4: Correlation of contact parameters under the loading path 0.01 (21_41)

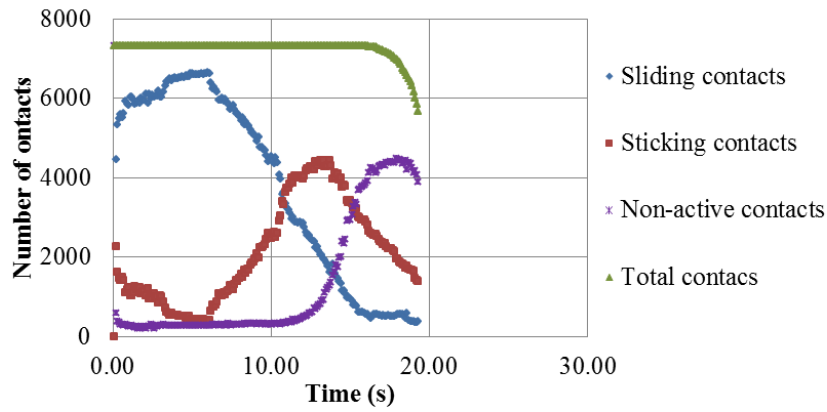


Figure B.5: Correlation of contact parameters under the loading path 0.01 (31_61)

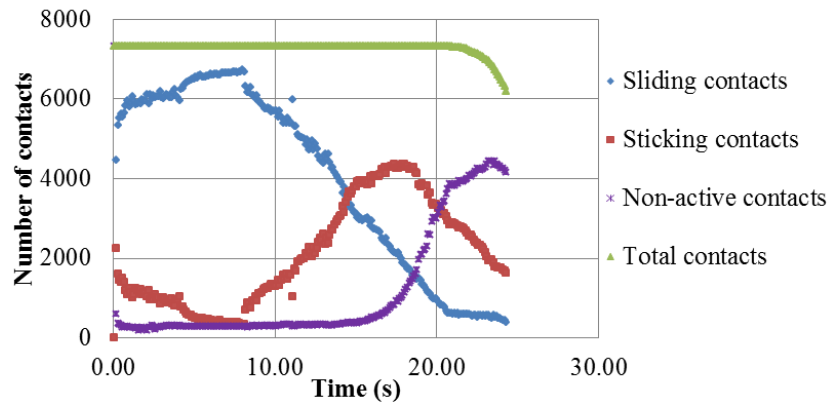


Figure B.6: Correlation of contact parameters under the loading path 0.01 (41_81)

B.3. Moving blocks of the model at the instable equilibrium of the contact number in the model

When the number of sticking and sliding contacts was instable equilibrate, some small blocks of the model moved and the results of the models in the six loading paths are presented.

Notation for the relevant figures:

- $\|X\|$: Displacement of rigid rock blocks of the model (m)
- $\|V\|$: Velocity of displacement rigid rock blocks of the model (m/s)

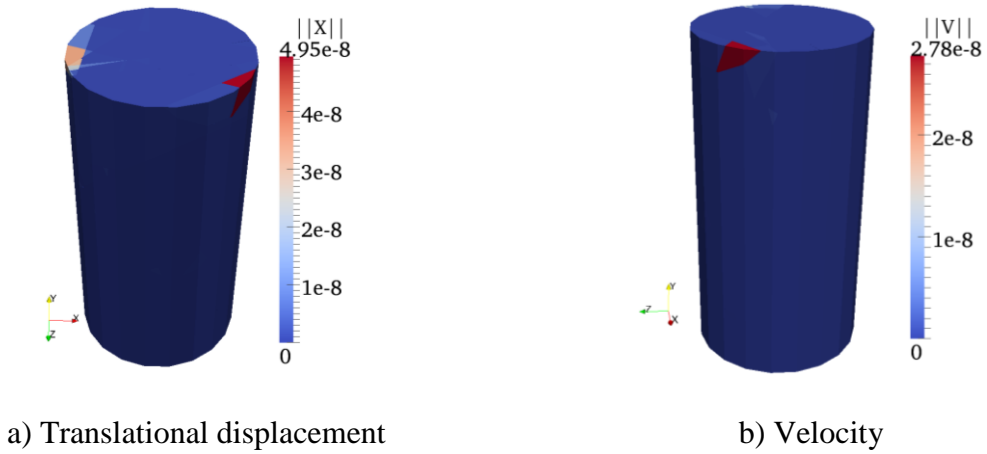


Figure B.7: Moving blocks of the specimen at $t = 7.1s$
of the loading path 0.001 (21_41)

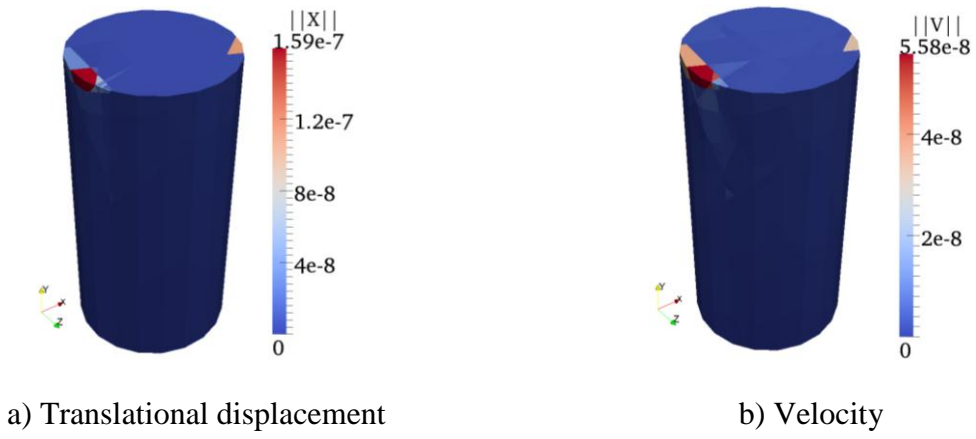


Figure B.8: Moving blocks of the specimen at $t = 10.9s$
of the loading path 0.001 (31_61)

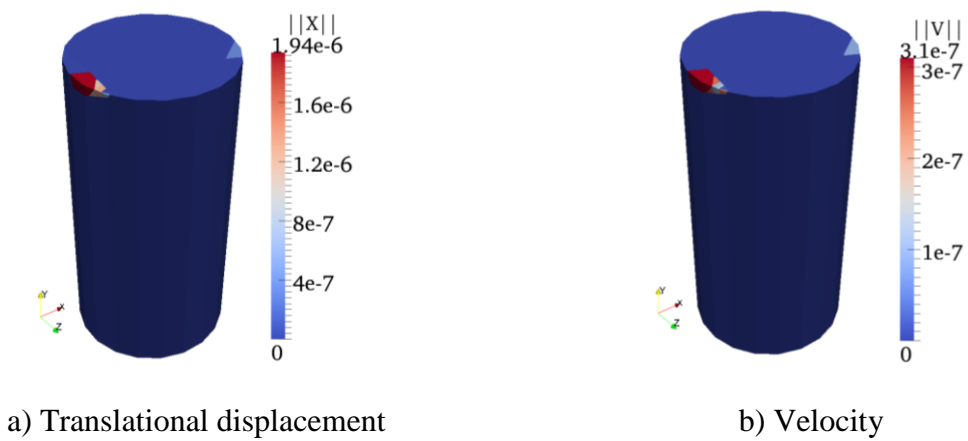


Figure B.9: Moving blocks of the specimen at $t = 14.0s$
of the loading path 0.001 (41_81)

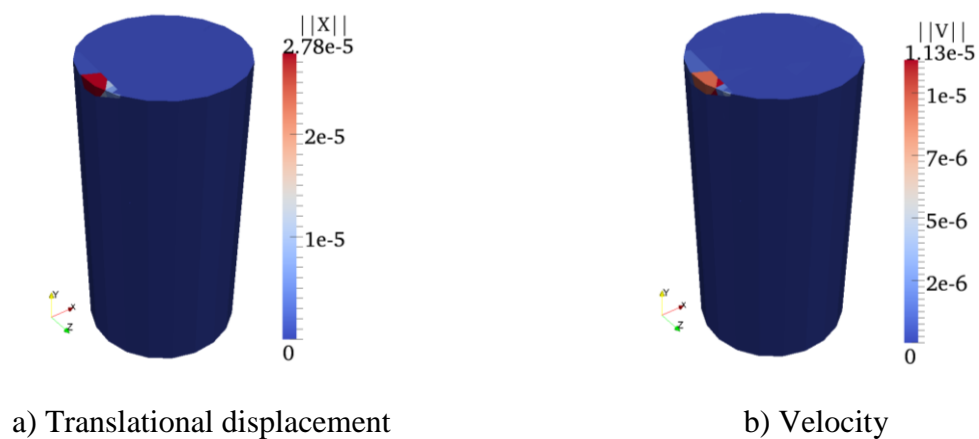


Figure B.10: Moving blocks of the specimen at $t = 7.2s$
of the loading path 0.001 (21_41)

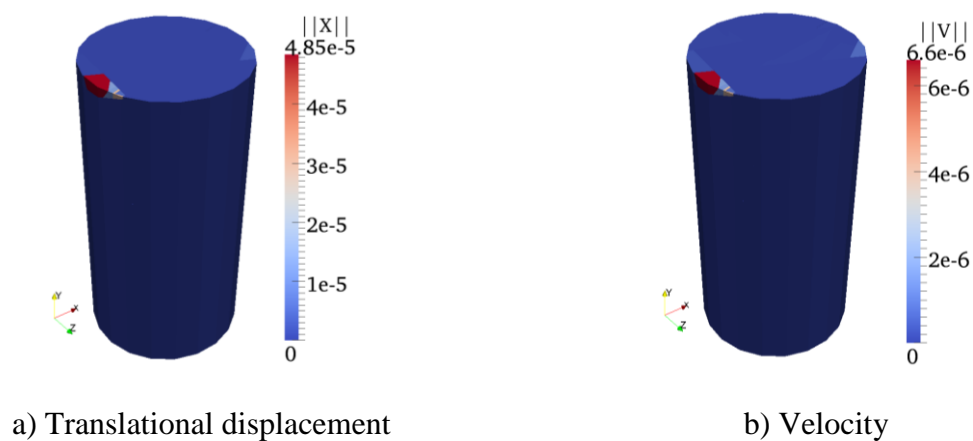


Figure B.11: Moving blocks of the specimen at $t = 10.7s$
of the loading path 0.01 (31_61)

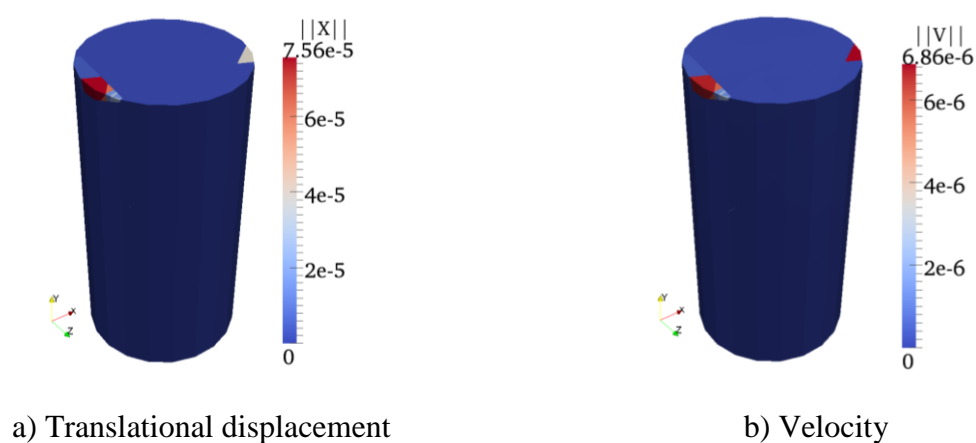


Figure B.12: Moving blocks of the specimen at $t = 14.4s$
of the loading path 0.01 (41_81)

B.4. Failure procedure of the model

The formation of the sliding faces on the numerical rock core under the application of the loading paths was clearly observed on the captures of the model in two moments of interest:

- At the start of the degradation of model;
- When the sticking contact quantity was maximal

Notation for the relevant figures:

- $||X||$: Displacement of rigid rock blocks of the model (m)
- $||V||$: Velocity of displacement rigid rock blocks of the model (m/s)

a) At the start of the degradation of model

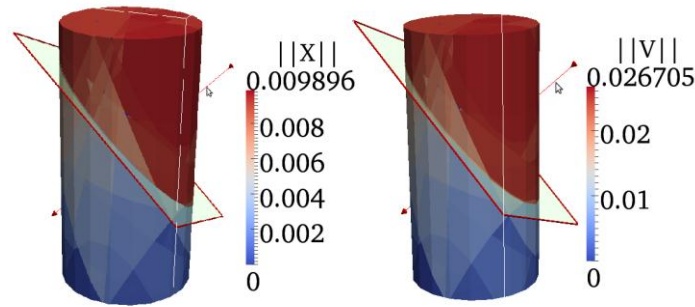


Figure B.13: Sliding plan on the specimen at $t = 12s$ under the loading path 0.001 (21_41)

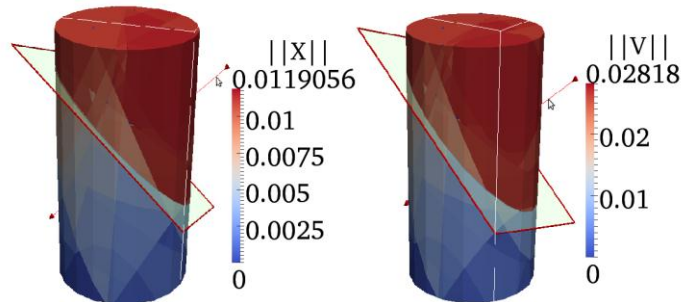


Figure B.14: Sliding plan on the specimen at $t = 17s$ under the loading path 0.001 (31_61)

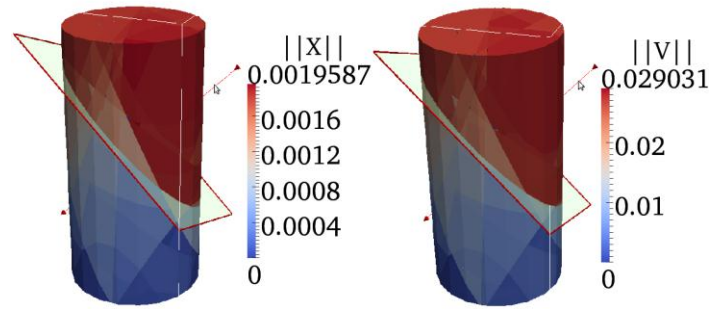


Figure B.15: Sliding plan on the specimen at $t = 22s$ under the loading path 0.001 (41_81)

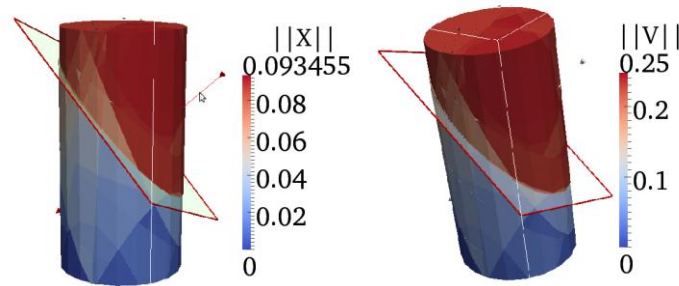


Figure B.16: Sliding plan on the specimen at $t = 11s$ under the loading path 0.01 (21_41)

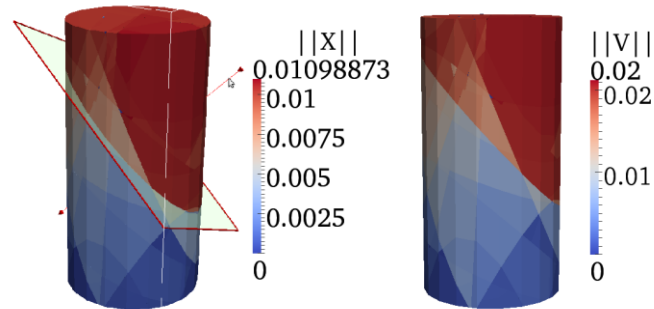


Figure B.17: Sliding plan on the specimen at $t = 12s$ under the loading path 0.01 (31_61)

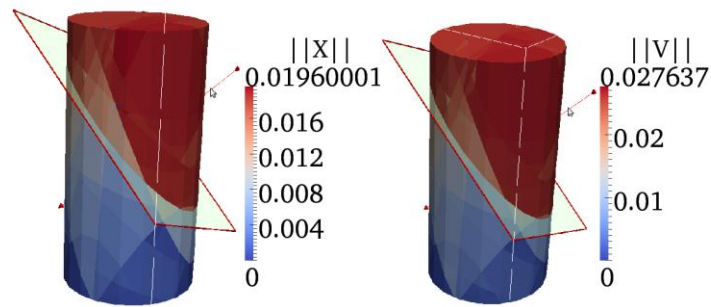


Figure B.18: Sliding plan on the specimen at $t = 21\text{s}$ under the loading path 0.01 (41_81)

b) When the sticking contact quantity was maximal

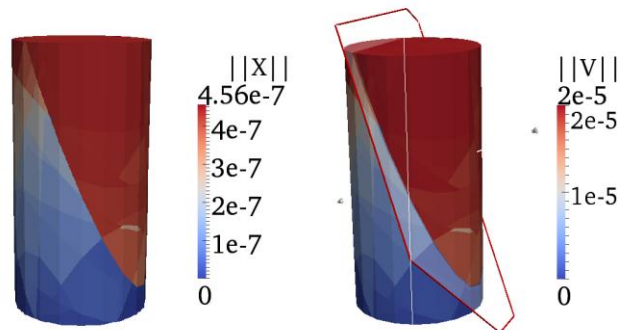


Figure B.19: Sliding plan on the specimen at $t = 9\text{s}$ under the loading path 0.001 (21_41)

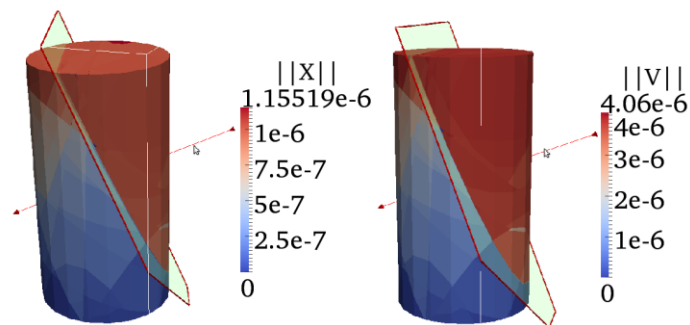


Figure B.20: Sliding plan on the specimen at $t = 13\text{s}$ under the loading path 0.001 (31_61)

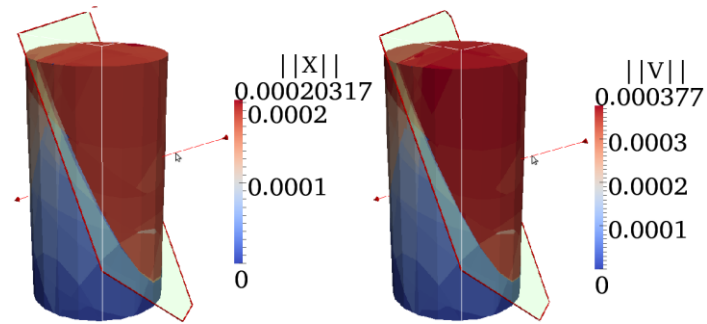


Figure B.21: Sliding plan on the specimen at $t = 18\text{s}$ under the loading path 0.001 (41_81)

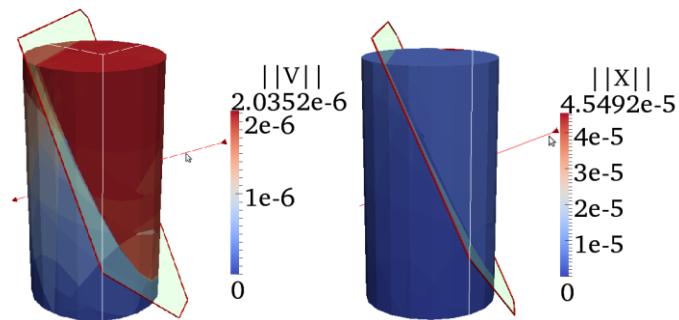


Figure B.22: Sliding plan on the specimen at $t = 9\text{s}$ under the loading path 0.01 (21_41)

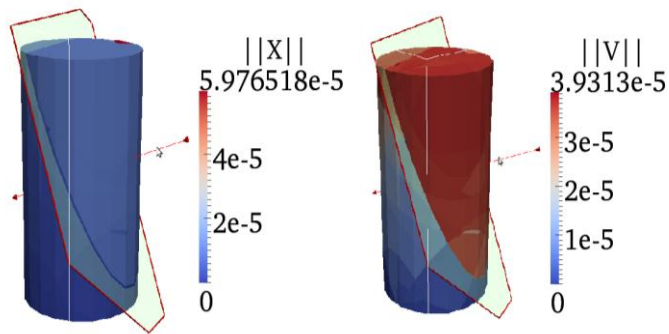


Figure B.23: Sliding plan on the specimen at $t = 13\text{s}$ under the loading path 0.01 (31_61)

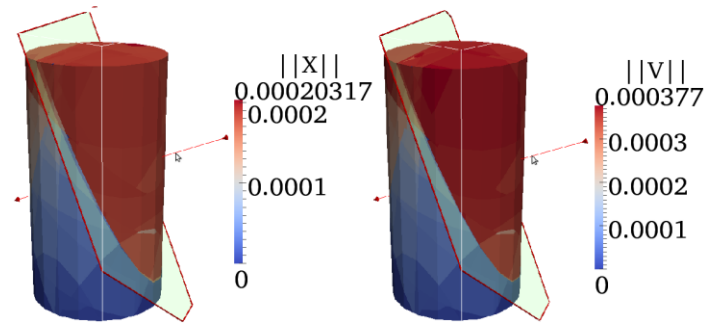


Figure B.24: Sliding plan on the specimen at $t = 18s$ under the loading path 0.01 (41_81)

B.4. Evolution of sliding planes occurring in the specimen during the simulation

Flow movements of the rock core under the six loading paths are presented. It is noted that the colours and the shapes of vectors are different in each scanned image of the rock core and are only appropriate with the magnitude scale placed under the rock core.

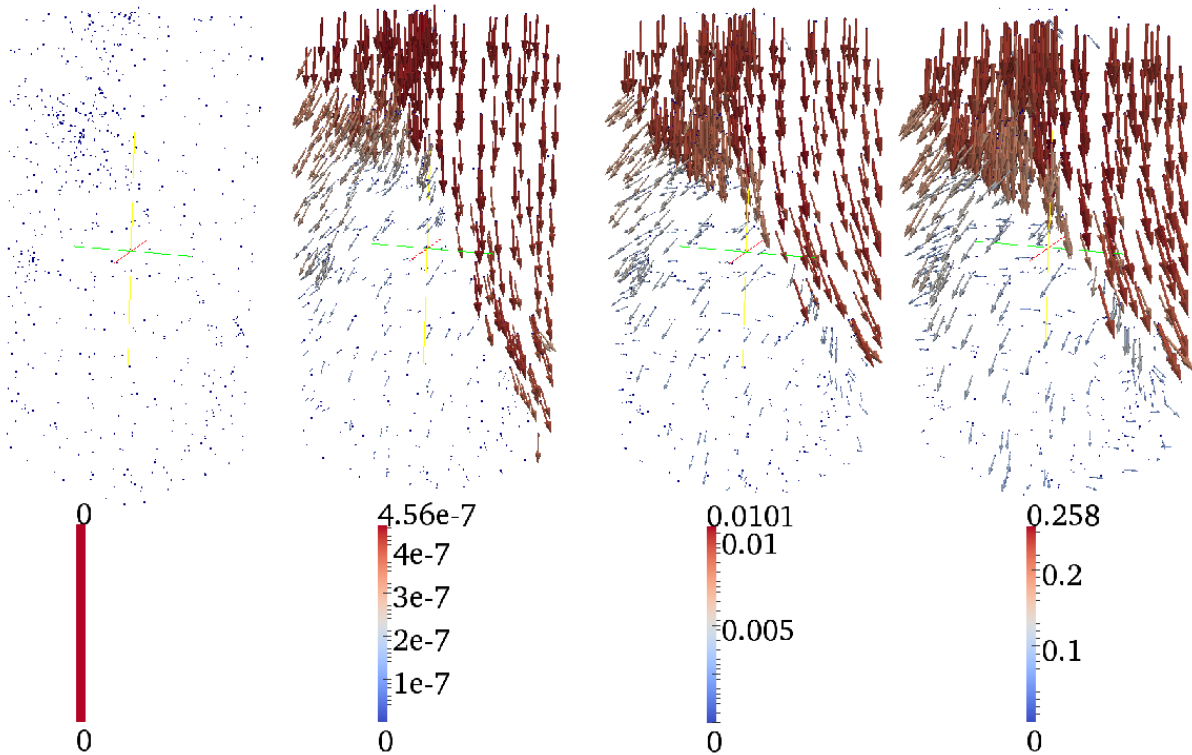


Figure B.25: Flows of movement of rigid rock blocks inside the model in case of 0.001 (21_41)

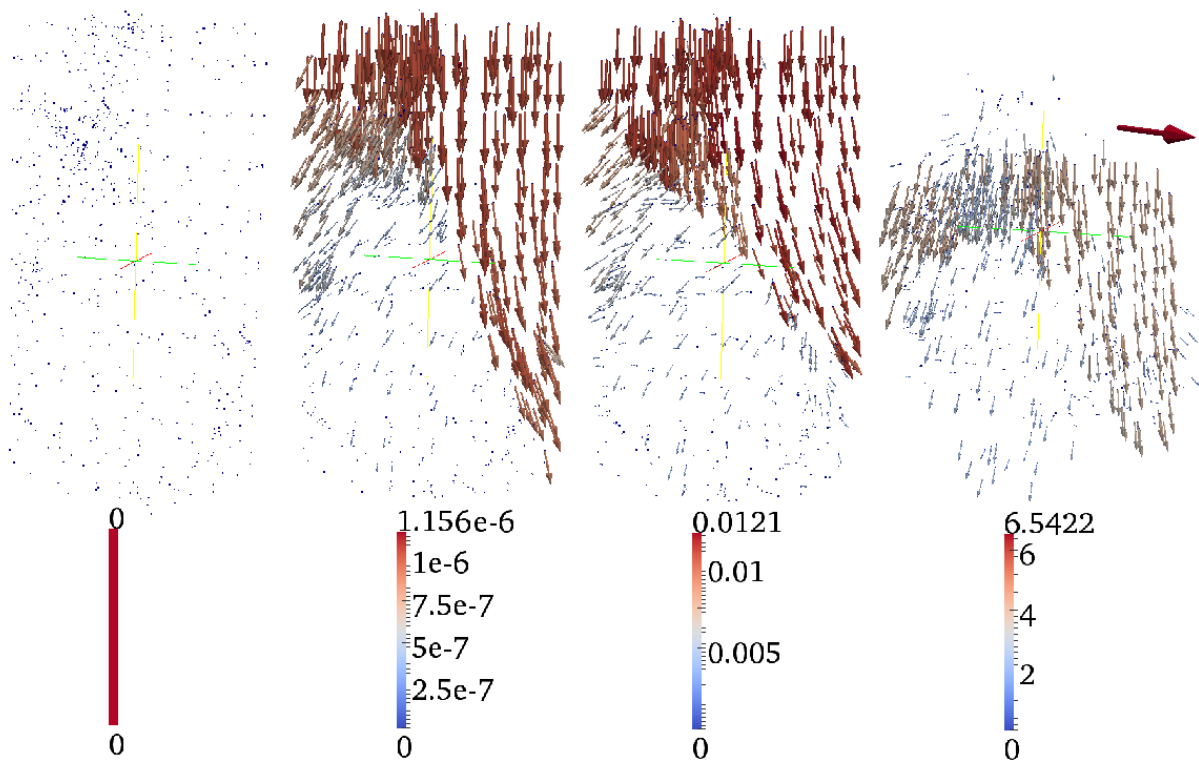


Figure B.26: Flows of movement of rigid rock blocks inside the model in case of 0.001 (31_61)

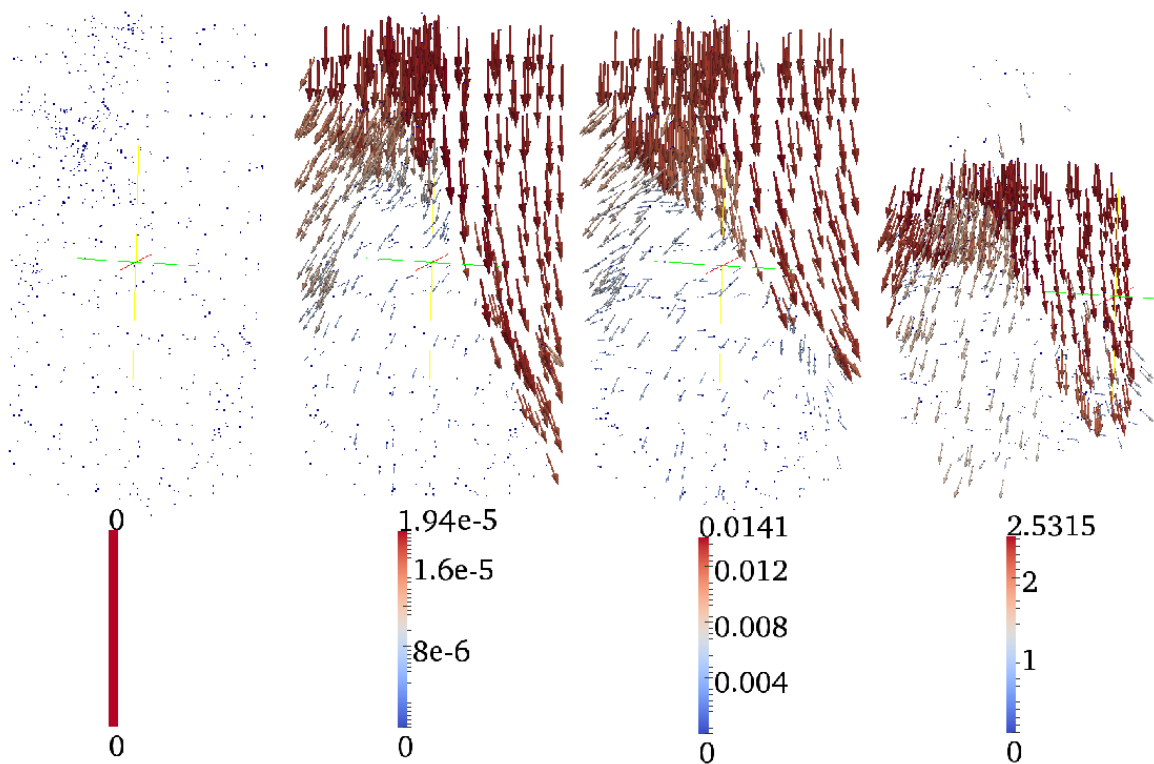


Figure B.27: Flows of movement of rigid rock blocks inside the model in case of 0.001 (41_81)

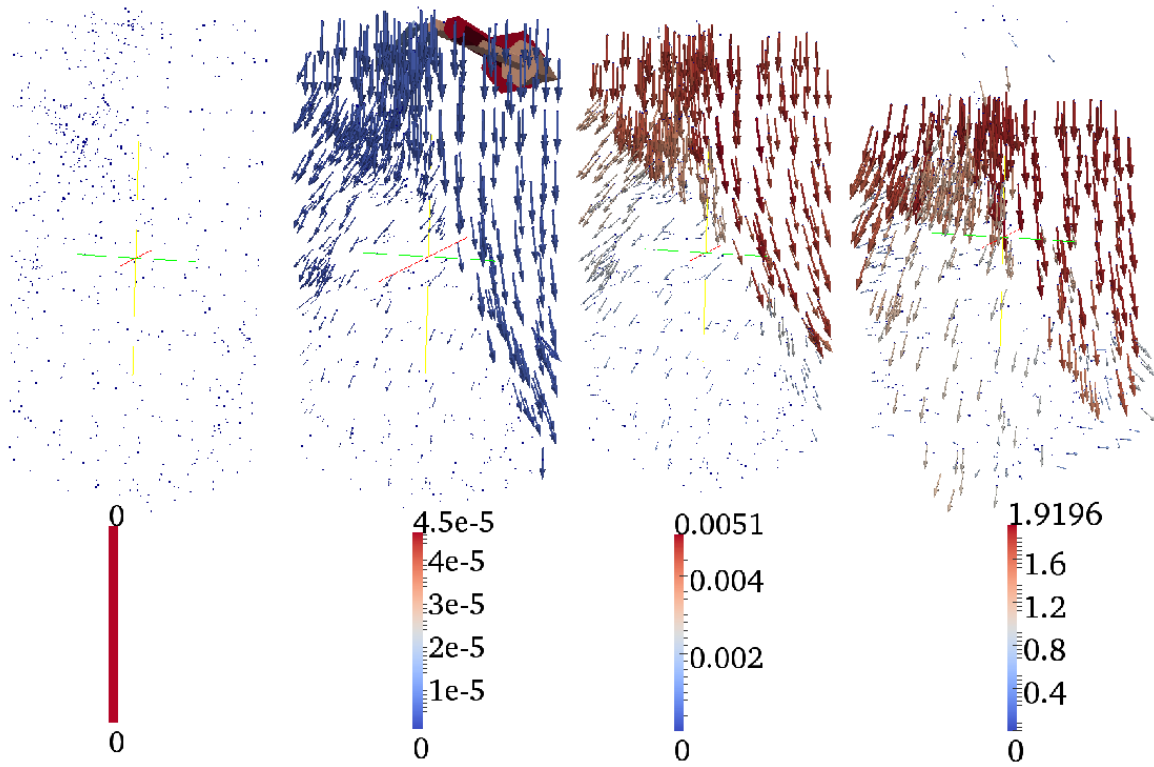


Figure B.28: Flows of movement of rigid rock blocks inside the model in case of 0.01 (21_41)

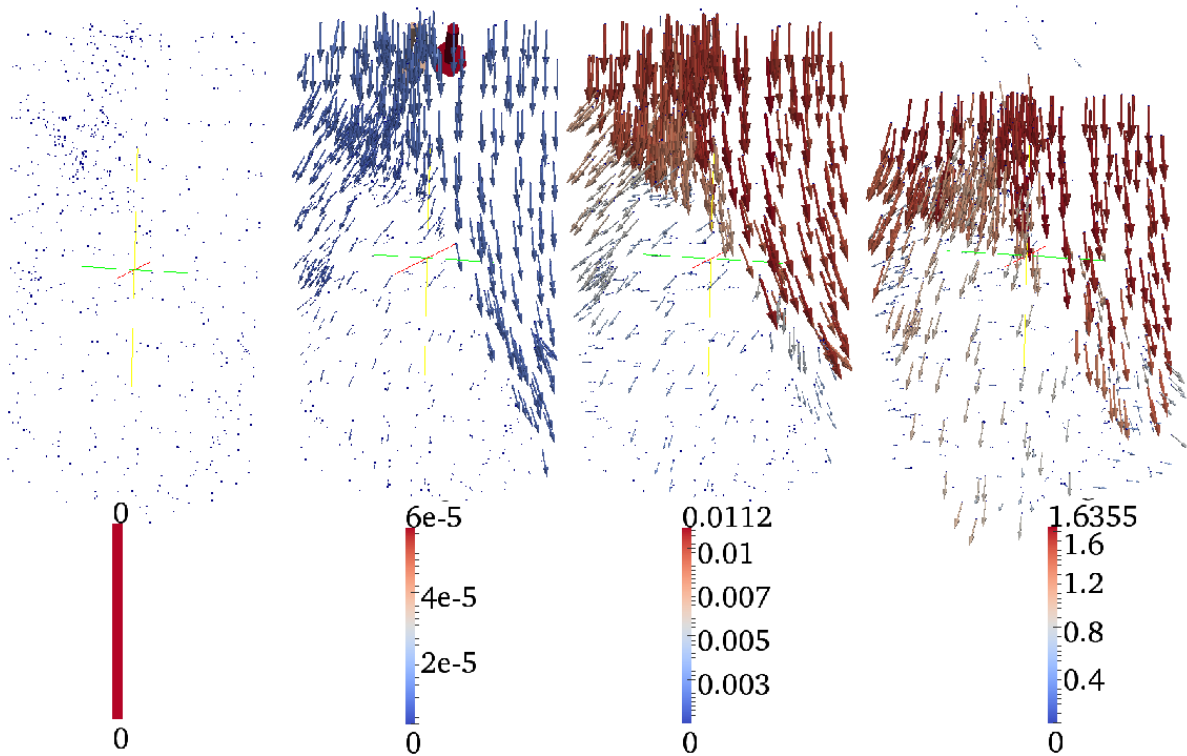


Figure B.29: Flows of movement of rigid rock blocks inside the model in case of 0.01 (31_61)

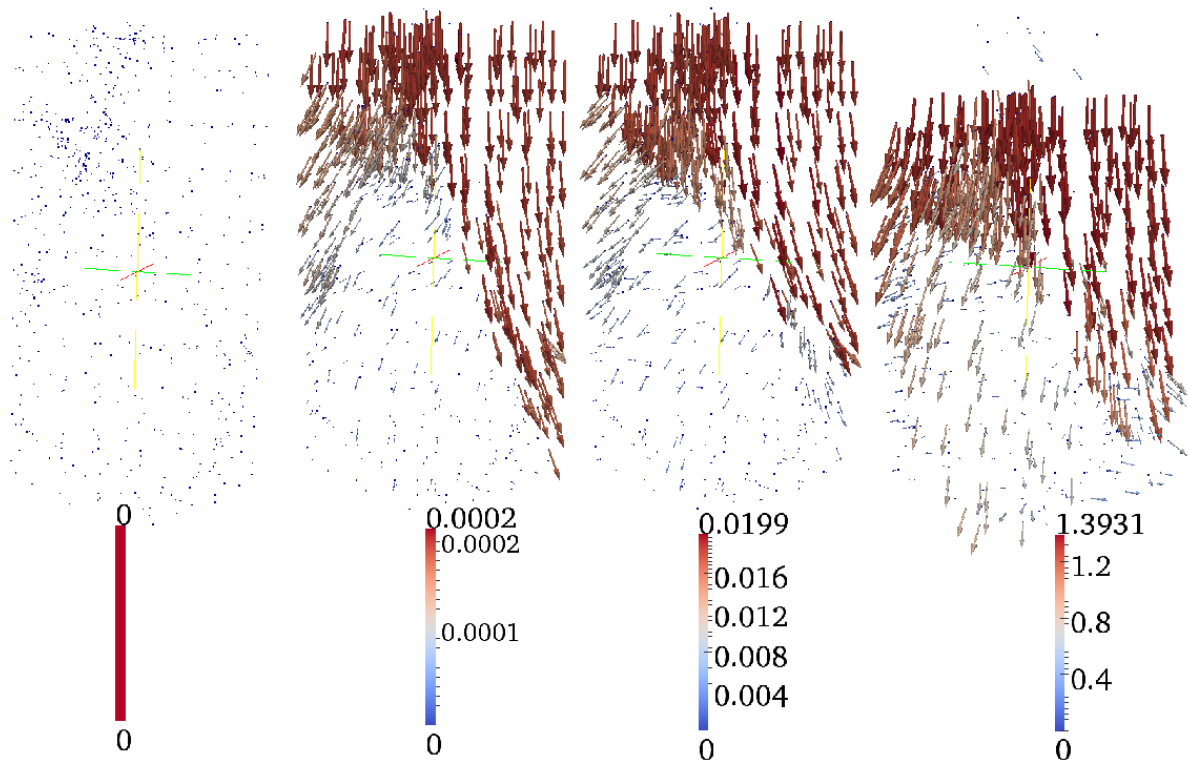


Figure B.30: Flows of movement of rigid rock blocks inside the model in case of 0.01 (41_81)

APPENDIX C:

FURTHER RESULTS OF THE EXCAVATION SIMULATION

C.1. Combination 2 under the 1st loading case

The displacement evolution of the rock blocks during the tunnelling schedule and the variation and the redistribution of the contact forces, the contact pressures between the contact blocks were studied. The obtained results are presented in the following figures and tables.

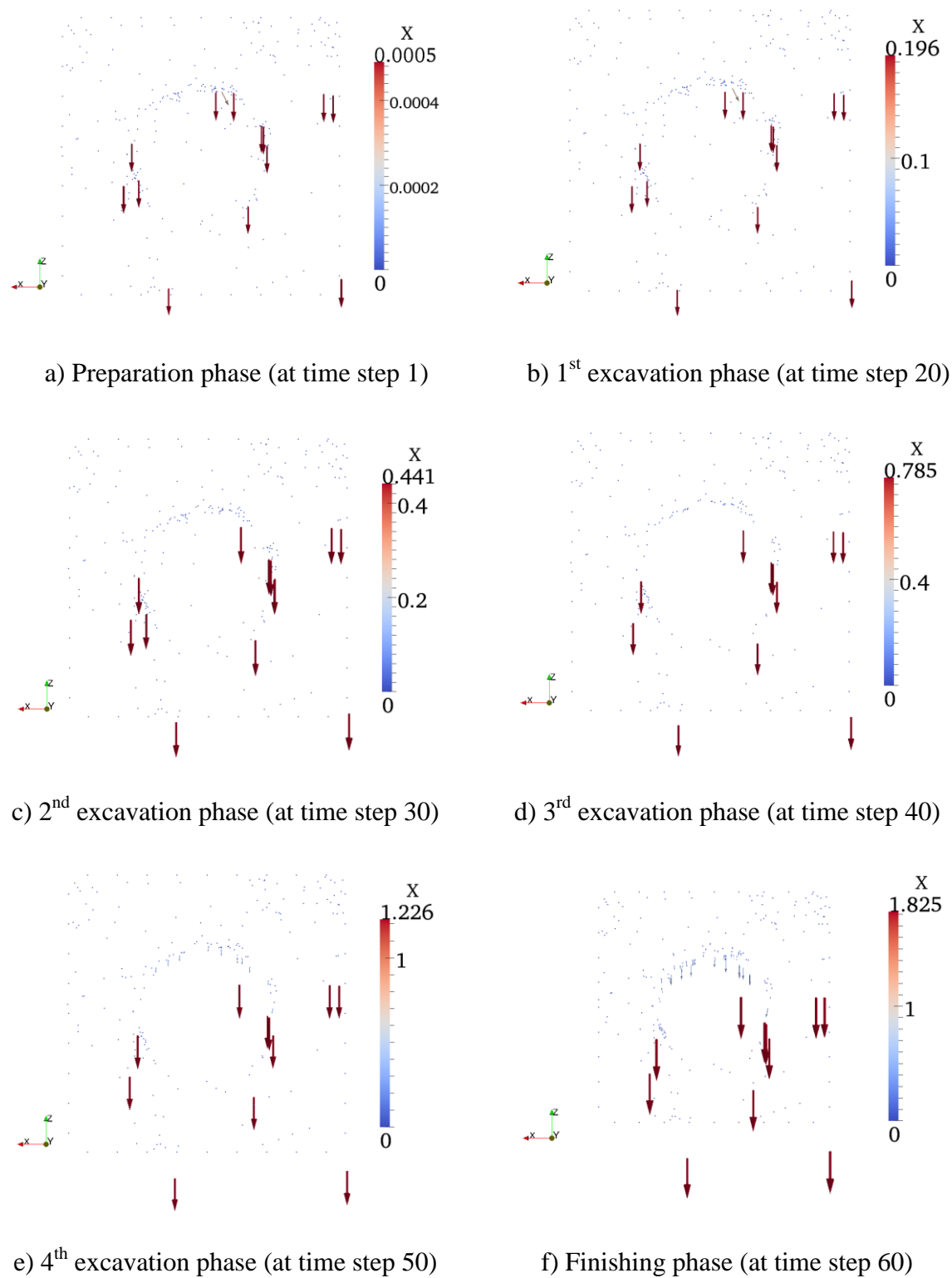
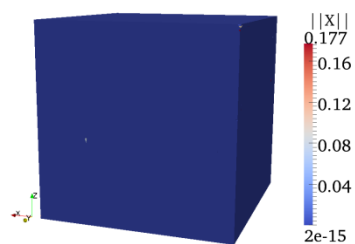
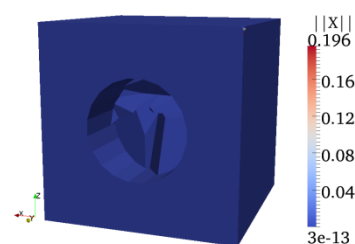


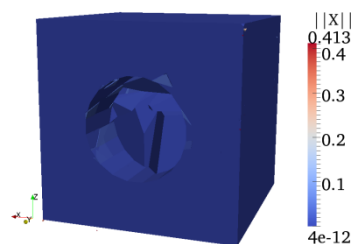
Figure C.1: Flows of displacement of rock blocks on the monitored slice of the Model 4 during the simulation time



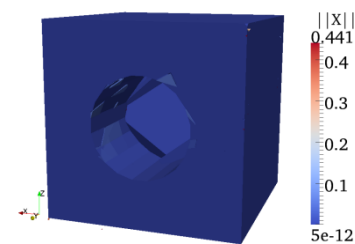
a) Before the 1st excavation (at time step 19)



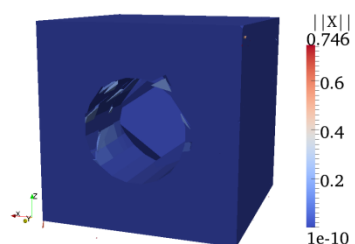
b) After the 1st excavation (at time step 20)



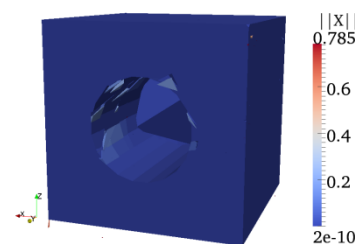
c) Before the 2nd excavation (at time step 29)



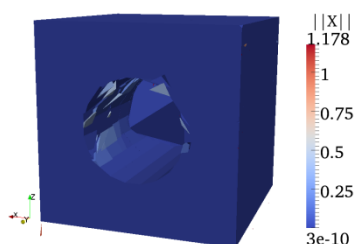
d) After the 2nd excavation (at time step 30)



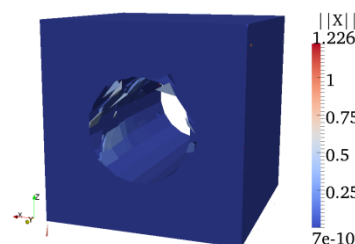
e) Before the 3rd excavation (at time step 39)



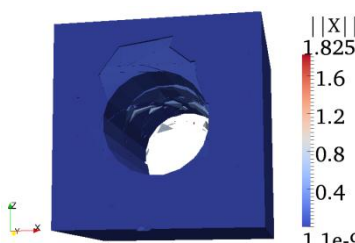
f) After the 3rd excavation (at time step 40)



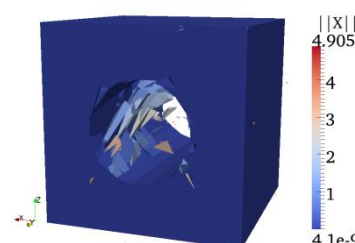
g) Before the 4th excavation (at time step 49)



h) After the 4th excavation (at time step 50)



i) Finishing phase (at time step 60)



j) Finishing phase (at time step 100)

Figure C.2: Moving rock blocks of the Model 4 during its tunnelling procedure

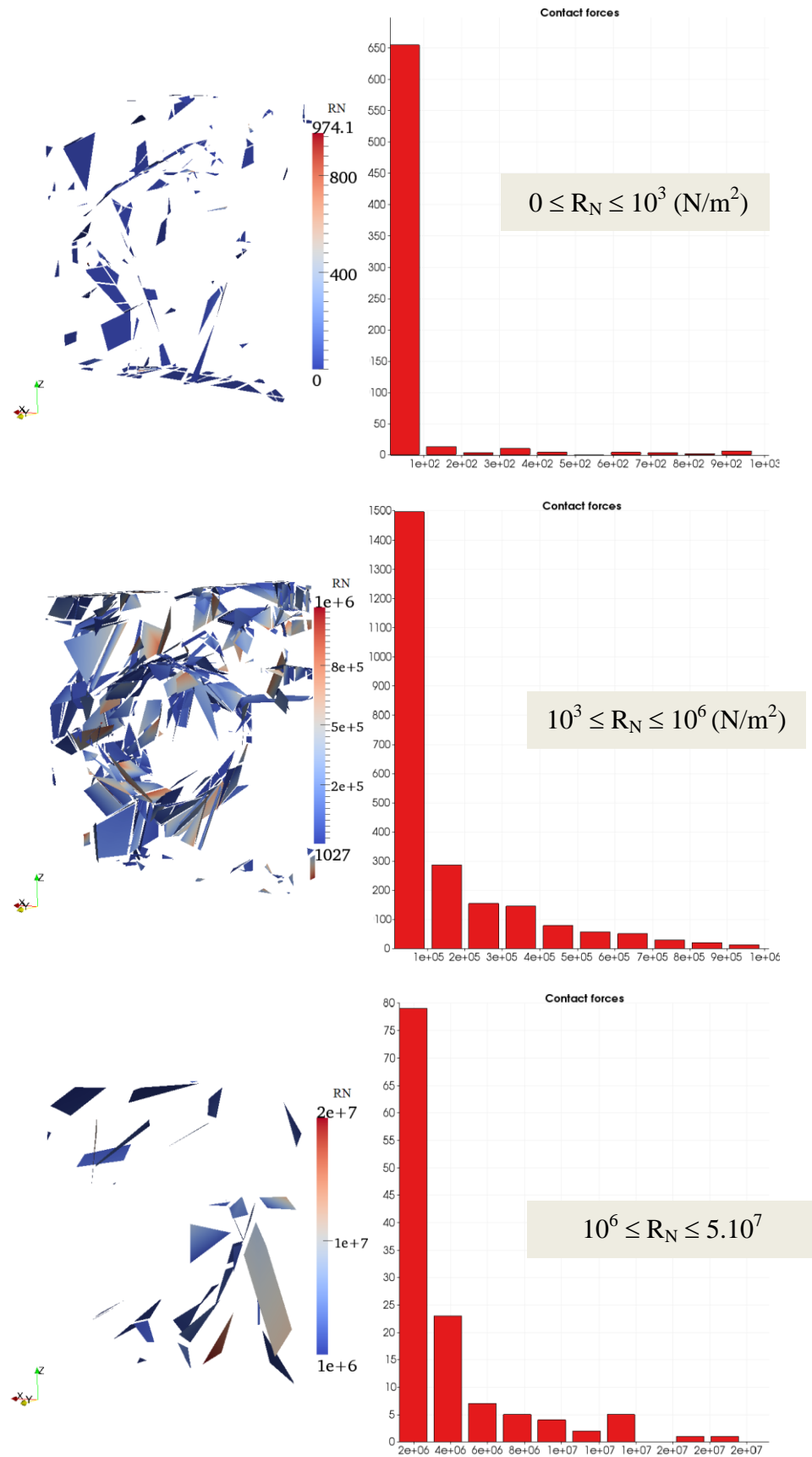


Figure C.3: Variations of the normal contact forces in the monitoring slice at the preparation phase (at time step 1)

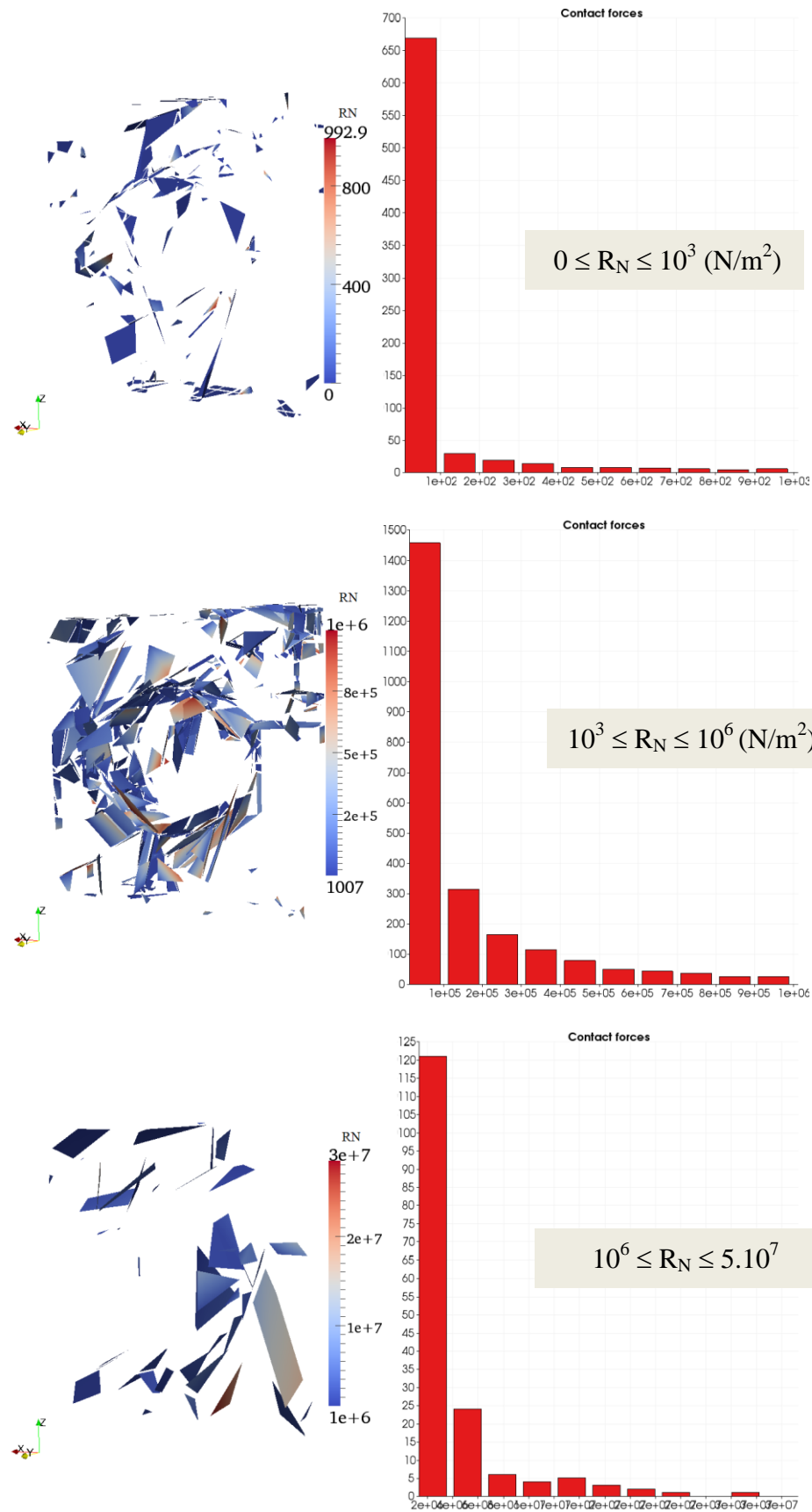


Figure C.4: Variations of the normal contact forces in the monitoring slice at the 1st excavation phase (at time step 20)

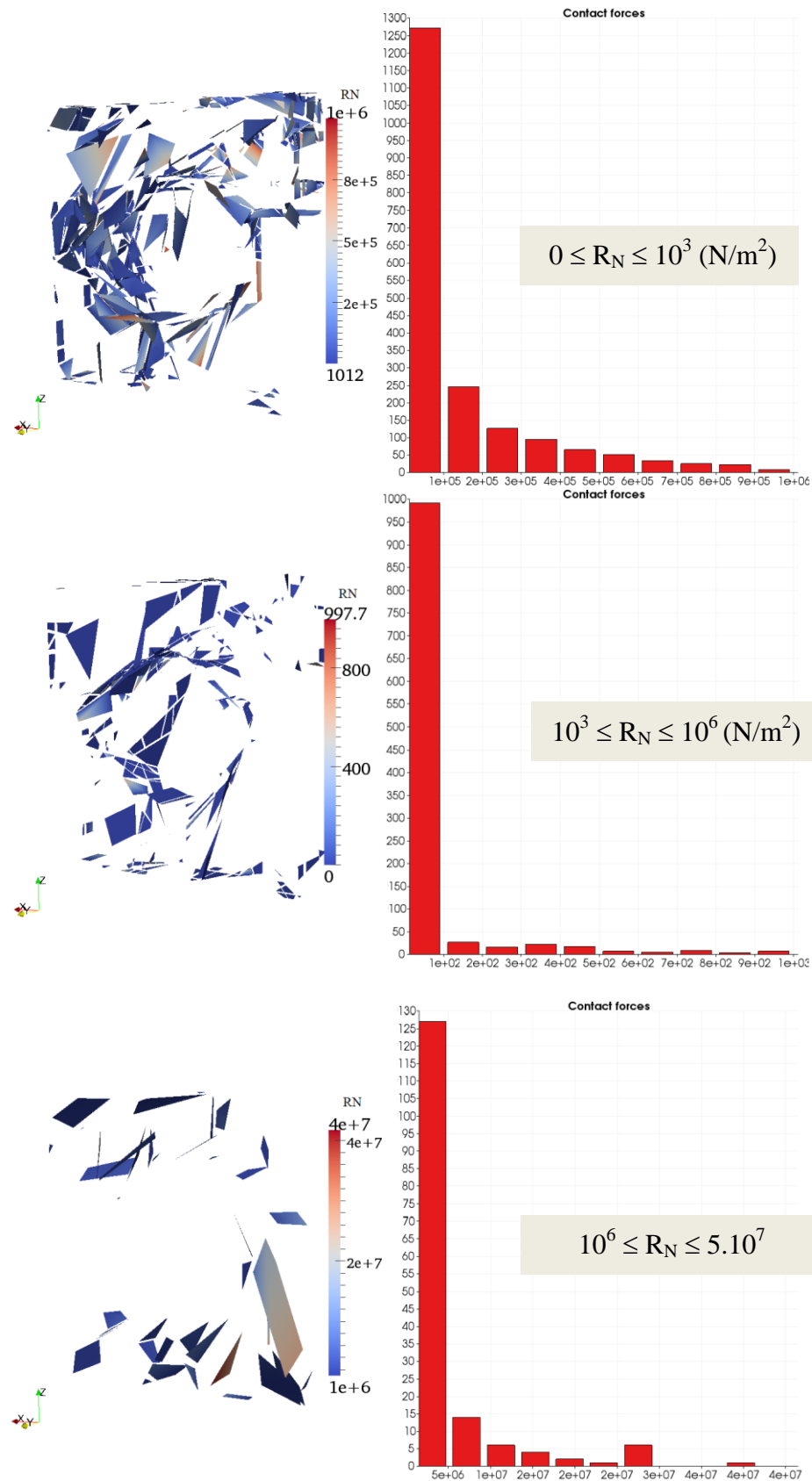


Figure C.5: Variations of the normal contact forces in the monitoring slice at the 2nd excavation phase (at time step 30)

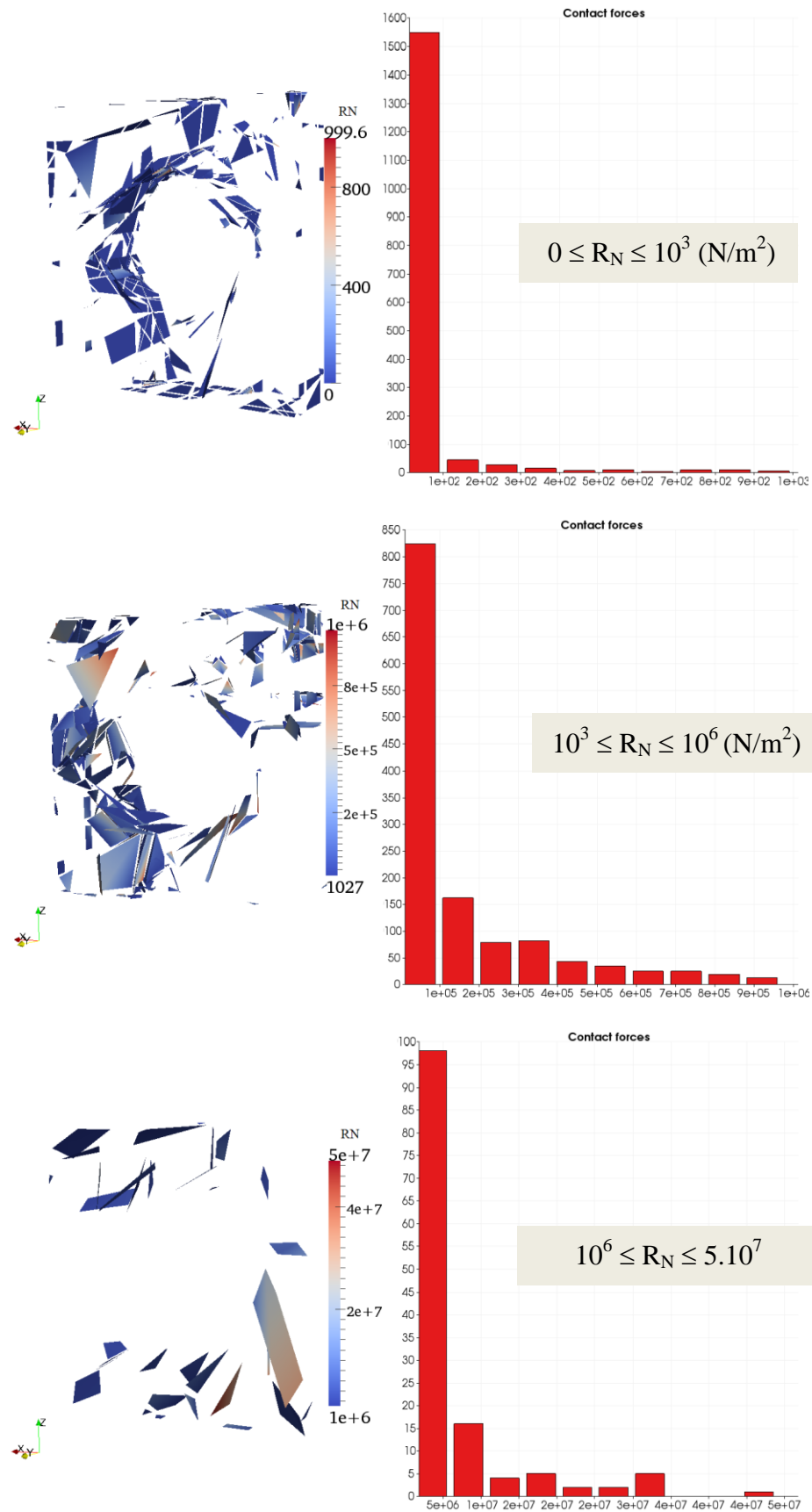


Figure C.6: Variations of the normal contact forces in the monitoring slice at the 3rd excavation phase (at time step 40)

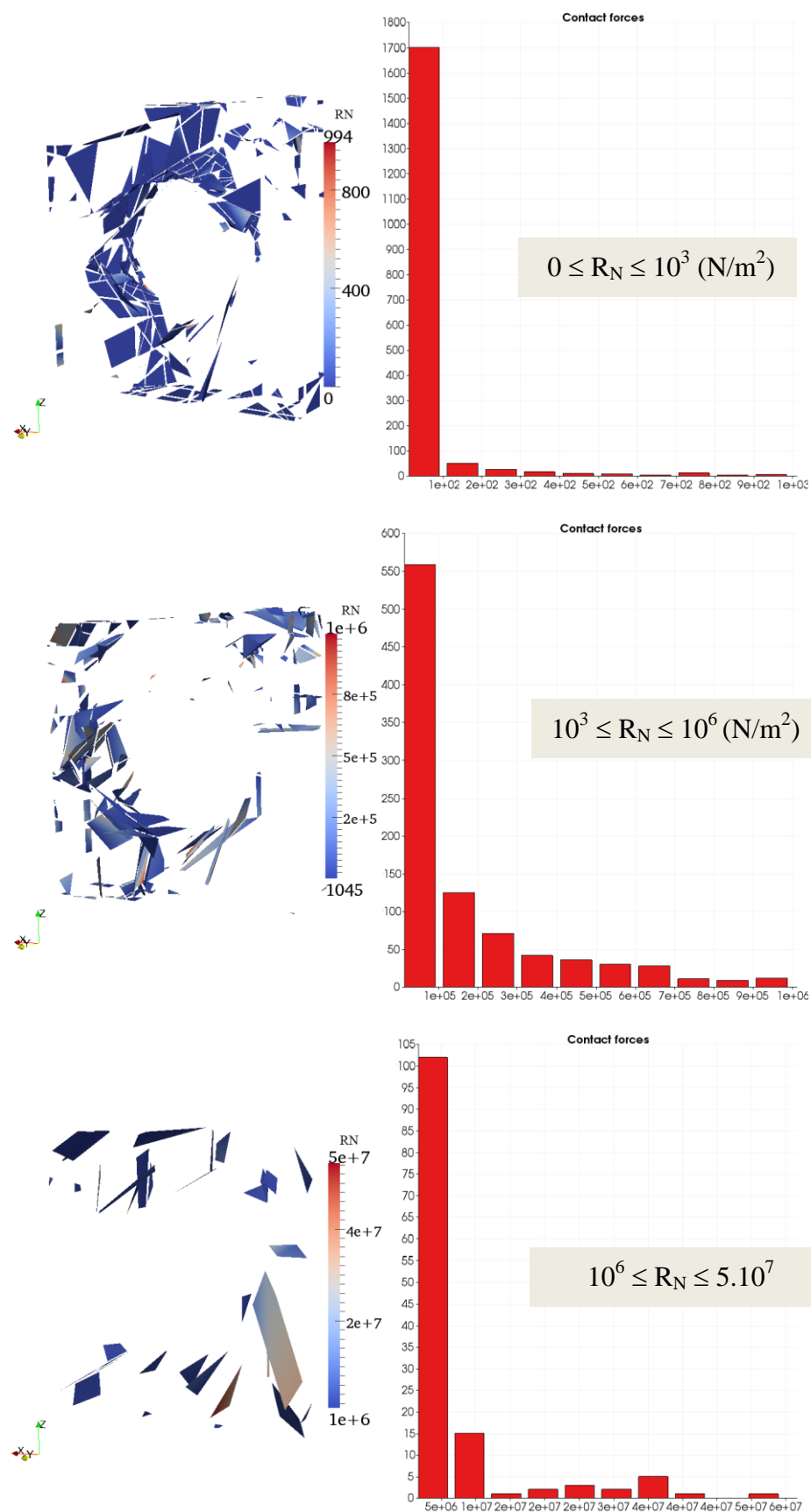


Figure C.7: Variations of the normal contact forces in the monitoring slice at the 4th excavation phase (at time step 50)

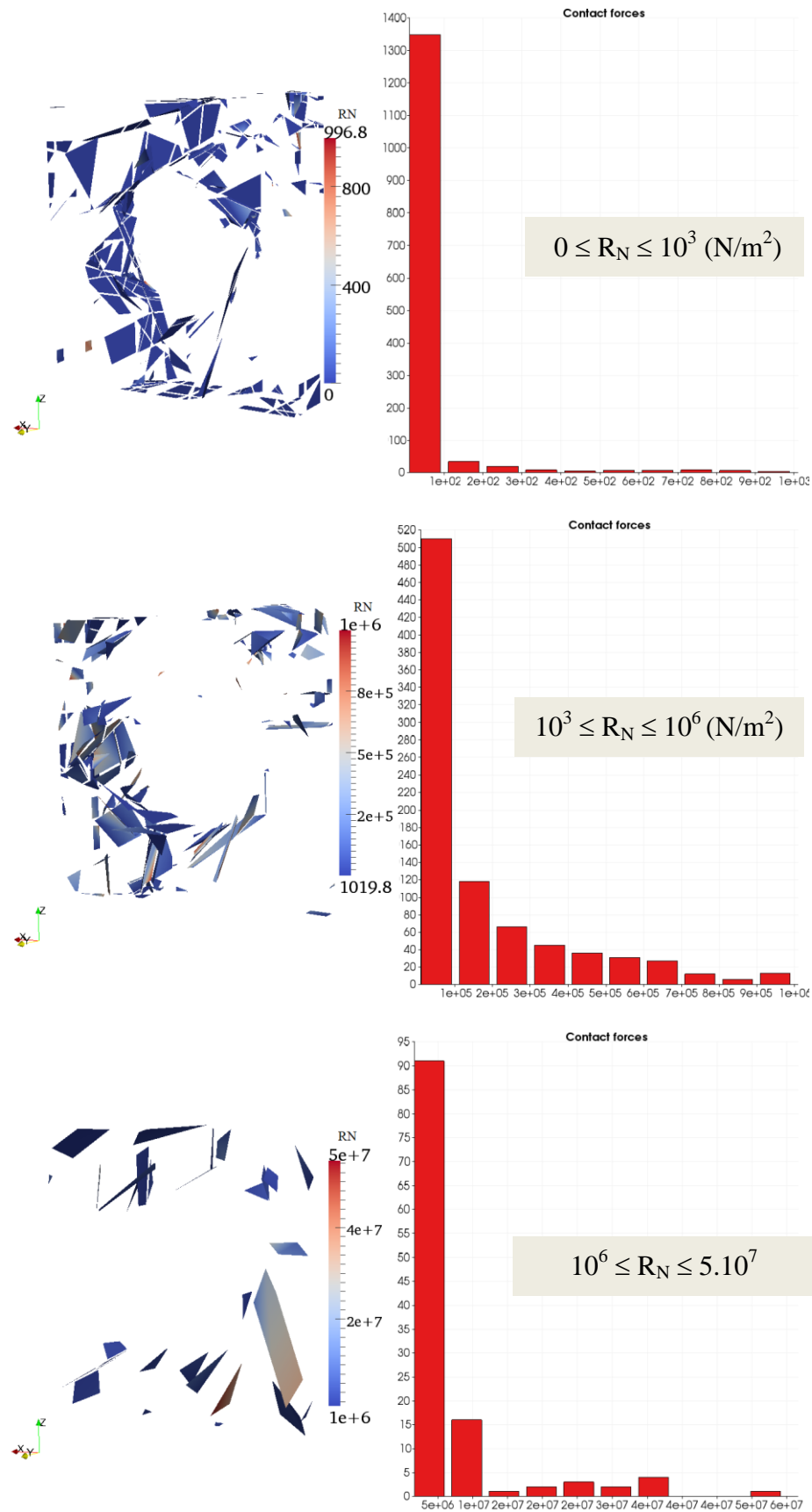
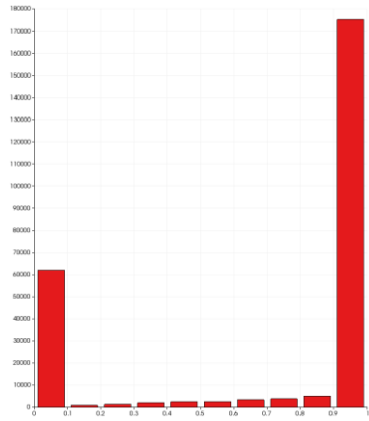
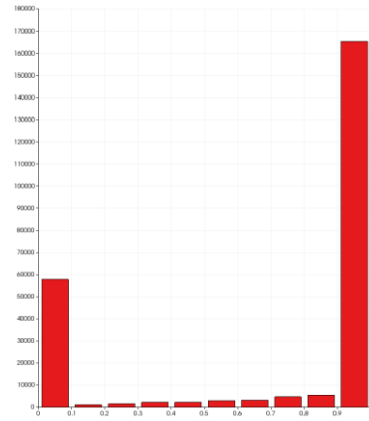


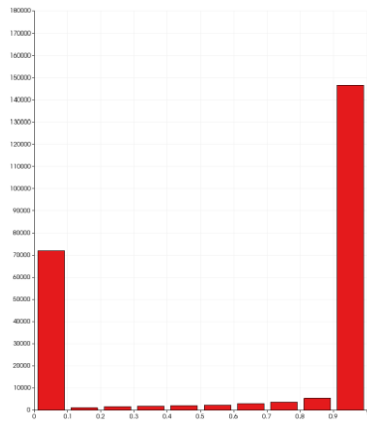
Figure C.8: Variations of the normal contact forces in the monitoring slice at the finishing phase (at time step 60)



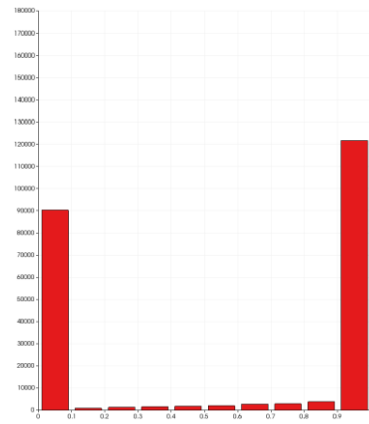
a) Preparation phase (at time step 1)



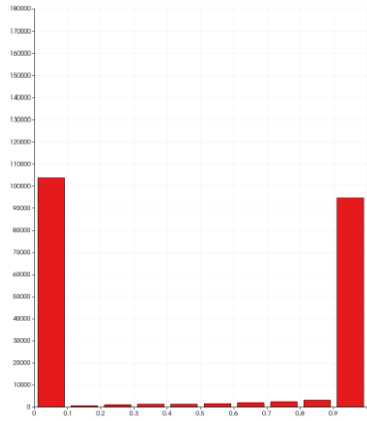
b) 1st excavation phase (at time step 20)



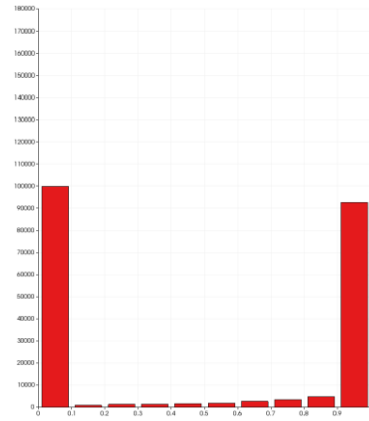
c) 2nd excavation phase (at time step 30)



d) 3rd excavation phase (at time step 40)



e) 4th excavation phase (at time step 50)



f) Finishing phase (at time step 60)

Figure C.9: Histograms of the stability parameter of rock blocks in the monitoring slice

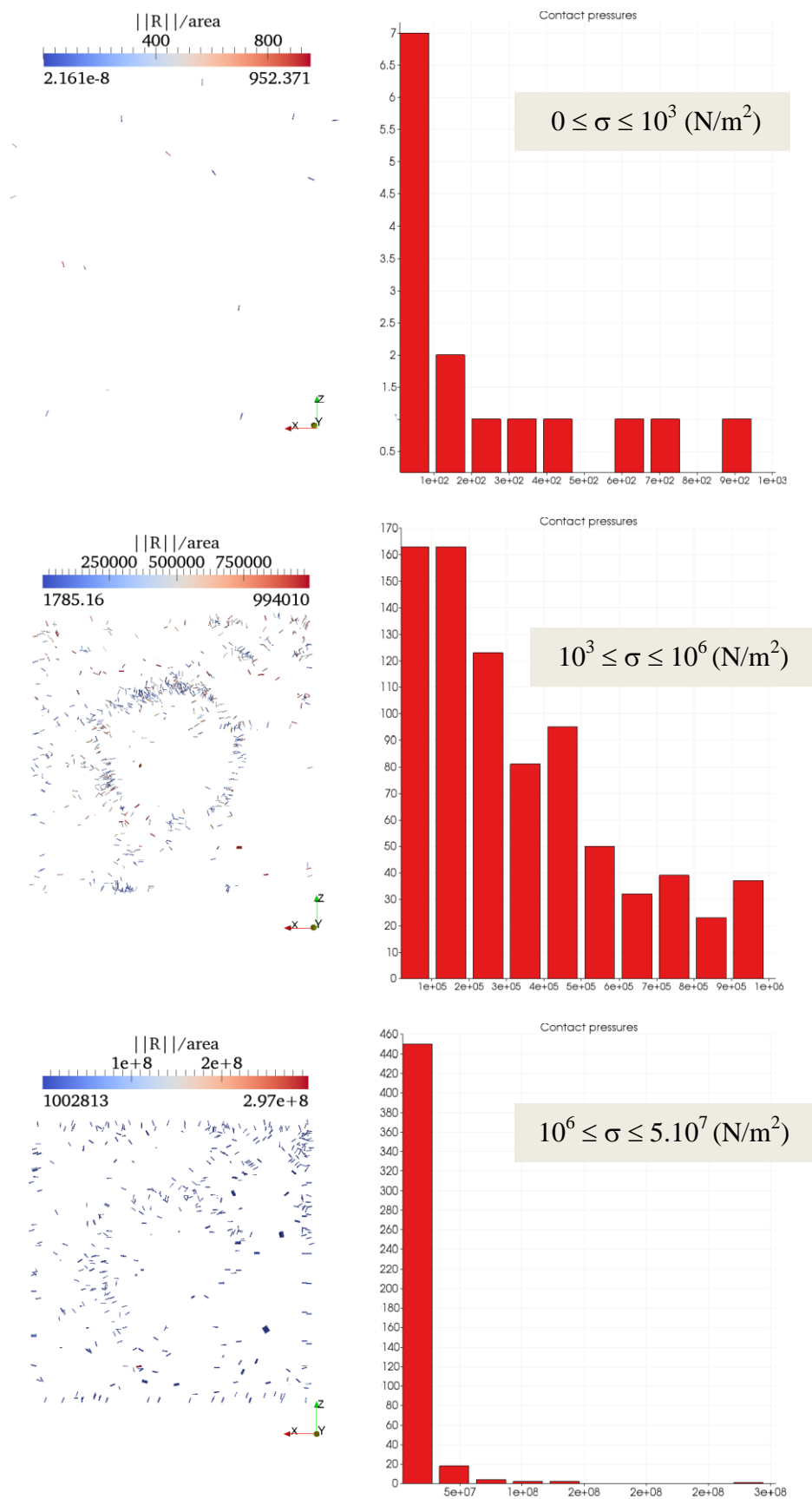


Figure C.10: Variations of the contact pressures in the monitoring slice
at the preparation phase (at time step 1)

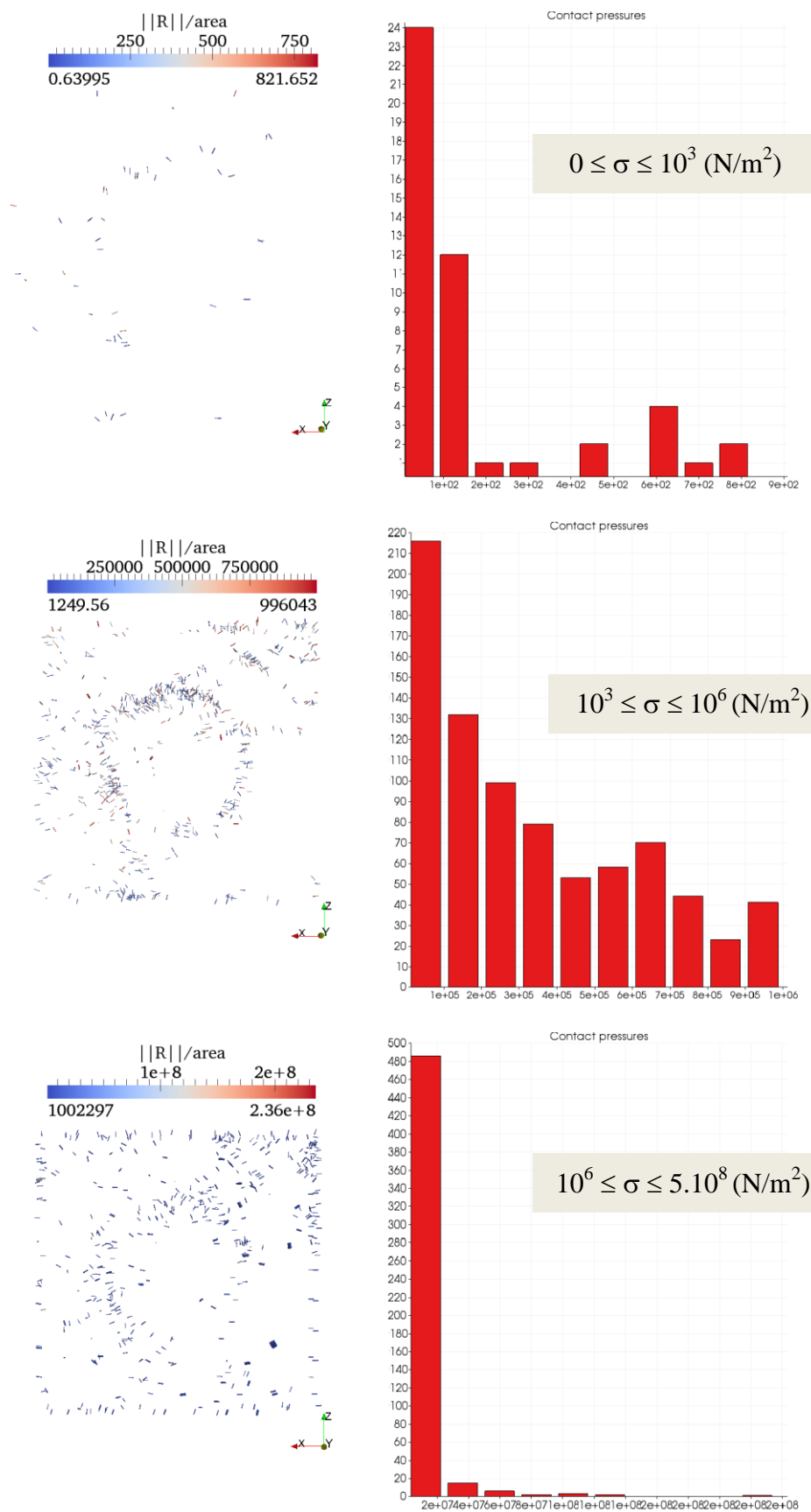


Figure C.11: Variations of the contact pressures in the monitoring slice at the 1st excavation phase (at time step 20)

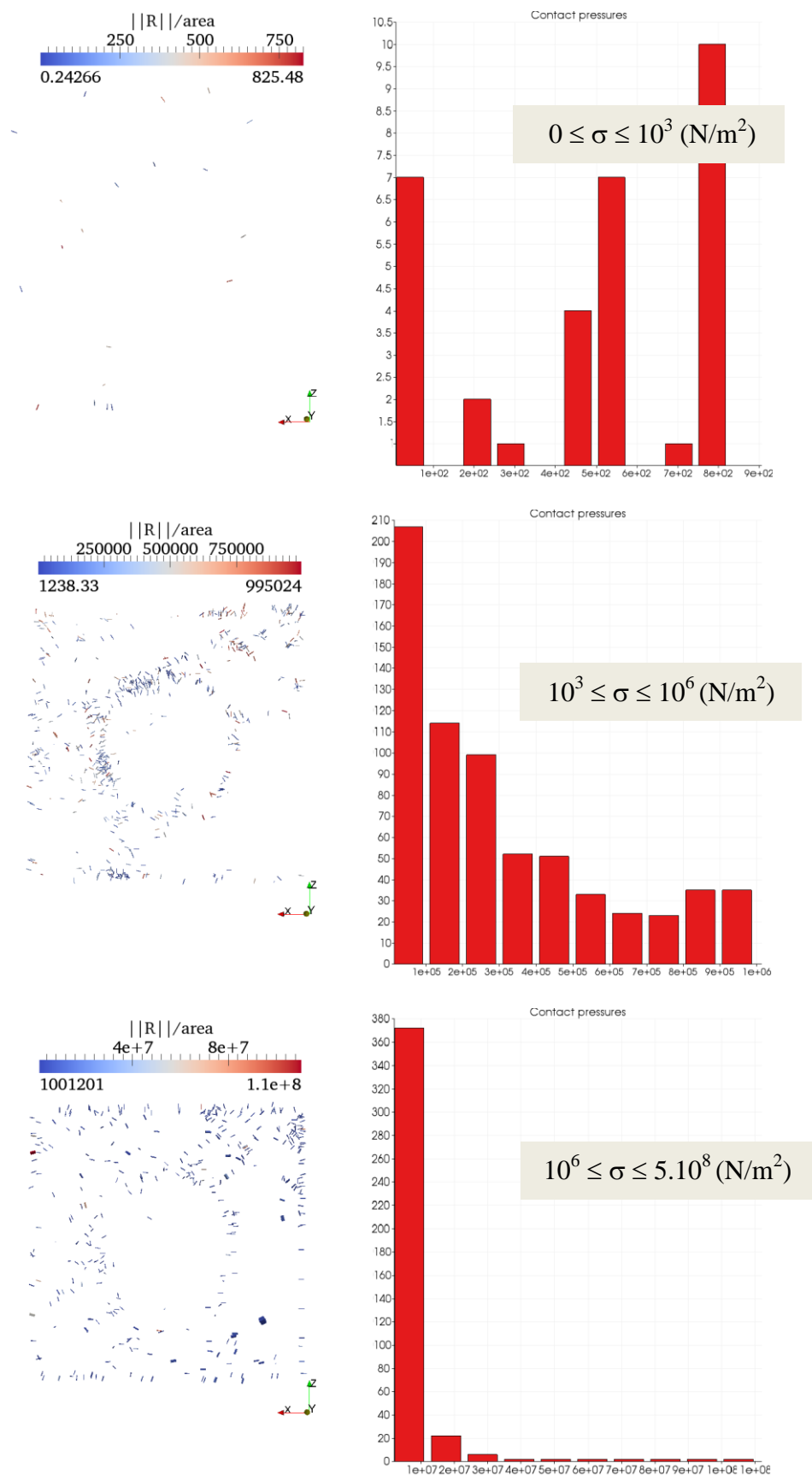


Figure C.12: Variations of the contact pressures in the monitoring slice at the 2nd excavation phase (at time step 30)

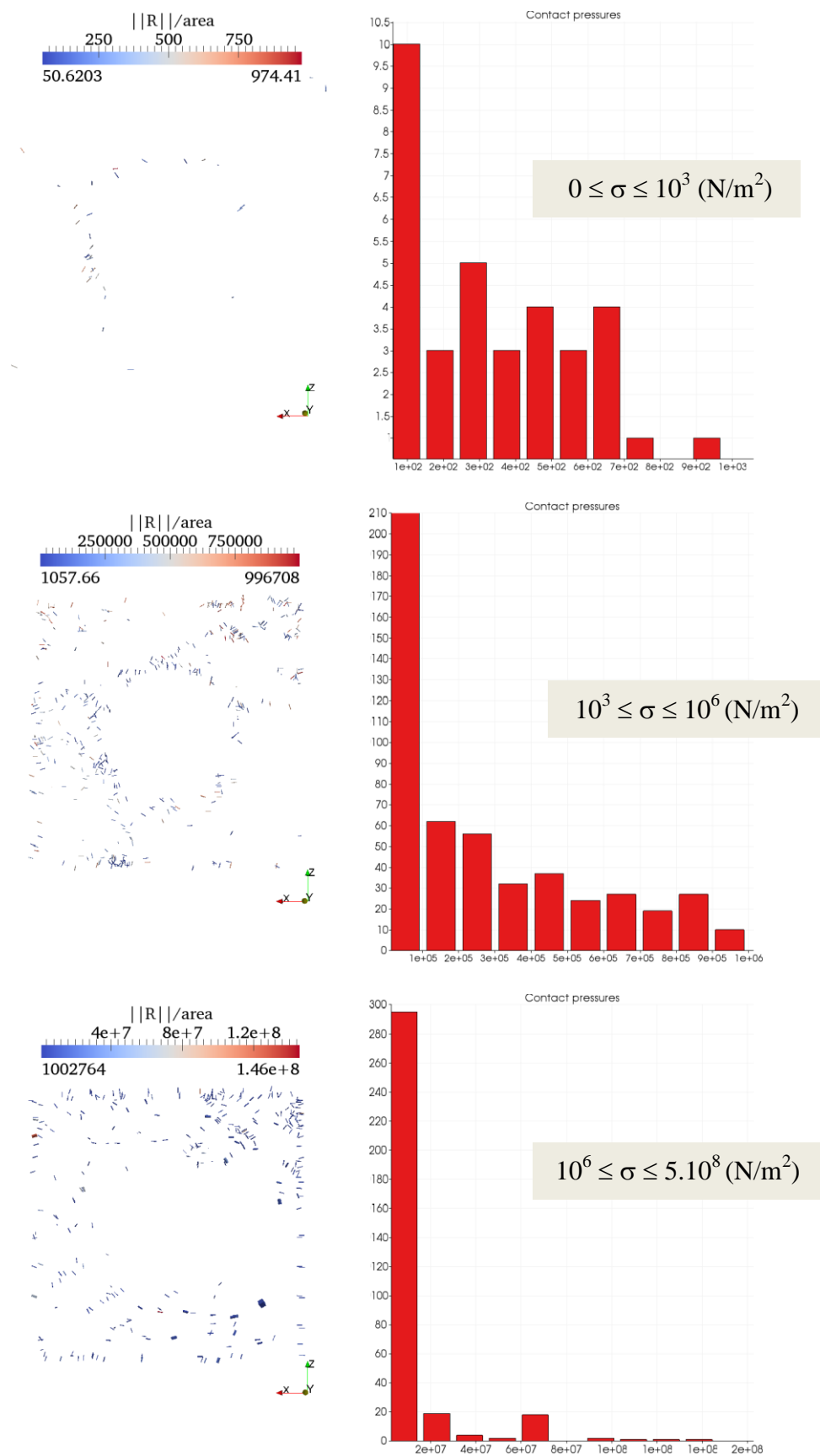


Figure C.13: Variations of the contact pressures in the monitoring slice at the 3rd excavation phase (at time step 40)

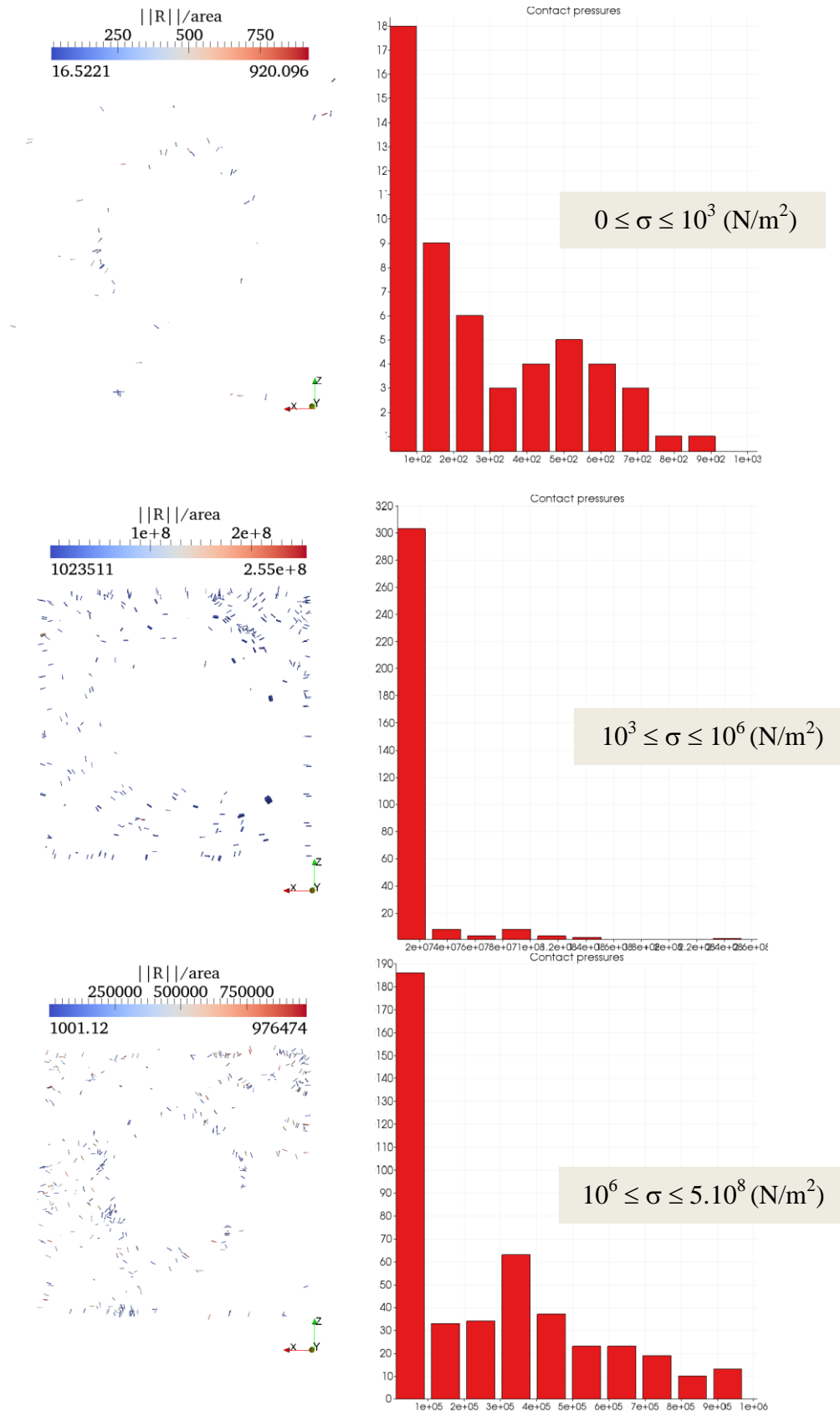


Figure C.14: Variations of the contact pressures in the monitoring slice at the 4th excavation phase (at time step 50)

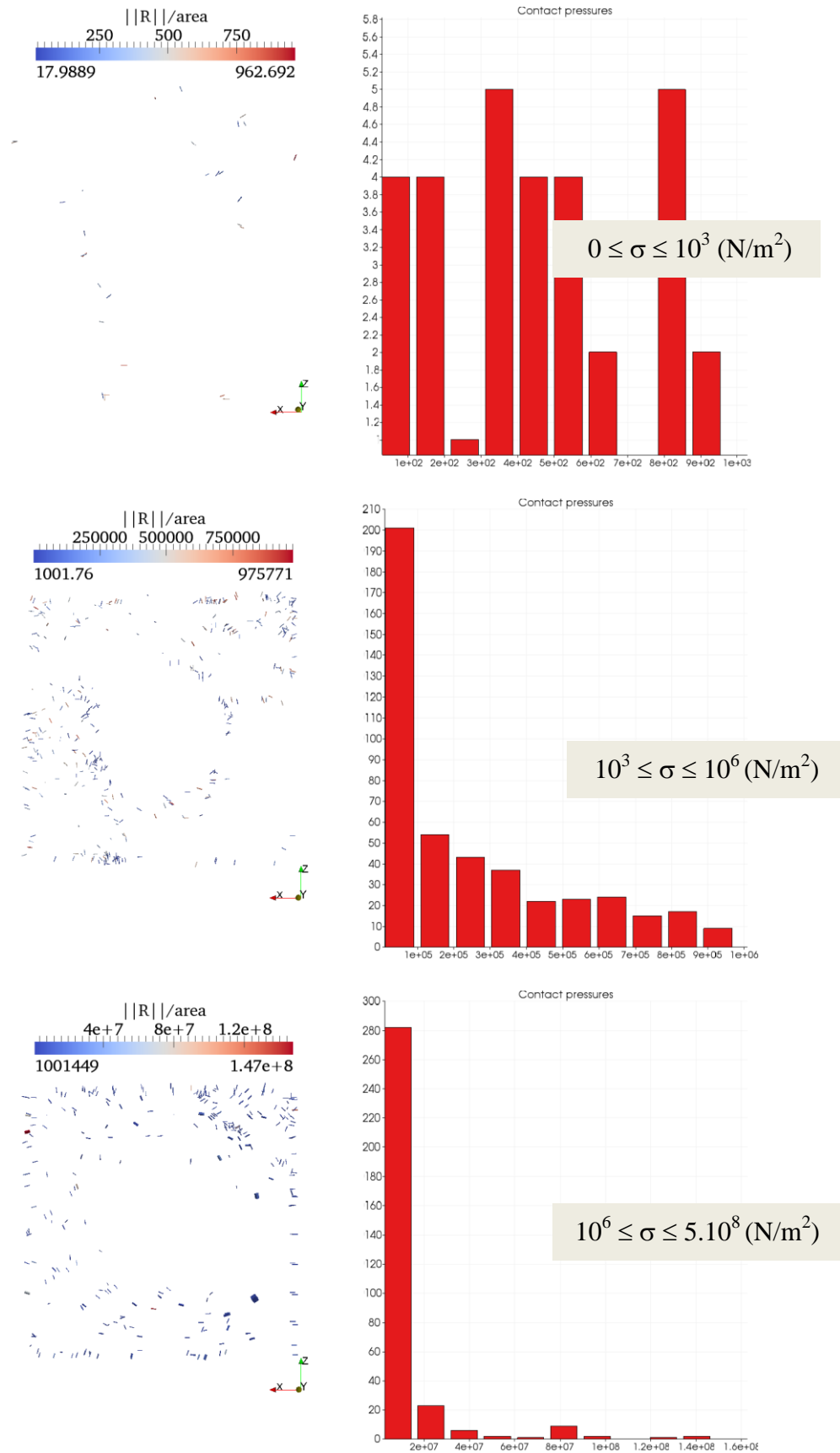


Figure C.15: Variations of the contact pressures in the monitoring slice at the finishing phase (at time step 60)

Table C.1: Variation of the contact force between the constitutive blocks on the monitoring slice (Part 1)

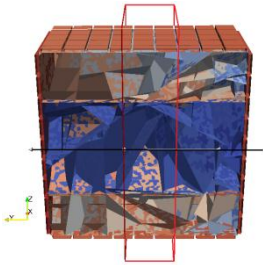
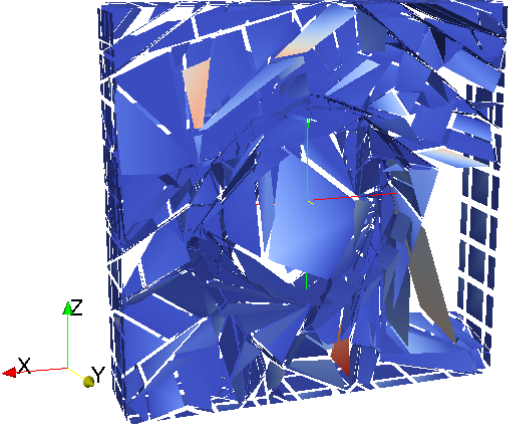
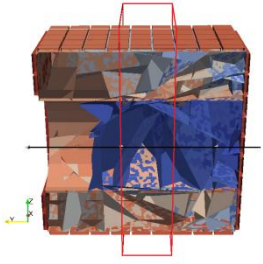
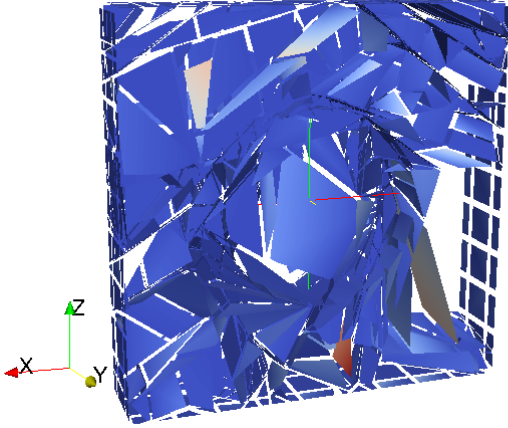
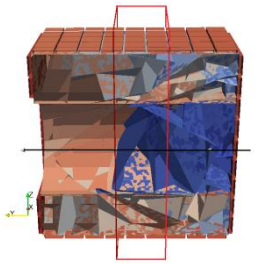
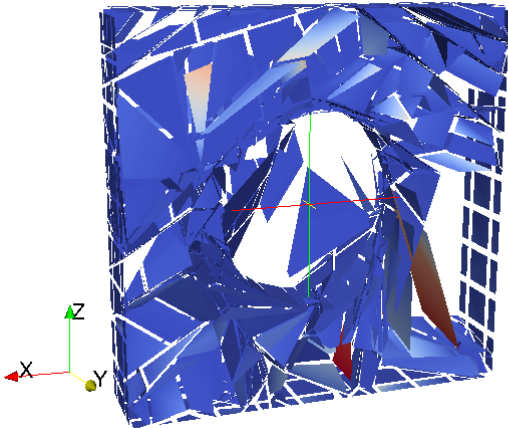
Position of the slice	Variation of the contact force
<p>a) Preparation phase (at time step 1)</p> 	 <p>R 2e+07 2e+07 1e+07 0</p>
<p>b) 1st excavation phase (at time step 20)</p> 	 <p>R 2.8e+07 2e+07 1e+07 0</p>
<p>c) 2nd excavation phase (at time step 30)</p> 	 <p>R 2.8e+07 2e+07 1e+07 0</p>

Table C.2: Variation of the contact force between the constitutive blocks on the monitoring slice (Part 2)

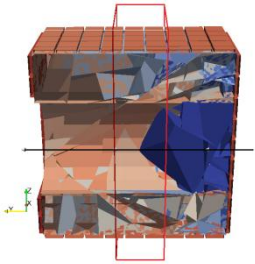
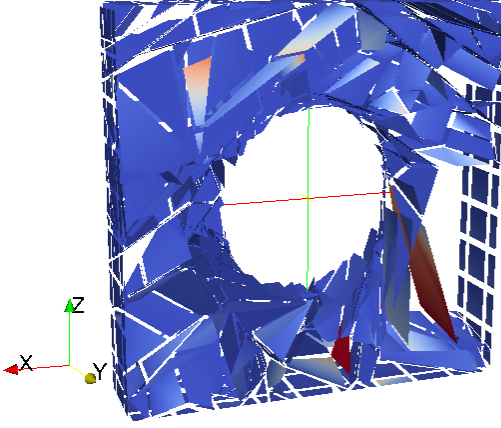
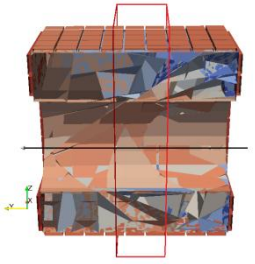
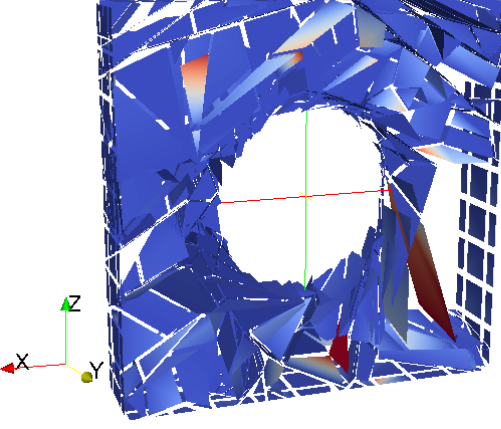
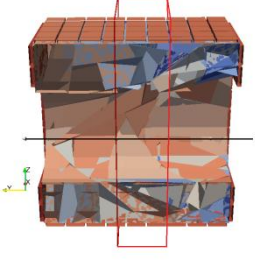
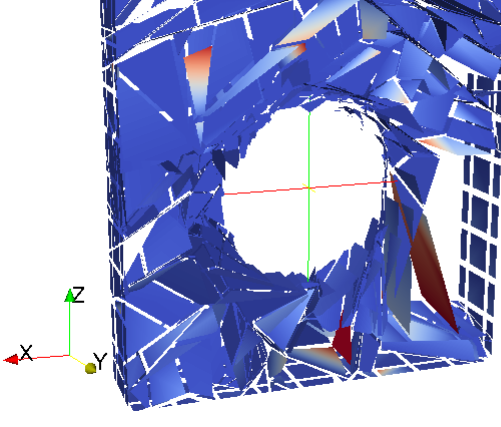
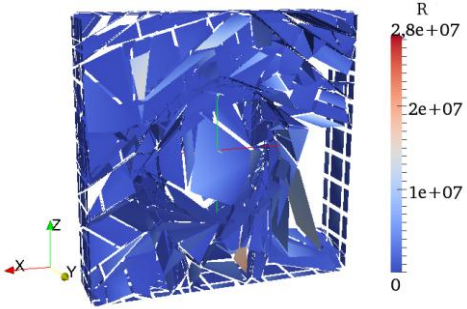
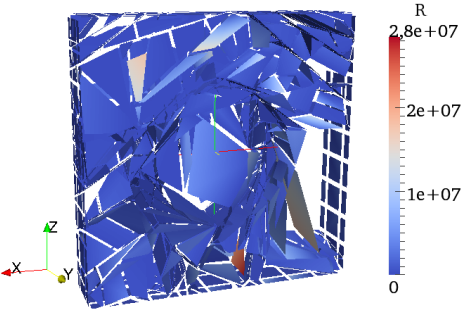
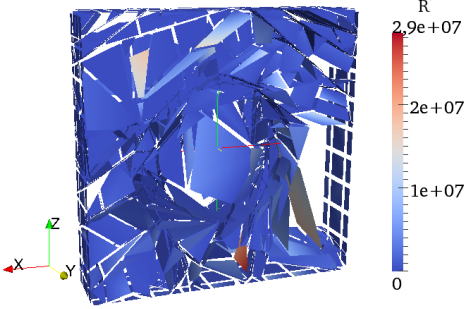
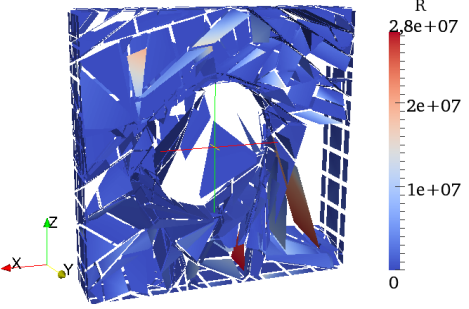
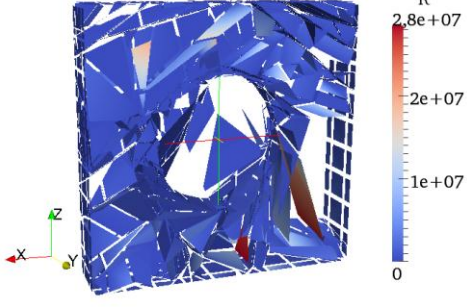
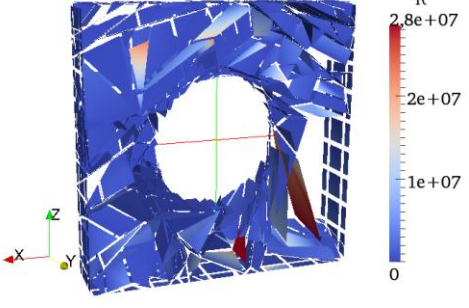
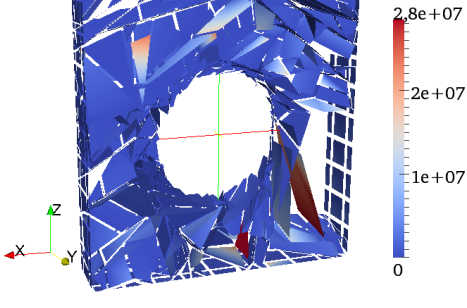
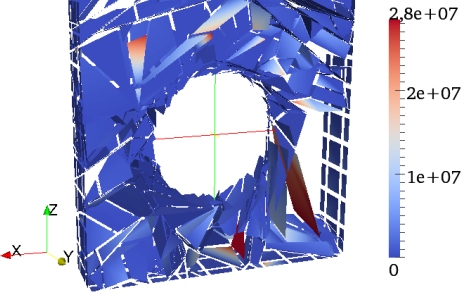
Position of the slice	Variation of the contact force
<p>d) 3rd excavation phase (at time step 40)</p> 	
<p>e) 4th excavation phase (at time step 50)</p> 	
<p>f) Finishing phase (at time step 60)</p> 	

Table C.3: Redistribution of the contact force between the constitutive blocks on the monitoring slice before and after each excavation

Excavation	Before	After
1 st		
2 nd		
3 rd		
4 th		

C.2. Combination 2 under the 3rd loading case

The obtained results of the mechanical responses of the model 4 under the application of the 3rd loading cases are showed.

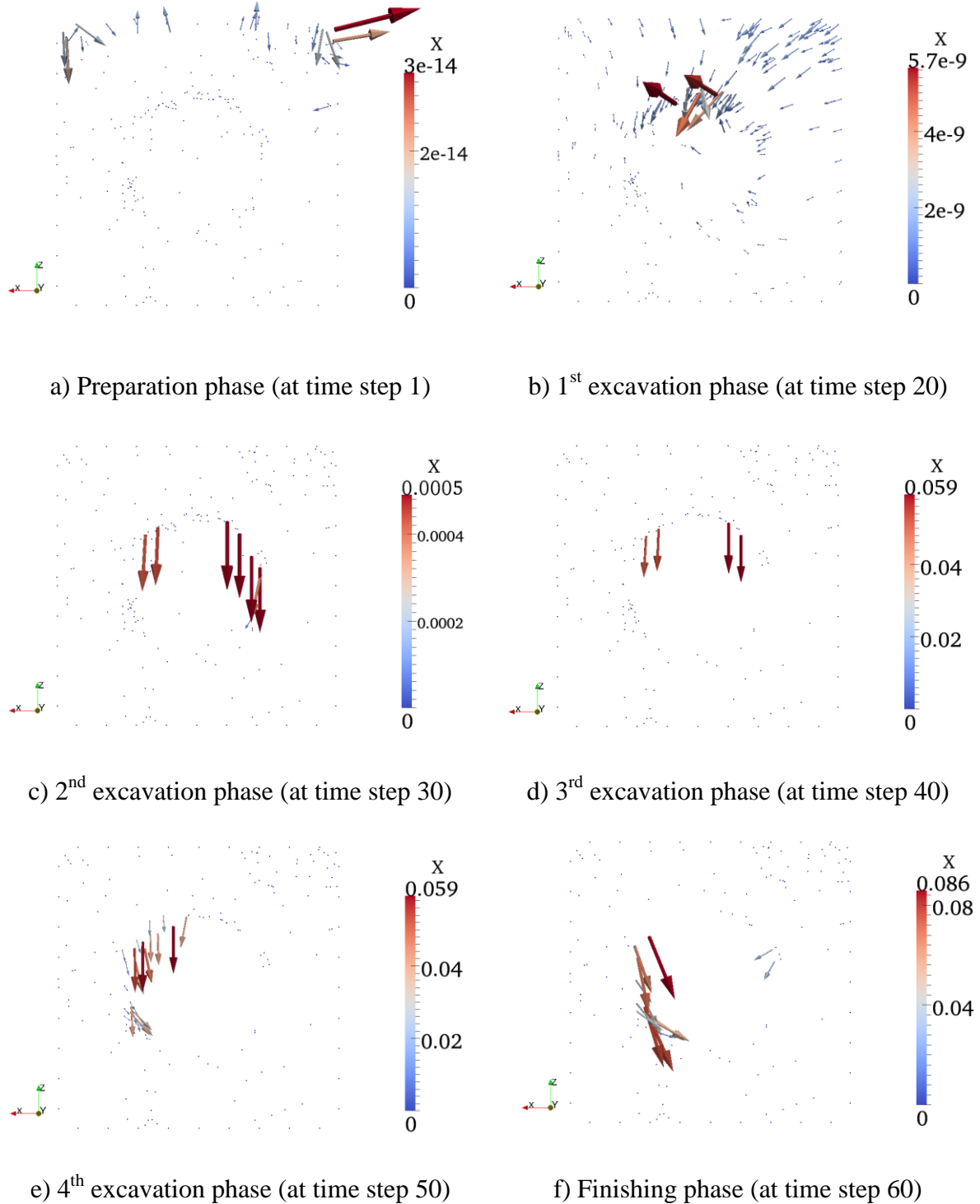
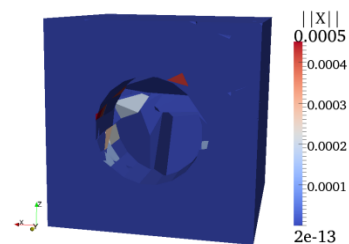


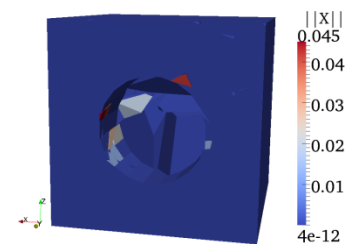
Figure C.16: Flows of displacement of rock blocks on the monitored slice of the Model 4 during the simulation time



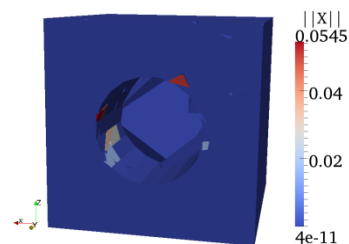
a) Before the 1st excavation (at time step 19)



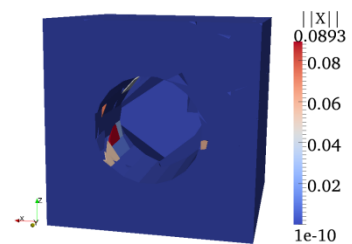
b) After the 1st excavation (at time step 20)



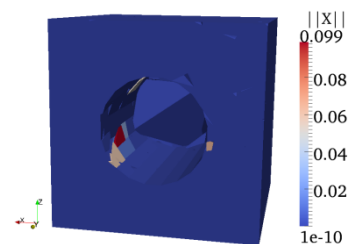
c) Before the 2nd excavation (at time step 29)



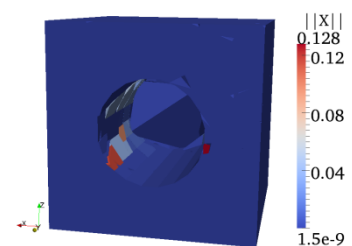
d) After the 2nd excavation (at time step 30)



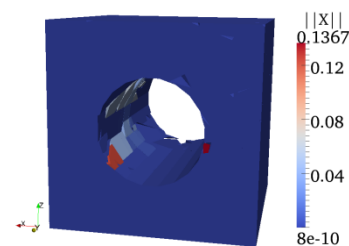
e) Before the 3rd excavation (at time step 39)



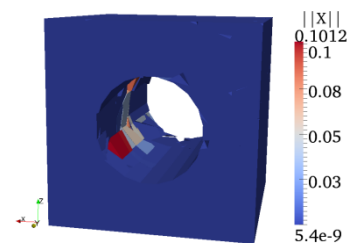
f) After the 3rd excavation (at time step 40)



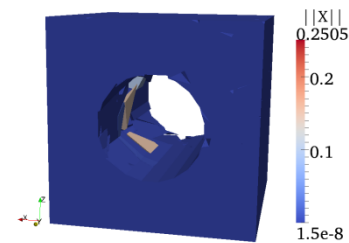
g) Before the 4th excavation (at time step 49)



h) After the 4th excavation (at time step 50)

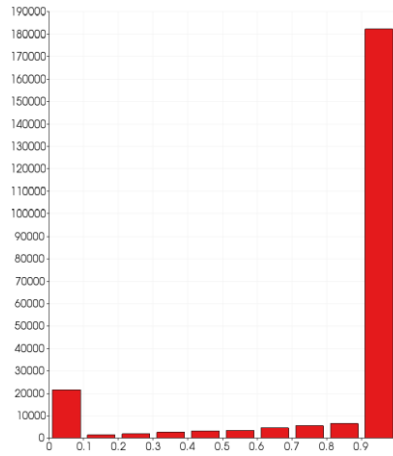


i) Finishing phase (at time step 60)

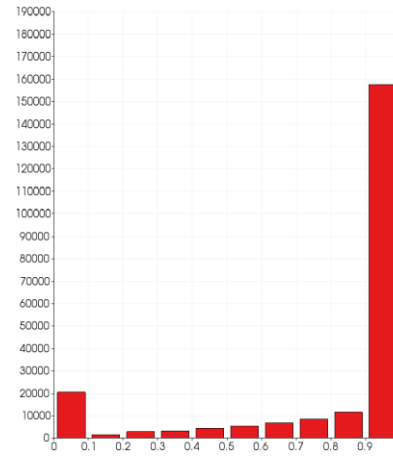


j) Finishing phase (at time step 100)

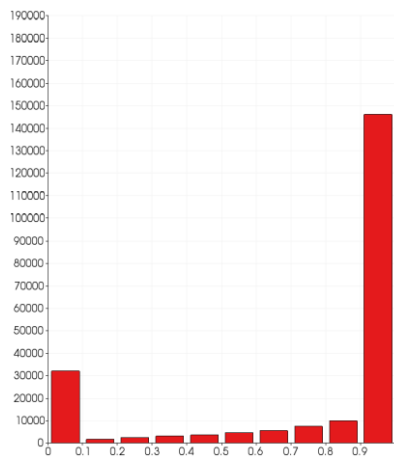
Figure C.17: Moving rock blocks of the Model 4 during its tunnelling procedure



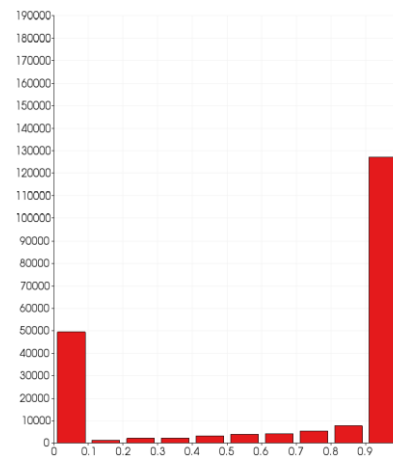
a) Preparation phase (at time step 1)



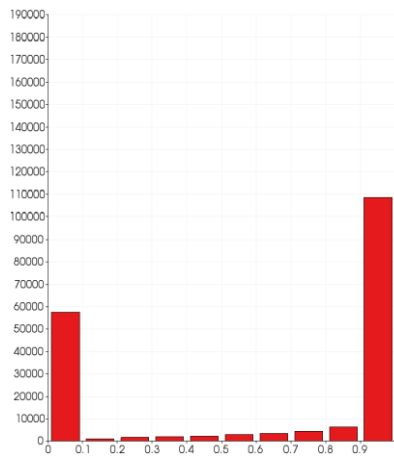
b) 1st excavation phase (at time step 20)



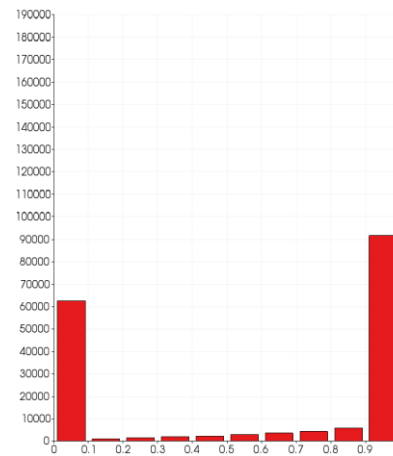
c) 2nd excavation phase (at time step 30)



d) 3rd excavation phase (at time step 40)



e) 4th excavation phase (at time step 50)



f) Finishing phase (at time step 60)

Figure C.18: Histograms of the stability parameter of rock blocks in the monitored slice

Table C.4: Variation of the contact force between the constitutive blocks on the monitoring slice (Part 1)

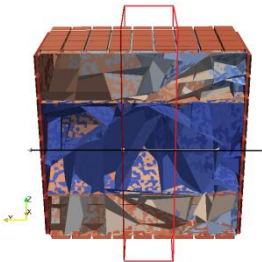
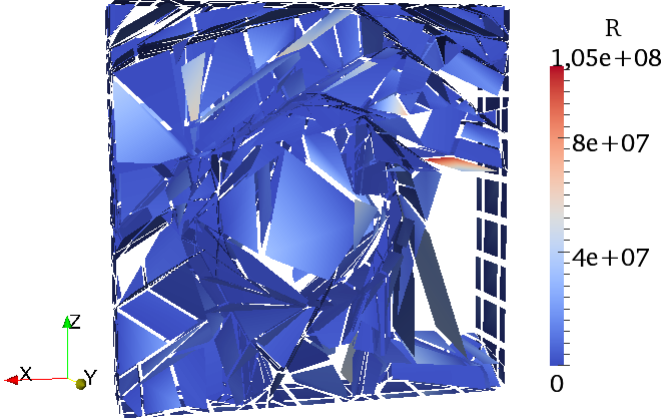
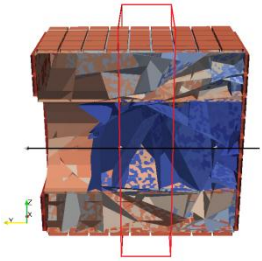
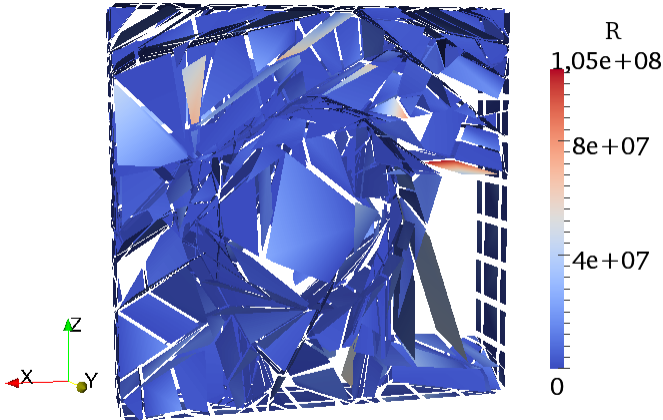
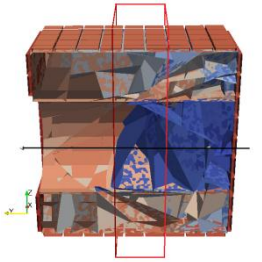
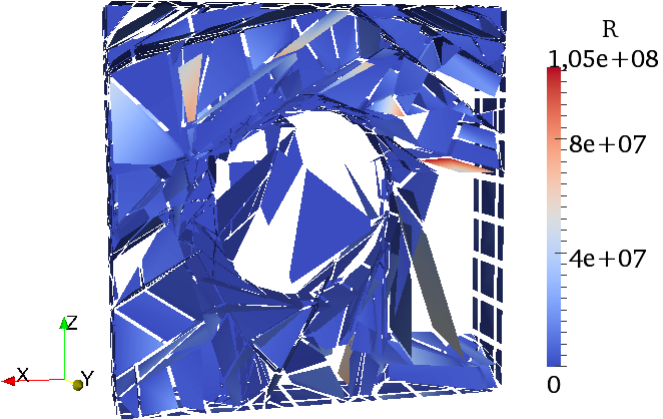
Position of the slice	Variation of the contact force
<p>a) Preparation phase (at time step 1)</p> 	
<p>b) 1st excavation phase (at time step 20)</p> 	
<p>c) 2nd excavation phase (at time step 30)</p> 	

Table C.5: Variation of the contact force between the constitutive blocks on the monitoring slice (Part 2)

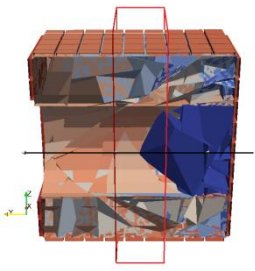
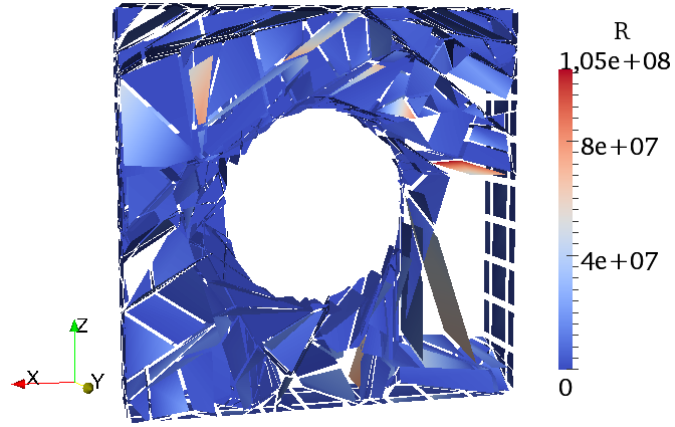
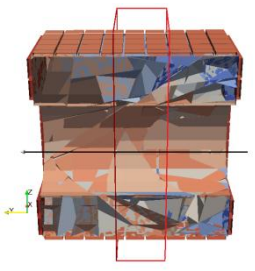
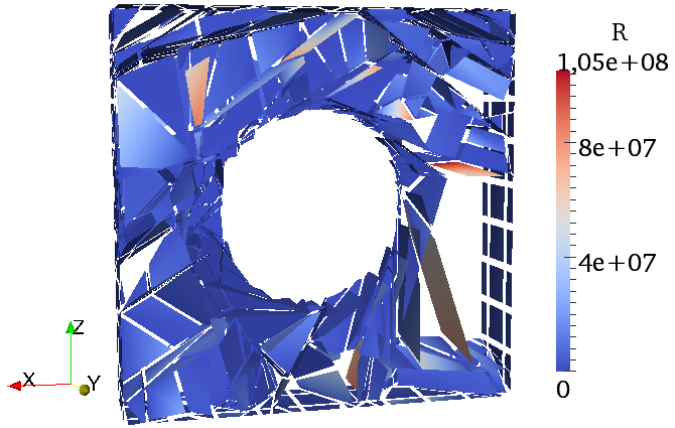
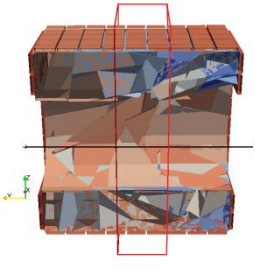
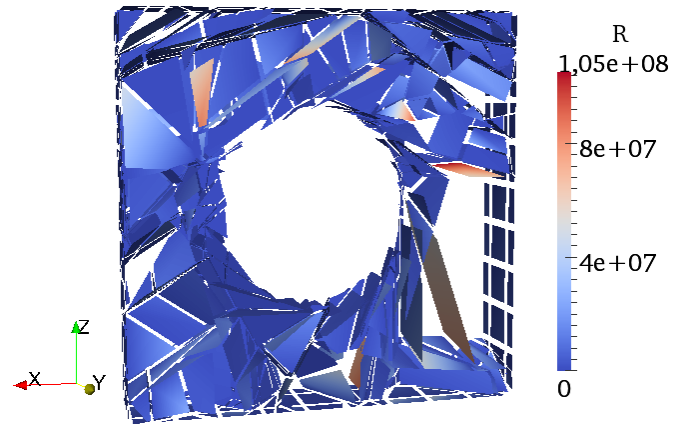
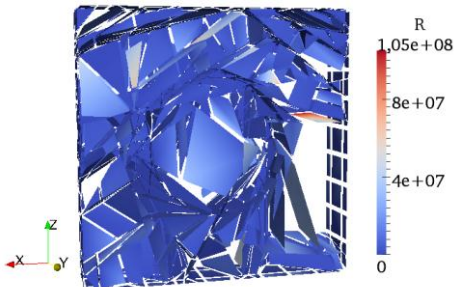
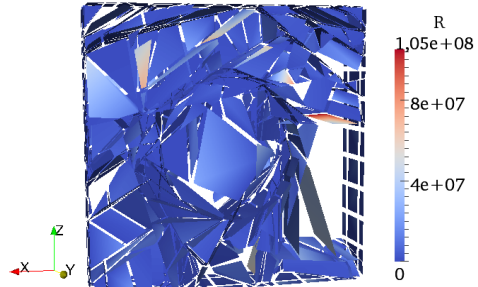
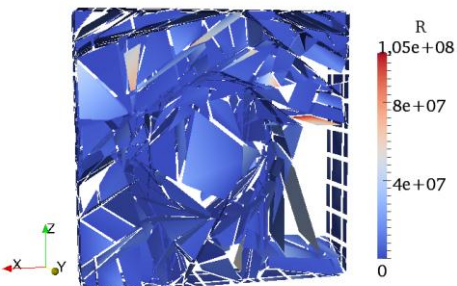
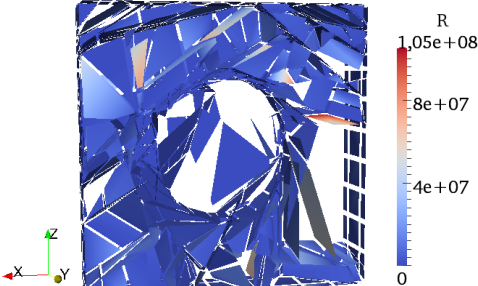
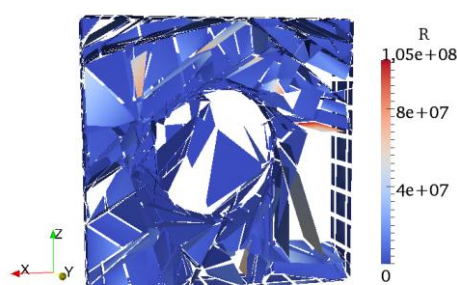
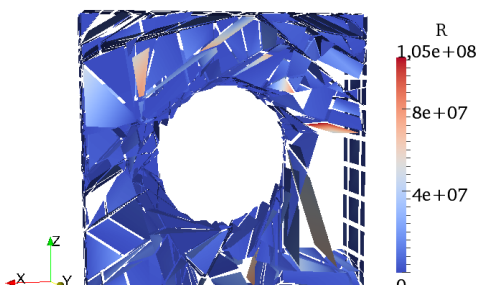
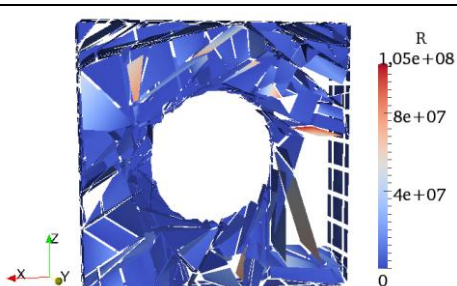
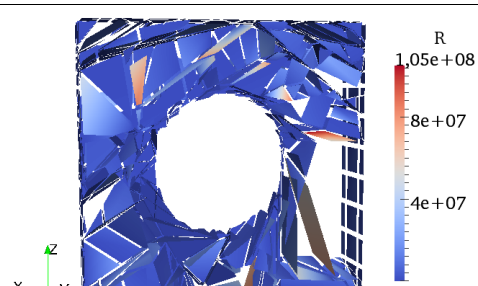
Position of the slice	Variation of the contact force
<p>d) 3rd excavation phase (at time step 40)</p> 	
<p>e) 4th excavation phase (at time step 50)</p> 	
<p>f) Finishing phase (at time step 60)</p> 	

Table C.6: Redistribution of the contact force between the constitutive blocks on the monitoring slice before and after each excavation

Excavation	Before	After
1 st		
2 nd		
3 rd		
4 th		

C.3. Comparison between the two loading cases

In this part, all the captures situated on the left column are dedicated to the responses of the model under the 1st loading case whereas all the captures situated on the right column are dedicated to the responses of the model under the 3rd loading case.

Table C.7: Deformation at the tunnel crown after the last excavation phase in the 1st and 3rd loading cases (observed from the furthest tunnel head)

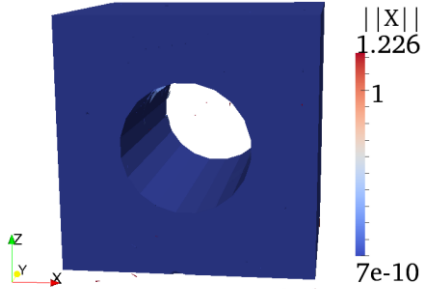
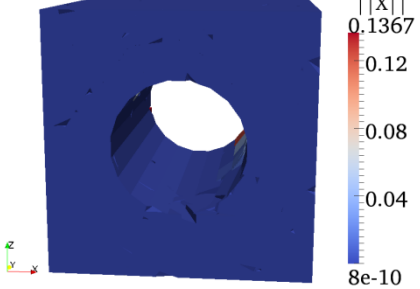
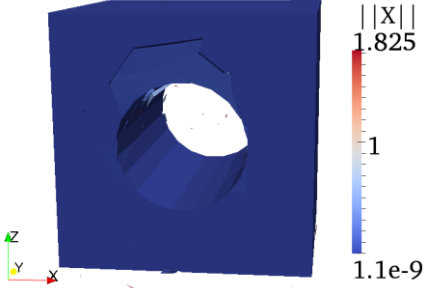
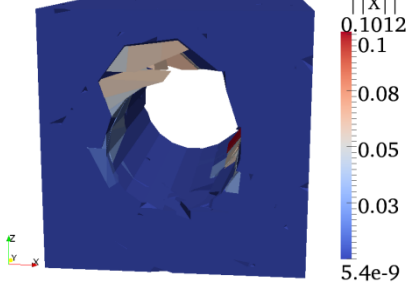
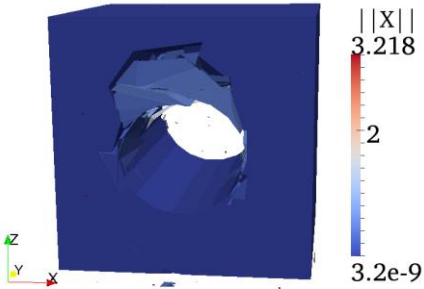
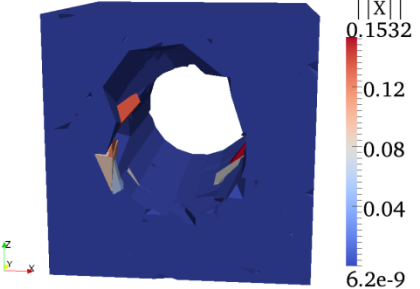
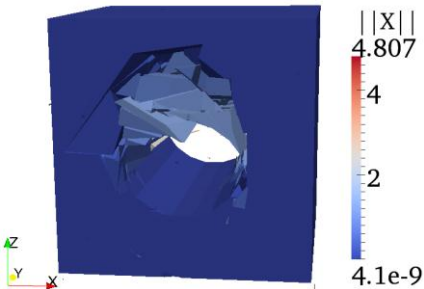
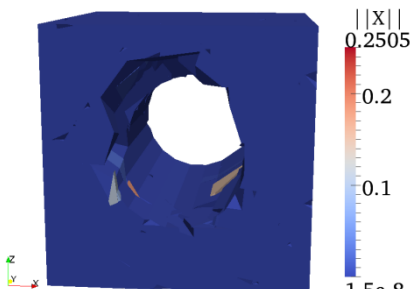

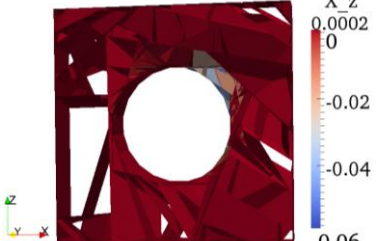

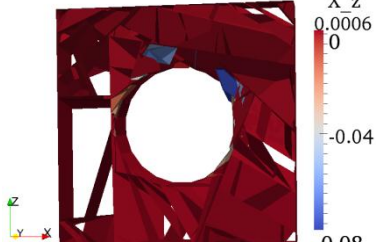
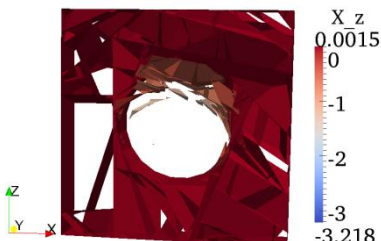

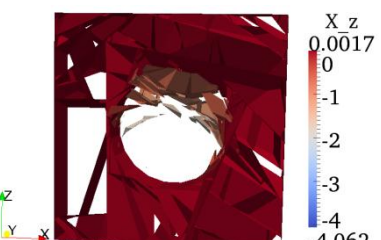



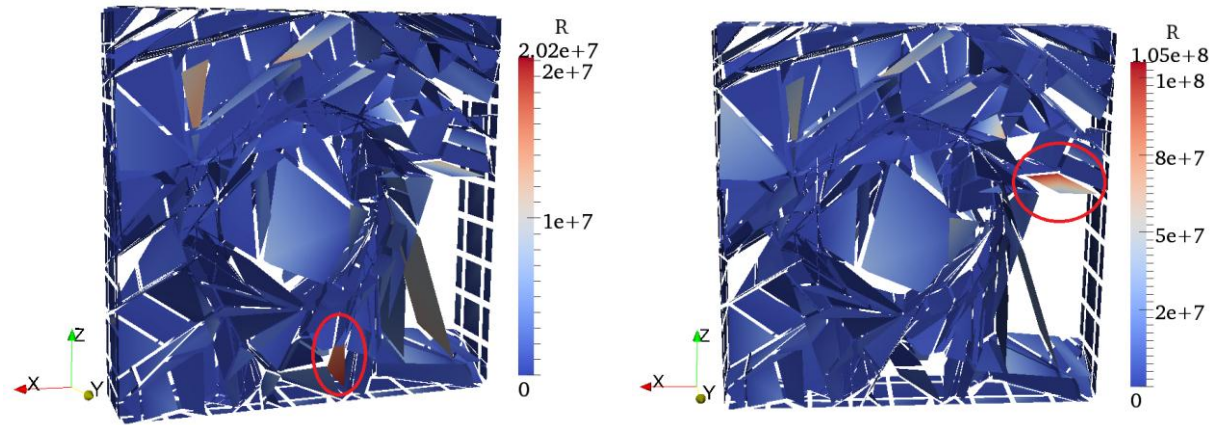
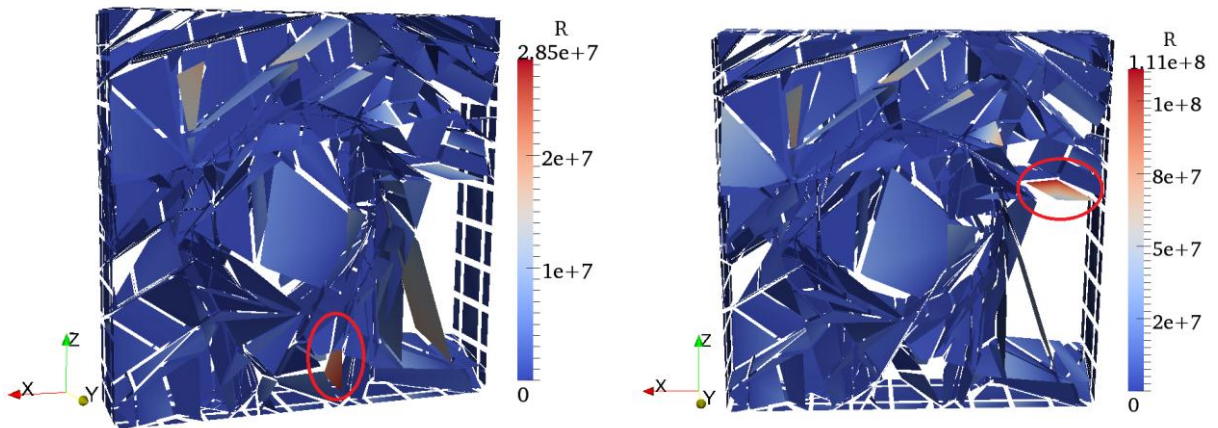
Simulation time	1 st loading case	3 rd loading case
50		
60		
80		
100		

Table C.8: Deformation zone at the tunnel crown after the last excavation phase in the 1st and 3rd loading cases (observed on the monitored slice)

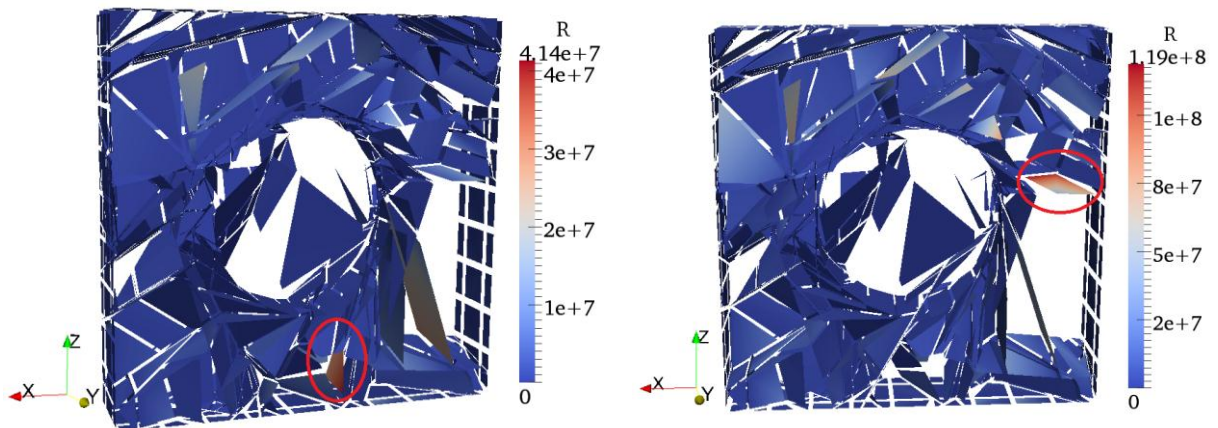
Simulation time	1 st loading case	3 rd loading case
50		
60		
80		
90		
100		



a) Preparation phase (at time step 1)



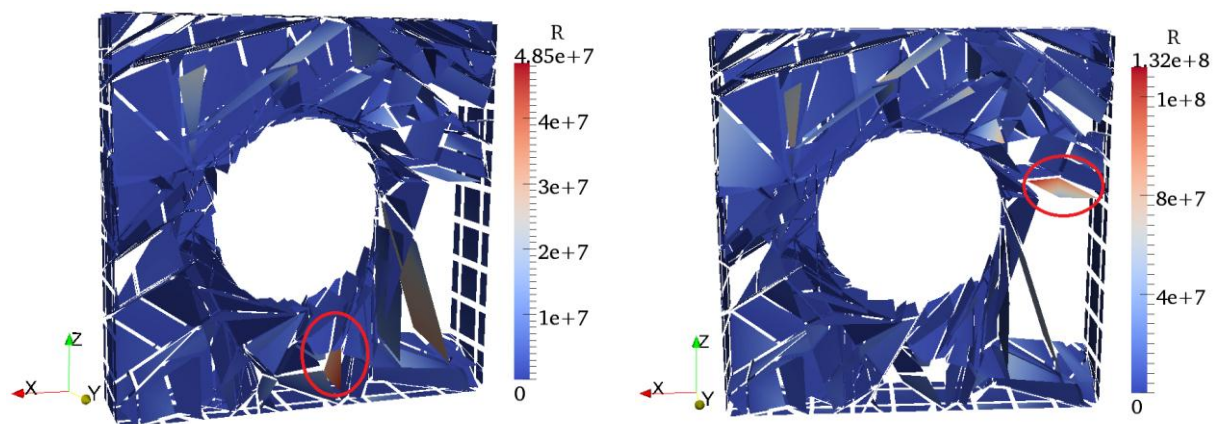
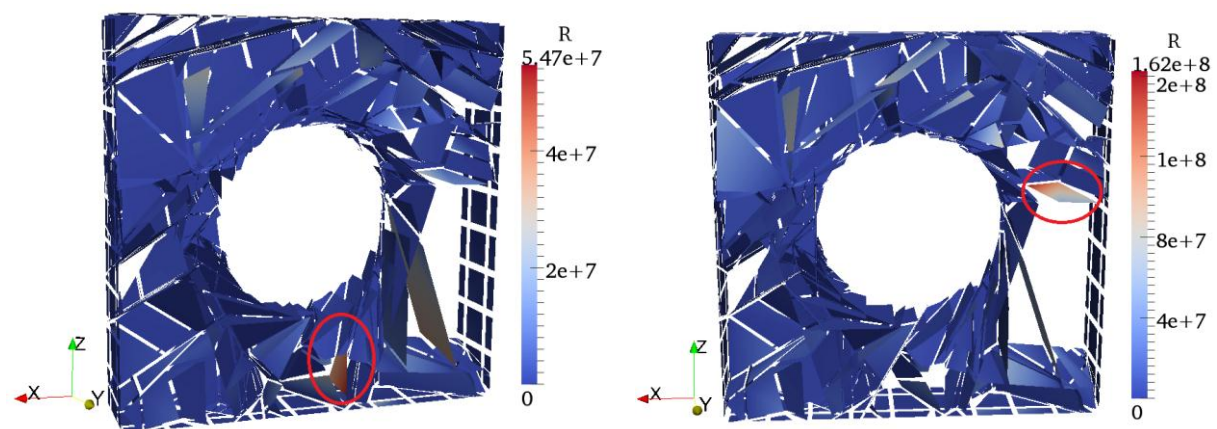
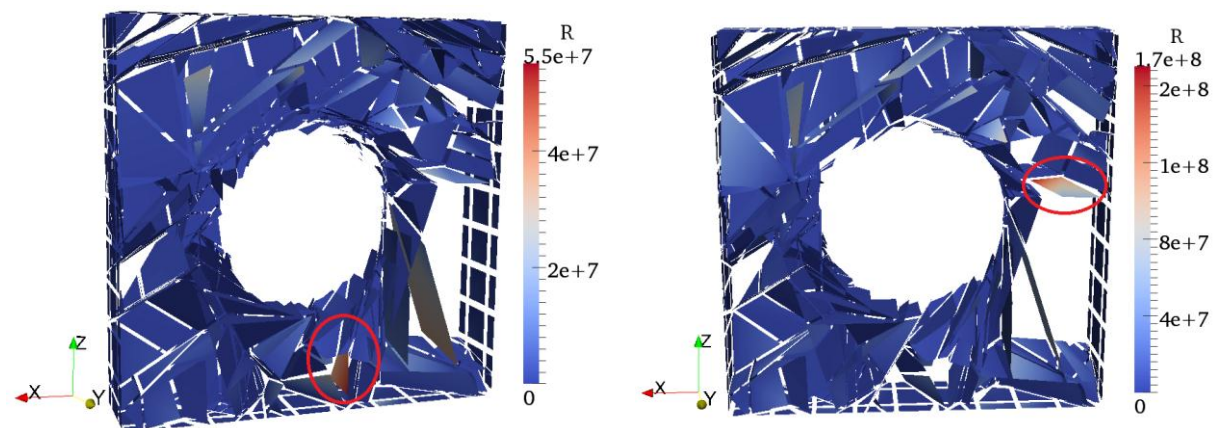
b) 2nd excavation phase (at time step 20)



c) 2nd excavation phase (at time step 30)

Figure C.19: Comparison of the contact forces of the model in the 1st and 3rd loading cases in the three first excavation phases

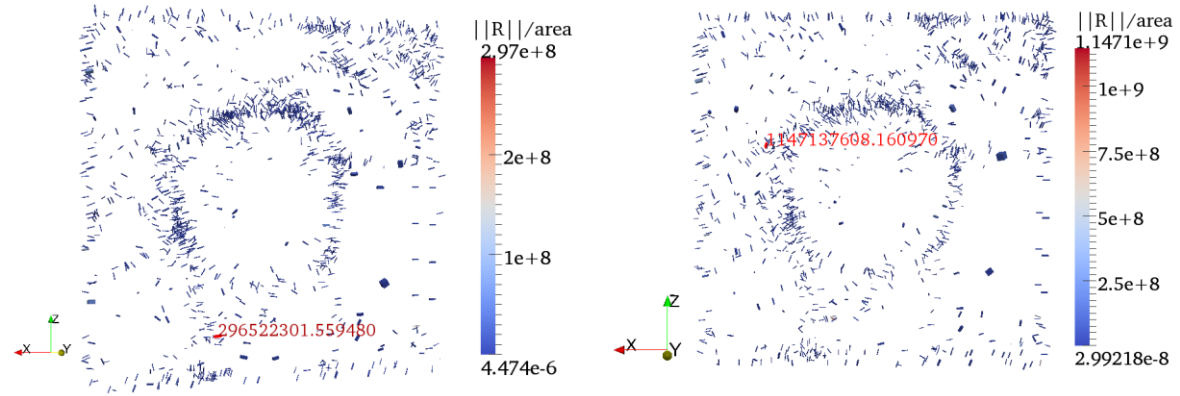
Notification: The red circles indicate the zones of the maximal contact forces

a) 3rd excavation phase (at time step 40)b) 4th excavation phase (at time step 50)

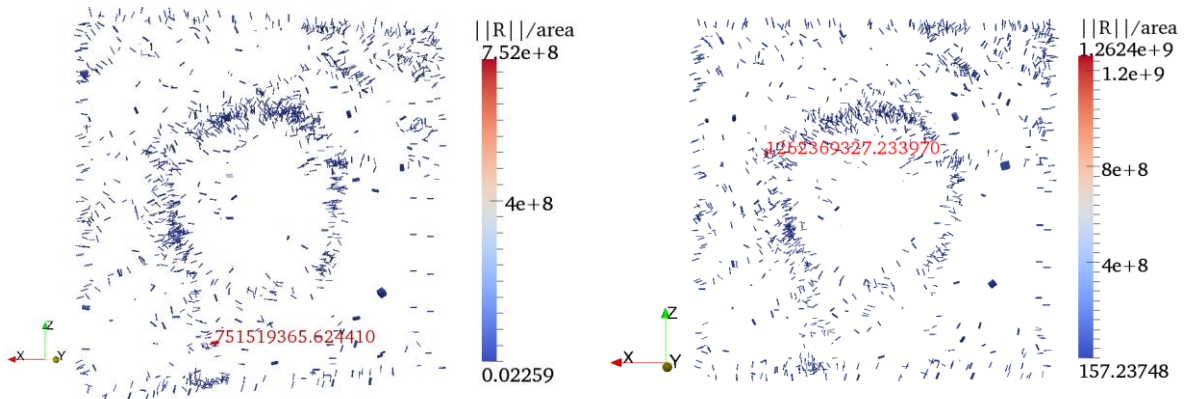
c) Finishing phase (at time step 60)

Figure C.20: Comparison of the contact forces of the model
in the 1st and 3rd loading cases in the three last excavation phases

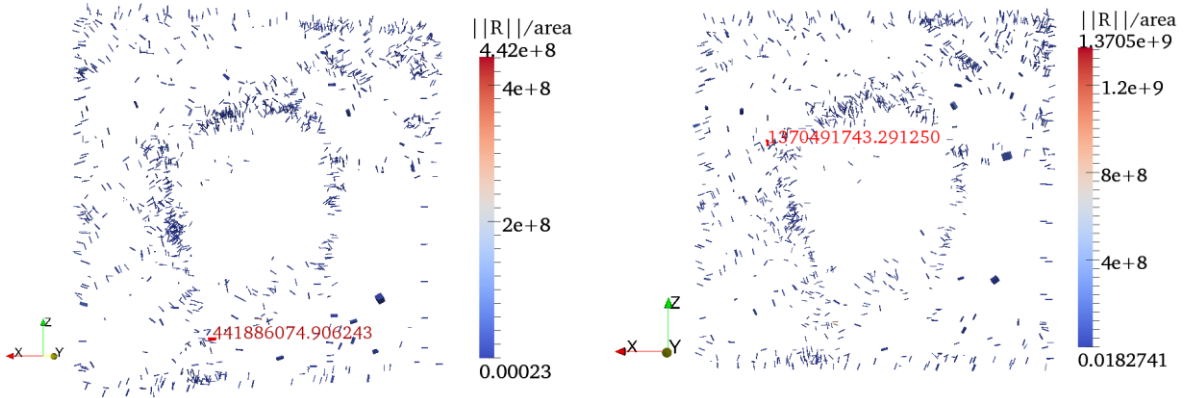
Notification: The red circles indicate the zones of the maximal contact forces



a) Preparation phase (at time step 1)



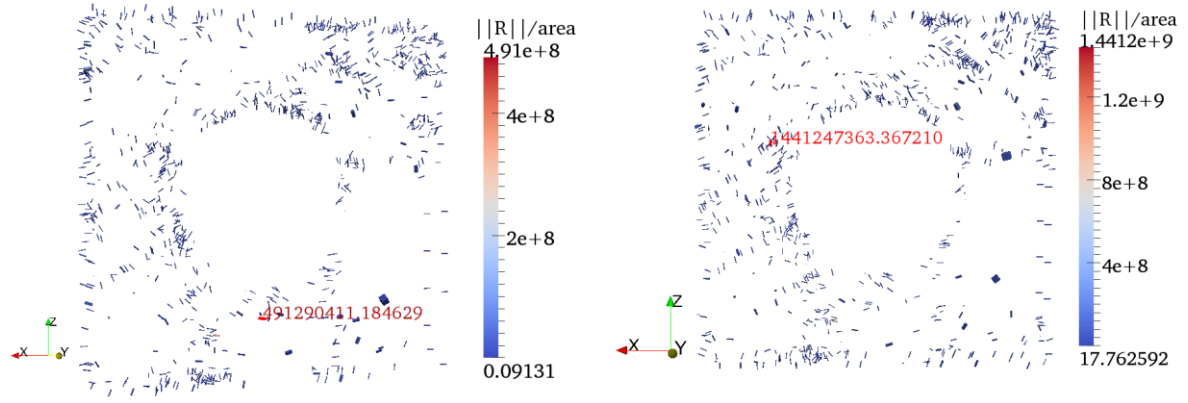
b) 1st excavation phase (at time step 20)



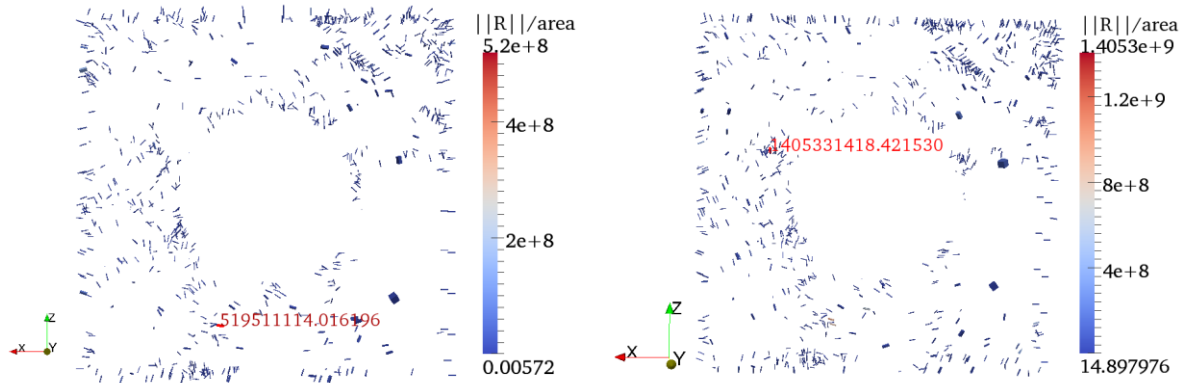
c) 2nd excavation phase (at time step 30)

Figure C.21: Comparison of the contact pressures of the model in the 1st and 3rd loading cases in the three first excavation phases

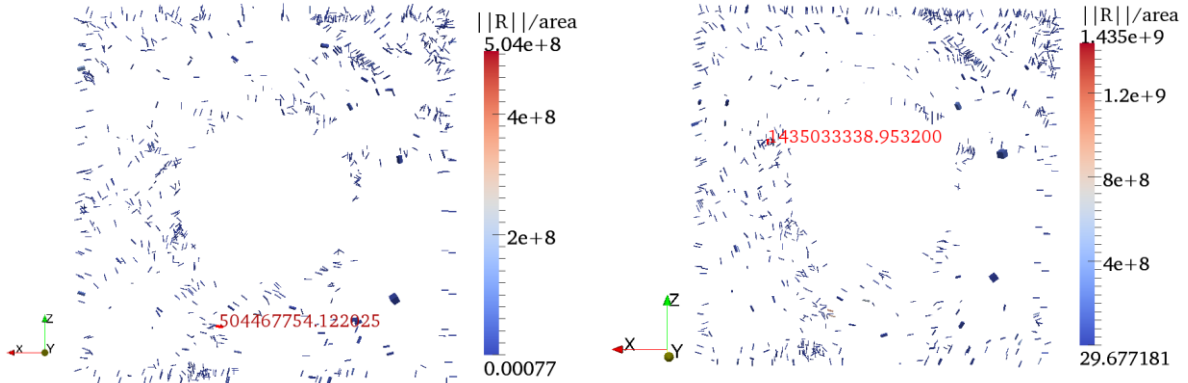
Notification: The red marks indicate the zones of the maximal contact pressures



a) 3rd excavation phase (at time step 40)



b) 4th excavation phase (at time step 50)



c) Finishing phase (at time step 60)

Figure C.22: Comparison of the normal contact pressures of the model in the 1st and 3rd loading cases in the three last excavation phases

Notification: The red marks indicate the zones of the maximal contact pressures

REFERENCE

- [1] M. Pidwirny, S. Jones. Fundamentals of Physical Geography online textbook. 2nd ed. <http://www.physicalgeography.net/about.html>; 17/12/2012.
- [2] Comité français de Mécanique des Roches. Manuel de mécanique des roches. Tome 1: Fondements. Paris : Les Presses de l'Ecole des Mines de Paris ; 2000.
- [3] Le Robert Plus. Dictionnaire de la langue française. Paris : Ed. France Loisirs ; 2007.
- [4] T. Ramamurthy. Engineering in rock for slopes, foundations and tunnels. 2nd ed. New Delhi: PHI Learning private limited; 2010.
- [5] AFTES. AFTES Recommendations. Characterization of rock masses useful for the design and the construction of underground structures. 1st version. France; 2003.
- [6] S. Priest. Discontinuity analysis for rock engineering. 1st ed. London: Chapman & Hall; 1993.
- [7] C. Edelbro. Rock mass strength - A review. Technical report. Luea University of Technology; ISSN: 1402-1536 – ISRN: LTU-TR-03/13-SE; 2003: 16.
- [8] US Army Corps of Engineers. Engineering and Design. Geotechnical Investigations. Appendix B: Geologic Mapping Procedures Open Excavations. EM 1110-1-1804; USA; 1/01/01.
- [9] B.B.S. Singhal, R.P. Gupta. Applied hydrogeology of fractured rocks. 2nd ed. Springer: 2010.
- [10] A. A. Afrouz. Practical handbook of rock mass classification systems and modes of ground failure. Boca Raton: CRC Press; 1992.
- [11] D.C. Wyllie and C.W. Mah. Rock slope engineering. Civil and mining. 4th ed. Taylor & Francis e-Library; 2005.
- [12] V. Merrien-Soukatchoff, T. Korini, A. Thoraval. Use of an integrated discrete fracture network code for stochastic stability analyses of fractured rock masses. Rock Mech. Rock Eng ; 2011 ; 45(2): 159-81.
- [13] Evert Hoek. Practical Rock Engineering. Ed. 2007. http://www.rocscience.com/hoek/corner/Practical_Rock_Engineering.pdf; 17/12/2012.

- [14] R.E. Hammah, T. Yacoub, B. Corkum. The practical modelling of discontinuous rock masses with finite element method. ARMA 08-180; 2008.
- [15] N. Hataf and M. Baharloo. An improved DEM for stability analysis of tunnel in rock mass. Iranian Journal of Science & Technology; 2004; Transaction B, Vol. 28, N° B1.
- [16] Università degli studi di Urbino "Carlo Bo". Rock Mechanics and Rock Engineering. http://www.uniurb.it/geoappl/gislab/formazione/corso2009_2010/MeccanicaRocce.pdf; 04/02/2013.
- [17] R. Yoshinaka and T. Yamabe. Joint stiffness and deformation behaviour of discontinuous rock. Int. J. Rock Mech. Min. Sci; 1986; 23(3): 19-28.
- [18] R. Mettler. Mass Transport in Fractured Media. Doctoral thesis of the geo-scientific faculty of the Eberhard Karl's university of Tübingen, Germany; 2007.
- [19] H.A. Keykha *et al.* Effect of discontinuities on the stability of rock blocks in tunnel. International Journal of Physical Sciences; 03/2012; Vol. 7(13): 2118 – 23.
- [20] P.M. Warburton. Vector stability analysis of an arbitrary polyhedral rock block with any number of free faces. Int. J. Rock. Mech. Min. Sci. & Geomech. Abstr.; 1981; 18: 415-27.
- [21] R.E. Goodman and G. Shi. Block theory and its application to rock engineering. New Jersey: Prentice-Hall; 1985.
- [22] L. Scholtes and F.V. Donze. Progressive failure mechanisms in jointed rocks: Insight from 3D DEM modelling. II International Conference on Particle-based Methods - Fundamentals and Applications; 2011.
- [23] E. Hoek and E.T. Brown. Underground Excavations in Rock, Institution of Mining and Metallurgy, London: 1980.
- [24] Ö. Aydan, R. Ulussay, T. Kawamoto. Assessment of rock mass strength for underground excavations. Int J. Rock Mech & Min Sci; 1997; 34(18): 3-4.
- [25] E. Hoek and E.T. Brown. Empirical strength criterion for rock masses. ASCE Journal of the Geotechnical Engineering Division; 1980a; 106 (GT9): 1013-35.
- [26] J.A. Hudson (Editor-in-Chief). Comprehensive rock engineering. Volume 2: Analysis and design methods. 1st ed. Pergamon Press: 1993.

- [27] D. Stead and E. Eberhardt. Developments in the characterization of complex rock slope deformation and failure using numerical modelling techniques. *Engineering Geology*; 2006; 83: 217-235.
- [28] E. Hoek and E.T. Brown. Practical estimates of rock mass strength. *International Journal of Rock Mechanics and Mining Sciences*; 1997; 34(8): 1165-86.
- [29] G. Mostyn and K. Douglas. Strength of intact rock and rock masses. *GeoEng2000*; Melbourne: 19 – 24/11/2000.
- [30] E. Hoek, C. Carranza-Torres, B. Corkum. Hoek-Brown failure criterion – 2002 edition. <http://www.rockscience.com/assets/files/uploads/7715.pdf>; 14/02/2013.
- [31] Yudhbir, W. Lemanza, F. Prinzl. An empirical failure criterion for rock masses. 5th International Congress on Rock Mechanics; Melbourne: 10 - 15/4/1983.
- [32] L. Jing. A review of techniques advances and outstanding issues in numerical modelling for rock mechanics and rock engineering. *Int J. Rock Meca & Min Sci*; 2003; 40: 283-353.
- [33] J.R. Taylor. Classical mechanics. University science books. USA: 2005.
- [34] L. Jing, J.A. Hudson. Numerical methods in rock mechanics. *Int J. Rock Meca & Min Sci*; 2002; 39: 409-27.
- [35] X-T. Feng, J.A. Hudson. The ways ahead for rock engineering design methodologies. *Int J. Rock Meca & Min Sci*; 2004; 41: 255-73.
- [36] E. Hoek. Rock engineering. Edition 2005; <http://www.vulcanhammer.net/rockengineering>; 10/12/2012.
- [37] J.P. Harrison, J.A. Hudson. Engineering rock mechanics. Edition Oxford: Pergamon; 2000.
- [38] M. Jean, "The non-smooth contact dynamics method", *Comput. Methods in Appl. Mech. Engrg.*; 1999; 177: 235-57.
- [39] J.J. Moreau. Some numerical methods in multi-bodies dynamics: application to granular materials. *European journal of mechanics-A/Solids*, suppl.4, 1994b: 93-114.
- [40] F. Dubois. Fracturation as a non smooth contact dynamic problem. VIII International Conference on Computational Plasticity COMPLAS VIII E. Onate and D.R.J. Owen (Eds). CIMNE, Barcelona; 2005.

- [41] P. Taforel. Apport de la méthode des éléments discrets à la modélisation des maçonneries en contexte sismiques : Ver une nouvelle approche numérique de la vulnérabilité sismique. Thesis de l'Université de Montpellier 2. Montpellier; 21/12/2012.
- [42] C. Mattuissi. A reference discretization strategy for the numerical solution of physical field problems. Journal of Advanced in imaging and electron physics; 2002: 121.
- [43] Wikipedia. Finite difference method.
http://en.wikipedia.org/wiki/Finite_difference_method; 19/12/2012.
- [44] A. Bobet. Numerical methods in Geomechanics. Arabian Journal for Science and Engineering; 2010; 35: Number 1B.
- [45] Z. Li. Finite Difference methods basics. Center for Research in Scientific Computation & Department of Mathematics. North Carolina State University; 2001.
- [46] CS 3200. Finite Difference Methods. School of Computing - The University of Utah.
<http://www.eng.utah.edu/~cs3200/notes/cs3200-Finite-Differences.pdf>; 19/12/2012.
- [47] Wikipedia. Finite element method.
http://en.wikipedia.org/wiki/Finite_element_method; 19/12/2012.
- [48] D. Roylance. Finite element analysis. Department of Materials Science and Engineering - Massachusetts Institute of Technology: 2001.
- [49] M. Costabel. Principles of boundary element methods. Technische Hochschule Darmstadt. Course document of the Institut Mathématique Université de Rennes 1; 2012.
- [50] J.T. Katsikadelis. Boundary Elements Theory and Applications. Oxford: Elsevier; 2002.
- [51] P.A. Cundall, R.D. Hart. Numerical modelling of discontinua. Engr. Comp.; 1992; 9(2): 101-13 in Comprehensive Rock Engineering, Vol. 2: 231-243. J. A. Hudson, Ed. Oxford: Pergamon Press, 1993.
- [52] S.A.R. Beyabanaki, R.G. Mikola, K. Hatami. Three-dimensional discontinuous deformation analysis (3-D DDA) using a new contact resolution algorithm. Journal of Computer and geotechnics; 2008; 35: 346-56.
- [53] F. Dubois, M. Renouf. Discrete Element Methods for the simulation of divided media. LMGC90v2 formation document. LMGC-University of Montpellier 2; 2011

- [54] Wikipedia. Discrete element method. [http://en.wikipedia.org/wiki/ Discrete_element_method](http://en.wikipedia.org/wiki/Discrete_element_method); 19/12/2012.
- [55] J. Sykut, M. Molenda, J. Horabik. Discrete Element Method (DEM) as a tool for investigation properties of granular materials. Polish Journal of Food and Nutrition sciences; 2007; 57(2A): 169-73.
- [56] J.R. Williams, R. O'Connor. Discrete element simulation and the contact problem. Archives of Computational methods in engineering; 1999; 6: 279-304.
- [57] Wikipedia. Explicit and implicit methods.
[http://en.wikipedia.org/wiki/ Explicit_and_implicit_methods](http://en.wikipedia.org/wiki/Explicit_and_implicit_methods). 19/12/2012.
- [58] V. Acary. Numerical methods for time integration of NonSmooth Mechanical systems. Nonsmooth contact mechanics. Spring school. Aussois: 2010.
- [59] V. Acary. Numerical methods and software for Non Smooth Dynamical Systems. The Siconos Platform. 5th international school "Topics in nonlinear Dynamics", Piecewise smooth Dynamical systems, Naples, 18 – 20/9/2006.
- [60] M. Jean. Documentation sur LMGC - Logiciel de Mécanique Gérant le Contact. LMA-CNRS, ESM2 ; 25/01/1996, Université de la Méditerranée (Aix-Marseille II).
- [61] Wikipedia. Discontinuous deformation analysis.
[http://en.wikipedia.org/wiki/ Discontinuous _ Deformation_Analysis](http://en.wikipedia.org/wiki/Discontinuous_Deformation_Analysis) ; 10/01/13.
- [62] W.S. Dershowitz, P.R. La Pointe, T.W. Doe. Advances in Discrete Fracture Network Modeling. 2004 U.S. EPA/NGWA Fractured Rock Conference. Maine, U.S; 2004.
- [63] J. Sausse, C. Dezayes, A. Genter, A. Bisset. Characterization of fracture connectivity and fluid flow pathways derived from geological interpretation and 3D modelling of the deep seated EGS reservoir of Soultz (France). Proceedings of the 33rd Workshop on Geothermal Reservoir Engineering; 2008: 8.
- [64] D. Heliot. Generating a blocky rock mass. Int. J. Rock Mech. Min. Sci.; 1988; 25(3): 127-38.
- [65] G. Fu, L. He, G. Ma. 3D Rock mass geometrical modelling with arbitrary discontinuities. International journal of applied mechanics; 2010; 2(4): 871-87.

- [66] Y. Zhang, M. Xiao, J. Chen. A new methodology for block identification and its application in a large scale underground cavern complex. *Tunnelling and Underground Space Technology*; 2010; 25: 168 – 80.
- [67] M. Elmouttie, G. Poropat, G. Krahenbuhl. Polyhedral modelling of rock mass structure. *International Int. J. Rock Mech. Min. Sci.*; 2010; 47: 544 – 52.
- [68] P.M. Warburton. A computer program for reconstructing blocky rock geometry and analysing single block stability. *Computer and Geosciences*; 1985; 11(6): 707 – 12.
- [69] A. Rafiee, M. Vinches. Technical note. Application of geostatistical characteristics of rock mass fracture systems in 3D model generation. *Int. J. Rock Mech. Min. Sci.*; 2008; 45: 644 – 52.
- [70] P.R. Sheorey, A.K. Biswas, V.D. Choubey. An empirical failure criterion for rocks and jointed rock masses. *Engineering Geology*; 1989; 26(2): 141–159.
- [71] P.M. Warburton. *Comprehensive rock engineering. Volume 2: Analysis and design methods. Some modern developments in Block theory for rock engineering.* 1st ed. Great Britain: Pergamon press; 1993.
- [72] A. Rafiee, M. Vinches, C. Bohatier. La méthode NSCD (Non-Smooth Contact Dynamics) appliquée à la simulation du comportement mécanique des massifs rocheux fracturés. *XXVIe Rencontres Universitaires de Génie Civil. Nancy*, 4 – 6/6/2008.
- [73] P. Pecol, S.D. Pont, S. Erlicher, P. Argoul. Smooth/non-smooth contact modeling of human crowds movement: numerical aspects and application to emergency evacuations. *Ann. Solid Struct. Mech*; 2011; 2: 69–85.
- [74] H.H. Einstein, W. Steiner, G. Baecher. Assessment of empirical design methods for tunnel in rocks. *Conference of Assessment of Empirical Design Methods for Tunneling in Rock*; Baecher; 1979.
- [75] E. Hoek, E.T. Brown. *Underground Excavation Engineering.* Institution of Mining and Metallurgy, London; 1978: 527.
- [76] The British Tunnelling Society and The Institution of Civil Engineers. *Tunnel lining design guide.* 1st Ed. Thomas Telford Publishing, London: 2004.
- [77] ITA Working group on General approaches to the Design of tunnels. *Guidelines for the Design of Tunnels.* *Tunnelling and underground space technology*; 1988; 3(3): 237-49.

- [78] B.H.G. Brady, E.T. Brown. Rock mechanics for underground mining. London: George Allen & Unwin; 1985: 527.
- [79] Brekke, T. L. and Ripley, B. D. Design Guidelines for Pressure Tunnels and Shafts. Electric Power Research Institute, Final report AP-5273 EPRI; 1987.
- [80] US department of transportation. Federal highway administration. Technical Manual for Design and Construction of Road Tunnels - Civil Elements.
<http://www.fhwa.dot.gov/bridge/tunnel/pubs/nhi09010>; 04/02/2013.
- [81] B. Maidl, M. Herrenknecht, U. Maidl, G. Wehrmeyer. Mechanised Shield Tunnelling. 2nd Ed. Ernst & Sohn, Berlin: 2011.
- [82] F.S. Feng and T.H. Huang. The holding mechanism of under-reamed rockbolts in soft rock. International Journal of Rock Mechanics and Mining Sciences; 1999; 36: 761-75
- [83] Z.T. Bieniawski. Tunnel design by rock mass classifications. Updated Technical report GL-79-19. Department of the Army - US Army Corps of Engineers; 01/1990.
- [84] A. Palmstrom, H. Stille. Ground behaviour and rock engineering tools for underground excavations. Tunnelling and Underground space technology; 2007; 22:363-76.
- [85] S. Tzamos, A.I. Sofianos. A correlation of four rock mass classification systems through their fabric indices. International Journal of Rock Mechanics & Mining Sciences; 2007; 44: 477–495.
- [86] T.R. Silverton, A.H.Thomas & D.B. Powell. Risk-Based Design using Numerical Modelling. <http://www.tunnels.mottmac.com/tunnelsexpertise/riskmanagement/>; 07/01/2013.
- [87] USACE. Engineering and Design - Tunnel and shafts in rock. CECW-EG Engineer manual 1110-2-2901; Washington: 30/5/1997.
- [88] O. Aydan. The stabilisation of rock engineering structures by rockbolts. PhD thesis. University of Nagoya; Japan: 1989.
- [89] British Standards Institution. EN 1997-1:2004. Eurocode 7: Geotechnical Design – Part 1: General Rules. Code of Practice. BSI, London: 2004.
- [90] K. Kovari, P. Lunardi. On the observation method in tunneling. Proceeding of the International conference GeoEng2000; Melbourne: 11/2000.
- [91] R. B. Peck. Advantages and Limitations of the Observational Method in Applied Soil Mechanics. Géotechnique; 1969; 19(2): 171 – 87

- [92] D Nicholson, N. Huybrechts, J. Maertens. The Observational Method in Geotechnics.
http://www.arup.com/_assets/_download/41A6ACB0-DD6E-06AC-F7C03C57BF321BA5.pdf; 09/01/2013.
- [93] H. Stille, A. Palmstrom. Classification as a tool in rock engineering. *Tunnelling and underground space technology*; 2003; 18: 331 – 45.
- [94] Z. Gurocak, P. Solanki, M.M. Zaman. Empirical and numerical analyses of support requirements for a diversion tunnel at the Boztepe dam site, eastern Turkey. *Engineering Geology*; 2007; 91: 194–208
- [95] S.C. Moller, P.A. Vermeer. On numerical simulation of tunnel installation. *Tunnelling and Underground Space Technology*; 2008; 23: 461–475.
- [96] S.Y. Wang, S.W. Sloan, C.A. Tang, W.C. Zhu. Numerical simulation of the failure mechanism of circular tunnels in transversely isotropic rock masses. *Tunnelling and Underground Space Technology*; 2012; 32: 231–244.
- [97] H. Mashimo, N. Isago and K. Fujii. Evaluation of loads acting on the tunnel supports. *GeoEng2000*; Melbourne: 19 – 24/11/2000.
- [98] H.Y. Liu, J.C. Small, J.P. Carter. Full 3D modelling for effects of tunnelling on existing support systems in the Sydney region. *Tunnelling and Underground Space Technology*; 2008; 23: 399–420.
- [99] G. Swoboda and A. Abu-Krishanumerical. Three-Dimensional Numerical Modelling for TBM Tunnelling in Consolidated Clay. *Tunnelling and underground space technology*, 1999; 14(3).
- [100] H. Mroueh, I. Shahrour. A simplified 3D model for tunnel construction using tunnel boring machines. *Tunnelling and Underground Space Technology*; 2008; 23: 38–45.
- [101] C. Yoo. Performance of multi-faced tunnelling – A 3D numerical investigation. *Tunnelling and Underground Space Technology*; 2009; 24: 562–573.
- [102] G. Galli, A. Grimaldi, A. Leonardi. Three-dimensional modelling of tunnel excavation and lining. *Computers and Geotechnics*; 2004; 31: 171–183.
- [103] J. Bartak, M. Hilar, J. Pruška. Numerical modelling of overburden deformations. Czech Technical University Publishing House, *Acta Polytechnica*; 2002; Vol. 42 No. 1.

- [104] M. Barla. Numerical simulation of the swelling behaviour around tunnels based on special triaxial tests. *Tunnelling and Underground Space Technology*; 2008; 23: 508–52.
- [105] G. Barla. Lessons learnt from the excavation of a large diameter TBM tunnel in complex hydro-geological conditions. *GeoEng* 2000.
- [106] J. Maryska, O. Severyn, M. Tauchman, D. Tondr. Modelling of processes in fractured rock using FEM/FVM on multidimensional domains. *Journal of Computational and Applied Mathematics*; 2008; 215: 495 – 502.
- [107] R. Adey and A. Calaon. Modelling Underground Mines For Rock Stability Assessment Using Boundary Elements. A New Approach For Large Scale Problems. 2nd International Conference on Waste Management and the Environment; Rhodes – Grece: 29/09/2004.
- [108] M. Cerrolaza and R. Garcia. Boundary elements and damage mechanics to analyze excavations in rock mass. *Engineering Analysis with Boundary Elements*; 1997; 20: 1-16.
- [109] J. Guittard, S. Souvignet, M. Gasc-Barbier, D. Virely. Field investigations campaign realized for St Beat tunnel (France –31). *Géoline – Lyon*: 23 - 25/5/2005.
- [110] M.J.M. Maynar and L.E.M. Rodriguez. Discrete Numerical Model for Analysis of Earth Pressure Balance Tunnel Excavation. *Journal of geotechnical and geoenvironmental engineering* © ASCE; 10/2005.
- [111] S. Chen, J. C. Chern, C. Y. Koo. Performance prediction of tunnel excavation in clean cobble-gravel deposits by DDA method. *Proceedings of the 2nd North American Rock Mechanics Symposium*; 1996.
- [112] J.H. Wu, Y. Ohnishi, S. Nishiyama. Study on Tunneling in Rock Masses with Inclined Layers Using Discontinuous Deformation Analysis (DDA). *International Society for Rock Mechanics. 10th Congress Technology roadmap for Rock Mechanics*; 2003; Volume 2.
- [113] M. Gasc-Barbier, P. Alfonsi. Open fractures on rock slopes: experimental and numerical analysis. *Géoline – Lyon*: 23 - 25/5/2005.
- [114] D.C.C.P Peacock, S.D. Harris, M. Mauldon. Use of curved scanlines and boreholes to predict fracture frequencies. *Journal of Structural Geology*; 2003; 25: 109-19.
- [115] A.K. Manda, S.B. Mabee. Comparison of three fracture sampling methods for layered rocks. *Int. J. Rock Mech. Min. Sci.*; 2010; 47: 218-26.

- [116] J. Kemeny, R. Post. Estimating three-dimensional rock discontinuity orientation from digital images of fracture traces. *Computers and Geosciences*; 2003; 29: 65-77.
- [117] M.J. Lato, M.S. Diederichs, D.J. Hutchinson. Bias correction for view-limited Lidar scanning or rock outcrops for structural characterization. *Rock Mech Rock Eng*, DOI 10.1007/s00603-010-0086-5.
- [118] B.V. Knapen, S. Slob. Identification and characterization of rock mass discontinuity sets using 3D laser scanning. *IAEG2006*: 438, London: 2006.
- [119] F. Lemy, J. Hadjigeorgiou. Discontinuity trace map construction using photographs of rock exposures. *Int. J. Rock Mech. Min. Sci.*; 2003; 40: 903-17.
- [120] A. Palmström. RMi – a rock mass characterization system for rock engineering purposes. PhD thesis, University of Oslo, Department of Geology; 1995.
- [121] M.A. Saliu, J.M. Akande. Fracture characterization: An effective technique for ensuring accurate blast design. *Journal of Emerging trends in Engineering and Applied sciences*; 2011; 2(6): 1015-19.
- [122] K. Grossenbacher, K. Karasaki, D. Bahat. Curved scanline theory. *Mathematical Geology*; 1997; Vol. 29, No. 5.
- [123] M. Mauldon, M. B. Rohrbaugh Jr., W. M. Dunne and W. Lawdermilk. Fracture intensity estimates using circular scanlines. 37th U.S. Symposium on Rock Mechanics; , Vail, CO: 7 – 9/6/1999.
- [124] P.J. Pahl. Estimating the mean length of discontinuity trace. *Int J Rock Mech Mining Sci*; 1981; 18: 221-8.
- [125] G.M. Laslett. Censoring and edge effects in areal and line transect sampling of rock joint traces, *Math. Geol.*; 1982; 14(2): 125 – 40.
- [126] E. Villaescusa and E.T. Brown. Characterising joint spatial correlation using geostatistical methods, *Proc. International Symposium on Rock Joints*, Barton and Stephansson (eds), Balkema, Norway; 1990; 115-122.
- [127] Q. Feng. Novel methods for 3-D semi-automatic mapping of fracture geometry at exposed rock faces. Doctoral thesis of Royal Institute of Technology, Stockholm. Sweden: 2001.

- [128] C. Feng. Correction of discontinuity spacing bias caused by finite length scanline survey. Trans. Nonferrous Met. Soc. China; 1996; Vol.6, Issue 3.
- [129] R.D. Terzaghi. Sources of error in joint surveys. Geotechnique ; 1965; 15(3): 287-304. DOI 10.1680/geot.1965.15.3.287.
- [130] R. Jimenez-Rodriguez, N. Sita. A spectral method for clustering of rock discontinuity sets. Int. J. Rock Mech. Min. Sci; 2006; 43: 1052-61.
- [131] N. Cardozo and R.W. Allmendinger. Spherical projections with OSXStereonet. Computers & Geosciences; 2013; 51: 193–205
- [132] M. J. Lato, M. S. Diederichs, D. J. Hutchinson. Bias Correction for view-limited Lidar scanning of rock outcrops for structural characterization. Rock Mech Rock Eng. DOI: 10.1007/s00603-010-0086-5.
- [133] R. E. Hammah, J. H. Curran. On distance measures for the Fuzzy K-means algorithm for joint data. Rock Mech. Rock Eng.; 1999; 32(1): 1-27.
- [134] J. MacQueen. Some methods for classification and analysis of multivariate observations. Proceedings of the Fifth Berkeley Symposium on Mathematical Statistics and Probability. Volume I, Statistics. Edited by Lucien M. Le Cam and Jerzy Neyman. University of California Press: 1967.
- [135] K. Teknomo. Numerical example of K-means clustering.
<http://people.revoledu.com/kardi/tutorial/kMean/NumericalExample.htm>; 23/11/2013.
- [136] R. Jimenez. Technical note. Fuzzy spectral clustering for identification of rock discontinuity sets. Rock Mech Rock Engng; Netherland; 2008; 41: 929-39.
- [137] LAEGO, Ecole des Mines de Nancy, France. RESOBLOK's V5.03 Notice d'utilisation. France: 2008.
- [138] R. Fisher. Dispersion on a sphere. Proc. R. Soc. Lond. A ; 1953 ; 217 : 295-305. DOI: 10.1098/rspa.
- [139] J. H. Shuenemeyer, L. J. Drew. Statistics for Earth and Environmental Scientists. John Wiley & Sons, Inc. New Jersey: 2011.
- [140] A. Banerjee, I. S. Dhillon, J. Ghosh and S; Sra. Clustering on the Unit Hypersphere using von Mises-Fisher Distributions. Journal of Machine Learning Research; 09/2005; 6(Sep): 1345–1382.
- [141] A.T.A Wood. Simulation of the von Mises - Fisher distribution. Communications in

Statistics - Simulation and Computation; 1994; 23(1): 157 - 164.

[142] T. Kobayashi, N. Otsu. Von Mises-Fisher Mean Shift for Clustering on a Hypersphere. 20th International Conference on Pattern Recognition. Istanbul, 2010.

[143] D. Lin and C. Fairhurst. Static analysis of the stability of three dimensional blocky systems around excavations in rock. Int. J. Rock. Mech. Min. Sc. & Geomech. Abstr; 1988; 25(3): 139 – 47.

[144] H. Baroudi, D. Hantz, M. Asof, J.P. Piguet. Bench stability in open pit Mines: a methodology for jointed Rock masses. Regional Conference on fractured and jointed rock masses, Lake Tahoe, California; 1992.

[145] NF P 94-423 Roches - Détermination de la résistance à la compression triaxiale

[146] NF P 94-425 Roches - Détermination du module de Young et du coefficient de Poisson

[147] ASTM D7012-10 Standard Test Method for Compressive Strength and Elastic Moduli of Intact Rock Core Specimens under Varying States of Stress and Temperatures

[148] ASTM D4543-08 Standard Practices for Preparing Rock Core as Cylindrical Test Specimens and Verifying Conformance to Dimensional and Shape Tolerances.

[149] TTN. Hoang. Mémoire de thèse: Etude du comportement d'un milieu rocheux fracturé: Application à la réalisation du tunnel de St Bât, Ecole des Ponts PariTech, Paris : 2010.

[150] TECHNOTEST, Catalogue 2010, 2nd Edition, <http://www.tecnotest.it> ; 12/11/2012.

[151] M. Potsch, W. Schubert, A. Goricki, A. Steidl. Determination of Rock Mass Behaviour Types - a Case Study. Eurock 2004 & 53rd Geomechanics Colloquium. Schubert (ed.) © 2004 VGE.

[152] M. Reeves. Course GEOE 118.3 Geology for Engineers. Department of Civil and Geological Engineering, University of Saskatchewan.

[153] J. Papay. Permeability as function rock mechanical behaviour. NAFTA;2012; 63(1-2): 99-104; <http://homepage.usask.ca/~mjr347/prog/geoe118/geoe118.035.html>; 20/2/2013.

[154] W. R. Wawersik, C. Fairhurst. A study of brittle rock fracture in laboratory compression experiments. Int. J. Rock Mech. Min. Sci.; 1970; 7: 561 - 75.

[155] C. He, S. Okubo and Y. Nishimatsu. A Study on the Class II Behaviour of Rock. Rock Mechanics and Rock Engineering; 1990; 23: 261 – 273.

- [156] F. Dubois. LMGC90 User's guide. Formation of LMGC90, University of Montpellier: 2012.
- [157] V. Louchnikov. A numerical investigation into the stress memory effect in rocks. Thesis of Master of Engineering Science (Geomechanics). The University of Adelaide. Australia:, 2004.
- [158] B. Amadei and O. Stephansson. Rock stress and its measurement. 1st ed. Chapman & Hall. London: 1997.
- [159] SINTEF. In-situ stress measurement. Brief introduction of methods applied by SINTEF. Updated version. Trondheim, Norway: 12/2005
- [160] A.K.Ghosh. Rock Stress Measurements for Underground Excavations. 12th International Conference of International Association for Computer Methods and Advances in Geomechanics; Goa, India: 1-6/10/2008.
- [161] F. Radjai, F. Dubois. Discrete Numerical Modelling of Granular Materials. 1st ed. London: ISTE Ltd and John Wiley & Sons Inc; 2011.
- [162] F. Dubois. Overview of LMGC90. Formation of LMGC90. University of Montpellier 2: 16/06/2010.
- [163] F. Dubois and M. Renouf. LMGC90 software: Toolbox for the simulation of multi-contact systems. Formation of LMGC90. University of Montpellier 2: 01/2008.
- [164] F. Dubois *et al.* LMGC90. CSMA 2011. 10e Colloque National en Calcul des Structures, Var, France : 9-13/05/2011.
- [165] A. Martin, M. Bagneris, F. Dubois, R. Mozul. LMGC90v2 Pré : le préprocesseur de LMGC90. Laboratoire de Mécanique et Génie Civil, Formation LMGC90. Université de Montpellier 2 : 05/2011.
- [166] C. Geuzaine, J.-F. Remacle. Gmsh: a three-dimensional finite element mesh generator with built-in pre- and post-processing facilities, Int. J. Numer. Methods Eng.; 2009; 79(11): 1309-31.
- [167] ITA. Working Group No. 2. Guidelines for the Design of Shield Tunnel Lining. Tunnelling and Underground Space Technology; 2000; 15(3): 303 – 31.
- [168] Y. Nielsen. Loads on tunnel. Course CE 439 - Railway and metro tunnels. Middle East Technical University of Turkey. <http://www.ce.metu.edu.tr/~CE439>; 10/10/2011.

- [169] Google satellite map, <http://maps.google.fr/maps?hl=fr&tab=wl> ; France : 12/11/2012.
- [170] Laboratoire Régional des Ponts et Chaussées de Toulouse. R.N. 125 – Tunnel de Saint-Béat. Géologie générale. Dossier N° 20-31-101-1999/20-027-97-471; France : 12/2006.
- [171] A. McCracken *et al.* (SRK Consulting), Mine de Marbre de Saint Béat – Géotechniques et Concept Minier; France: 12/2005.
- [172] M. Renard *et al.* Rapport final d'étude des différents faciès (dit "faciès marteau") des marbres de Saint Béat, Université Pierre de Marie Curie ; France : 2006.
- [173] F. Hadj-Hassen. Evaluation des conditions de stabilité de la nouvelle méthode d'exploitation par sous niveau abattus du gisement de marbre de Saint Béat. Ecole des Mines de Paris ; France : 12/2006.
- [174] CETE Méditerranée. Analyse de l'aléa sismique au tunnel de Saint Béat, RN125. France : 10/2006.
- [175] WikiSara, Route national N125,
http://routes.wikia.com/wiki/Route_nationale_fran%C3%A7aise_125 ; France : 14/11/2012.
- [176] D. Virely, J. Guittard, M. Gasc-Barbier. Caractérisation expérimentale et in-situ de la matrice et des discontinuités rocheuses: Cas du tunnel de St-Beat. Journées Nationales de Géotechnique et de Géologie de l'Ingénieur ; Lyon : 2006.
- [177] CETE Lyon. Tunnel de Saint Béat. Mesures de contraintes par surcarottage et vérin plat. Lyon : 10/2005.
- [178] INERIS, Direction des Risques du Sol et du Sous-sol. Mesures de contraintes par surcarottage au droit du projet du tunnel de déviation de la route RN 125 (31). Rapport final DRS-11-121146-12690A. France: 28/11/2011.
- [179] Consortium Scilab – Digiteo – Michael Baudin. Introduction to Scilab. Update 09/2011, <http://www.Scilab.org/support/documentation/tutorials>; 06/12/2112.
- [180] J. Handin, On the Coulomb – Mohr failure criterion, Journal of Geophysical Research; 1969; Vol. 74, No. 22.
- [181] I. Munoz. Modélisation numérique du massif de Saint-Béat (Haute-Garonne). Progiiciel CESAR-LCPC. Report of stage for Master 2. University of Blaise Pascal - Clermont-Ferrand, France: 2010.
- [182] Préfecture de la région Midi-Pyrénées, Communiqué de Presse. France : 01/08/2012.

[183] DREAL Midi-Pyrénées, Opérations du PDMI. Département de la HAUTE-GARONNE. Opérations sur RN124 et RN125. Maîtrise d'ouvrage: DREAL Midi-Pyrénées, http://www.midi-pyrenees.developpement-durable.gouv.fr/IMG/pdf/RN124_125_HGfichesPDMI_conventions_signees_cle05f5c1.pdf ; France : 121/11/2012.

[184] P.R. Sheorey. Empirical rock failure criteria. Rotterdam: A.A. Balkema; 1997.

[185] R.G. Takwale and P.S. Puranik. Introduction to classical mechanics. 34th reprint. New Delhi: Tata McGraw-Hill; 206.

[186] V. Merrien-Soukatchoff. Milieux discontinus. Ecole des Mines de Nancy.

<http://www.mines.inpl-nancy.fr/geoingenierie/T041/T041/RESOBLOK/Milieux%20discontinus.pdf>. France : 0/1/2013.

TITLE: Combined application of structural geology, the mechanics of discrete media and the analysis of in situ stresses and displacements for the modelling of mechanical behaviour of fractured rock masses

ABSTRACT: Aimed at studying the mechanical behaviour of rock mass and considering the presence of the discontinuity network in the intact rock, this research concentrates on how the rock can be represented in suitable geometrical models, on the basis of site measurements, and then appropriately analysed using computer tools developed for the study of granular media. The first chapter deals with a bibliographical study on fractured rock and tunnel engineering. Different computational methods of rock mechanics are introduced. Simultaneously, three principal approaches for tunnel structural design are recalled. These studies lead to the proposition of a methodology from the in situ investigation to in-door modelling and mechanical analysis, presented in the second chapters. The rock mass is first geometrically represented through the distribution of discontinuities in the rock mass and the use of the RESOBLOK code based on the Discrete Fracture Network method. Mechanical models of rock mass are then presented from the data of historical studies on the rock mass and from laboratory and *in situ* measurements. The 3D computational models are analysed using the LMGC90 based on the Non Smooth Contact Dynamics method. The first two applications of the methodology are introduced: the generation of the numerical rock for the simulation of the triaxial compression test, and the simulation of multi-phase excavation of rock tunnel. The proposed methodology has been applied on the white marble of Saint B  at (Haute Garonne, France) and the initial results are given in the third chapter. The mechanical responses of the numerical rock mass are analysed and the bulk behaviour of the rock is evaluated.

KEYWORDS: Rock mechanics, tunnel, fractured rock, *in situ* investigation, measurement, scan-line sampling, geo-statistics, clustering, geometrical modelling, mechanical modelling, simulation, mechanical analysis, mechanical behaviours, stability analysis, Discrete Fracture Network (DFN) method, RESOBLOK, Non-Smooth Contact Dynamics (NSCD) method, LMGC90, Saint B  at.

TITRE : Application combin  e de la g  ologie structurale, de la m  canique des milieux discrets et de l'analyse de contraintes et d  placements in situ    la mod  lisation du comportement m  canique de massifs rocheux fractur  s

RESUME : Pour   tudier le comportement m  canique des massifs rocheux, en prenant en compte le r  seau des discontinuit  s au sein de la roche intacte, cette recherche a pour objectif la repr  sentation du massif par des mod  les g  om  triques bas  s sur des relev  s de terrain et l'analyse de ces mod  les par l'utilisation d'outils informatiques adapt  s pour les milieux granulaires. Le premier chapitre fait l'  tat de l'art des roches fractur  es, des m  thodes num  riques de la m  canique des roches et des approches du calcul de structure d'un tunnel. Ces   tudes conduisent    la proposition d'une m  thodologie depuis les recherches in situ jusqu'   la mod  lisation et l'analyse m  canique, pr  sent  e dans le deuxi  me chapitre. Le massif rocheux est d'abord repr  sent   g  om  triquement par la distribution de ses discontinuit  s, et l'utilisation du logiciel RESOBLOK bas   sur la m  thode du R  seau de Fractures Discr  tes. Les mod  les m  caniques de massifs rocheux sont ensuite pr  sent  s    partir des donn  es sur les   tudes de l'histoire du massif, et des mesures faites sur site et en laboratoire. Les mod  les num  riques en 3D sont analys  s par l'utilisation du logiciel LMGC90 bas   sur la m  thode de la Dynamique des Contacts Non R  guliers. Les premi  res applications de la m  thodologie sont expos  es : la cr  ation d'une roche num  rique pour simuler un essai de compression triaxiale, et la simulation d'une excavation multi phases d'un tunnel au rocher. La m  thodologie propos  e a   t   appliqu  e sur le marbre blanc de Saint B  at (Haute Garonne, France) et les r  sultats pr  liminaires sont donn  s dans le chapitre trois. Les r  ponses m  caniques de la roche num  rique sont analys  es et son comportement est caract  ris  .

MOTS CLES: M  canique des roches, tunnel, roche fractur  e, recherche in situ, ligne-scann  e, g  ostatistique, regroupement, mod  lisation g  om  trique, mod  lisation m  canique, simulation, analyse m  canique, comportement m  canique, analyse de stabilit  , m  thode du R  seau de Fractures Discr  tes (DFN), RESOBLOK, m  thode de la Dynamique des Contacts Non-R  guliers (NSCD), LMGC90, Saint B  at.

Travaux r  alis  s    l'**Ecole des Mines d'Al  s**, 6 avenue de Clavi  res, 30319 Al  s Cedex, France.